POLITECNICO
MILANO 1863

SCHOOL OF CIVIL, ENVIRONMENTAL, AND LAND MANAGEMENT ENGINEERING

Master of Science in Civil Engineering

A Study on Seismic Behavior of Masonry Church in Milan, Italy by Linear and Non-Linear Analysis

By

Mert Col

Matr. Number: 940540

April 2022, Milan, Italy

Supervisor: Prof. Claudio Chesi

Co-advisor: Eleonora Magrinelli

Abstract

In this study, the seismic behavior of the ancient masonry church namely “San Carpoforo” which is located in Milan, Italy is examined. Since the seismic actions leave behind a trail of huge damage on the ancient masonry churches, and masonry churches are characterized by box behavior that is totally different from frame behavior, seismic assessment is essential, especially for the ones that are still available to be used. To be able to do that, in this study, the 3-D geometric model is discretized in ABAQUS software by using second-order tetrahedral elements (C3D10). Then, the concrete damage plasticity (CDP) model is adopted in order to reflect the behavior of the masonry. In the end, linear static analysis, and non-linear static analysis (pushover analysis) are carried out for reaching the conclusion about the situation of the church. Ultimately, static non-linear analysis results point out that the demand displacements are lower than the capacity of the structure.

Keywords: Masonry, Cultural Heritage, FE analysis, Concrete Damage Plasticity, Response Spectrum Analysis, Pushover Analysis, N2 Method

Abstract (Italian)

In questo studio viene esaminato il comportamento sismico dell'antica chiesa in muratura denominata "San Carpoforo" che si trova a Milano, in Italia. Poiché le azioni sismiche lasciano dietro di sé una scia di ingenti danni sulle antiche chiese in muratura, e le chiese in muratura sono caratterizzate da un comportamento a scatola totalmente diverso dal comportamento a telaio, la valutazione sismica è essenziale, soprattutto per quelle che sono ancora disponibili all'uso. Per poterlo fare, in questo studio il modello geometrico 3D viene discretizzato nel software ABAQUS utilizzando elementi tetraedrici del secondo ordine (C3D10). Quindi, viene adottato il modello di plasticità del danno concreto (CDP) per riflettere il comportamento della muratura. Al termine si procede all'analisi statica lineare e statica non lineare (analisi pushover) per giungere alla conclusione sulla situazione della chiesa. In definitiva, i risultati dell'analisi statica non lineare evidenziano che gli spostamenti della domanda sono inferiori alla capacità della struttura.

Keywords: Muratura, Patrimonio Culturale, Analisi FE, Plasticità dei danni al calcestruzzo, Plasticità dei danni al calcestruzzo, Risposta Analisi dello Spettro, Analisi Pushover, Metodo N2

Acknowledgment

I would like to express my deepest gratitude and thanks to Prof. Claudio Chesi for his support and guidance that makes the study possible. I also want to present my appreciation to Eleonora Magrinelli who provided full support for the software used in this thesis.

Lastly, I am grateful to my family for their love and infinite support for me.

Table of Contents

List of Tables

List of Figures

1 Introduction

Churches, being among the historical structures, has played a significant role in the western world. It is known that the masonry churches are characterized by their seismic vulnerability since these structures have been constructed on the basis of empirical approaches in a way that only gravity loads are factored in. Hence, generally, masonry churches suffer from horizontal actions arising due to seismic actions. The barriers against conducting analysis of masonry churches are related to their complex geometries and material properties. [1] To explain, Huerta pointed out that although masonry was used as a primary material instead of concrete, and steel reinforcements, these structures have not been kept their dominance in the world, especially in Europe, after the beginning of the 20^{th} century. [2] Nevertheless, it may sometimes be required to make an analysis of the structures that have a different purpose to be used. This situation specifically corresponds to the case study of San Carpoforo church in Milan, Italy which has been used for a special academic purpose since 2002. The masonry materials are endowed with low tensile strength and they show non-linear behavior. [3] In the past, it was not possible to reflect this kind of material properties, but ABAQUS allows a large variety of material properties. In this study, Concrete Damage Plasticity Model was used in order to obtain realistic masonry material behavior. Furthermore, since the churches are characterized by high external walls, large spans without slabs, and complex vaults, and suffer from the inadequate horizontal diaphragm and interlock of the walls, they may not have box behavior successfully. [4] In order to sort these difficulties out, a macro-modeling approach was used, and the global behavior of the San Carpoforo church was investigated in this thesis. To do so, the 3D model was handled in AutoCAD, and the geometric model was discretized in ABAQUS software. Having obtained the modal analysis results that give the basic insight into the behavior of structures, in turn, static linear and static non-linear analyses were performed.

2 Masonry Buildings

2.1 Brief History of Masonry

Since the supply of masonry is directly from nature, it is well known that masonry construction is a pioneering technique in civil engineering. [5] It is a composite material consisting of blocks and mortar. While mortar may be lime or cement, blocks can be of various types such as clay bricks, concrete blocks, and stone blocks. Taly stated that masonry construction began with the “random rubble dry masonry” which is a constructive approach in which mortar is not used. [5] In the pursuit of this, “brick” material appeared 10-12 thousand years ago. In addition, it turned into “sun-dried bricks” that were used in Egypt, Babylon, etc. over time. It was pointed out that the invention of the fired brick about 3500 B.C. paved the way for the molded brick became to be used about 5000 B.C. [5] Moreover, many special structures such as the Great Wall of China, Taj Mahal, Hagia Sophia, and the Hanging Gardens can be given as examples for the brick-based structures. [5] Additionally, there have been many different materials used as binders throughout history. The first mortars were obtained by a mixture of clay and mud. [6] Afterward, the ancient Persians and Egyptians introduced bitumen, and gypsum as a binder, respectively. [6] Como indicated that the last milestone of masonry took place with the discovery of lime by the Etruscans. [6] Furthermore, the lime having the ability of hardening in time was produced by burning limestone and combining it with the water. Como stated that the mixture of lime and pozzolana provides an improvement in the quality of mortars. [6]

2.2 Modeling of Masonry Structures

Masonry structures can be mainly modeled in 3 different ways. [7] In the case of detailed micro-modeling, while the unit-mortar interface is considered as discontinuous elements, units and mortar at the joints are supposed as continuum ones. In the second approach named macro-modeling, it is accepted that both units, the mortar, and the mortar-unit interface are smeared out in the continuum. For the third one called homogenization, the complexity of the cell composed of mortar and unit is transformed into the homogenized continuum.

In the study of Lourenço et. al, it has been stated that in the case of determining the global behavior consideration for the unit and mortar interface can be neglected. [8] It has been pointed out that in this approach, the material is accepted as an anisotropic composite having different tensile and compressive strengths along the axes. [8]

Italian Guidelines for Cultural Heritage provide three classifications of the seismic assessment of the existing structures as follows. [1]

- EL1 (LV1): It is based on the qualitative analysis and prediction of the vulnerability index.
- EL2 (LV2): It is related to local collapse mechanisms.
- EL3 (LV3): It concerns the global assessment of the seismic response of structures.

Zizi et al. stated that the EL3 level of analysis is performed by linear and non-linear numerical analyses.

For this case study, EL3 has been adopted in order to capture the global behavior of the San Carpoforo Church.

In conclusion, global intervention can be only handled by adopting global analysis (EL3), restoration or local interventions can be done by mechanical methods on limited portions (EL2), fast assessment can be obtained by doing simplified mechanical statistical methods (EL1), and damage scenario can be predicted by empirical methods (EL0). [1]

3 Literature Review

There have been several studies on the finite element analysis of ancient structures all over the world. Jain et. Al studied the numerical analysis of the church San Francesco, Amatrice by considering the damage and collapse mechanisms due to the seismic events in Italy, in 2016. [9] By means of dynamic non-linear analysis, they compared the real damages and the one obtained from ABAQUS, and they found out that it is an extremely effective tool to estimate the seismic behavior of structures.

Formisano et. al studied the seismic vulnerability assessment for an isolated masonry palace as an internal oratory in Italy by means of both the simplified LV1 level and refined LV3 level approaches and they compared these two methods. [10] Italian Guidelines on Cultural heritage provide three different levels. They found out that while the LV3 analysis level carried out by nonlinear numerical analysis reflects the global behavior of the structure, the LV1 analysis level underestimates the capacity acceleration of the irregular structures.

In the study of Ferrante et. al, both Finite Element (FE) and Discrete Element (DE) approaches were carried out for numerical modeling of the Santissimo Crocifisso Church in Pretare which was exposed to severe damages during the 2016 seismic sequence. [11] They declared that both continuous and discontinuous methods are in good agreement with the real crack pattern. The Concrete Damage Plasticity model reflecting the complex non-linear behavior was used for the FE approach whereas the Non-Smooth Contact Dynamics Method providing a chance to examine the local failure mechanisms was exploited for the DE approach. It was also affirmed that modeling time is higher in the DE model compared to the FE model, and the computational cost of non-linear dynamic analysis is extremely expensive for both models.

Clementi et al. investigated the impact of the annex that was constructed later than the church of Santa Maria della Carita in Ascoli Piceno on the seismic behavior of the historical complex and they extended it by generalization for the case of structures endowed with asymmetric mass. [4] They used 8 different models by taking into account interventions and considering solely the church, and both church and annex. [4] In this paper, firstly, 50 modes are extracted in order to fulfill to provide at least 80 percent of the total mass for these models. From all 8 models, they deduced that the most vulnerable part concerns the bell tower since both the first and second modes are related to the bell tower. Then, nonlinear static analysis was carried out

by means of pushover analysis. Ultimately, the Seismic Risk Index (I_R) was computed for the models.

In addition, Giordano et al. performed the numerical modeling in order to carry out the damage assessment in Sant'Agostino's Sanctuary in Offida during the central Italy 2016-2017 seismic sequence. [12] It was stated that since many local modes influence the monastery, 300 modes were extracted to have more than 85 percent of the total mass. According to observations, the structure was firstly hit by the L'Aquila earthquake having a magnitude M_W = 6.3. [12] Following this, there was an impact on the school building and cracks were observed at the main façade of the church this led to doing some interventions. After the seismic sequence of 2016, the church was exposed to severe damage, and the square in front of the church was closed due to protection precautions. They developed two finite element models regarding the slab considerations composed of 454829 solid elements in MIDAS software. They compared the seismic capacity obtained by pushover analysis which is a non-linear static approach with the seismic demand gained by linear dynamic analysis provided by Italian code spectra.

Clementi carried out the damage analysis of 6 masonry churches that have been damaged during the 2016 central Italy seismic sequence and compared them with the results of non-linear static analysis in the developed finite element models. [13] It was used 16,466 elements, 57,889 elements, 29,706 elements, 5642 elements, 24,814 elements, and 169,935 elements in the numerical models performed in MIDAS FEA software for San Francesco Church in Montefortino, San Francesco church in Sarnano, Sant'Anna Church in Camerino, Sant'Antonio church in Ussita, Madonna of Valcora Sanctuary in Fiuminata, and Santissimo crocifisso in Arquata del Tronto, respectively. In this study, since churches are sensitive in terms of local modes, many modes were extracted in order to meet 85 percent of the total mass. 34 modes, 271 modes, 30 modes, 28 modes, 40 modes, and 52 modes were extracted for the churches in turn as given above. Then, the frequencies of the churches were compared with the spectra provided by accelerograms in the epicenters of the seismic sequence in 2016. Lastly, pushover analysis that is a non-linear static approach was applied to each church and it was found out that the pushover analysis is well capable of predicting the failure mechanisms and eigenvalue analysis related to natural spectra from accelerograms can provide the possible areas that may lead to collapse when masonry is loaded lower than the elastic limit.

Illampas et al. studied the seismic behavior of the St. Mary of Carmel Church which is a stone masonry structure in Famagusta, Cyprus by means of non-linear static analysis and time-

history analysis. [14] It was pointed out that the modal identification tests are beneficial in terms of having a chance to calibrate the finite element model. [14] They obtained the data for masonry material through laboratory and in situ tests. It was indicated that the results of capacity estimations and damage patterns which were acquired by non-linear static analysis with mass-proportional loading and the one which was provided by non-linear dynamic analysis with real-time accelerograms were in agreement with each other. It was also underlined that the major cause of the seismic failure is the combination of the out-of-plane mechanisms. They proposed some approaches for the future by stating that non-smooth contact dynamics methods can be exploited to be able to show the interaction of the discrete bodies characterizing the response of masonry ruins that is impossible to carry out by using continuum mechanics.

Brandonisio et al. investigated the seismic behavior of 4 masonry basilica churches in the 2009 L'Aquila earthquake by means of 3D linear dynamic analysis in SAP 2000 giving the seismic demand and non-linear analysis of macro elements in ABAQUS with a smeared crack model giving the horizontal strength capacity and the failure mechanisms of the relevant macro elements. [3] For modal analysis both the response spectrum provided by accelerograms and the elastic response spectrum offered by the Italian Building Code was used. It was also emphasized that since many modes have small participation factors generally less than 10 percent, it was not expected high values of base shear on the churches.

Betti et al. studied the assessment of seismic behavior of the basilica type church, "Farneta Abbey" by means of static non-linear analysis and dynamic non-linear analysis in ANSYS software. [15] Firstly, the structure was analyzed in linear elastic static and dynamic analysis in order to have prior knowledge of the global behavior of the structure. Then, non-linear static analysis was carried out on the numerical model composed of 5963 solid65 elements by adopting the Drucker Prager perfectly plastic criterion. At the end of the analysis, 3 different models were also introduced in order to take into account the interventions. Finally, it was worth mentioning that the structural reinforcement increases the seismic capacity of the structure dramatically.

Jain et al. carried out the linear and non-linear interpretation models for the damage that occurred in San Francesco church, Amatrice due to the seismic sequence of 2016-2017. [9] They stated that since the roof has no beneficial impact on the out-of-plane behavior of the structure, only the mass of the roof was factored in the analysis by ignoring the stiffness effect of the roof. In addition, since experimental tests were not available, Masonry Quality Index

(MQI) method was used to be able to estimate the material properties. They chose the Concrete Damaged Plasticity (CDP) model in order to reflect the non-linear behavior of the material. It was also highlighted that the viscosity parameter should be taken quite low for speeding up convergence. Furthermore, it was pointed out that the selection of the damage parameters plays a significant role in the convergence rate in ABAQUS. To explain, if the damage variables are taken greater than 0.99, a 99 percent reduction in stiffness is expected. Firstly, they performed static analysis by considering only gravity loads and they neglected the geometrical non-linear effects. Then, they carried out, a dynamic implicit non-linear analysis by considering the material and geometric effects.

Fiore et. al performed the non-linear analysis of masonry towers named Qutb Minar by adopting the damage plasticity model. [16] In order to check the correctness of the damage plasticity model, they calibrated the parameters by means of curve-fitting methods that are based on the experimental data obtained at the TREES laboratory of the EUCENTRE Institute. They found out that while the values of the strength ratio (F_{b0}/F_{c0}), eccentricity (ε), and K_c are similar to the ones belonging to concrete, the viscosity parameter, and dilation angle affect severely the results of the masonry. They established 6 different numerical models for the validation of the damage plasticity mode, and at the end, they presented the result by showing the capacity curves of each model. They pointed out that, the damage plasticity model is capable of reflecting the global behavior of the structure. In addition, they carried out three types of analysis namely self-weight, eigenvalue, and non-linear static analysis by means of different models that are distinguished by the kind of elements. Ultimately, it was deduced that while the 3-D solid model is the best option for determining the global behavior of the masonry structures, it has the most expensive model in terms of computation cost. It was also stated that although shell finite elements are capable of reflecting global behavior, they have a low ability to examine the local effects.

Moreover, literature is not only restricted to the masonry churched but there are also broad studies for masonry minarets and mosques. Hökenekli et al. carried out both linear and non-linear analyses to determine the behavior of the historical masonry minaret under earthquake loads. [17] They performed the convergence analysis in ABAQUS software to find the most suitable mesh size and they used 61,107 C3D4 elements for their numerical analyses. They considered both linear time history and non-linear time history analysis by using acceleration records in Turkey and by adopting the concrete damage plasticity model (CDP) in which dilation angle, eccentricity, strength ratio (F_{b0}/F_{c0}), and K_c were taken as 100, 0.1, 1.16 and

0.666, respectively. Ultimately, they found out that linear time history analysis can only be used for detecting the damaged regions whereas the non-linear time history analysis gives accurate results.

Altunışık et al. investigated the seismic behavior of the masonry Kaya Çelebi Mosque in Turkey that underwent restoration in the pursuit of the 2011 Van Earthquake. [18] They prepared the numerical model in SAP 2000 software and implemented modal analysis with the CQC method and response spectrum analysis.

Cakir et al. studied the seismic assessment of historical masonry Erzurum Lala Pasha Mosque by conducting static and dynamic analyses.[19] Once they carried out the three-point bending and compression experiments, they formed the 3-D numerical model for applying static analysis, modal analysis, and time history analysis on the basis of linear-elastic constitutive laws.

4 San Carpoforo Church

4.1 The Historical Overview of the San Carpoforo Church

The history of the church goes back to the year 813 in an official manner. It is seen that the church was governed by 2 parish priests. It was found out that the church underwent a gigantic change in its form in the sixteenth century. In the 17th century, it was rebuilt in line with the decision of Archbishop Federico Borromeo due to the damages to the structure. Hence, it is possible to say that an up-to-date appearance corresponds to this rebuilt decision. In spite of all these developments, the church at those times had been losing its prominence day by day. It paved the way for it to be considered as a subsidiary of the church, Santa Maria del Carmine. The municipality of Milan invested in the San Carpoforo church in 1864, and it was granted to the Academy of Fine Arts of Brera in 1933. It still hosts students of the academy and participants in various organizations and seminars. [20]

Figure 1: Facade of the San Carpoforo Church, Milan, Italy [21]

4.2 Geometric Model

Church geometry is mainly characterized by certain parts such as nave, apse, vaults, arches, slender columns bell tower, and transepts. San Carpoforo church is composed of naves of approximately 20 m in length, two transepts with 9.35 m and 7.34 m dimensions, a bell tower with 26.15 m, barrel vaults, and semicircular apse. (Figure 3: 3D Model of San Carpoforo Church)

Kucukkagnici and Sejdani measured the dimension of the San Carpoforo church by digital tape, and they stated that some regions in the church are impossible to see by the naked eye. Hence, they also used different approaches such as Raddrizzamento Digitale Fotogrammetrico (RDF) software to be able to estimate the dimension of some parts that cannot be possible to be measured. They presented the plans of the structure for each elevation level as seen in Figure 2.

The façade is one of the important parts of churches due to its aesthetic values. San Carpoforo church has a total of 5 openings. While the door opening has 2.94 m in width and 5.95 m in height, the window openings have smaller dimensions. In addition, the circular holes have a 1.80 m diameter, the windows opening with 1.38 m and 2.35 m dimensions, and the upper rectangular window opening has 3.51 m and 4.48 m dimensions are denoted by Figure 6. In Figure 5, it may be seen the façade in the geometric model and in the real form.

The apse is a rounded part that is located at the end of the church. In this case study, the semicircular apse contains 4 rectangular window openings. Kucukkagnici and Sejdani stated that the wooden panels have been placed up to 3.5 m in height of the apse for the academic purposes of the structure as shown in Figure 9.

The bell tower of the church is characterized by 26 m height and 51 and 50 cm thicknesses as shown in Figure 10. According to previous observations, the bell has been removed due to the safety of the structure

Furthermore, in Figure 8, it may be seen both the geometric model and real form of the right transept and bell tower connection.

Besides, the main nave is covered by vaults. Just above the vault, there is an entire roof system which means that the number of timber trusses covers a very long span. The complex situation at the roof level can be seen in Figure 11.

As seen in the following figures, the roof of the church was not taken into account in the geometric model since it was observed that trusses do not contribute a beneficial effect on the connection between the lateral walls. That's why, the tiles and supporting structure were not included in the geometrical model, their effects were considered only for mass, not stiffness. The mass of the trusses and the tiles were taken as 1.5 kN/m^2. The details of the mass contribution of the roof can be found in the following sections of the thesis.

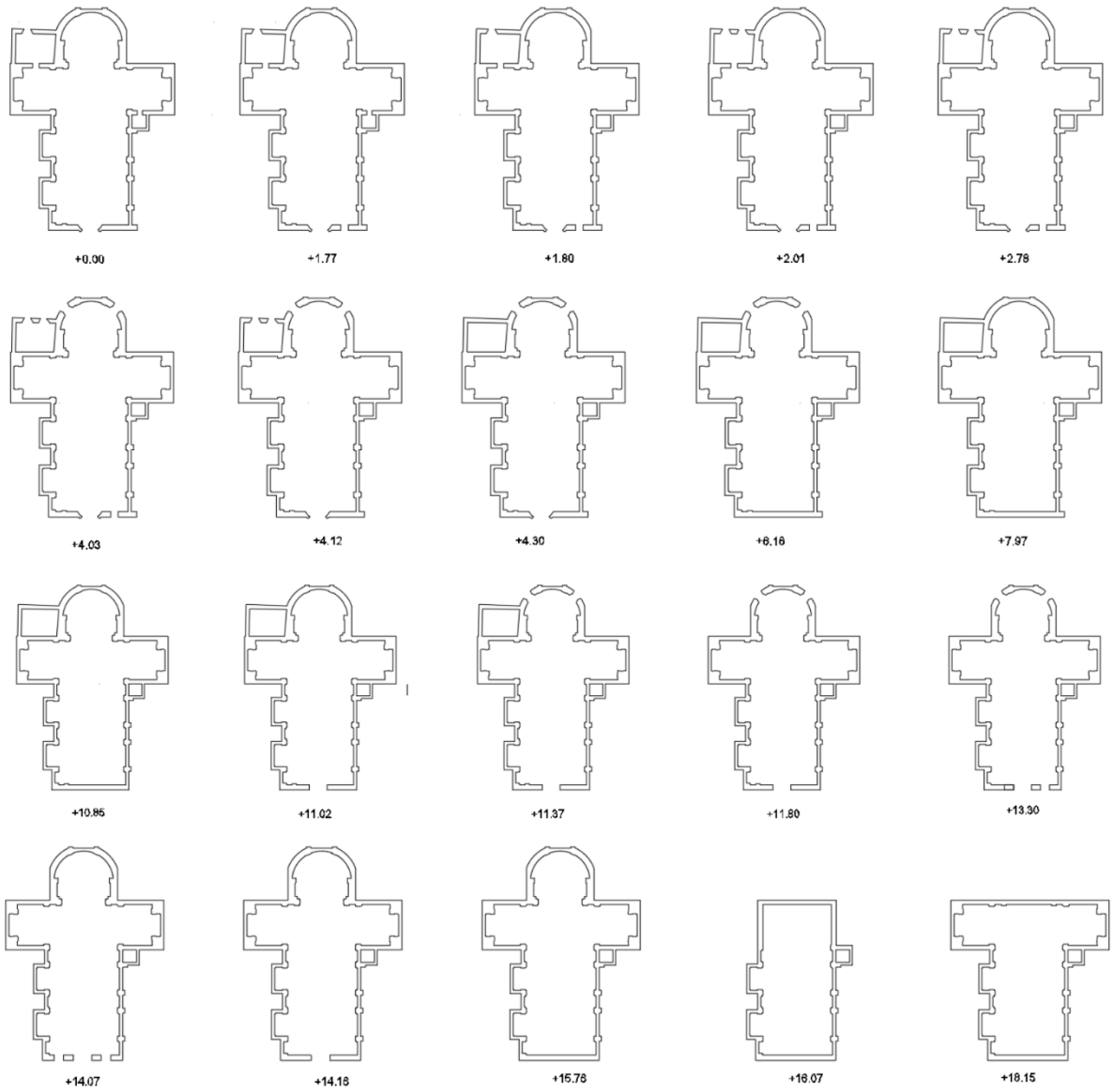

Figure 2: Plans of the Structure

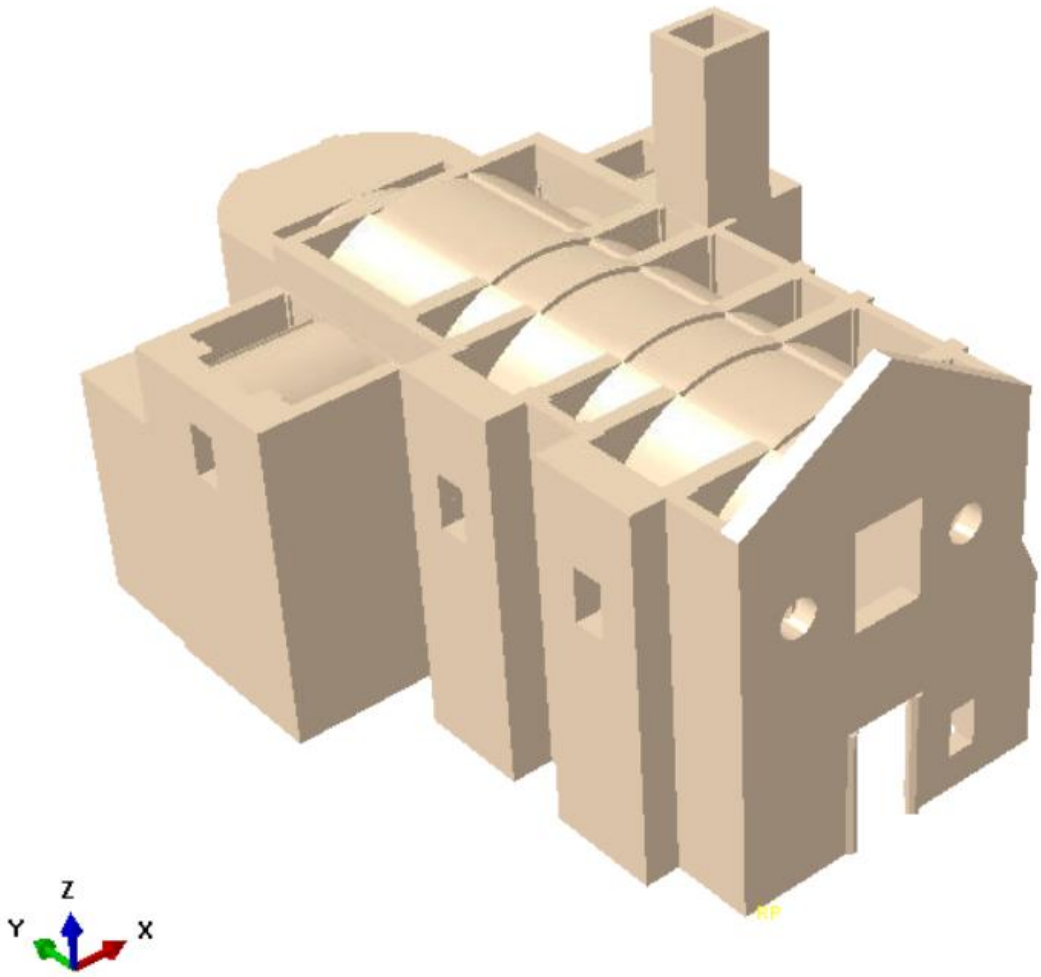

Figure 3: 3D Model of San Carpoforo Church

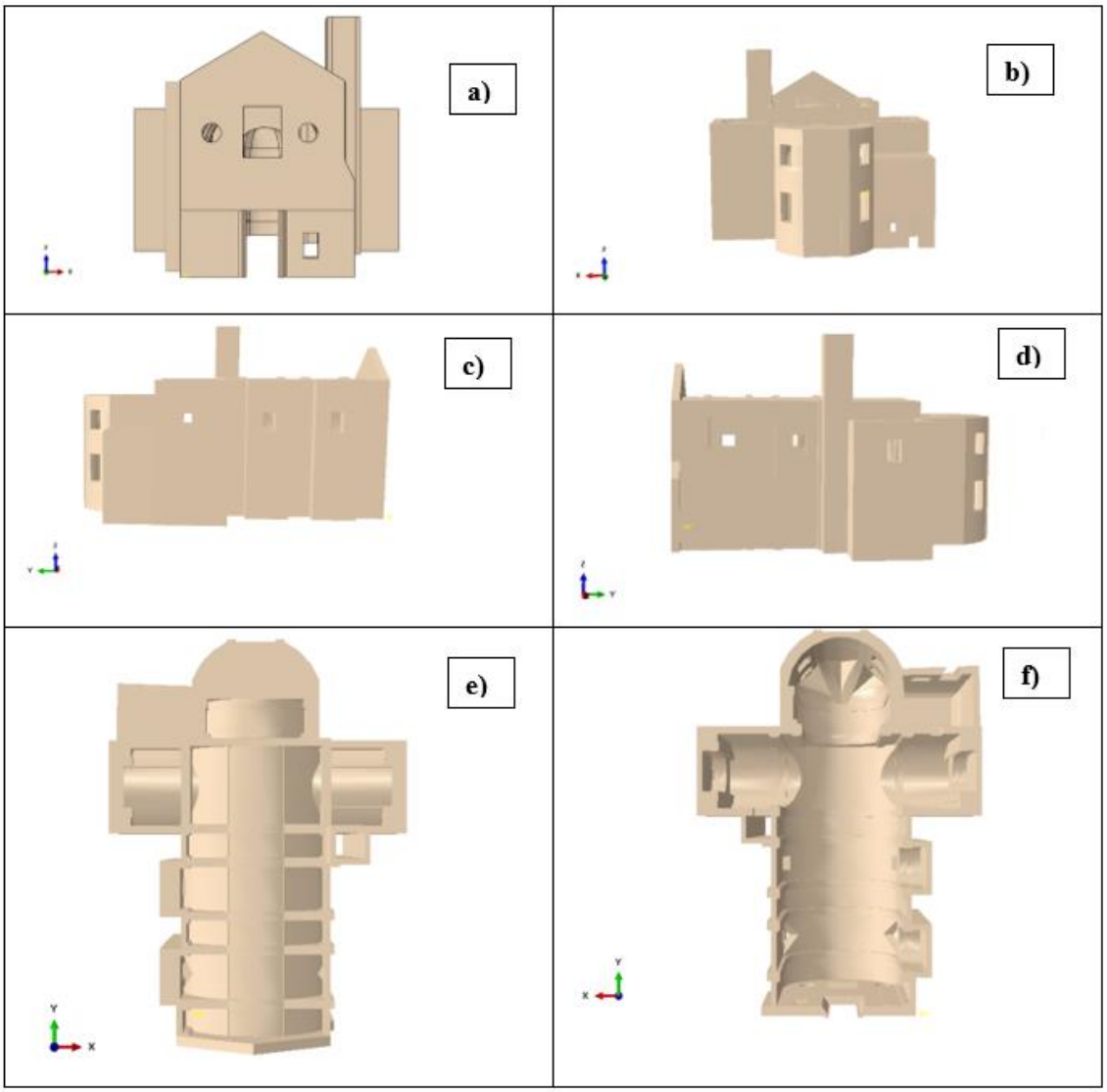

Figure 4: Views of 3D Model, a) Top b) Back c) Left d) Right e) Top f) Bottom

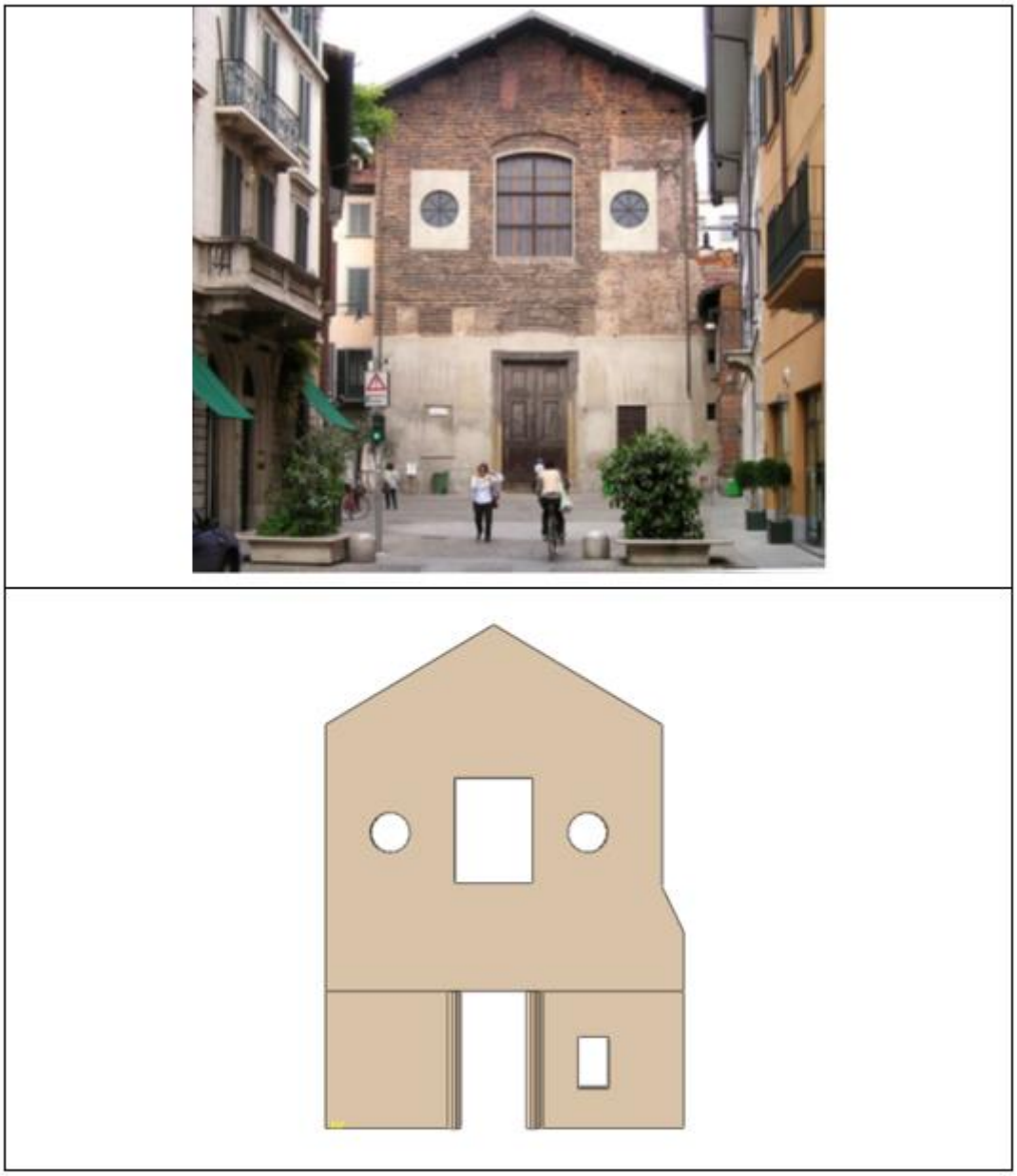

Figure 5: Façade of the San Carpoforo Church

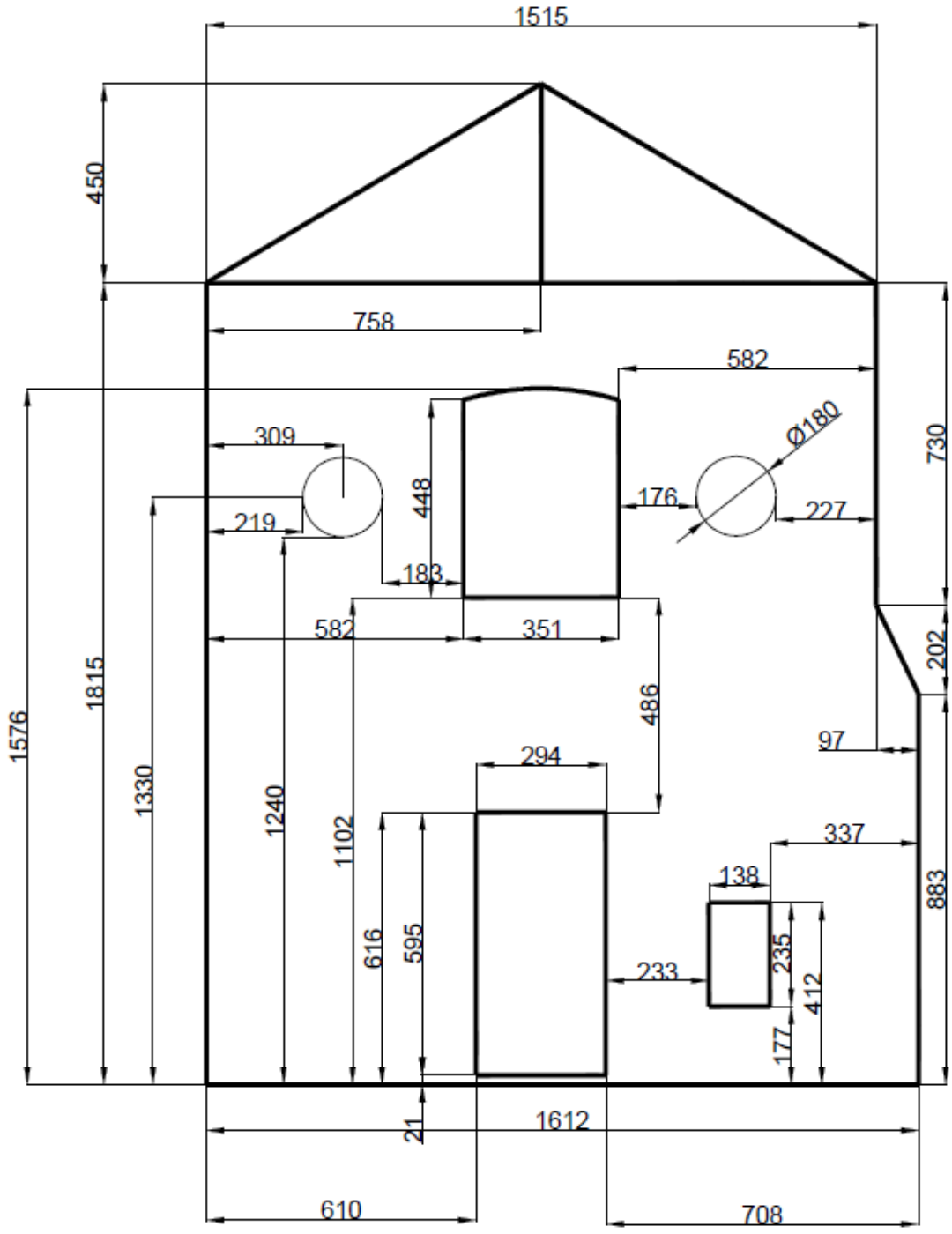

Figure 6: Dimensions of the Façade

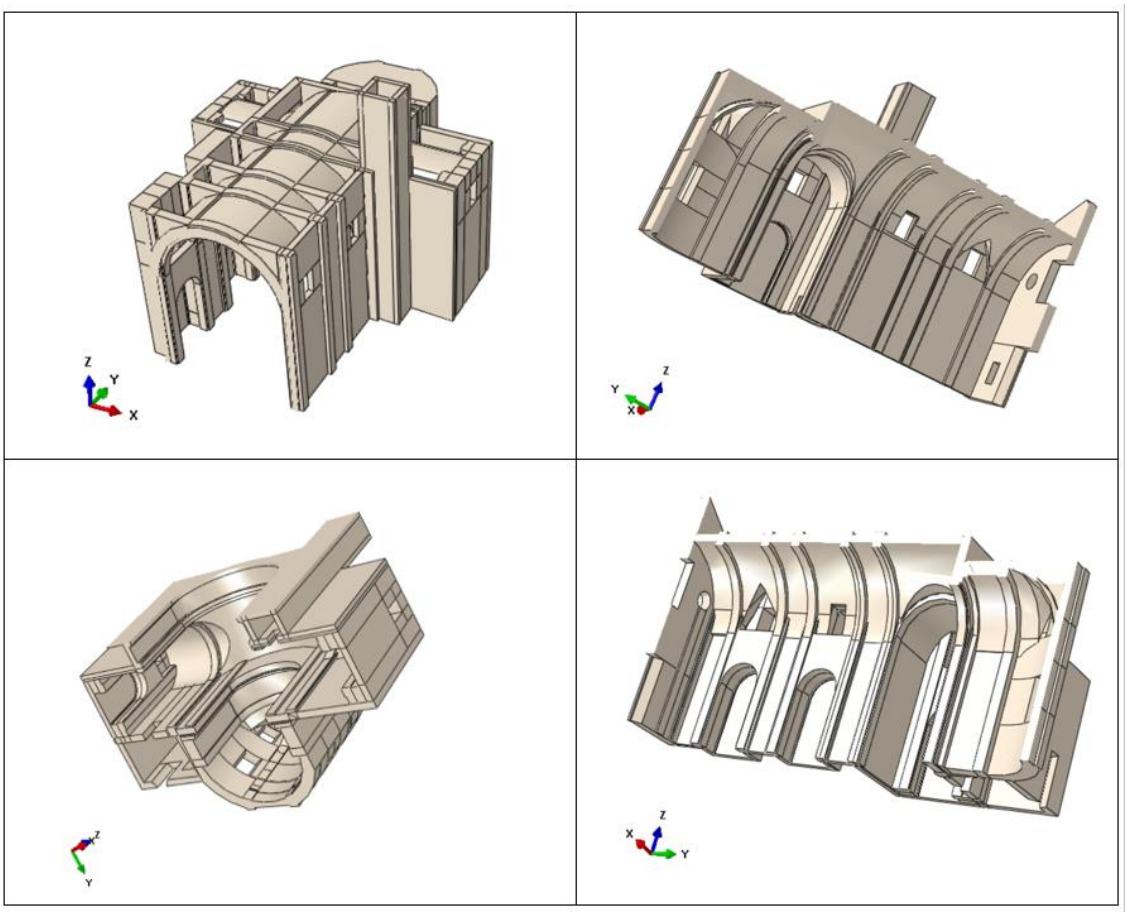

Figure 7: Views of the Inner Parts of the Structure

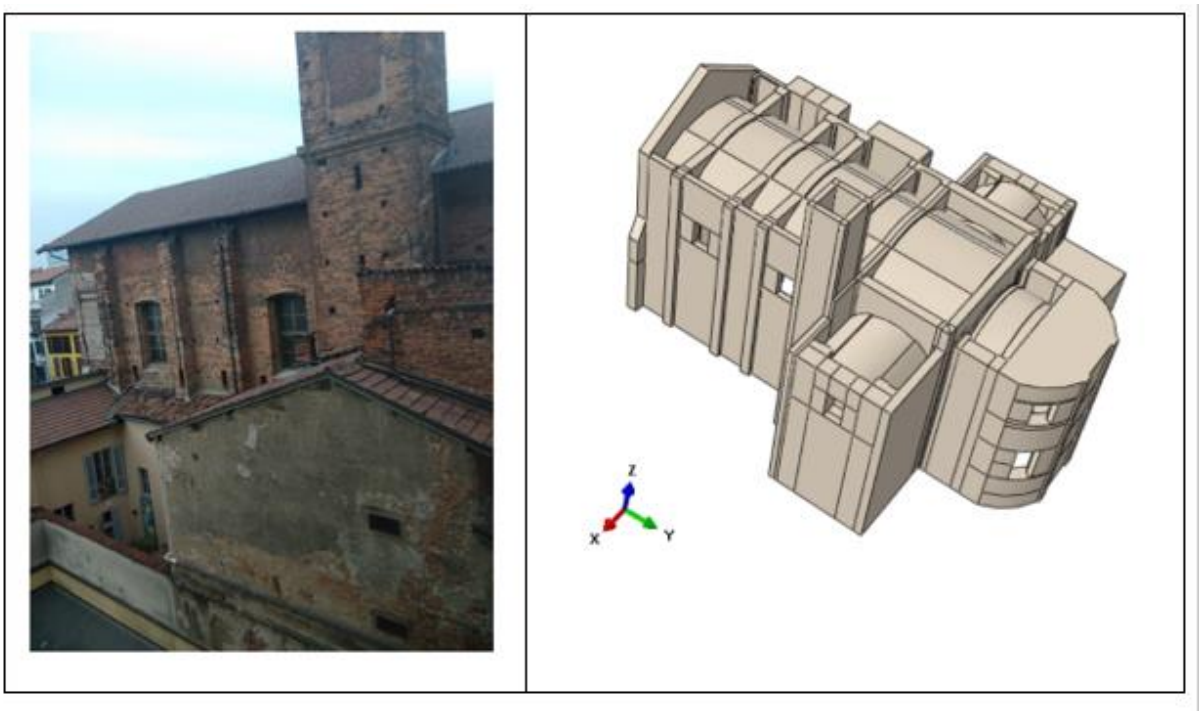

Figure 8: Bell Tower and Right Transept

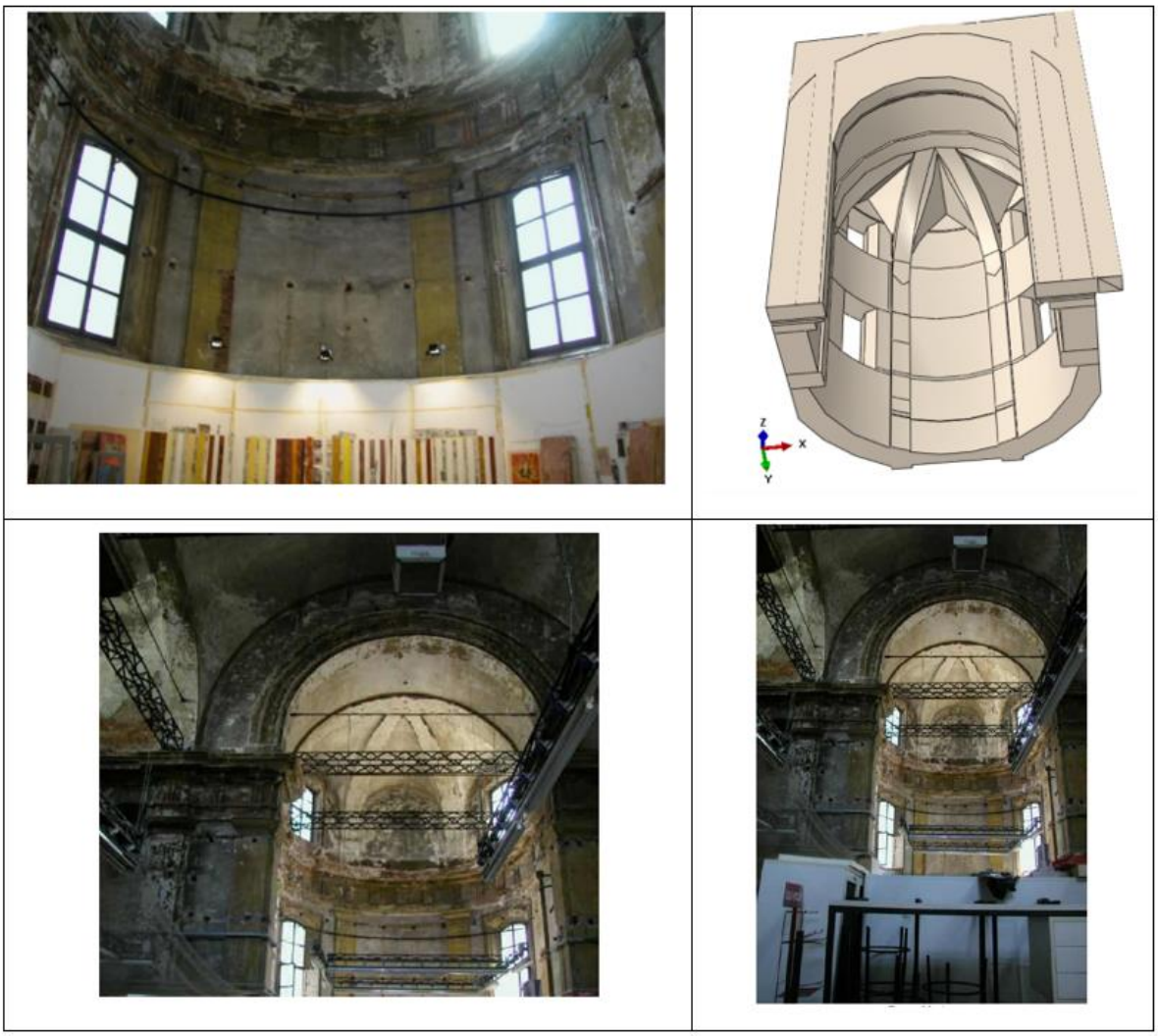

Figure 9: Apse of the Structure

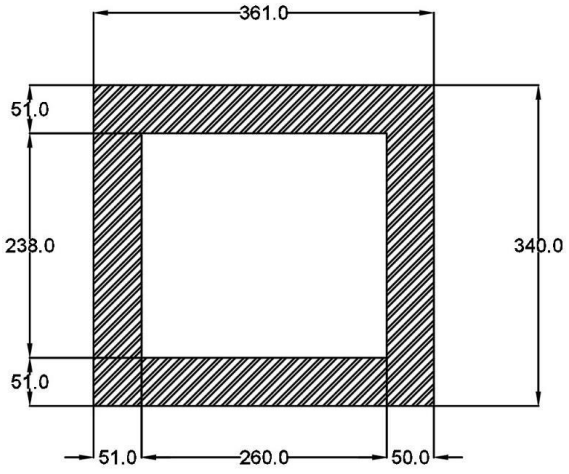

Figure 10: Section of the Bell Tower

Figure 11: Trusses at the Roof of the structure

4.3 Characteristic Behaviors of Masonry Buildings

Masonry can be subjected to a combination of various stress states including compression, tension, shear, and bending. In the presence of thin masonry walls, buckling may also be important to be considered. Seismic forces lead to shear actions, bending, and normal actions.

In addition, masonry is a material that is non-homogeneous, anisotropic, and brittle. In general, masonry has a good resistance level in compression whereas it has quite low resistance in tension. To illustrate, the reference values for the resistance in compression for ancient masonry structures are in the range 1-2 MPa according to the table C8.5.1 in NTC18, and the one in tension corresponds to 1/10 of resistance in compression.

Due to the combination of the two different materials (blocks and mortar) to have stone, it is expected to have vertical cracks passing through blocks under vertical loads (self-weight). The reason for vertical cracks is connected with the mechanics of composite materials.

Firstly, the strength of the stone block is higher than the one of the mortar. So, it is clear to postulate to have higher strains in the mortar than in masonry units. Hence, Poisson's ratio of mortar is higher than masonry units. When the vertical load is applied in a way that passes through both the masonry unit and mortar, what happens is that the masonry bed tries to expand transversally, and undergoes horizontal strains. In the transversal direction, the compression state of stresses takes place in mortar whereas tension stresses occur in masonry units. Ultimately, a favorable condition in a mortar and a negative condition in a masonry unit characterize the behavior of masonry under compression. This leads to a significant amount of reduction in the compressive stress that masonry units withstand. In other words, it is analogous to the situation seen in reinforced concrete structures in the case of computation of the bearing capacity of the inclined struts. In this case, the compressive strength of concrete is decreased to 0.25 of its original strength.

While the compressive strength of the masonry wall is lower than the one of masonry units, it is greater than the one of mortar. In addition, failure of masonry occurs due to the failure of strong material instead of the weaker one that is the mortar in the bed joints. To explain, Young's modulus of mortars is far smaller than the one of units but it's Poisson's ratio is far higher. Thus, while the mortar is subjected to triaxial compression whereas units are exposed to both tension and compression stress states that are not appropriate for the units.

In Eurocode 6, the formula that is the combination of the two strengths with exponents, and parameters depending on the adopted construction modalities (0.4-0.6) is presented in equation (1).

$$f_k = k \cdot f_b^{0.7} \cdot f_m^{0.3} \qquad (1)$$

It should be taken into account that the thickness of the mortar bed is significant. Hence, the formula is valid only if the thickness of the mortar does not exceed 1.5 cm.

For historical masonry, empirical formulas are also presented in the literature. Tassios et al. proposed estimation of the global strength of masonry walls as shown in equation (2). [22]

$$f_{wc} = \frac{\left(\frac{2}{3}\sqrt{f_{bc}} + k_1 f_{mc} - k_2\right)}{\left(1 + 3.5\left(\frac{V_m}{V_w} - 0.3\right)\right)} \quad (2)$$

Where:

V_w: Volume of Masonry

V_m: Volum of Mortar

f_{mc}: Compressive Strength of Mortar

f_{bc}: Compressive strength of Blocks

$k_1 \; and \; k_2$: Coefficients depending on the type of masonry

In masonry buildings, the “box” behavior is considered instead of frame behavior due to their special geometries. Instead of columns and beams, walls are the main structural elements in masonry buildings. It is obvious that seismic actions may lead to either in-plane actions or out-of-plane actions. While out-of-plan actions cause bending, in-plane actions give rise to normal and shear actions. Bending is not a desired condition for masonry walls since bending leads to tension stresses. Mendes et al. stated that although the in-plane behavior of masonry buildings has been investigated numerically, and experimentally, the out-of-plane behavior of the masonry building needs to be discovered. [23] Out-of-plane behavior is affected by the material properties of masonry that are characterized by low tensile and shear strength, stiffness of the horizontal diaphragms, the quality of the connection between the walls, and irregularities. [23]

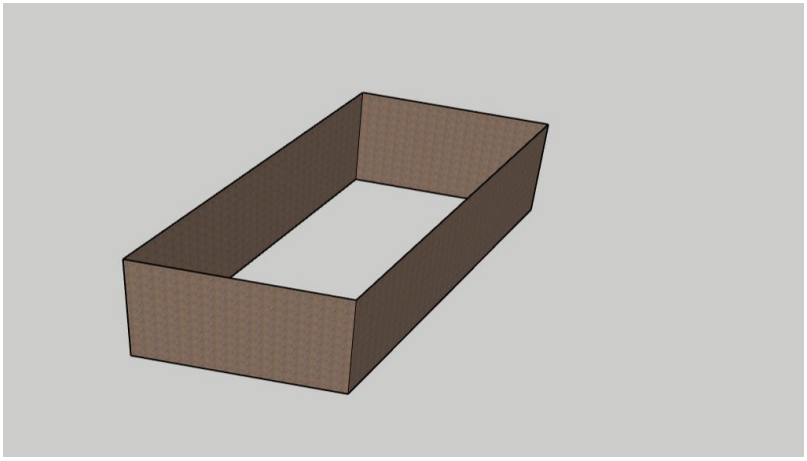

Figure 12: Box Analogy for Masonry Structures

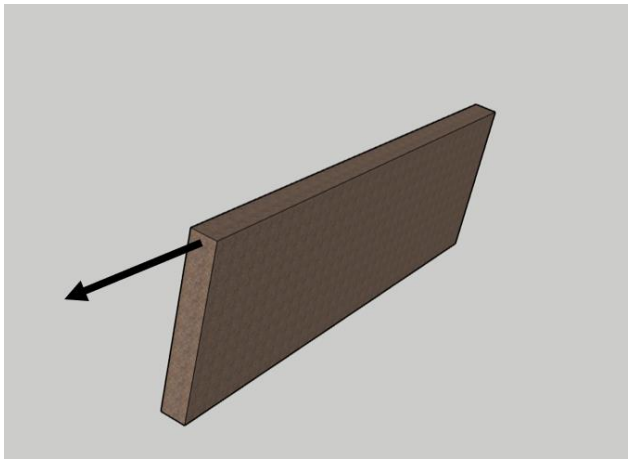

Figure 13: In-plane Actions

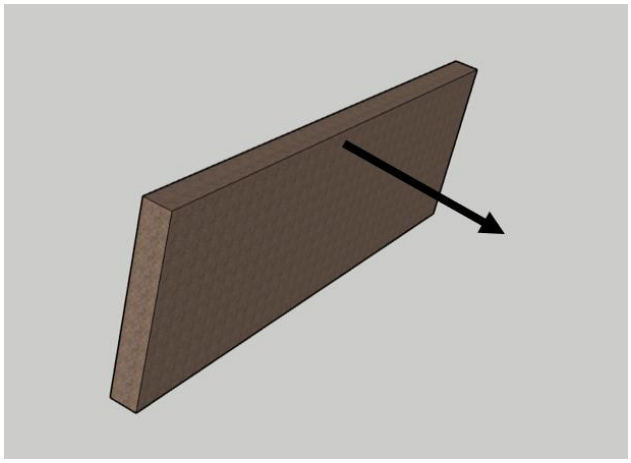

Figure 14: Out-of-Plane Actions

Churches are religious buildings that have a special structural typology containing a wide room with large spans, curved elements such as vaults, domes, arches, high and slender columns, and bell towers. They have also had positive impacts on the social life of the Christian people as it happens for mosques and synagogues for Muslim, and Jewish people, respectively. Italy is quite a wealthy country in terms of having a high number of churches.

Large empty room with large spans gives rise to a discontinuity in the building aggregate. To explain, behind the façade, there is a large empty space in the church whereas the buildings that are located on the right and left sides of the church have slabs in all the story levels. Hence, the seismic vulnerability of the entire complex of the aggregate increases. This situation is also valid for this case study, in the sense that there are concrete-typed buildings on the sides of the San Carpoforo Church. However, in this study, the effects of the buildings in the neighborhood of the church were eliminated.

Figure 15: Building Aggregates

Churches are quite vulnerable to earthquakes due to their characteristics. In the pursuit of the L'Aquila earthquake (2009), post-event surveys of cultural heritage buildings were conducted. L'Aquila earthquake having 6.3 magnitudes left behind a trail of huge destruction. Officially, it led to 288 deaths and about 1,500 injured and damage to many medieval buildings. Totally 1677 structures were examined, and 973 of these belong to churches. However, only 324 churches could be able to be reopened without interventions.

Table 1: Survey Results of the L'Aquila Earthquake (2009)

The outcome of the Survey	Numbers of Churches	Percent of Churches [%]
Accessible	324	33
Accessible with provisions	161	17
Partially accessible	28	3
Temporarily not accessible	88	9
Not accessible	367	38
Not accessible for external reasons	5	0.5
Total	973	100

Pioneer studies on churches go back to dates after the Friuli Earthquake (1976). Following of Friuli Earthquake, many surveys were conducted in order to have knowledge about damages and collapses. Thus, studies put an effort to find out the typical behavior of churches under earthquake actions. In this regard, different levels of damage were observed in churches. Besides, different crack patterns were obtained.

It can be considered that the church is an assemblage of the different elements called macro elements. In this sense, each of the elements may undergo local collapse mechanisms.

4.4 Survey and Damage Analysis

At the end of the analysis of 400 cases of damage to churches between 1976-and 1997, it was found out that 28 local collapse mechanisms can be possible to describe any kind of damage that can be noticed in the churches.

Visual descriptions of the possible 28 local collapse mechanisms are provided by a codified document called “Scheda Per il Rilievo Del Danno Ai Beni Culturali-Chiese” which was prepared by the Italian Civil Protection department and the mechanisms were denoted in Figure 16. For instance, while 1st mode mechanism is related to the overturning of the façade, 2nd mode mechanism is the shear behavior of the façade.

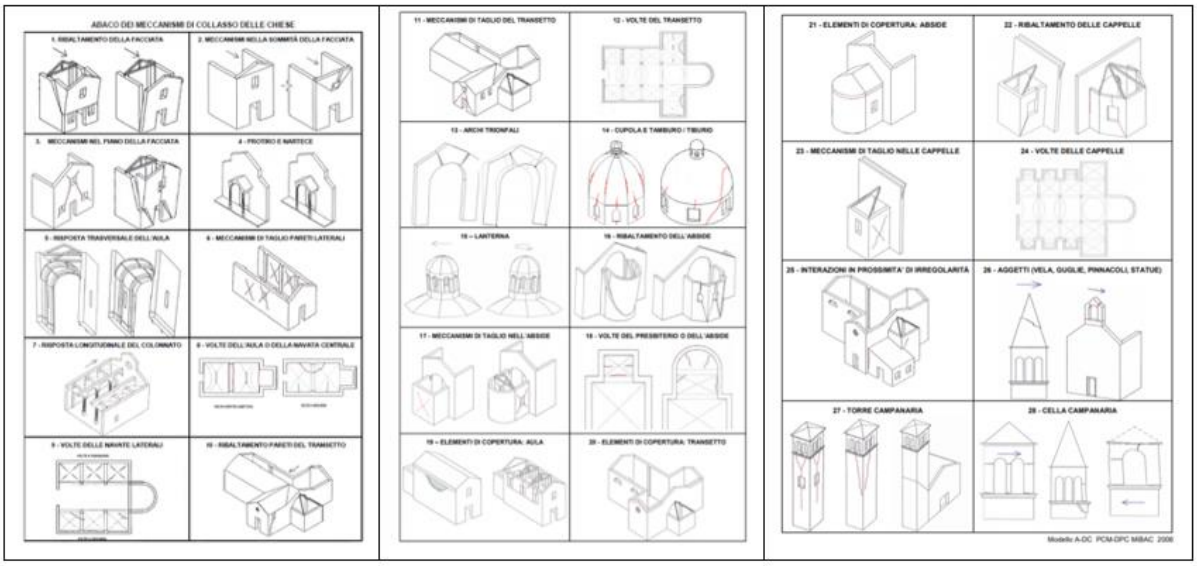

Figure 16: 28 Local Collapse Mechanisms

The survey form (Modello A-DC) provides 5 different damage levels. The meanings of these damage levels are indicated as follows:

- Damage Level 0: no damage
- Damage Level 1: just crack pattern showing that just specific collapse mechanism exists, and it is identified by the earthquake
- Damage Level 2: mechanism has been activated and the initial motion is present
- Damage Level 3: motion is progressing
- Damage Level 4: limit conditions before total collapse
- Damage Level 5: total collapse

Owing to these 5 damage levels, it is possible to reflect the real situation of each possible mechanism. Hence, it is possible to perform a simple qualitative approach meaning that no computation is done.

MODELLO A – DC

Seconda sezione

A_{14} - RIFERIMENTO SCHEDA DELLA VULNERABILITA' DELLE CHIESE

N° Scheda _____	Data ___ ___ _____	Ente ______

A_{15} - STATO DI MANUTENZIONE GENERALE

Buono ❍	Discreto ❍	Scadente ❍		Pessimo ❍	In corso lavori ❑
Eventuali precedenti lesioni esistenti		NO ❍	SI ❍	Limitate ❍ Estese ❍	Gravi ❍

A_{16} - DANNO SISMICO (Abaco dei meccanismi di collasso delle chiese)

LIVELLO DI DANNO

0 - □□□□□ assenza di danno 1 - ■□□□□ danno lieve 2 - ■■□□□ danno moderato

3 - ■■■□□ danno grave 4 - ■■■■□ danno molto grave 5 - ■■■■■ crollo

IDENTIFICAZIONE DEL DANNO

❑ danno sismico

❑ danno pregresso

❑ aggravamento

1	RIBALTAMENTO DELLA FACCIATA	❑
danno	DISTACCO DELLA FACCIATA DALLE PARETI O EVIDENTI FUORI PIOMBO	❑❑❑❑❑
2	MECCANISMI NELLA SOMMITÀ DELLA FACCIATA	❑
danno	RIBALTAMENTO DEL TIMPANO, CON LESIONE ORIZZONTALE O A V – DISGREGAZIONE DELLA MURATURA O SCORRIMENTO DEL CORDOLO – ROTAZIONE DELLE CAPRIATE	❑❑❑❑❑
3	MECCANISMI NEL PIANO DELLA FACCIATA	❑
danno	LESIONI INCLINATE (TAGLIO) – LESIONI VERTICALI O ARCUATE (ROTAZIONE) – ALTRE FESSURAZIONI O SPANCIAMENTI	❑❑❑❑❑
4	PROTIRO – NARTECE	❑
danno	LESIONI NEGLI ARCHI O NELLA TRABEAZIONE PER ROTAZIONE DELLE COLONNE – DISTACCO DALLA FACCIATA – MARTELLAMENTO	❑❑❑❑❑
5	RISPOSTA TRASVERSALE DELL'AULA	❑
danno	LESIONI NEGLI ARCONI (CON EVENTUALE PROSECUZIONE NELLA VOLTA) – ROTAZIONI DELLE PARETI LATERALI – LESIONI A TAGLIO NELLE VOLTE – FUORI PIOMBO E SCHIACCIAMENTO NELLE COLONNE	❑❑❑❑❑
6	MECCANISMI DI TAGLIO NELLE PARETI LATERALI (RISPOSTA LONGITUDINALE)	❑
danno	LESIONI INCLINATE (SINGOLE O INCROCIATE) – LESIONI IN CORRISPONDENZA DI DISCONTINUITÀ NELLA MURATURA	❑❑❑❑❑
7	RISPOSTA LONGITUDINALE DEL COLONNATO NELLE CHIESE A PIÙ NAVATE	❑
danno	LESIONI NEGLI ARCHI O NEGLI ARCHITRAVI LONGITUDINALI – SCHIACCIAMENTO E/O LESIONI ALLA BASE DEI PILASTRI – LESIONI A TAGLIO NELLE VOLTE DELLE NAVATE LATERALI	❑❑❑❑❑
8	VOLTE DELLA NAVATA CENTRALE	❑
danno	LESIONI NELLE VOLTE DELL'AULA CENTRALE – SCONNESSIONI DELLE VOLTE DAGLI ARCONI	❑❑❑❑❑
9	VOLTE DELLE NAVATE LATERALI	❑
danno	LESIONI NELLE VOLTE O SCONNESSIONI DAGLI ARCONI O DALLE PARETI LATERALI	❑❑❑❑❑
10	RIBALTAMENTO DELLE PARETI DI ESTREMITÀ DEL TRANSETTO	❑
danno	DISTACCO DELLA PARETE FRONTALE DALLE PARETI LATERALI – RIBALTAMENTO O DISGREGAZIONI DEL TIMPANO IN SOMMITÀ	❑❑❑❑❑
11	MECCANISMI DI TAGLIO NELLE PARETI LATERALI DEL TRANSETTO	❑
danno	LESIONI INCLINATE (SINGOLE O INCROCIATE) – LESIONI ATTRAVERSO DISCONTINUITÀ	❑❑❑❑❑
12	VOLTE DEL TRANSETTO	❑
danno	LESIONI NELLE VOLTE O SCONNESSIONI DAGLI ARCONI E DALLE PARETI LATERALI	❑❑❑❑❑
13	ARCHI TRIONFALI	❑
danno	LESIONI NELL'ARCO – SCORRIMENTO DI CONCI – SCHIACCIAMENTO O LESIONI ORIZZONTALI ALLA BASE DEI PIEDRITTI	❑❑❑❑❑

Figure 17: Italian Survey Form

According to the study of Sejdani and Kucukagnici, the possible damage mechanisms in the San Carpoforo church, are reported in Table 2. [24]

Table 2: Damage Mechanisms in San Carpoforo Church

Damage Mechanism	Number of Mechanisms	Damage Level	Macro elements
Overturning of the façade	M1	D2	Façade
Mechanisms on the top of the façade	M2	D2	Façade
Shear mechanisms of the lateral walls	M6	D1	Room
Longitudinal response of the columns	M7	D1	Room
Vault of the room or central nave	M8	D1	Room
Overturning the walls of the transept	M10	D1	Transept
Transept shear mechanism	M11	D1	Transept
Vaults of the transept	M12	D1	Transept
Dome and drum or tiburium	M14	D1	Dome
Overturning the apse	M16	D1	Apse
Shear mechanisms in the apse	M17	D1	Apse
Vaults of the apse	M18	D1	Apse
Bell tower	M27	D1	Overhang, bell tower

.

It is possible to predict the seismic vulnerability of churches by means of empirical methods and observations. [1] This approach corresponds to the lowest level of the seismic assessment of the existing structures.

Global damage index (i_d) can be computed by equation (3) that is given by Italian Guidelines.

$$i_d = \frac{1}{5N}\sum_{i=1}^{N} d_i \qquad (3)$$

Where:

N: number of damage mechanism

d_i: damage level for each mechanism

In this case study, the global damage index (i_d) was determined as 0.231. In addition, Zizi et al. also affirmed that the equation of the global damage index (i_d) may be elaborated by multiplying the damage level for each mechanism (d_i) with score factor (ρ_k) that varies with respect to the importance of damage mechanisms. [1] For the sake of simplicity, values of the score factors were taken as 1 by assuming that each mechanism has the same importance.

Zizi et al. classified the global damage levels (D_k) with respect to the range of the global damage index (i_d) as given in Table 3.

Table 3: Global Damage Levels

Global damage level (D_k)	Range
Grade 0	$i_d \leq 0.05$
Grade 1	$0.05 < i_d \leq 0.25$
Grade 2	$0.25 < i_d \leq 0.4$
Grade 3	$0.4 < i_d \leq 06$
Grade 4	$0.6 < i_d \leq 0.8$
Grade 5	$i_d > 0.8$

Ultimately, the value of the global damage index falls in Grade 1 of the global damage level (D_k). Zizi et al. stated that in this grade level, no structural damage is expected whereas non-structural damages can be observed. Details of the procedure can be found in the paper of Zizi et al. As stated, priorly, this level of analysis called EL0 is the lowest accuracy level among the structural assessment levels. Hence, it is worth underlining that the highest level of assessments should be carried out in order to reach the global response of the structure. In the following sections, EL3 was presented.

In 1999, some interventions were done on the roof system of the structure since significant deterioration was observed at the trusses that connect the vaults and roof clays due to

infiltration of water. [24] In addition, the change of the position of the trusses in height level led to the situation in which vaults are subjected to concentrated forces.

4.5 Masonry Quality Index (MQI)

The L'Aquila earthquake had a huge impact on the masonry buildings. To be able to reach the characteristics of the masonry buildings it was needed to conduct experimental tests. For this reason, a qualitative criterion was developed by Borri A. and De Maria A. [25]–[27]

In addition, Rovero et. al studied the validation of the masonry quality index (MQI) method by comparing it with flat-jack tests. They concluded that the results were in agreement, and the MQI method can be adopted in order to determine the mechanical properties of the masonry structures in case of a lack of experimental tests. [28]

Basically, there are 7 evaluation parameters for reflecting construction practice.

Evaluation levels are the following:

- Respected (R)
- Partially Respected (PR)
- Not Respected (NP)

Reference Load conditions are the following:

- Vertical Load
- Out of plane bending
- In-plane actions

These evaluations are done for each parameter in accordance with the reference load conditions.

Vertical load means the self-weight of the structure. Out of plane bending and in-plane actions are related to the possible presence of the horizontal forces generated by the earthquake. Depending on the direction of the seismic force with respect to the wall surface, there are different situations. If the forces are normal to the wall, the bending problem takes place. In other words, out-of-plane forces lead to out-of-plane bending. In the case seismic forces are

parallel to the wall plane, in-plane actions should be considered, and it is a favorable situation. The behavior of the wall is different in relation to the 2 possibilities of the horizontal actions.

EVALUATION PARAMETERS

1. Presence of regular horizontal layers (OR.)
2. Transversal interlocking/ transversal connecting elements (P.D)
3. Element shape (F.E.L)
4. Lack of alignment of vertical joints (S.G)
5. Element Size (D.E.L.)
6. Good quality mortar/ effective contact between elements/ filling elements (MA.)
7. Adequate resistance levels for the elements (R.EL.)

(Abbreviations were written in Italian.)

1. Presence of regular horizontal layers (OR.)

Figure 18: Presence of regular horizontal layers (OR.), MQI

Continuity of the horizontal mortar beds varies and is categorized into 3 categories, and it is an important parameter for the compression and lateral strength of the walls.

According to Borri et. al, bed joints are continuous; stone masonry walls with bricks courses are considered “respected” (R). Only one leaf with a continuous bed joint; and a double-leaf wall are included in “partially respected” (PR). Non-continuous ones are regarded as “non-respected” (NR). [29]

Borri et. al articulated that cylindrical hinges may form due to the continuity and horizontality of the beds in case of an earthquake. Moreover, the continuity of the bed joints maximizes the frictional reaction by vertical static loads. [30]

In this study, bed joints were deemed as partially continuous for each reference loading condition.

2. Transversal interlocking/ transversal connecting elements (P.D)

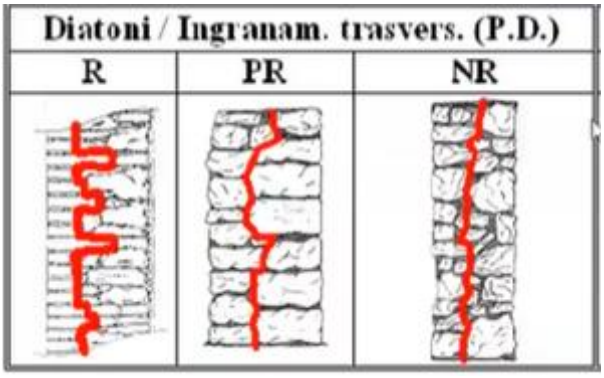

Figure 19: Transversal interlocking/ transversal connecting elements (P.D), MQI

It is expected to have a good interlocking between 2 layers constituting the masonry wall, through the thickness of the wall. Borri et. al stated that the existence of headers between the leaves plays a significant role in the out-of-plane behavior of the masonry.[29] Besides, they articulated that, qualitative analysis or quantitative analysis can be used depending on the visibility of the wall section [29] If the wall section is not visible, then a qualitative approach is chosen. In contrast, a quantitative approach is preferred if the wall section is visible. [30] To be able to do this, a minimum length called M_I is calculated. According to Borri et. al, minimum length can be defined as the ratio of the minimum distance passing through mortar joints to the straight distance between the 2 points. [30] They reported that, if $M_I > 1.6$, then it is regarded as “respected”. As opposed to that, in the case of $M_I < 1.4$, it is considered as “non-respected”. [30]

In this study, transversal interlocking parameters were considered as “non-respected” for each reference load condition.

Element shape (F.E.L)

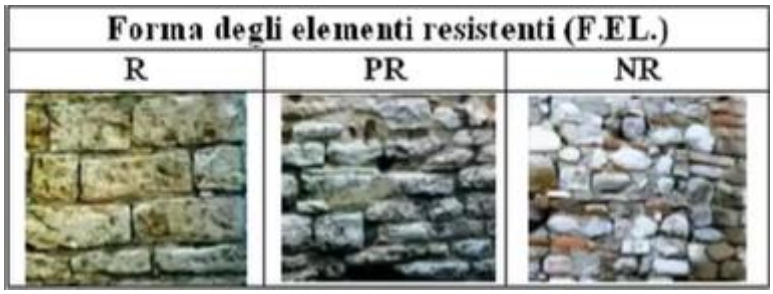

Figure 20: Element Shape (F.EL.), MQI

If clay bricks are used, there is only one case that is a regular one shown with "respected" (R). In contrast, stone masonry has 3 different cases in accordance with the regularity of the elements.

According to the study by Borri, et al, rubble, rounded, or pebble stonework on both masonry leaves are considered "non-respected." Besides, they stated that co-presence of rubble, rounded or pebble stonework and barely/perfectly cut stone and bricks on both masonry leaves; one masonry leaf made of perfectly cut stones or bricks; masonry made of irregular (rubble, rounded, pebble) stones, but with the presence of pinning Stones are deemed as "partially respected" (PR). Barely cut stones or perfectly cut stones on both masonry leaves (predominant); brickwork is included as "respected" (R). [29]

In this case study, according to the observations, element shapes were taken as "partially respected" (PR) for all reference load conditions and reported in Table 4.

3. Lack of alignment of vertical joints (S.G)

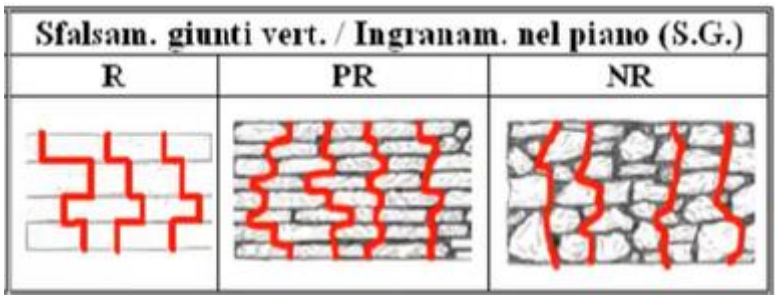

Figure 21: Lack of alignment of vertical joints (S.G), MQI

This parameter is related to the Identification of the vertical path through the mortar joints. First, it can be seen that there is good interlocking between elements. In the second one, there is no straight line but a close to the straight line.

It was decided to take “partially respected” (PR) for this parameter, in this case study.

4. Element Size (D.E.L.)

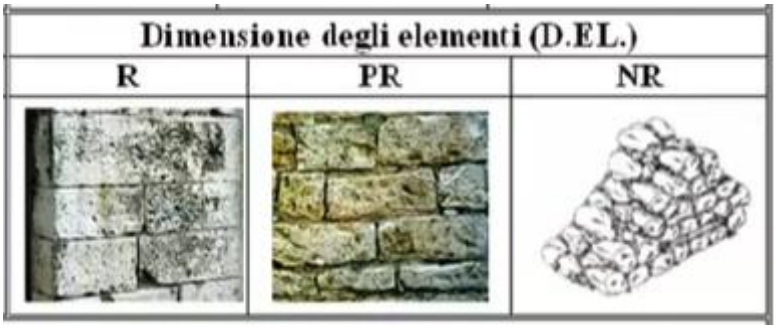

Figure 22: Element Size (D.E.L.), MQI

The reference parameter is the thickness of the wall. In the first picture, all the elements are in a similar size that is comparable to the thickness of the wall. Second, there are regular but different-sized blocks. Third, rounded blocks, different sized blocks.

Borri et. al expressed that the large-sized blocks show better behavior under seismic and static conditions. [30]

According to the observations, the element size parameter was taken as “partially respected” for each reference load condition.

5. Good quality mortar/ effective contact between elements/ filling elements (MA.)

Figure 23: Good quality mortar/ effective contact between elements/ filling elements (MA.), MQI

In the first case, mortar beds in the horizontal direction are very regular. In contrast, in the third picture, there is no regularity in the horizontal mortar beds

Borri et. al determined that undamaged elements or damaged elements less than 10 percent, hollow-core bricks where solid is less than 30 percent, mud bricks, unfired bricks; damaged elements less than 50 percent and greater than 10 percent, hollow bricks where solid is in the range of 30 percent to 55 percent, sandstone or tuff elements; solid fired bricks; undamaged elements less than 10 percent, solid fired bricks, hollow bricks where solid less than 55 percent, concrete units, and hardstones were categorized as "non-respected", "partially-respected", and "respected", respectively. [30]

San Carpofora Church's mortar quality is dropped to "partially respected."

6. Adequate resistance levels for the elements (R.EL.)

Masonry Quality Index can be computed by equation (4).

$$MQI = RE.EL.\times (OR.+P.D.+F.EL.+S.G.+D.EL.+MA.) \qquad (4)$$

Table 4 contains the numbers that are dependent on the aforementioned reference load conditions and the evaluation levels.

Table 4: Evaluation Parameters and Scores

	Vertical loads			Out-of-plane actions			In-plane actions		
Parameters	NR	PR	R	NR	PR	R	NR	PR	R
OR.	0	1	2	0	1	2	0	0.5	1
P.D.	0	1	1	0	1.5	3	0	1	2
F.EL.	0	1.5	3	0	1	2	0	1	2
S.G.	0	0.5	1	0	0.5	1	0	1	2
D.EL.	0	0.5	1	0	0.5	1	0	0.5	1
MA.	0	0.5	2	0	0.5	1	0	1	2
RE.EL.	0.3	0.7	1	0.5	0.7	1	0	0.7	1

The final global interpretation of masonry can be determined by means of MQI numbers.

Wall categories are divided into 3 categories that are poor condition, average condition, and good condition. Depending on the Index, the final conditions of the wall can be obtained in Table 5.

Table 5: Masonry Wall Classification for the Type of Actions

Type of Action	Wall Category		
	C	B	A
Vertical	0≤ MQI ≤2.5	2.5≤ MQI ≤5	5≤ MQI ≤10
Out-of-Plane	0≤ MQI ≤4	4≤ MQI ≤7	7≤ MQI ≤10
In-Plane	0≤ MQI ≤3	3≤ MQI ≤5	5≤ MQI ≤10

Table 6: R parameters for the Type of Actions

Parameter- MA.	$r_{vertical}$	$r_{out\text{-}of\text{-}plane}$	$r_{in\text{-}plane}$
NR	0.2	1	0.1
PR	0.6	1	0.7
R	1	1	1

$$MQI_v = r_v \times RE.EL_v.\times (OR._v + P.D._v + F.EL._v + S.G._{vl} + D.EL._v + MA._v) \quad (5)$$

$$MQI_{op} = r_{op} \times RE.EL_{op}.\times (OR._{op} + P.D._{op} + F.EL._{op} + S.G._{op} + D.EL._{op} + MA._{op}) \quad (6)$$

$$MQI_{ip} = r_{ip} \times RE.EL_{ip}.\times (OR._{ip} + P.D._{ip} + F.EL._{ip} + S.G._{ip} + D.EL._{ip} + MA._{ip}) \quad (7)$$

In accordance with the site observations, scores of the parameters for each action are denoted in Table 7.

Table 7: Scores of the Structure

Parameters	Vertical	In-plane	Out-of-plane
OR.	1 (P.R.)	0.5 (P.R.)	1 (P.R.)
P.D.	0 (N.R.)	0 (N.R.)	0 (N.R.)
F.EL.	1.5 (P.R.)	1 (P.R.)	1 (P.R.)
S.G.	0.5 (P.R.)	1 (P.R.)	0.5 (P.R.)
D.EL.	0.5 (P.R.)	0.5 (P.R.)	0.5 (P.R.)
MA.	0.5 (P.R.)	1 (P.R.)	0.5 (P.R.)
RE.EL.	1 (R.)	1 (R.)	1 (R.)

Ultimately, while masonry has class B for the vertical and in-plane actions, it has a lower class (C) in out-of-plane actions.

Table 8: Masonry Classes for the actions

	Class
Vertical	B
In-plane	B
Out of plane	C

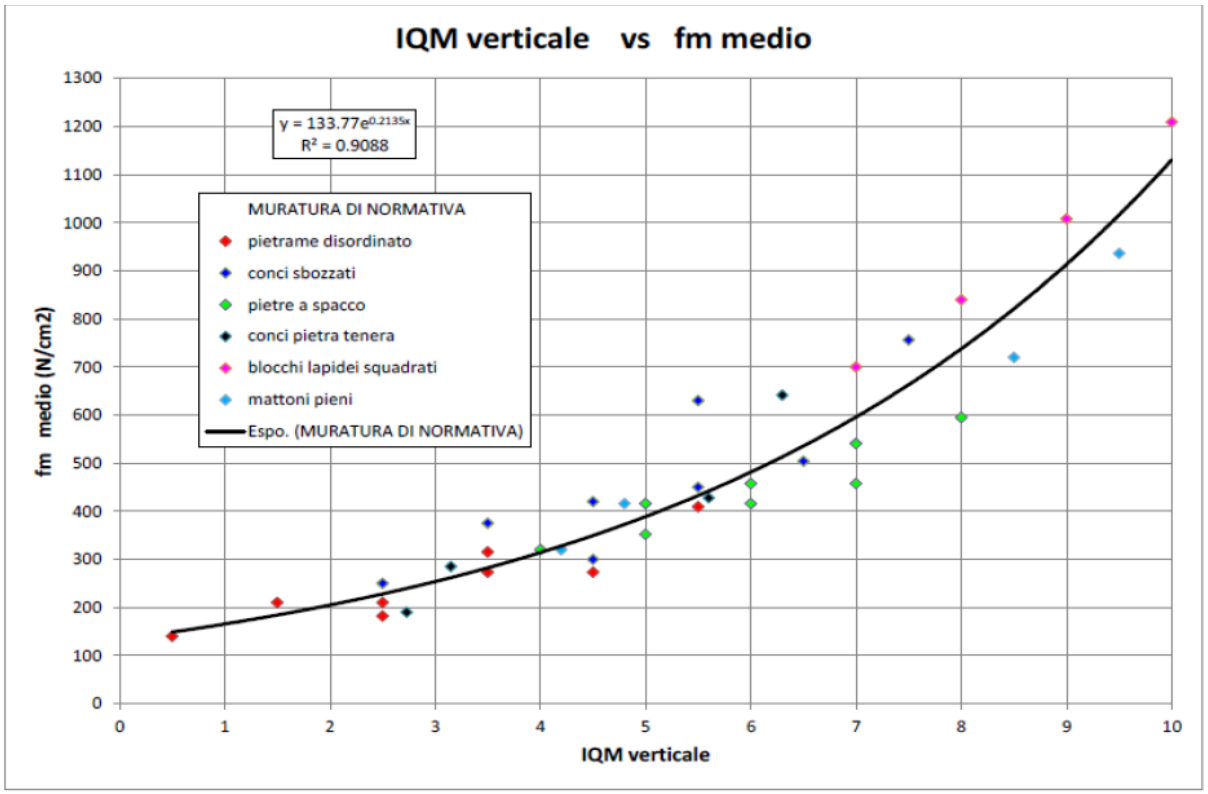

Figure 24: Compressive Strength Curve

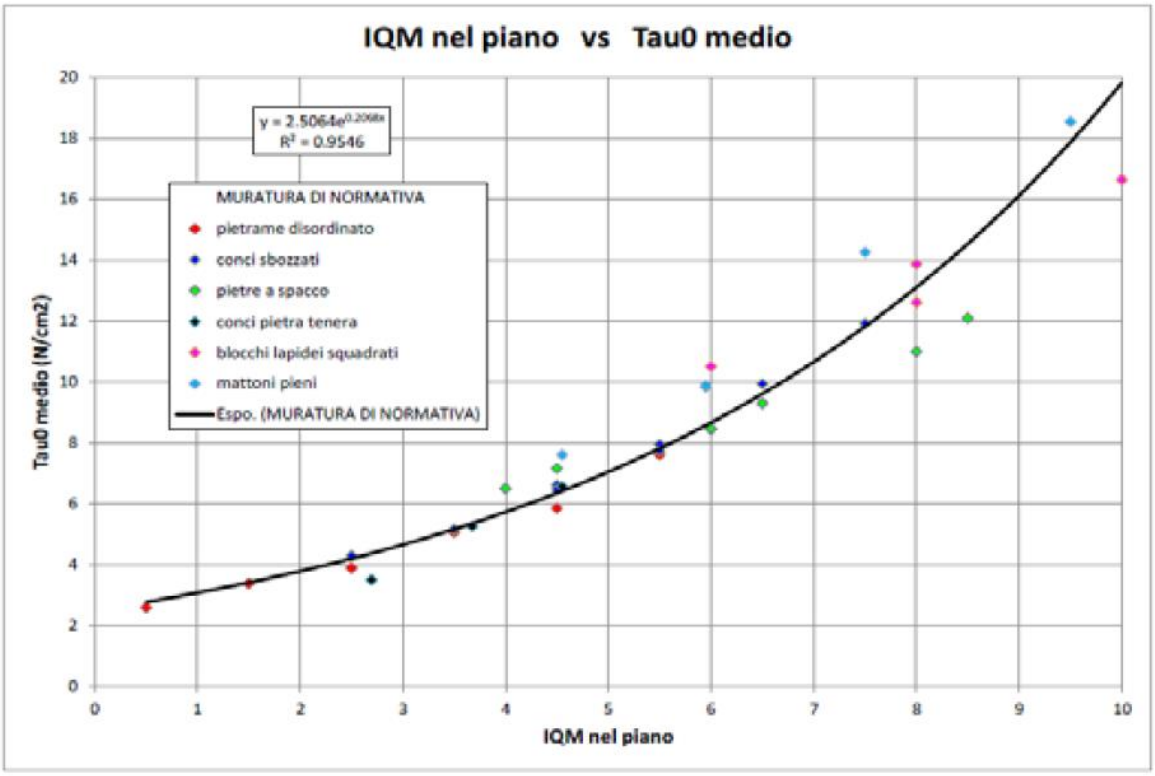

Figure 25: Shear Strength Curve

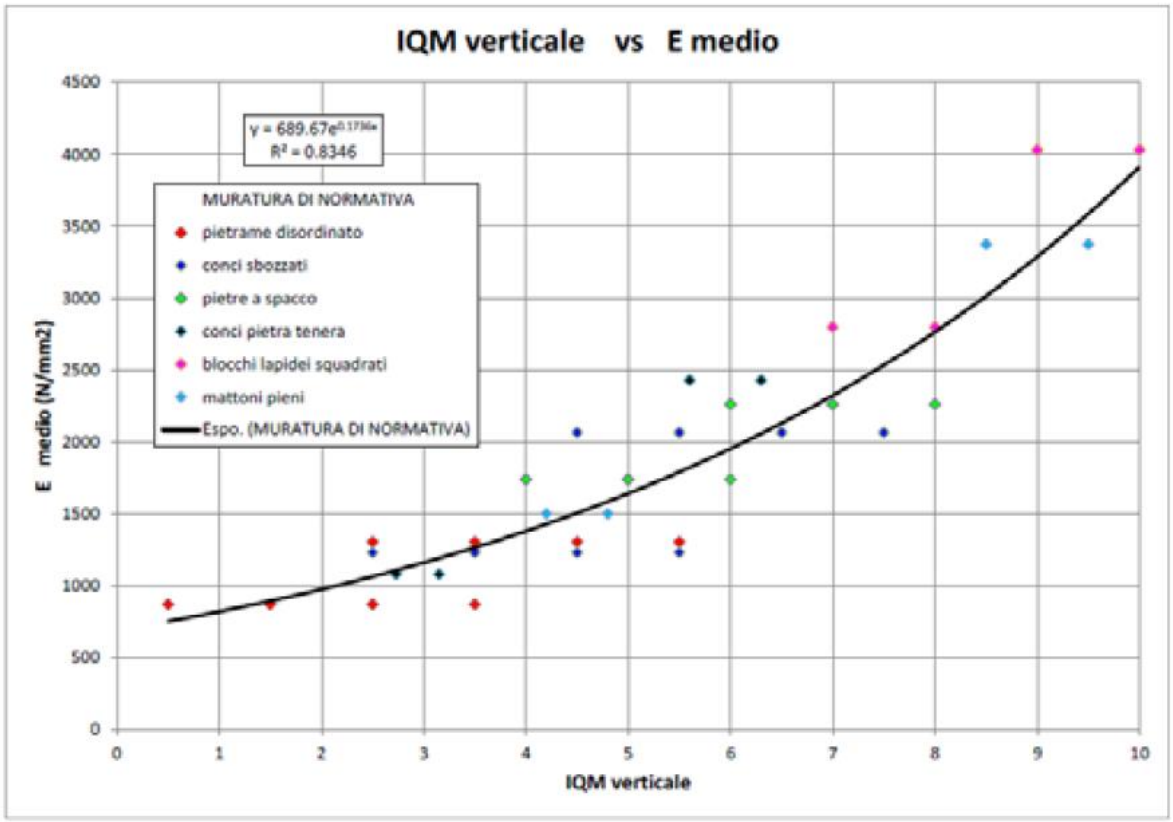

Figure 26: Elastic Modulus Curve

To be able to pass the numerical values for mechanical properties, computed masonry quality index values and the curves for the compressive strength curve, shear strength curve, and elastic modulus curve are used. (See Figure 24: Compressive Strength Curve, Figure 25: Shear Strength Curve, and Figure 26: Elastic Modulus Curve)

Table 9: Types of Masonry

Tipologia di muratura	f (N/mm²)	τ_0 (N/mm²)	f_{v0} (N/mm²)	E (N/mm²)	G (N/mm²)	w (kN/m³)
	min-max	min-max		min-max	min-max	
Muratura in pietrame disordinata (ciottoli, pietre erratiche e irregolari)	1,0-2,0	0,018-0,032	- -	690-1050	230-350	19
Muratura a conci sbozzati, con paramenti di spessore disomogeneo (*)	2,0	0,035-0,051	- -	1020-1440	340-480	20
Muratura in pietre a spacco con buona tessitura	2,6-3,8	0,056-0,074	- -	1500-1980	500-660	21
Muratura irregolare di pietra tenera (tufo, calcarenite, ecc.,)	1,4-2,2	0,028-0,042	- -	900-1260	300-420	13 ÷ 16(**)
Muratura a conci regolari di pietra tenera (tufo, calcarenite, ecc.,) (**)	2,0-3,2	0,04-0,08	0,10-0,19	1200-1620	400-500	
Muratura a blocchi lapidei squadrati	5,8-8,2	0,09-0,12	0,18-0,28	2400-3300	800-1100	22
Muratura in mattoni pieni e malta di calce (***)	2,6-4,3	0,05-0,13	0,13-0,27	1200-1800	400-600	18
Muratura in mattoni semipieni con malta cementizia (es,: doppio UNI foratura ≤40%)	5,0-8,0	0,08-0,17	0,20-0,36	3500-5600	875-1400	15

Finally, the material properties of the masonry for the structure are reported in Table 10. It is also noticed that the values of the material properties fall into the “clay bricks” category.

Table 10: Material Properties of the Masonry

Property	Value
Compressive Strength [f_m]	3.142 MPa
Tensile Strength [f_t]	0.3142 MPa
Shear Strength [τ_0]	0.07169 MPa
Young’s Modulus [E]	1381.069 MPa
Mass Density [ρ]	1385.478 kg/m^3

5 Numerical Modeling

5.1 Introduction

3-D finite element analysis plays a significant role to obtain a global evaluation of the seismic behavior of churches. For the finite element analyses, ABAQUS software was chosen. Once the geometric model is completed in AutoCAD, it was saved in *.SAT* extension and it was imported in ABAQUS/ CAE 2021.

Boundary conditions were set as" encastre" in which 3 translation and 3 rotation components are impeded at the base of the structure.

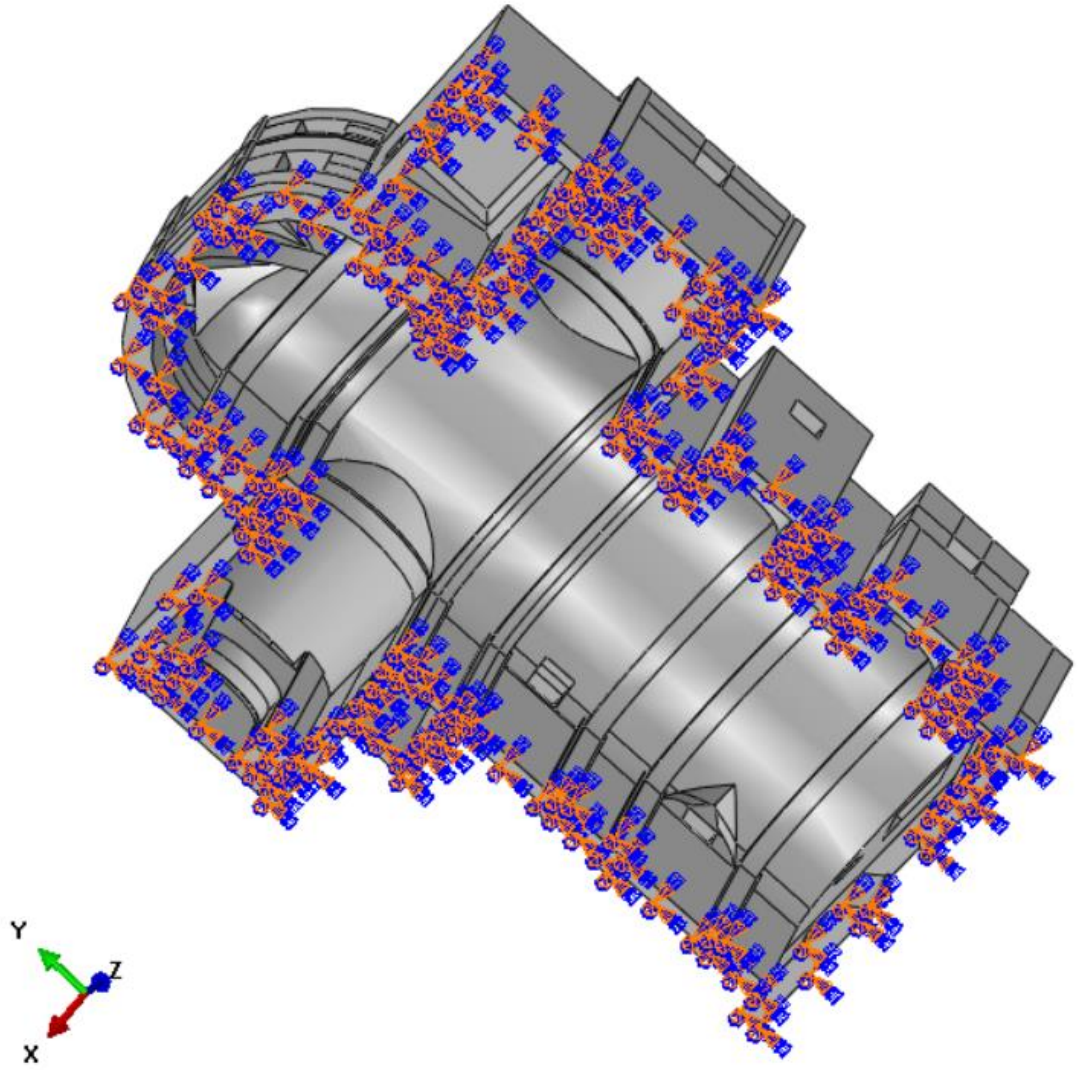

Figure 27: Boundary Condition of the Structure

Since linear tetrahedral elements (C3D4) gives rise to inaccurate solutions and lack the capability of capturing the geometric details, second-order elements should be used in this kind of geometric model.

Although it was strongly suggested to use hexahedral elements as much as possible, quadratic tetrahedral elements are able to give accurate results by setting the number of elements. As stated, in the aforementioned parts of the thesis, the structure has quite complicated parts endowed with sharp edges and high curvatures that are difficult to be modeled. Since the geometry of the structure is quite complicated and difficult to be discretized with the hexahedral elements, 144,467 quadratic tetrahedral elements (C3D10) and 27,313 linear tetrahedral elements (C3D4) were used for the discretization of the church. (Table 11: Element Types and Numbers) Numerical model having 246,253 nodes of San Carpoforo church is shown in Figure 28.

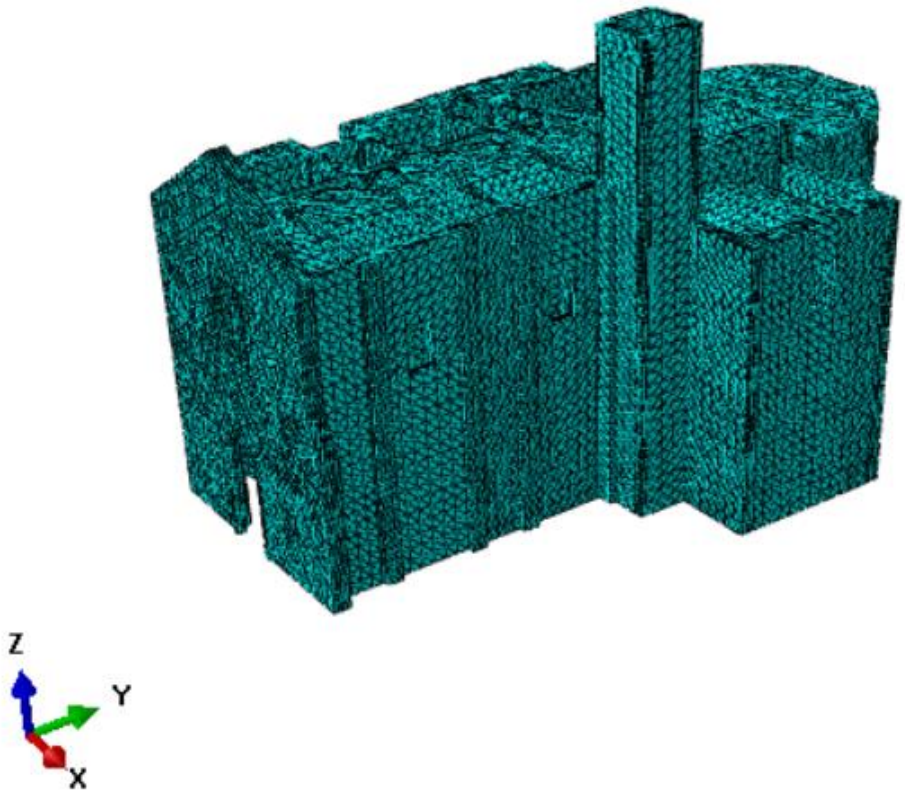

Figure 28: 3D Numerical Model of San Carpoforo Church

Table 11: Element Types and Numbers

Element Name	Number of Elements
Linear Tetrahedral Elements of type C3D4	27,313
Quadratic Tetrahedral Elements of type C3D10	144,467
Total	171,780

10-node quadratic tetrahedral element (CD10) and 4-node linear tetrahedral elements (C3D4) are given in Figure 29. C3D4 element has 1 integration point, and it may not be able to give accurate solutions unless they are highly refined because they are too stiff. In contrast, the C3D10 element has 4 integration points and gives better accuracy.

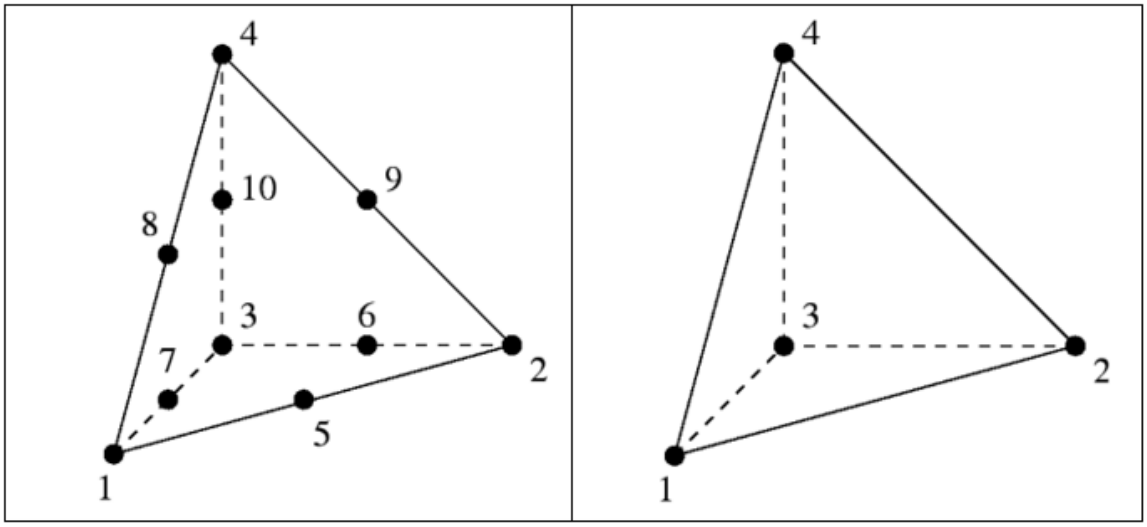

Figure 29: C3D10 and C3D4 elements, respectively

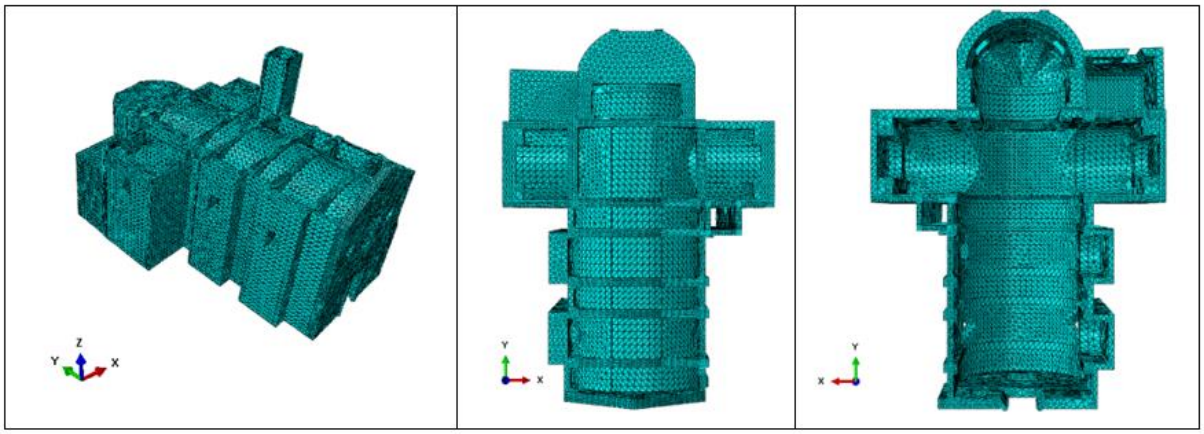

Figure 30: Views of the Finite element Model

5.2 Damage Model

In this study, Concrete Damaged Plasticity (CDP) model that is associated with isotropic damage was used in order to represent the non-linear behavior of the material. Albeit the CDP model has been developed for fragile and isotropic materials such as “concrete”, it can also be used for masonry materials. [31] By means of the CDP model, it is possible to define the properties of the material in tension and compression differently. This difference is based on the distinct damage parameters in tension and compression. [31] In this model, basically, there are two failure mechanisms that are cracking due to tension and crushing due to compression.

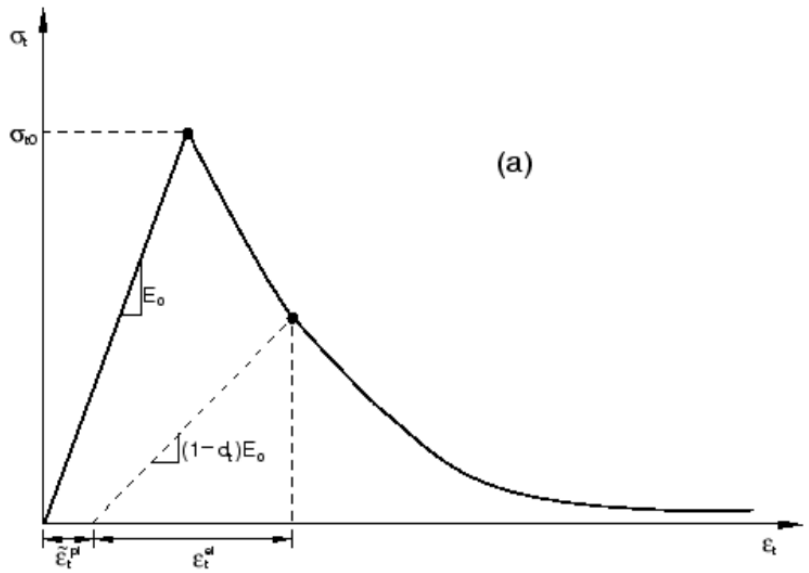

Figure 31: Uniaxial Tension Behavior of Material in Concrete Damage Plasticity (CDP) Model

It is seen that up to reaching the failure stress (σ_{t0}) corresponding to the initiation of micro-cracks in material, the response remains in the linear elastic phase. Once the failure stress (σ_{t0}) is exceeded, it is expected to have a softening response that gives rise to the localization of strain.

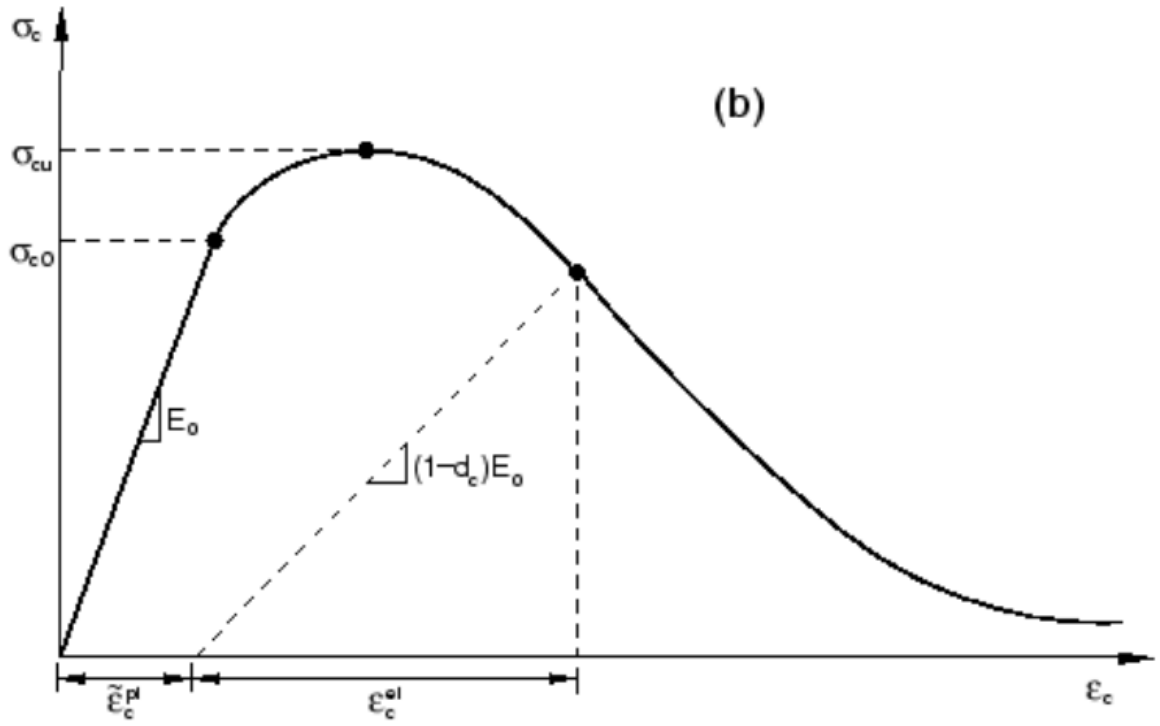

Figure 32: Uniaxial Compression Behavior of Material in Concrete Damage Plasticity (CDP) Model

In uniaxial compression, linear elasticity governs the behavior until the yield stress (σ_{c0}) is reached. In the plastic regime, the stress hardening behavior takes place up to ultimate stress (σ_{cu}). In the pursuit of this value (σ_{cu}), softening of strain governs the behavior.

In addition, ABAQUS allows users to transform the uniaxial stress vs. strain curves for tension and compression into stress vs. plastic strain curves automatically. In this step, ABAQUS uses the stress and inelastic strain data set that is entered by the user.

$$\sigma_t = \sigma_t\left(\tilde{\varepsilon}_t^{pl}, \dot{\varepsilon}_t^{pl}, \theta, f_i\right) \quad (8)$$

$$\sigma_c = \sigma_c\left(\tilde{\varepsilon}_c^{pl}, \dot{\varepsilon}_c^{pl}, \theta, f_i\right) \quad (9)$$

Where:

$\tilde{\varepsilon}_t^{pl}$: equivalent plastic strain in tension

$\tilde{\varepsilon}_c^{pl}$: equivalent plastic strain in compression

$\dot{\varepsilon}_t^{pl}$: equivalent plastic strain rate in tension

$\dot{\varepsilon}_c^{pl}$: equivalent plastic strain rate in compression

θ: temperature

f_i: other predefined field variables

Furthermore, if the material is unloaded from a point falling in the strain-softening regime in the uniaxial stress vs. strain curve, the elastic stiffness of a material is exposed to be damaged. Uniaxial damage variables d_t and d_c governs the reduction of elastic stiffness. These variables can be defined as a function of temperature, strains, and field variables and they must be within the range between 0 and 1, as below.

$$d_t = d_t\left(\tilde{\varepsilon}_t^{pl}, \theta, f_i\right) \quad (10)$$

$$d_c = d_c\left(\tilde{\varepsilon}_c^{pl}, \theta, f_i\right) \quad (11)$$

Where:

$$0 \leq d_t \leq 1 \quad (12)$$

$$0 \leq d_c \leq 1 \tag{13}$$

Being damage parameter 1 means that material is undamaged, whereas in the case of damage parameter having 0 corresponds to have total loss of strength in the material. Stress and strain relation can be elaborated by considering the damage parameters (d_t, d_c) as indicated in equations (14) and (15).

$$\sigma_t = (1 - d_t)E_0\left(\varepsilon_t - \tilde{\varepsilon}_t^{pl}\right) \tag{14}$$

$$\sigma_c = (1 - d_c)E_0\left(\varepsilon_c - \tilde{\varepsilon}_c^{pl}\right) \tag{15}$$

Where:

E_0: undamaged elastic stiffness of the material

To be able to evaluate the size of the yield surface, the effective cohesion stresses ($\bar{\sigma_t}, \bar{\sigma_c}$) can be defined as denoted in equations (16) and (17).

$$\bar{\sigma_t} = \frac{\sigma_t}{1 - d_t} = E_0\left(\varepsilon_t - \tilde{\varepsilon}_t^{pl}\right) \tag{16}$$

$$\bar{\sigma_c} = \frac{\sigma_c}{1 - d_c} = E_0\left(\varepsilon_c - \tilde{\varepsilon}_c^{pl}\right) \tag{17}$$

It was assumed that the masonry material abides by the Drucker-Prager criterion that determines the 3-dimensional behavior of the material. Failure surfaces for Drucker-Prager and Mohr-Coulomb criteria are shown in Figure 33.

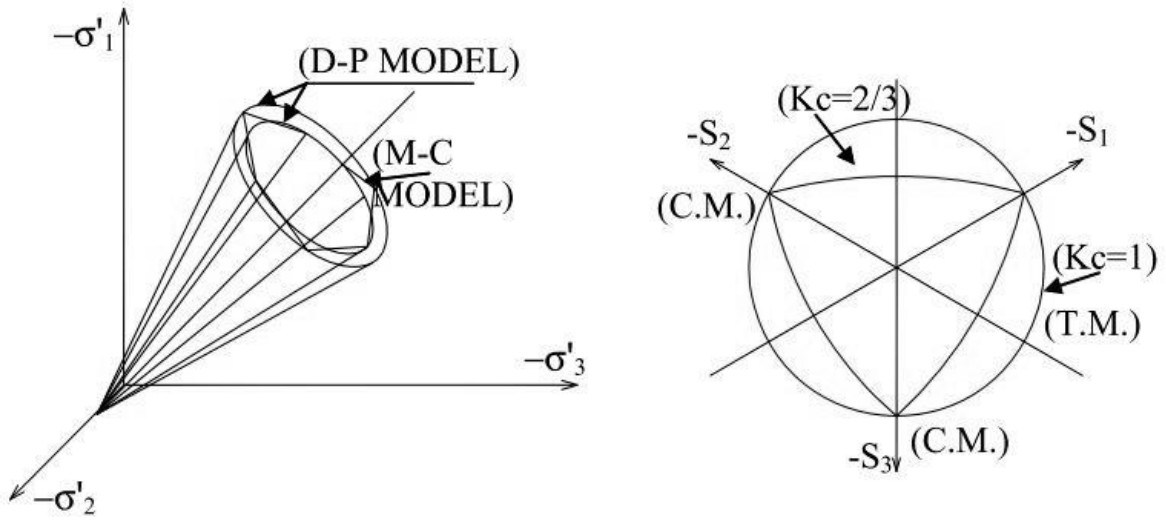

Figure 33: Drucker-Prager and Mohr-Coulomb Failure Criteria

Table 12: Mechanical Parameters for the CDP model

Name	Value
Eccentricity (ε)	0.1
Strength Ratio (F_{b0}/F_{c0})	1.15
Dilation Angle	10°
K_c	0.667
Viscosity Parameter	5E-05

K_c is a parameter that stands for the ratio between the distance from the hydrostatic axis of the maximum compression and tension. [31] This parameter has been suggested to be taken as 0.667 by the user's guide in order to make an approximation to the Mohr-Coulomb failure criterion. [31] The dilation angle governing ductility is recommended at 10° for existing structures. [9], [32] Besides, in the literature, it is suggested that the viscosity parameter should be low for the convergence of analysis. [31], [33] Strength ratio is defined as the ratio between the biaxial and uniaxial compression strength and it is reasonable to be taken as 1.16. [33] In addition, the eccentricity value (ε) is used to make the conical Drucker-Prager strength

domain smoother by means of a hyperbola. [31], [33] This parameter has a feature to keep at numerical instabilities bay. [32]

Tabular data set for defining CDP model, was entered as input to ABAQUS, and shown in Table 13.

Table 13: Concrete Damage Plasticity Model Data

Compression and Tension Behavior				Compression and Tension Damage			
Compression		Tension		Concrete		Tension	
Stress [Pa]	Inelastic Strain [ε]	Stress [Pa]	Inelastic Strain [ε]	Damage Parameter [dt]	Inelastic Strain [ε]	Damage Parameter [dt]	Inelastic Strain [ε]
934628.8	0	124720.1	0	0	0	0	0
1678174	0.0006	106506.3	0.007	0	0.0023679	0	7.89E-05
2245187	0.0009	72639.22	0.1	0	0.003551851	0.1	0.001
2650216	0.0012			0.1	0.003946501	0.95	0.009
2907814	0.0015			0.8	0.01		
3032531	0.0018						
3038916	0.0021						
2941521	0.0024						
2754896	0.0027						
2493592	0.003						
2172159	0.0033						
1805147	0.0036						
1407107	0.0039						
992590	0.0042						
576145.9	0.0045						
172325.2	0.0048						

5.3 Roof Loading

As mentioned in the previous part of the study, in this analysis, it was found out that there is no positive stiffness effect provided by the roof of the structure. Hence, it would be a reasonable assumption to consider only its mass effects. The section view of the church can be seen in Figure 34.

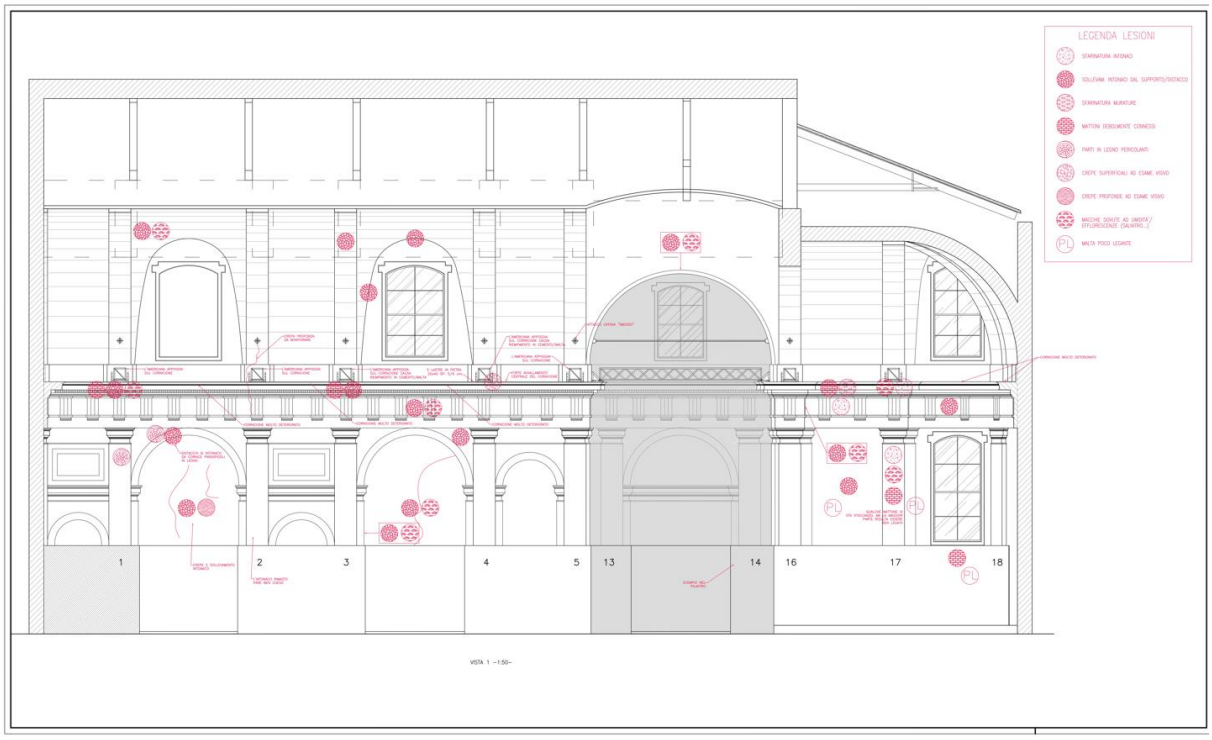

Figure 34: Section View of the church for truss locations

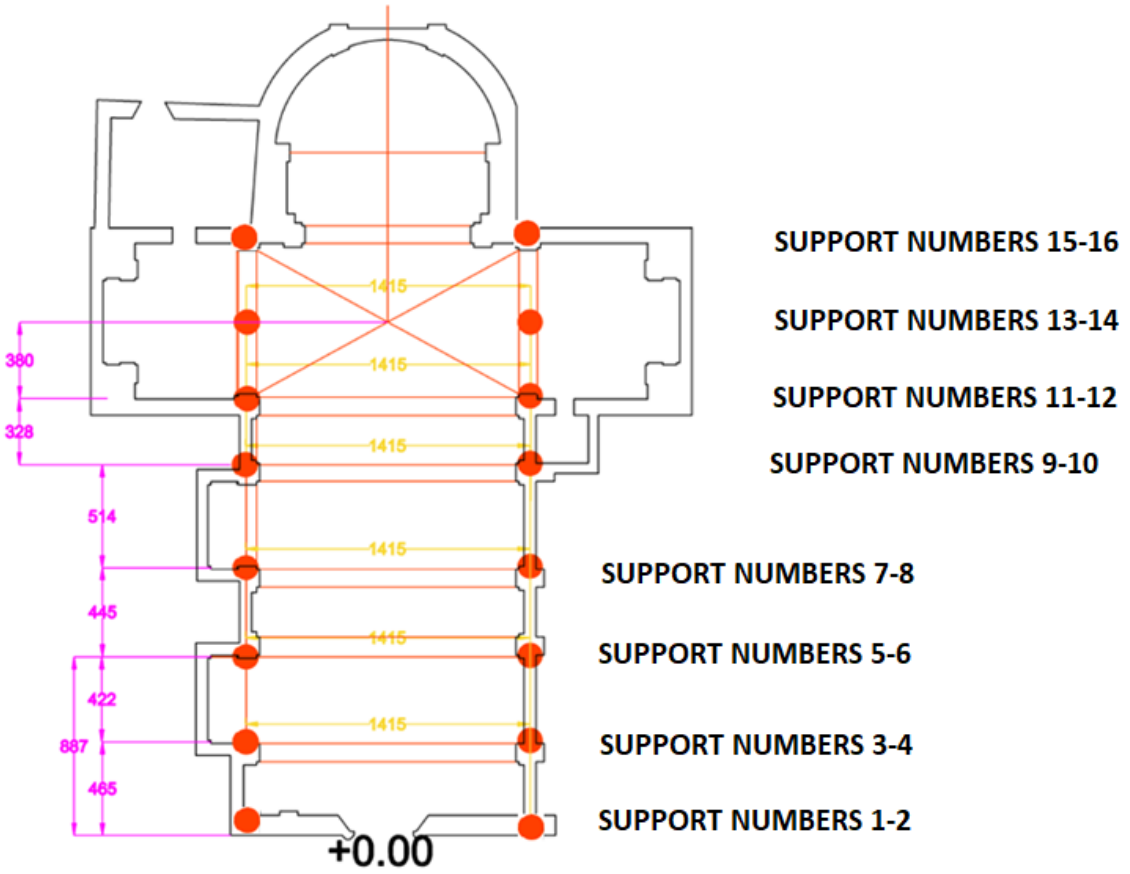

Figure 35: Locations of the Point Masses

From the field observations, there are timber trusses carrying the clay tiles. To be able to consider the self-weight of the roof system including timber and clay tiles, it is required to convert them into point masses. It was possible to consider trusses as equivalent beams that are subjected to uniformly distributed load and that are supported at the points. Self-weight of the roof system was considered as uniformly distributed with a magnitude of 1.5 kN/m^2.

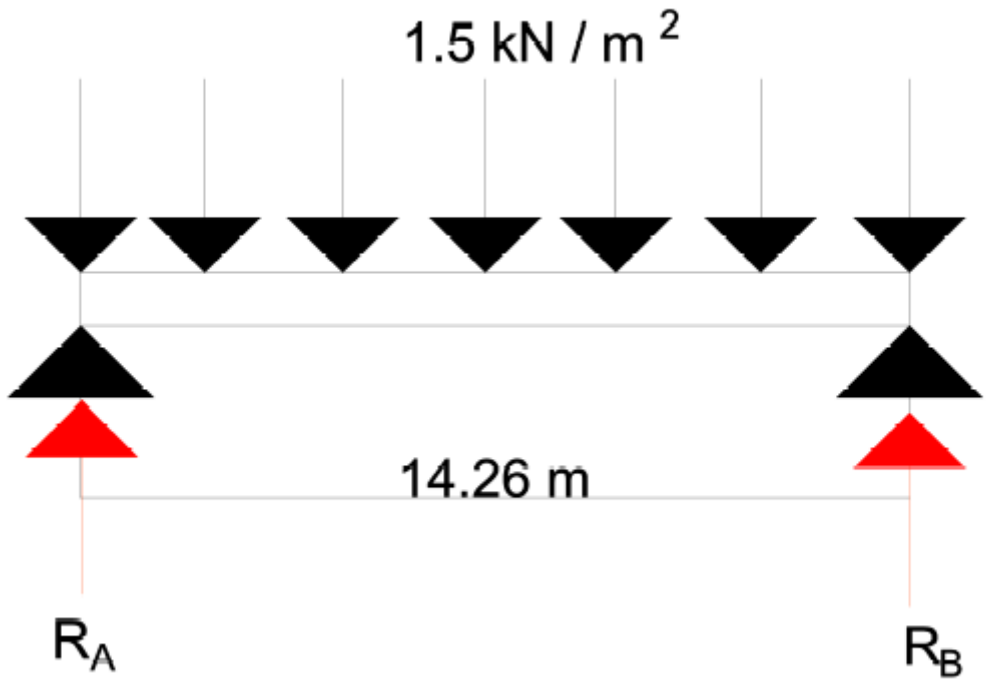

Figure 36: Equivalent Beams Subjected to Roof Load

Tributary areas were computed for each truss, and then point masses were computed. Point masses are denoted in Table 14. In the pursuit of this, the values shown in Table 14, were divided into 2 in order to find the reactions at each support point. For instance, the reactions at support number 1, were taken as 24.68 kN.

Table 14: Point Mass Values for each Truss

Support Numbers	Tributary Area [m^2]	Point Mass [kN]
1-2	$(14.15\ m) \cdot \left(\frac{4.65}{2} m\right) = 32.9$	49.35
3-4	$(14.15\ m) \cdot \left(\frac{4.22 + 4.65}{2} m\right) = 62.76$	94.13
5-6	$(14.15\ m) \cdot \left(\frac{4.22 + 4.45}{2} m\right) = 61.34$	92.01
7-8	$(14.15\ m) \cdot \left(\frac{5.14 + 4.45}{2} m\right) = 67.85$	101.77
9-10	$(14.15\ m) \cdot \left(\frac{5.14 + 3.28}{2} m\right) = 59.57$	89.36
11-12	$(14.15\ m) \cdot \left(\frac{3.28 + 3.8}{2} m\right) = 50.09$	75.14
13-14	$(14.15\ m) \cdot \left(\frac{3.8 + 3.8}{2} m\right) = 53.77$	80.66
15-16	$(14.15\ m) \cdot \left(\frac{3.8}{2} m\right) = 26.89$	40.33

In addition, it is no need to choose any units in ABAQUS, it is automatically recognized by itself if one of the following sets of units is adopted. In this thesis, SI units are adopted.

Table 15: ABAQUS Unit System

Quantity	SI	SI [mm]	US Unit [ft]	US Unit [inch]
Length	m	mm	ft	in
Force	N	N	Ibf	Ibf
Mass	kg	tonne (10^3 kg)	slug	Ibf s^2/in
Time	s	s	s	s
Stress	Pa (N/ m^2)	MPa (N/ mm^2)	Ibf/ft^2	Psi (Ibf/in^2)
Energy	J	mJ (10^{-3} J)	Ft Ibf	In Ibf
Density	kg/m^3	tonne/mm^3	Slug/ft^3	Ibf s^2/in^4

6 Method of Analysis

Basically, seismic analysis is divided into two categories being linear and non-linear analysis as shown in Figure 37. It is worth stating that modal analysis plays a significant role in the estimation of the distribution of mass, and stiffness of the structure no matter which kind of analysis is carried out. In other words, it is essential to perform modal analysis in order to extract the seismic characterization of the structure. Besides, in the case of time history analysis, time step integration can be obtained from the modal analysis.

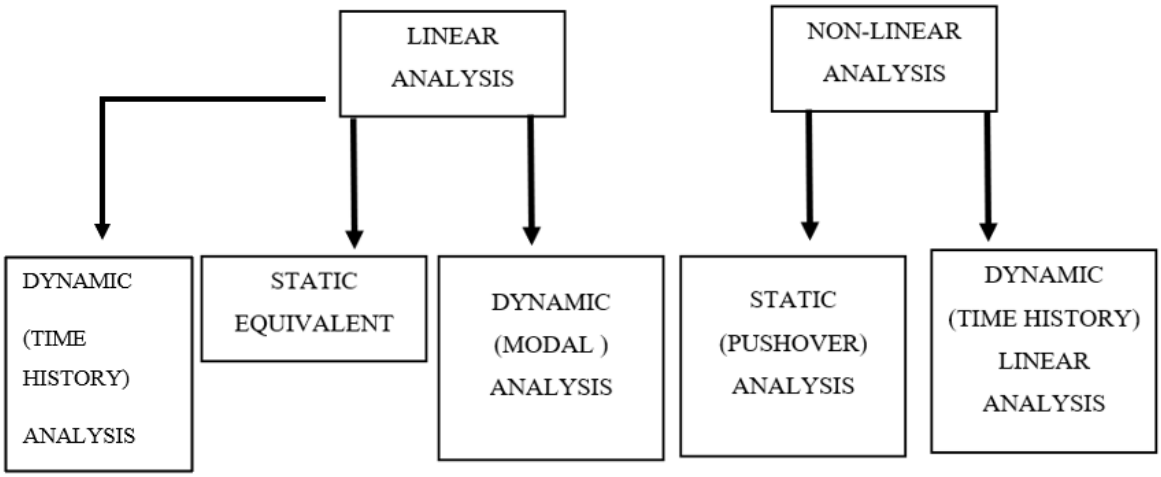

Figure 37: Methods of Seismic Analysis

While the lateral force method (static equivalent linear analysis) gives rise to conservative results, the modal analysis presents much more accurate results, and it may be applied not only on frames but also to the structures endowed with box behavior (masonry structures).

In Eurocode-8 (EC-8), design approaches are based on the static equivalent and modal analysis whereas non-linear analyses are optional. However, in the case of assessment of existing structures, it is required to perform non-linear analyses.

6.1 Static Analysis for the Self Weight of the church

Since the gravity load leads to significant and the self-weight of the structure is constant during its life, it is worth carrying out a preliminary static analysis with the Concrete Damaged Plasticity (CDP) model. Indeed, the nature of the masonry structures is

characterized by having not constant thickness through the wall. Hence, it gives rise out of plane displacements due to eccentric axial loads. In the analysis, only gravity loads were considered and clamped boundary conditions at the base were used. Moreover, since the roof has no positive effect on the stiffness of the structure, only its weight was taken into account. [9]

Out of Plane Displacements under Self Weight

Since the out-of-plane behavior plays a critical role in ancient masonry structures, it should be worth to be checked by means of out-of-plane displacement. It is observed that maximum out-of-displacement takes place at the right walls between the openings (at z=10.67 m). It was computed as 8.397 mm. Considering the height of the wall is 18.12 m, the maximum out-of-plane displacement corresponds to 0.045 % of the wall height.

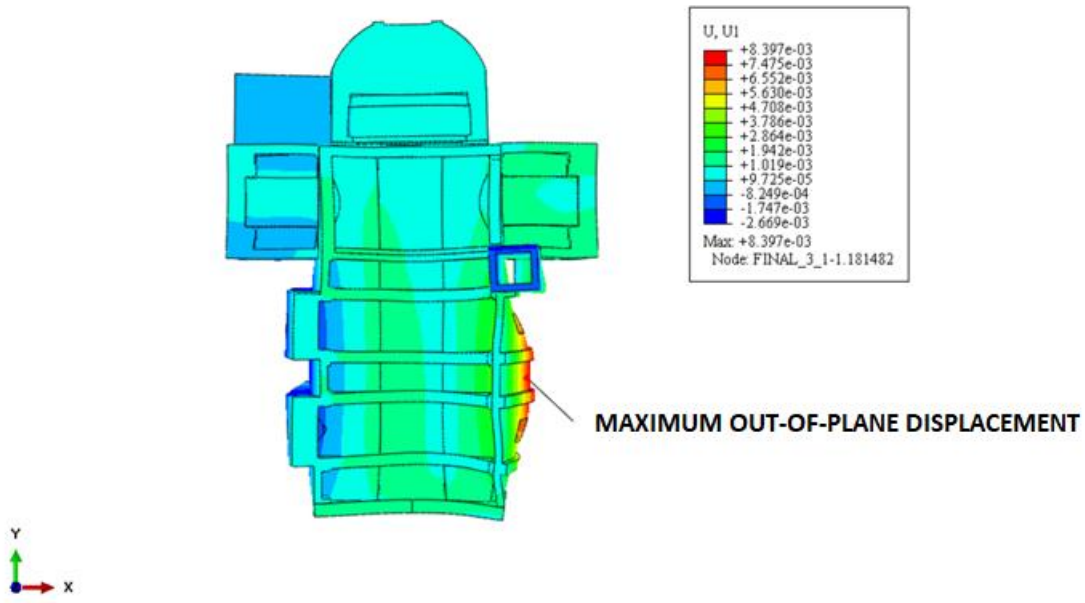

Figure 38: Maximum Out-of-Plane Displacement under Self Weight of the Church

The maximum principal stresses (tensile stresses) are denoted in Figure 39. As it can be seen, maximum principal stresses are not high level.

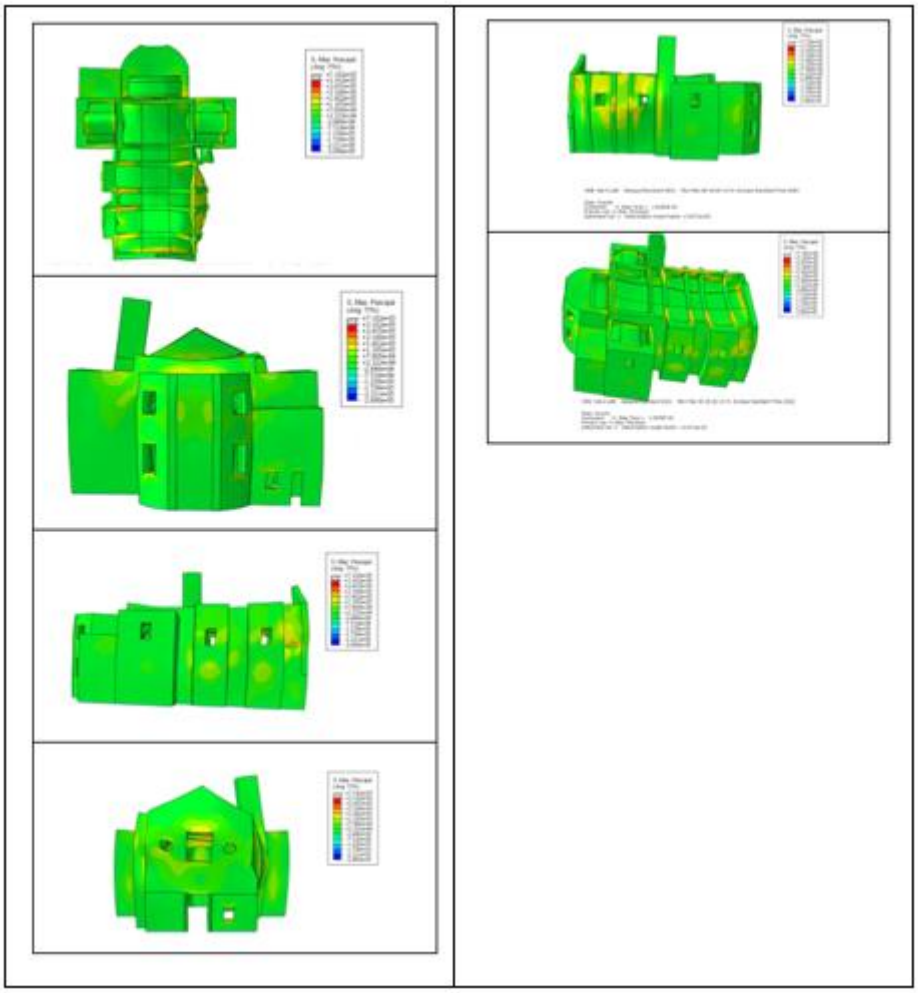

Figure 39: Tensile Stress Distribution under Self Weight of the structure

Minimum Principal Stresses (compressive stresses) are demonstrated below. As it can be anticipated, there are no critical regions suffering from compressive stress.

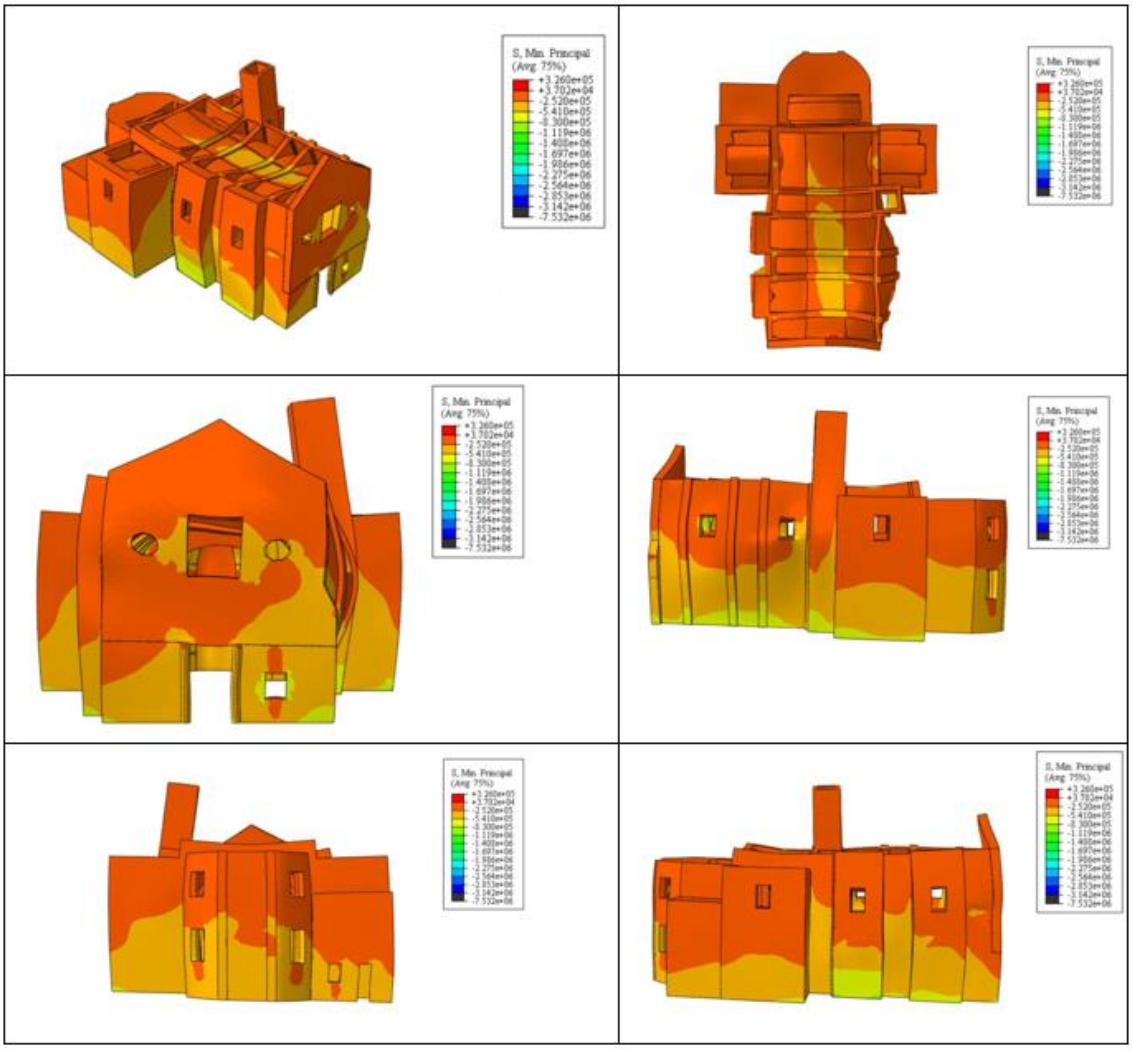

Figure 40: Compressive Stress Distribution under Self Weight of the Structure

Horizontal Sections of the tensile stress distribution are denoted below. Although there is no region exceeding the tensile strength of the masonry corresponding to 0.3142 MPa, in some regions considerable magnitude of stresses is observed as follows.

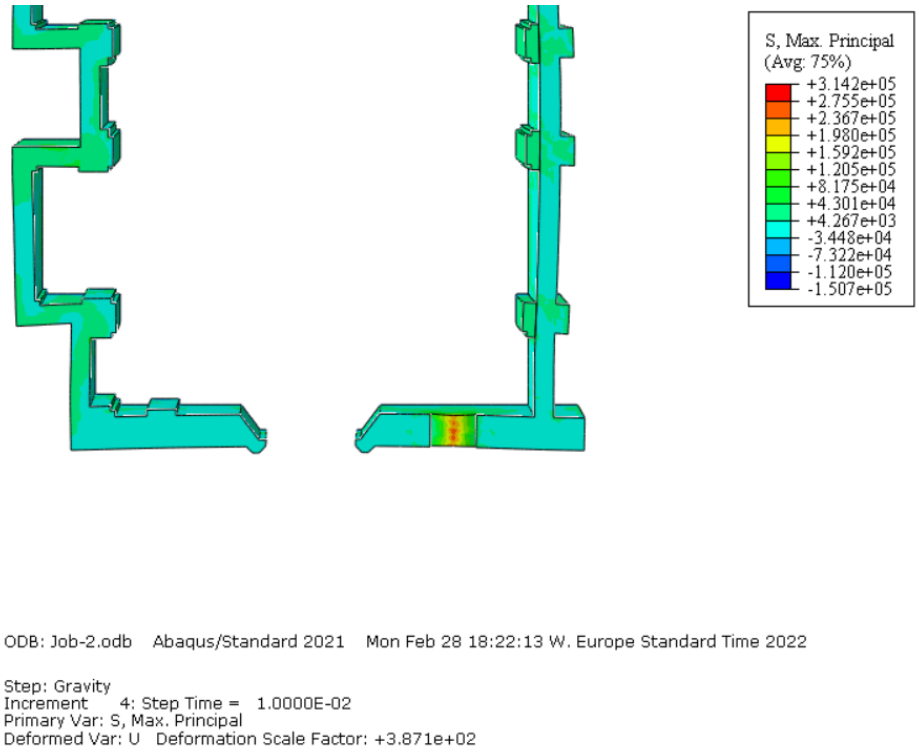

Figure 41: At z= 1.72 m (at the left window opening of the façade), Tensile Stress Distribution under Gravity Load

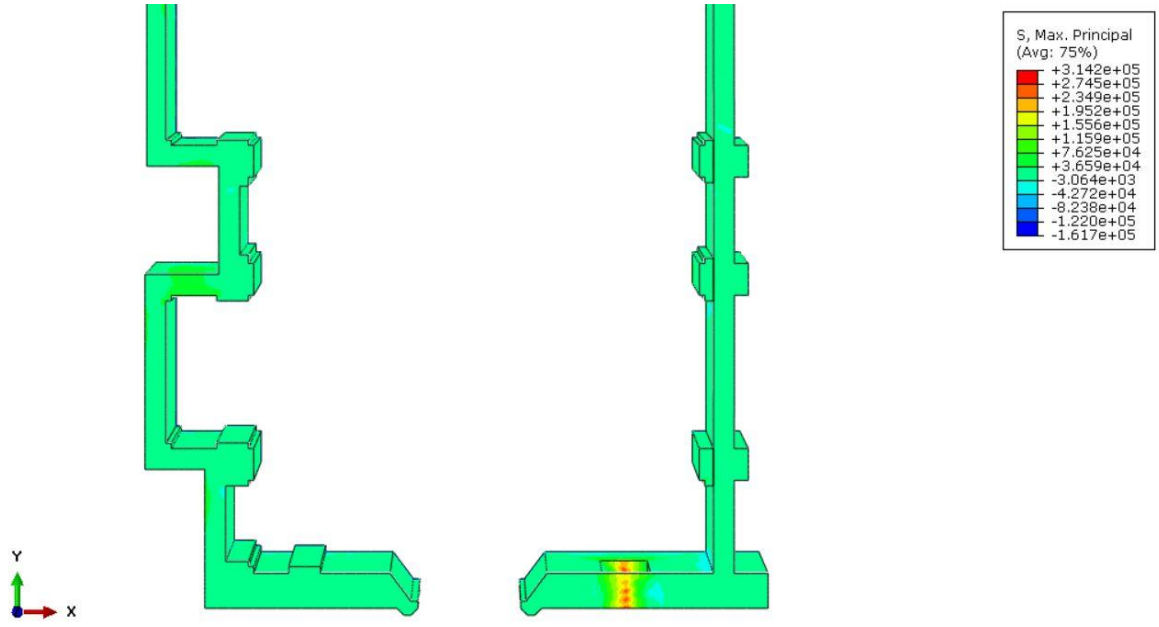

Figure 42: At z= 4.13 m (at the left window opening of the façade), Tensile Stress Distribution under Gravity Load

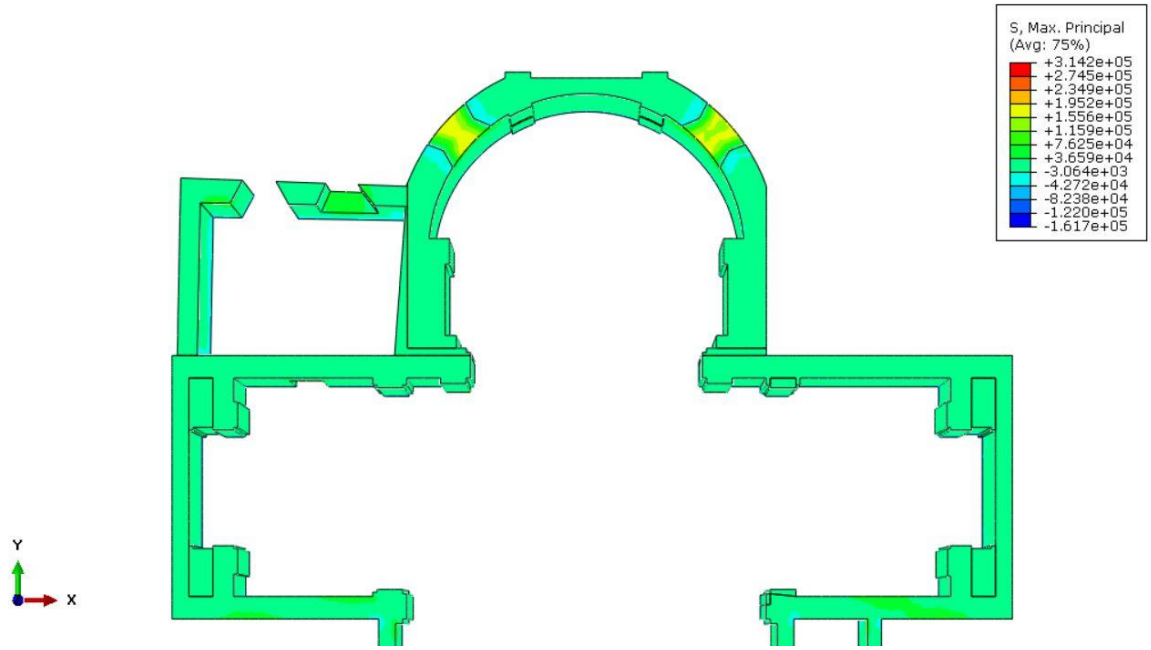

Figure 43: At z= 4.13 m (at the openings in the apse), Tensile Stress Distribution under Gravity Load

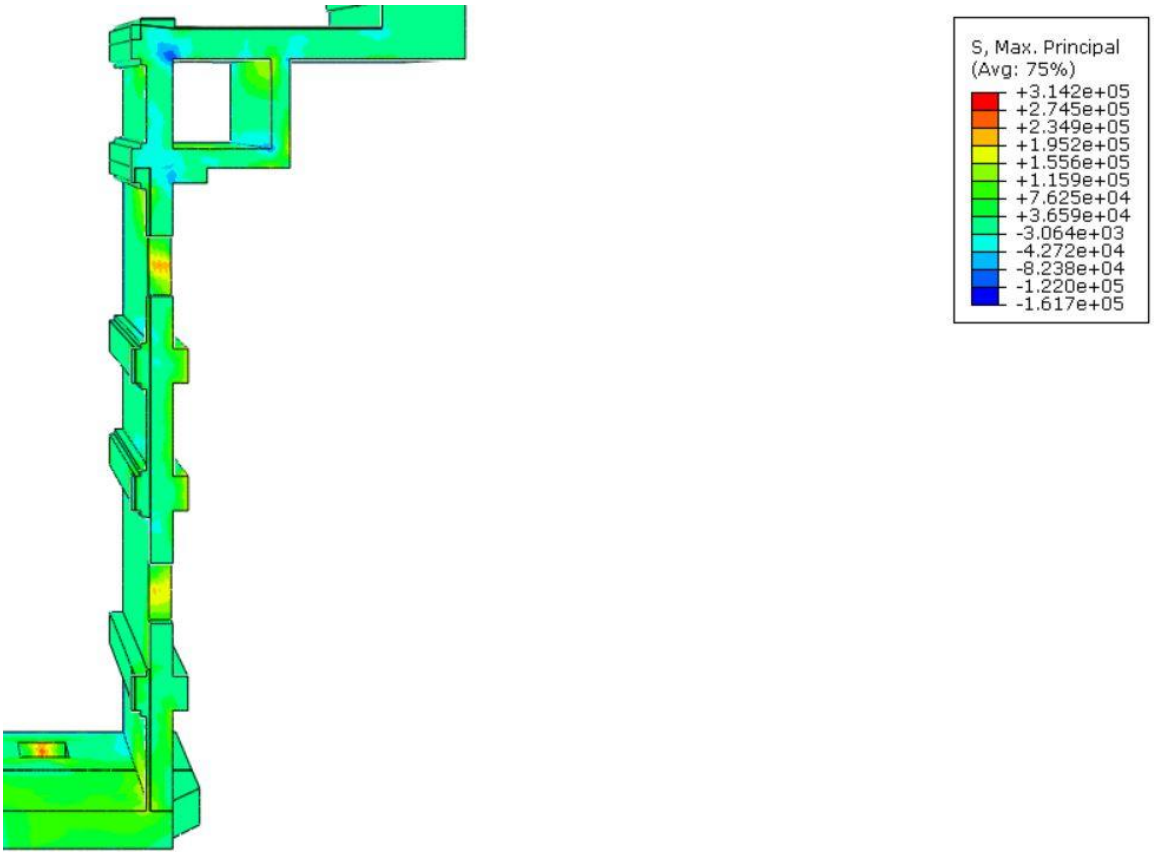

Figure 44: At z= 12.02 m (at the left walls), Tensile Stress Distribution under Gravity Load

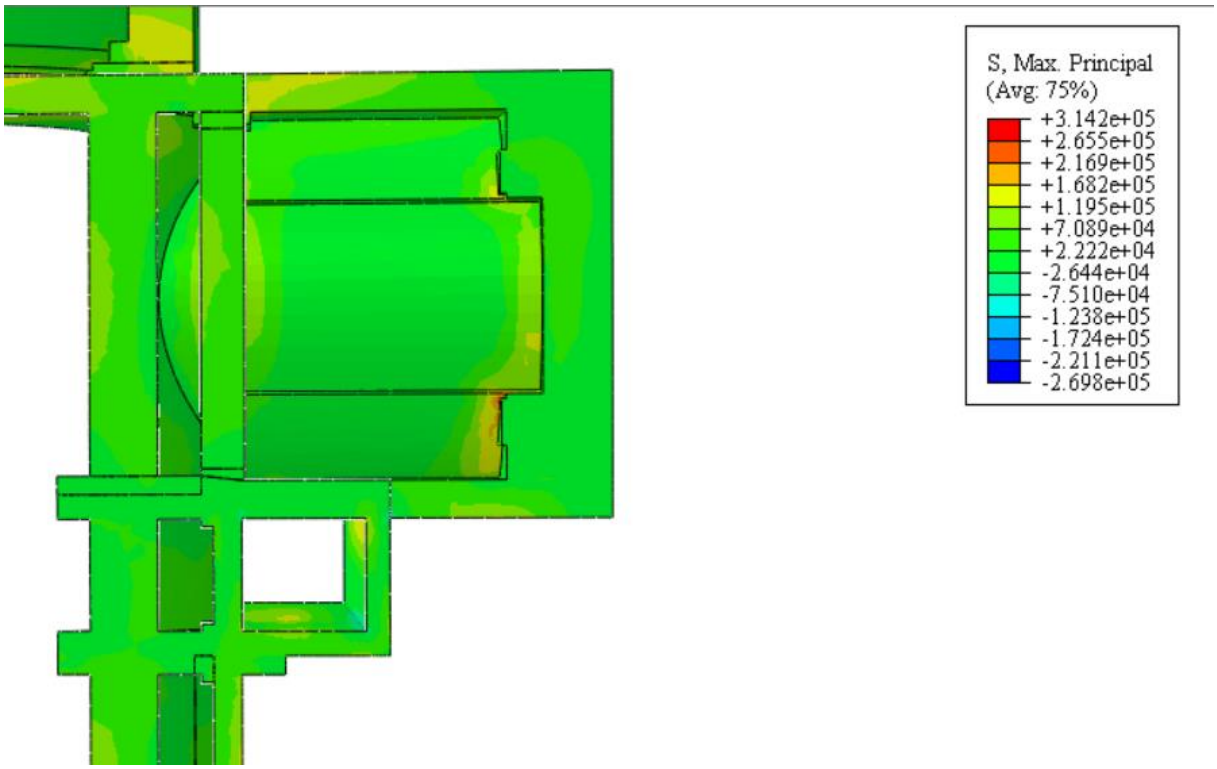

Figure 45: At z= 16.2032 m (at the connection between the bell tower and left transept), Tensile Stress Distribution under Gravity Load

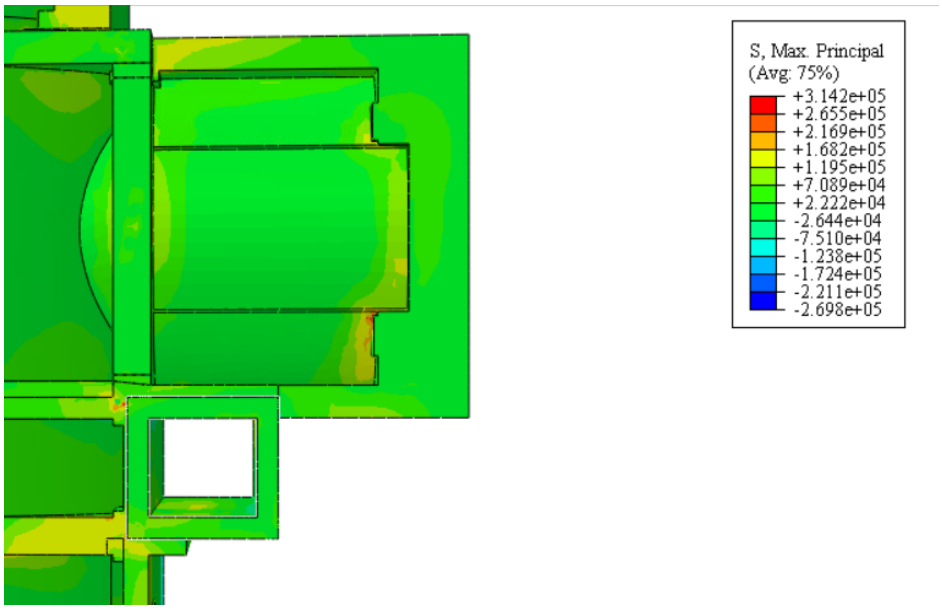

Figure 46: At z= 18.1645 m (at the connection between the bell tower and the nave), Tensile Stress Distribution under Gravity Load

6.2 Modal Analysis

6.2.1 Methodology of Modal Analysis

It is known that modal analysis is exploited for learning the vibration characteristics of linear elastic structures. The most important step in case carrying out modal analysis is to seek an answer to the question "If certain natural frequencies of the structure coincide with the dynamic loading or not?". If the natural frequency of the structure coincides with the dynamic loading, then the "resonance" condition takes place, and it leads to the failure of the structure. In addition, the natural frequencies obtained from the modal analysis are used to understand more complex dynamic behaviors. Furthermore, modal analysis can also indicate the possible modeling issues. [9] The governing equation of the modal analysis is denoted in equation (18).

$$[M]\{\ddot{u}\} + [C]\{\dot{u}\} + [K]\{u\} = \{f(t)\} \qquad (18)$$

Where:

M: Mass

C: Damping

K: Stiffness

u: Displacement

f(t): Load

The unknowns of the equation of the motion are displacement, velocity, and acceleration of the structure. Due to the fact that mode shapes and natural frequencies are the structure's inherent features, they are not dependent on the loads. Hence the right-hand side of the equation of motion corresponding to f(t) vanishes. For a general analysis, the effect of damping is not taken into account in the solution of the problem. Hence, the equation of motion turns out as shown in Equation (19).

$$[M]\{\ddot{u}\} + [K]\{u\} = 0 \tag{19}$$

Assuming that each point undergoes harmonic motion, it is possible to transform the time domain into the frequency domain. Hence, displacement and acceleration can be expressed in harmonic form as shown in Equation (20) and Equation (21).

$$\{u\} = \{\emptyset\}\sin(\omega t + \theta) \tag{20}$$

$$\{\ddot{u}\} = -\omega^2\{\emptyset\}\sin(\omega t + \theta) \tag{21}$$

Where:

$\emptyset$: Amplitude

θ: Phase Angle

ω: Angular Frequency

In this case, unknowns become amplitude ($\emptyset$), phase angle (θ), and angular frequency (ω). For this reason, if Equation (20) and Equation (21) are plugged into Equation (18), then the equation of motion turns out the one given by Equation (22).

$$([K] - \omega^2[M])\{\emptyset\} = 0 \qquad (22)$$

Where:

ω: Eigenvalue

$\emptyset$: Eigenvector

Computing the point masses at the supports, they were introduced in ABAQUS, by means of the following commands Module: Interaction, Special: Inertia, Create Inertia: Point mass/ inertia.

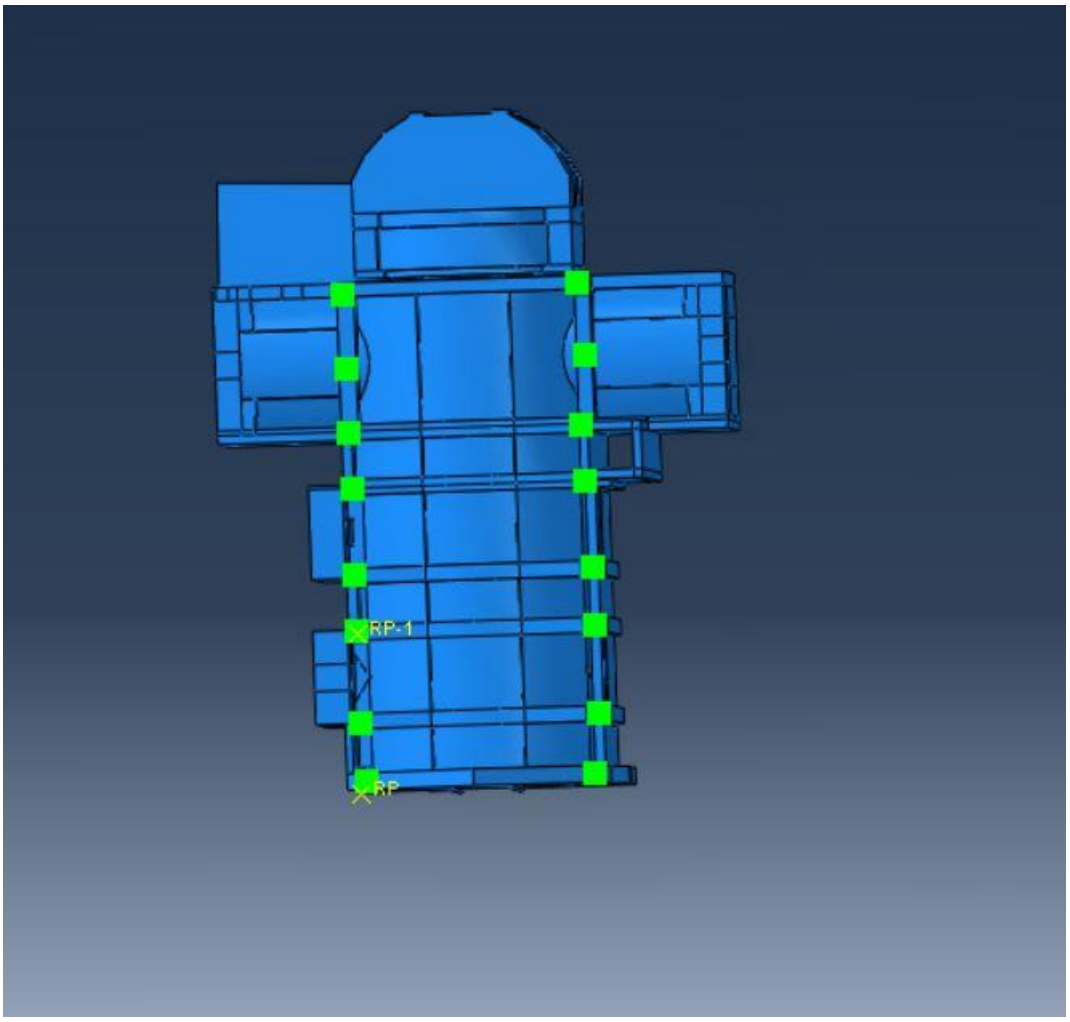

Figure 47: Application of the Point Masses on ABAQUS

Modal analysis was carried out and the results were listed containing natural frequency, and period values in the following table. ABAQUS offers 3 different eigensolvers including Lanczos, AMS, and subspace iteration, in order to extract the natural frequencies. Eigen solver was chosen as Lanczos algorithm for the analysis.

6.2.2 Lanczos Algorithm

It is known that the eigenvalue problem can be defined as shown in Equation (23) by assuming that $[K]$ is symmmetric. [34]

$$(-\omega^2[M] + [K])\{\emptyset\} = 0 \qquad (23)$$

It is one of three algorithms that are provided by ABAQUS in order to implement frequency extraction. In the case of Lanczos eigensolver, spectral transformation is carried out as shown in Equation (24).

$$[M]([K]-\sigma[M])^{-1}[M]\{\emptyset\}=\theta[M]\{\emptyset\} \quad (24)$$

Where:

σ: Shift

θ: Eigenvalue

$\{\emptyset\}$: Eigenvector

While eigenvectors of the original problem and the transformed problem provided by the Lanczos case are identical, it is required to use Equation (25) to be able to obtain the eigenvalues.

$$\omega^2=\frac{1}{\theta}+\sigma \quad (25)$$

In this study, Lanczos was chosen as an eigensolver to extract the eigenvalues. In addition, the number of interested eigenvalues was taken as 80. Block size and maximum number of block Lanczos steps were put as “Default”.

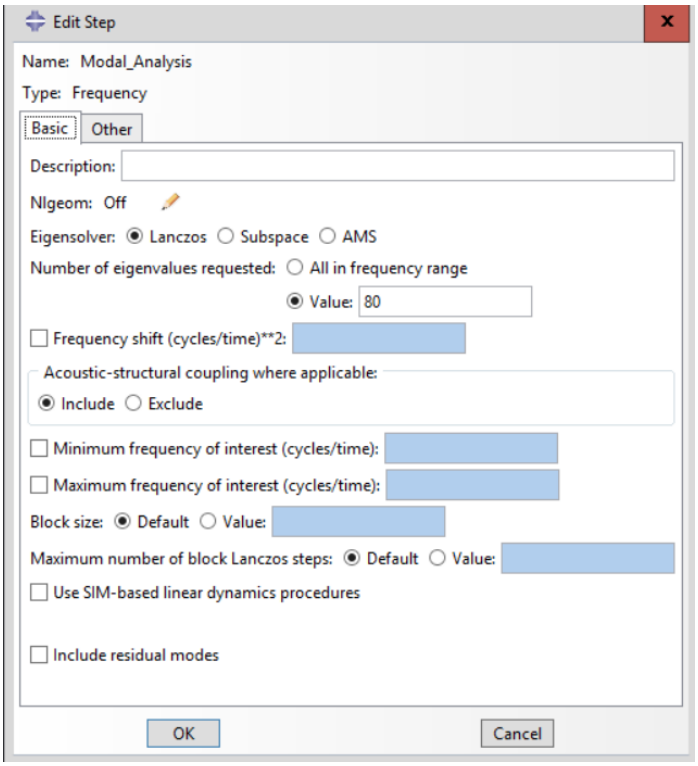

Figure 48: Modal Analysis, Edit Step-1

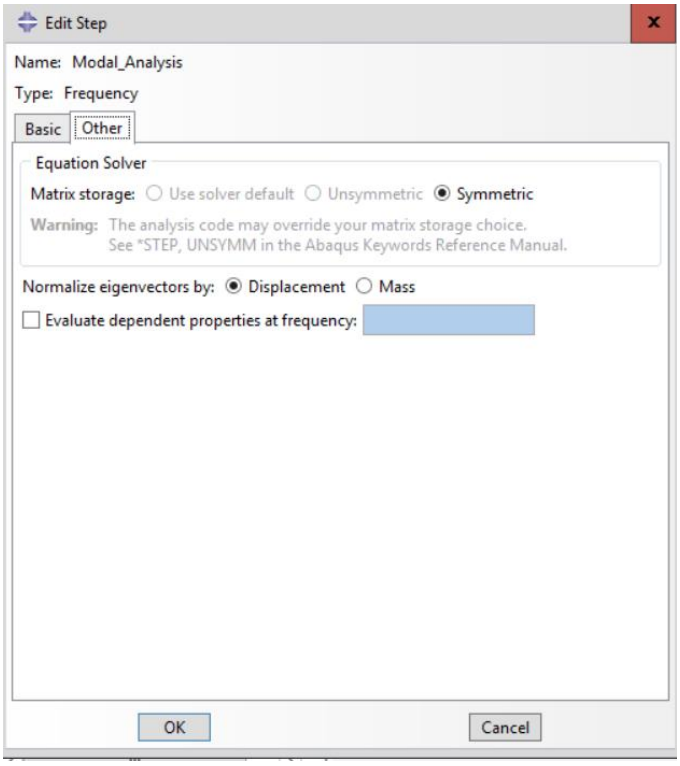

Figure 49: Modal Analysis, Edit Step-2

6.2.3 Results of Modal analysis

Model shapes explain the response of churches under the effect of ground motion. Additionally, they may be exploited to determine the possible local collapse mechanisms. Natural Frequency and period values were obtained from ABAQUS and listed in Table 16. In previous studies, it was stated that since historical masonry churches contain many local modes, it is suggested to extract the high number of modes. [4], [12] Although the rule of exciting at least 90 percent of mass holds for frame structures, and it is not necessary for masonry structures, at the first attempt, 80 modes were extracted. It is seen that the periods of the first two dominant modes are 0.363 s, and 0.276 s, respectively.

Table 16: Natural Frequency and Period Values of the Modes

Mode Number	Frequency [Hz]	Period [T]
1	2.754	0.363
2	3.630	0.276
3	4.118	0.243
4	4.480	0.223
5	4.856	0.206
6	5.168	0.193
7	5.189	0.193
8	6.062	0.165
9	6.334	0.158
10	6.928	0.144
11	7.052	0.142
12	7.461	0.134
13	7.740	0.129
14	7.966	0.126
15	8.025	0.125
16	8.471	0.118
17	8.659	0.115
18	8.880	0.113
19	9.051	0.110
20	9.197	0.109
21	9.632	0.104
22	9.777	0.102
23	9.995	0.100
24	10.100	0.099
25	10.535	0.095
26	10.706	0.093
27	11.058	0.090
28	11.136	0.090
29	11.184	0.089
30	11.443	0.087

31	11.563	0.086
32	12.103	0.083
33	12.119	0.083
34	12.257	0.082
35	12.540	0.080
36	12.590	0.079
37	12.846	0.078
38	13.019	0.077
39	13.250	0.075
40	13.349	0.075
41	13.445	0.074
42	13.544	0.074
43	13.702	0.073
44	14.063	0.071
45	14.312	0.070
46	14.367	0.070
47	14.643	0.068
48	14.685	0.068
49	14.772	0.068
50	14.916	0.067
51	15.012	0.067
52	15.199	0.066
53	15.421	0.065
54	15.543	0.064
55	15.678	0.064
56	15.797	0.063
57	15.928	0.063
58	16.076	0.062
59	16.225	0.062
60	16.285	0.061
61	16.474	0.061
62	16.742	0.060
63	16.855	0.059
64	16.925	0.059
65	17.079	0.059
66	17.284	0.058
67	17.307	0.058
68	17.526	0.057
69	17.611	0.057
70	17.677	0.057
71	18.049	0.055
72	18.145	0.055
73	18.271	0.055
74	18.391	0.054
75	18.552	0.054
76	18.657	0.054
77	18.813	0.053
78	18.853	0.053

79	19.012	0.053
80	19.226	0.052

In order to decide the importance of the modes, it is required to investigate the effective mass and participation factor values for the extracted modes.

Effective mass values for translation and rotations are shown in Table 17 and Table 18. Specifically, it is seen that the most important modes for X-translation are mode 1 (64.9%), mode 3 (2.31%), mode 6 (6.74 %), mode 9 (2.32 %), and mode 12 (1.90 %). In other words, at the end of first 12 modes, more than 80 percent of mass is excited in X direction. For the T-translation, mode 2 (68.03 %), mode 5 (1.51 %), mode 7 (2.61 %), mode 10 (3.22 %), and mode 13 (1.63 %) are the dominant modes. Similarly, more than 80 percent of mass is excited with the first 13 modes. Finally, at the end of 80 modes, approximately, 90 percent of mass is excited in both X-Translation and Y-Translation.

Table 17: Effective Mass Values for X-Translation and Y-Translation Components

	Effective Mass X-Translation			Effective Mass Y-Translation		
Mode Number	Value [kg]	Percent [%]	Cumulative Percent [%]	Value [kg]	Percent [%]	Cumulative Percent [%]
1	4.21E+06	64.90%	64.90%	1.86E+03	0.03%	0.03%
2	6.49E+03	0.10%	65.00%	4.42E+06	68.03%	68.06%
3	1.50E+05	2.31%	67.31%	1.23E+05	1.90%	69.96%
4	3.24E+04	0.50%	67.81%	2.14E+04	0.33%	70.29%
5	4.52E+04	0.70%	68.50%	9.82E+04	1.51%	71.80%
6	4.20E+05	6.47%	74.98%	2.70E+03	0.04%	71.84%
7	4.53E+04	0.70%	75.67%	1.69E+05	2.61%	74.45%
8	1.50E+04	0.23%	75.90%	5.06E+04	0.78%	75.23%
9	1.50E+05	2.32%	78.22%	2.66E+03	0.04%	75.27%
10	2.98E+04	0.46%	78.68%	2.09E+05	3.22%	78.49%
11	3.70E+03	0.06%	78.74%	7.94E+02	0.01%	78.50%
12	1.23E+05	1.90%	80.64%	3.32E+03	0.05%	78.55%
13	8.97E+03	0.14%	80.78%	1.06E+05	1.63%	80.18%
14	6.37E+03	0.10%	80.87%	5.26E+03	0.08%	80.26%
15	1.66E+03	0.03%	80.90%	1.02E+04	0.16%	80.42%
16	3.73E+04	0.57%	81.48%	2.07E+04	0.32%	80.74%
17	4.20E+03	0.06%	81.54%	5.44E+02	0.01%	80.75%
18	1.55E+03	0.02%	81.56%	5.50E+02	0.01%	80.76%
19	2.05E+02	0.00%	81.57%	1.52E+04	0.23%	80.99%
20	7.06E+03	0.11%	81.68%	1.50E+04	0.23%	81.22%
21	7.40E+02	0.01%	81.69%	3.67E+04	0.57%	81.79%
22	8.87E+02	0.01%	81.70%	6.07E+02	0.01%	81.80%
23	2.47E+04	0.38%	82.08%	2.28E+04	0.35%	82.15%
24	5.90E+04	0.91%	82.99%	1.59E+04	0.24%	82.39%

25	2.69E+04	0.41%	83.40%	3.55E+03	0.05%	82.44%
26	3.71E+04	0.57%	83.98%	3.20E+02	0.00%	82.45%
27	1.06E+02	0.00%	83.98%	1.51E+00	0.00%	82.45%
28	7.20E+03	0.11%	84.09%	1.71E+02	0.00%	82.45%
29	1.64E+04	0.25%	84.34%	4.45E+03	0.07%	82.52%
30	4.51E+03	0.07%	84.41%	2.25E+03	0.03%	82.56%
31	1.42E+03	0.02%	84.43%	2.08E-01	0.00%	82.56%
32	8.07E+03	0.12%	84.56%	1.95E+04	0.30%	82.86%
33	7.23E+03	0.11%	84.67%	5.17E+04	0.80%	83.65%
34	1.03E+04	0.16%	84.83%	1.15E+04	0.18%	83.83%
35	6.05E+04	0.93%	85.76%	4.11E+04	0.63%	84.46%
36	1.73E+04	0.27%	86.03%	4.45E+03	0.07%	84.53%
37	1.63E+04	0.25%	86.28%	1.06E+04	0.16%	84.69%
38	5.58E+03	0.09%	86.36%	7.56E+02	0.01%	84.71%
39	8.52E+02	0.01%	86.38%	1.17E+04	0.18%	84.89%
40	3.26E+03	0.05%	86.43%	4.85E+04	0.75%	85.63%
41	1.04E+04	0.16%	86.59%	8.13E+03	0.13%	85.76%
42	5.40E+01	0.00%	86.59%	1.71E+04	0.26%	86.02%
43	1.46E+04	0.22%	86.81%	6.12E+02	0.01%	86.03%
44	2.34E+04	0.36%	87.17%	3.57E+03	0.05%	86.09%
45	4.30E+02	0.01%	87.18%	4.20E+04	0.65%	86.73%
46	1.89E+04	0.29%	87.47%	6.12E+03	0.09%	86.83%
47	2.52E+03	0.04%	87.51%	1.05E+04	0.16%	86.99%
48	2.22E+03	0.03%	87.54%	9.32E+03	0.14%	87.13%
49	1.60E+04	0.25%	87.79%	3.00E-01	0.00%	87.13%
50	1.49E+04	0.23%	88.02%	6.77E+03	0.10%	87.24%
51	2.85E+04	0.44%	88.46%	1.17E+03	0.02%	87.26%
52	1.74E+03	0.03%	88.49%	9.95E+03	0.15%	87.41%
53	4.52E+03	0.07%	88.56%	1.30E+04	0.20%	87.61%
54	1.90E+04	0.29%	88.85%	1.29E+03	0.02%	87.63%
55	6.34E+03	0.10%	88.95%	3.31E+03	0.05%	87.68%
56	1.42E+03	0.02%	88.97%	1.23E+04	0.19%	87.87%
57	1.39E+03	0.02%	88.99%	8.49E+02	0.01%	87.88%
58	4.65E+03	0.07%	89.06%	1.29E+02	0.00%	87.89%
59	8.78E+02	0.01%	89.08%	2.32E+03	0.04%	87.92%
60	1.27E+02	0.00%	89.08%	8.18E+00	0.00%	87.92%
61	2.66E+03	0.04%	89.12%	4.08E+03	0.06%	87.98%
62	5.55E+02	0.01%	89.13%	1.00E+04	0.15%	88.14%
63	6.23E+03	0.10%	89.22%	2.41E+04	0.37%	88.51%
64	1.52E+03	0.02%	89.25%	3.54E+03	0.05%	88.56%
65	9.45E+01	0.00%	89.25%	6.16E+00	0.00%	88.56%
66	5.59E+02	0.01%	89.26%	2.78E+01	0.00%	88.56%
67	4.61E+03	0.07%	89.33%	1.48E+04	0.23%	88.79%
68	1.90E+03	0.03%	89.36%	1.07E+03	0.02%	88.81%
69	1.91E+03	0.03%	89.39%	5.47E+02	0.01%	88.82%
70	4.30E+00	0.00%	89.39%	2.66E+03	0.04%	88.86%
71	2.42E+02	0.00%	89.39%	3.66E+03	0.06%	88.91%
72	6.96E+03	0.11%	89.50%	2.60E+02	0.00%	88.92%

73	3.20E+03	0.05%	89.55%	1.97E+00	0.00%	88.92%
74	3.21E+02	0.00%	89.55%	6.12E+03	0.09%	89.01%
75	1.37E+04	0.21%	89.76%	1.82E+04	0.28%	89.29%
76	2.03E+02	0.00%	89.77%	1.47E+02	0.00%	89.30%
77	1.99E+01	0.00%	89.77%	4.81E+02	0.01%	89.30%
78	3.94E+03	0.06%	89.83%	3.70E+03	0.06%	89.36%
79	3.07E+03	0.05%	89.87%	9.91E+01	0.00%	89.36%
80	2.95E+03	0.05%	89.92%	3.65E+01	0.00%	89.36%
Total	5.84E+06	89.92%	89.92%	5.80E+06	89.36%	89.36%

Table 18: Effective Mass Values for Rotations around X, Y and Z directions

Mode Number	Effective Mass X-Rotation	Effective Mass Y-Rotation	Effective Mass Z-Rotation
1	3.01E+09	1.43E+12	1.09E+13
2	1.73E+10	1.23E+13	1.77E+16
3	6.67E+10	3.19E+13	4.43E+14
4	1.07E+12	4.98E+14	7.59E+13
5	4.27E+10	2.00E+13	4.18E+14
6	7.78E+09	3.60E+12	1.89E+12
7	1.60E+11	7.21E+13	7.10E+14
8	1.04E+12	4.81E+14	2.13E+14
9	1.53E+10	7.05E+12	1.94E+13
10	6.24E+10	3.00E+13	8.06E+14
11	2.92E+09	1.58E+12	2.55E+12
12	1.47E+12	6.84E+14	6.83E+12
13	6.48E+11	3.00E+14	4.35E+14
14	6.17E+10	2.83E+13	2.33E+13
15	3.44E+11	1.59E+14	3.92E+13
16	2.65E+12	1.24E+15	7.28E+13
17	3.17E+12	1.47E+15	2.77E+12
18	6.76E+12	3.14E+15	2.55E+12
19	3.58E+11	1.66E+14	6.01E+13
20	3.60E+12	1.67E+15	6.37E+13
21	7.74E+10	3.81E+13	1.49E+14
22	4.61E+12	2.13E+15	2.16E+12
23	4.06E+12	1.89E+15	8.24E+13
24	5.49E+11	2.50E+14	7.52E+13
25	1.04E+11	5.06E+13	1.81E+13
26	1.36E+11	6.30E+13	2.88E+12
27	2.21E+11	1.01E+14	1.17E+10
28	2.52E+12	1.15E+15	3.30E+11
29	4.21E+09	1.76E+12	2.11E+13
30	4.03E+12	1.85E+15	1.02E+13

31	1.72E+11	7.91E+13	6.84E+09
32	7.18E+10	3.36E+13	7.34E+13
33	4.03E+11	1.86E+14	2.00E+14
34	3.03E+11	1.40E+14	5.01E+13
35	9.29E+10	4.23E+13	1.46E+14
36	1.19E+12	5.48E+14	2.12E+13
37	3.49E+09	1.68E+12	4.74E+13
38	1.09E+12	5.03E+14	3.83E+12
39	8.13E+11	3.75E+14	4.57E+13
40	3.92E+11	1.81E+14	1.89E+14
41	1.23E+10	5.44E+12	2.91E+13
42	1.35E+10	6.01E+12	6.78E+13
43	7.16E+10	3.34E+13	3.68E+12
44	9.88E+10	4.46E+13	1.11E+13
45	4.36E+11	2.00E+14	1.70E+14
46	1.86E+11	8.52E+13	2.86E+13
47	3.18E+11	1.47E+14	4.02E+13
48	9.43E+07	4.86E+10	3.56E+13
49	1.01E+11	4.68E+13	1.15E+11
50	7.54E+10	3.46E+13	3.09E+13
51	7.99E+09	3.73E+12	7.10E+12
52	8.81E+10	4.05E+13	4.13E+13
53	1.98E+11	9.16E+13	5.49E+13
54	1.67E+11	7.70E+13	3.47E+12
55	3.90E+11	1.80E+14	1.50E+13
56	5.79E+10	2.72E+13	5.10E+13
57	9.86E+11	4.55E+14	3.00E+12
58	3.62E+11	1.67E+14	8.44E+11
59	8.93E+08	4.19E+11	8.74E+12
60	4.11E+11	1.89E+14	2.23E+10
61	1.86E+11	8.65E+13	1.51E+13
62	3.09E+06	1.49E+09	4.10E+13
63	4.14E+10	1.91E+13	1.01E+14
64	6.47E+10	2.97E+13	1.33E+13
65	3.43E+10	1.56E+13	1.62E+10
66	4.77E+08	1.99E+11	6.96E+10
67	4.72E+10	2.19E+13	5.63E+13
68	3.78E+10	1.74E+13	3.75E+12
69	8.82E+09	4.16E+12	1.82E+12
70	1.23E+11	5.63E+13	1.07E+13
71	7.41E+09	3.38E+12	1.43E+13
72	5.52E+09	2.50E+12	1.60E+12
73	8.44E+10	3.92E+13	5.97E+09
74	3.15E+08	1.60E+11	2.39E+13
75	2.33E+10	1.07E+13	7.86E+13
76	9.62E+09	4.43E+12	6.52E+11
77	3.20E+09	1.42E+12	1.88E+12
78	4.55E+10	2.10E+13	1.62E+13

79	4.64E+10	2.12E+13	2.18E+11
80	2.77E+07	1.44E+10	2.93E+11
Total	4.72E+13	2.18E+16	2.32E+16

Like effective masses, participation factors are another indicator of the important modes. All the participation factor values are presented in Table 19.

Table 19: Participation Factor Values for the Modes

Mode Number	X-Translation	Y-Translation	X-Rotation	Y-Rotation	Z-Rotation
1	2.46128	0.0517771	-65.8152	1432.04	-3950.54
2	-0.14053	3.66665	229.656	-6122.35	232239
3	0.718788	0.651854	479.215	-10491.8	39055.1
4	0.39542	0.321114	-2275.37	48995.4	19125.2
5	0.802457	-1.18207	-779.8	16854.7	-77121.2
6	-2.82795	-0.226845	384.74	-8276.59	-5994.64
7	0.553849	-1.07138	1042.83	-22109.8	-69377
8	0.300636	-0.551556	2504.56	-53774.5	-35750.8
9	0.535782	-0.0712012	170.708	-3668.91	-6091.09
10	-0.724795	-1.9176	-1048.05	22981	-119111
11	0.057228	0.0264913	50.8152	-1183.49	1502.75
12	0.708595	0.116155	2444.26	-52734.5	5269.34
13	0.0786107	-0.270291	-668.43	14367.7	-17313.9
14	-0.290182	0.263894	-903.718	19336.1	17539.8
15	0.316515	0.78312	-4550.84	97813.5	48563.2
16	-0.357373	-0.266202	3014.1	-65090.6	-15782.2
17	0.0811561	-0.0292307	2231.07	-47999.5	-2086.28
18	0.0720886	-0.0428993	4755.06	-102491	-2921.55
19	-0.0130932	-0.112867	547.737	-11779	-7095.27
20	0.115732	-0.168453	-2613.76	56245.7	-10986.2
21	-0.0304684	0.214643	-311.586	6915.2	13661.9
22	-0.0452717	-0.037452	3265.39	-70185.7	-2234.31
23	0.280664	0.269546	-3600.37	77619.5	16219.1
24	-0.265093	0.137393	-808.807	17239.2	9465.91
25	0.183116	-0.0664794	360.372	-7935.78	-4740.91
26	-0.56625	0.0525857	-1084.32	23332.3	4989.59
27	0.0134715	-0.00161061	616.236	-13175.3	-141.718
28	-0.131696	-0.0202641	-2461.64	52724	-891.69
29	-0.465719	0.242316	-235.593	4825.26	16692.6
30	0.0952092	-0.0672719	-2844.69	60899.3	-4536.09
31	0.0780696	0.000943276	-857.521	18403.8	-171.154
32	0.131498	0.204474	-392.17	8485.88	12538.2
33	-0.138558	-0.370527	-1034.77	22212.7	-23016.7
34	-0.13542	0.143052	-734.177	15815.3	9444.59
35	-0.40455	-0.333394	-501.283	10697.6	-19887.2
36	-0.320527	0.162804	2662.76	-57092.8	11233.8

37	0.252451	-0.203349	116.682	-2557.9	-13596.1
38	0.12618	-0.0464485	-1766.31	37878.8	-3308.13
39	-0.0539199	-0.200059	-1666.19	35760.3	-12494.6
40	-0.081915	-0.31623	-898.638	19288.1	-19753.2
41	0.161033	0.142456	174.906	-3686.05	8530.32
42	-0.0158946	-0.282433	-251.486	5301.18	-17809.7
43	-0.333782	0.0684396	-739.957	15977.4	5303.45
44	-0.219687	-0.0856828	450.965	-9580.67	-4769.71
45	-0.049926	0.493618	-1589.15	34022.3	31355.1
46	-0.418486	0.23778	1311.04	-28063.6	16264.8
47	0.14158	0.289051	-1590.68	34118.8	17861.9
48	0.122717	0.251582	25.3042	-574.381	15541.7
49	-0.422487	-0.00182787	-1057.51	22810.1	1129.67
50	0.343761	-0.232061	774.46	-16588.3	-15680
51	0.599967	-0.12165	-317.54	6861.48	-9464.17
52	-0.153137	0.365745	1088.48	-23345.6	23575.6
53	0.198237	-0.336237	1312.3	-28212.1	-21844.8
54	0.401842	0.10441	-1188.54	25551.6	5423.65
55	-0.31751	0.229295	-2489.87	53469.9	15426.5
56	0.0589161	-0.173991	-376.957	8168.06	-11178.5
57	-0.0703463	-0.0549559	-1872.04	40222	-3267.02
58	-0.124411	0.0207224	1097.34	-23594	1675.5
59	0.0878593	0.14273	-88.609	1920.09	8763.04
60	-0.0535276	-0.0135702	-3040.2	65184.7	-708.599
61	0.0993474	0.123172	831.365	-17927.3	7490.86
62	-0.113422	0.482438	-8.46267	185.748	30833.7
63	-0.174568	0.342969	449.9	-9670.3	22198.8
64	0.106985	0.163525	-698.897	14984.3	10021.3
65	0.0177344	0.00452908	337.764	-7199.98	232.286
66	-0.0781922	-0.0174323	72.224	-1475.8	-872.584
67	-0.214292	-0.384429	-685.588	14790.8	-23680
68	-0.151732	-0.113754	677.242	-14546.2	-6744.13
69	0.23738	0.126978	509.944	-11079.4	7331.36
70	0.00741784	-0.184652	1255.44	-26858.3	-11693.7
71	0.14478	0.562272	800.402	-17101.3	35123.7
72	-0.802359	0.155036	-714.614	15197.9	12164.4
73	0.166565	0.00413185	855.526	-18450.3	-227.65
74	-0.0473425	-0.206641	-46.9168	1057.59	-12928.6
75	0.307079	-0.353464	400.237	-8578.44	-23248.2
76	-0.206095	0.175267	-1418.36	30444.6	11679.8
77	-0.0242954	-0.119425	308.066	-6501.09	-7476.23
78	-0.293714	0.284392	-998.026	21424.2	18844.9
79	0.209922	0.0377282	-816.527	17465	1770.14
80	0.35376	-0.0393506	-34.3086	780.973	-3527.41

First 24 mode shapes and the points that undergoes maximum effect (see black line) were denoted by following figures.

Moreover, some local modes are also given in Figure 74, Figure 75, Figure 76, Figure 77, and Figure 78.

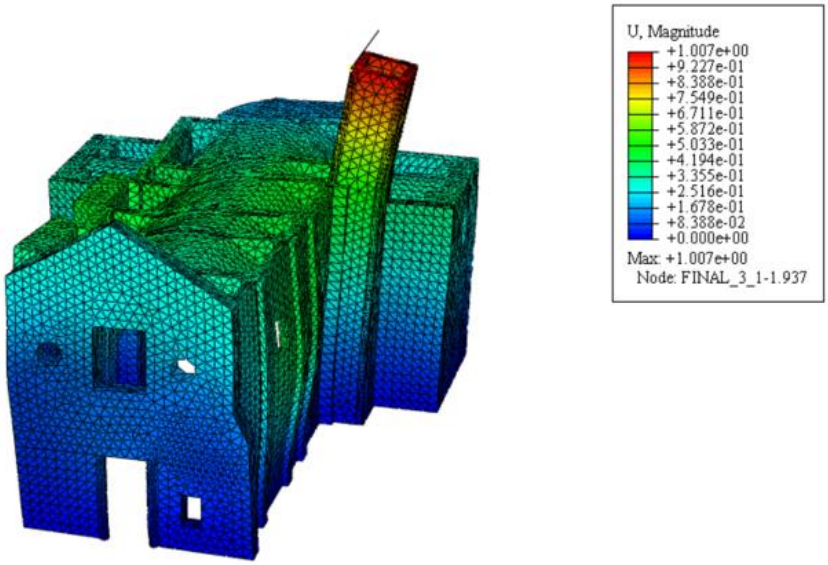

Figure 50: Mode 1, Modal Analysis

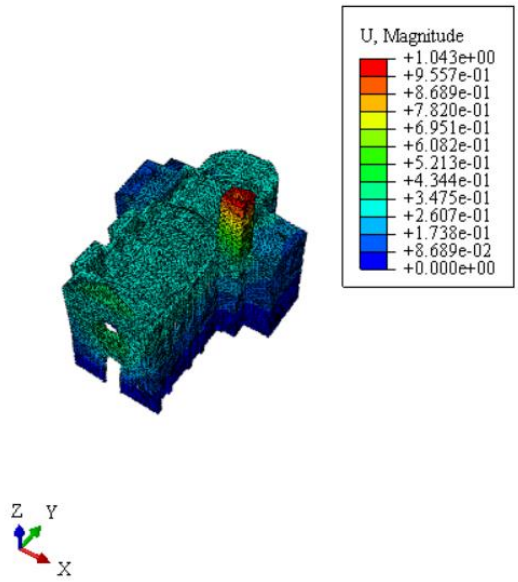

Figure 51: Mode 2, Modal Analysis

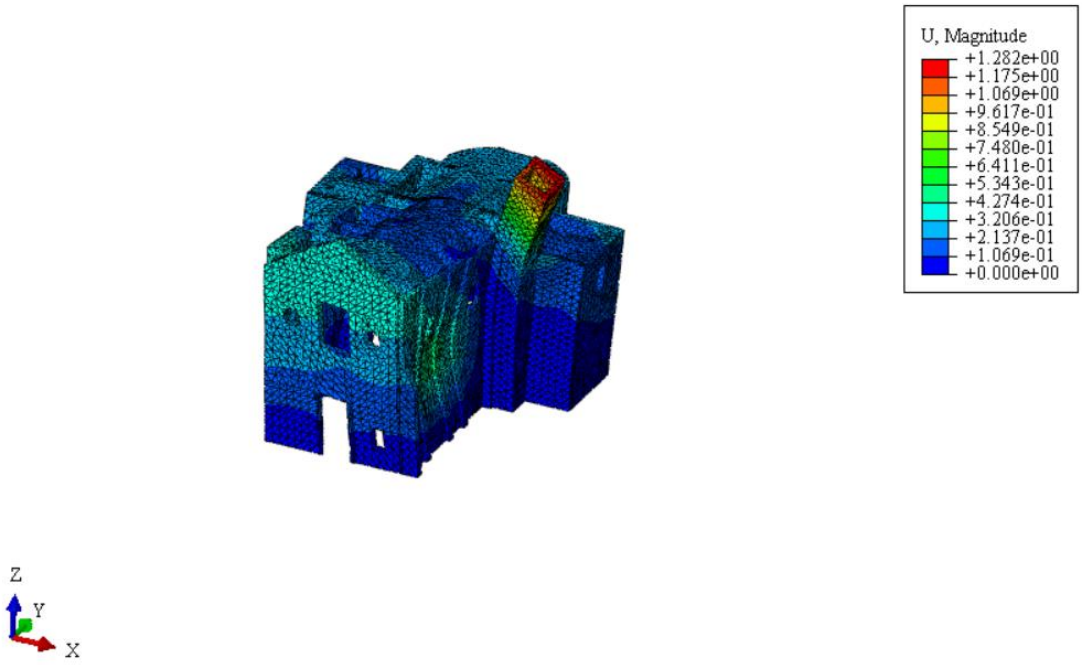

Figure 52: Mode 3, Modal Analysis

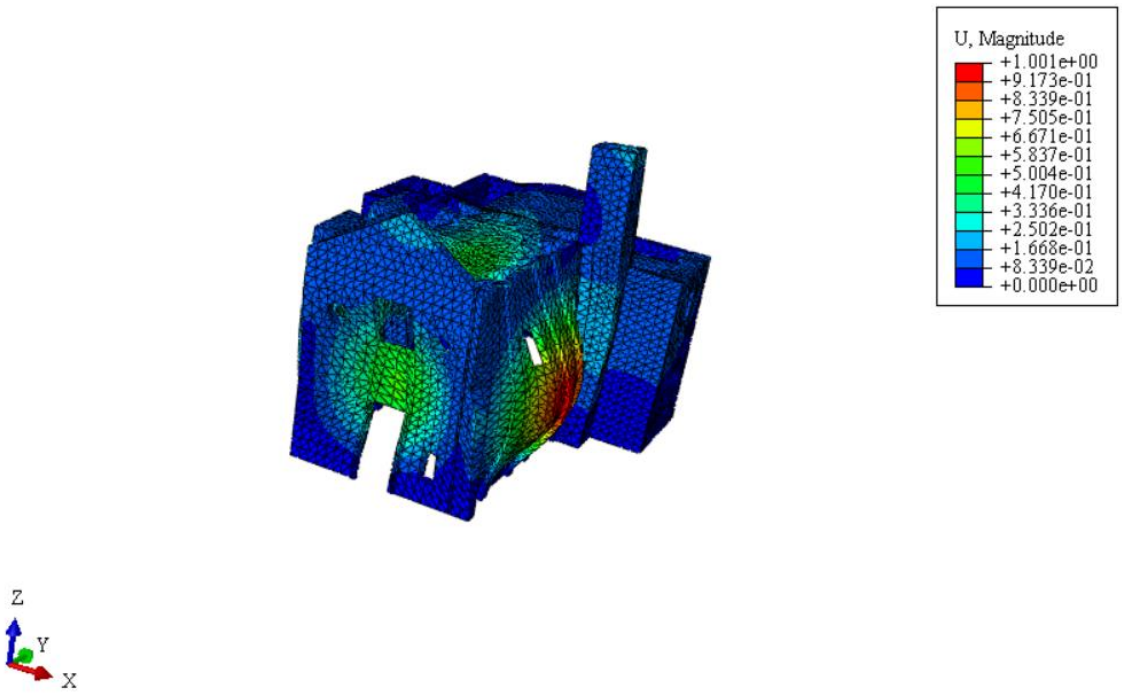

Figure 53: Mode 4, Modal Analysis

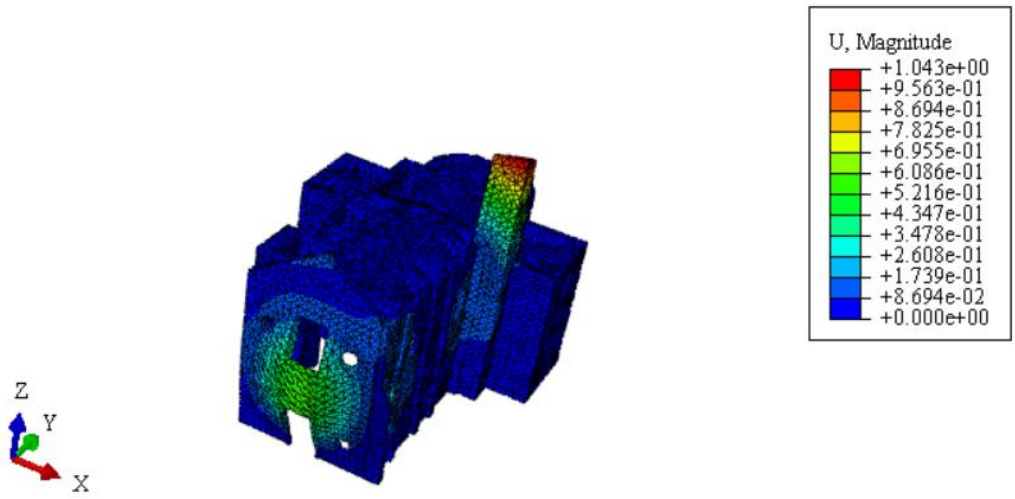

Figure 54: Mode 5, Modal Analysis

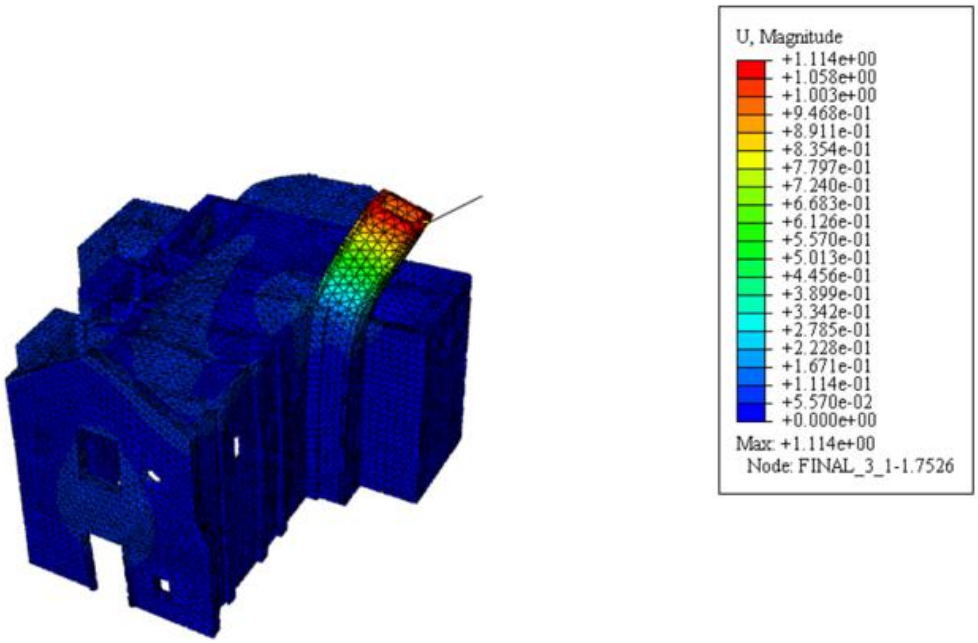

Figure 55: Mode 6, Modal Analysis

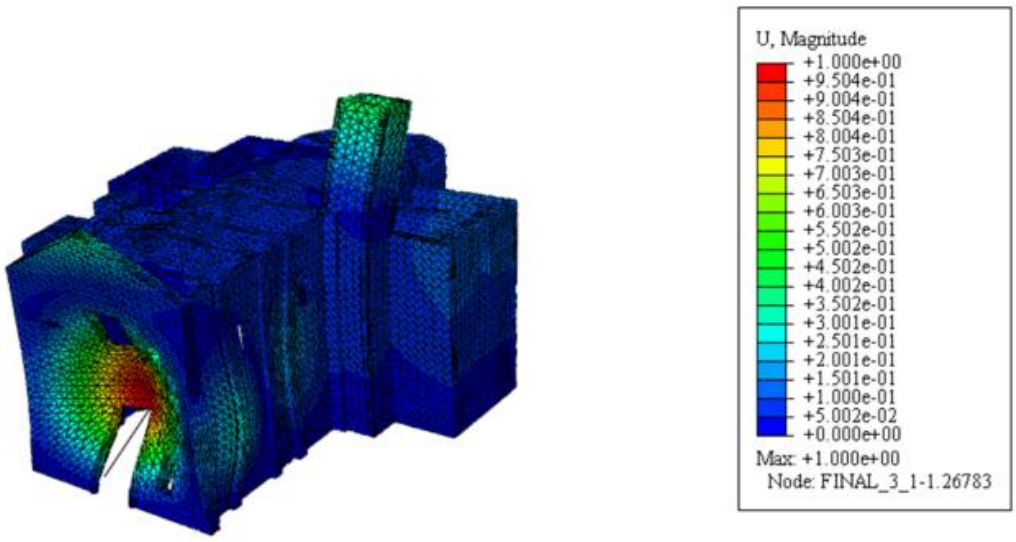

Figure 56: Mode 7, Modal Analysis

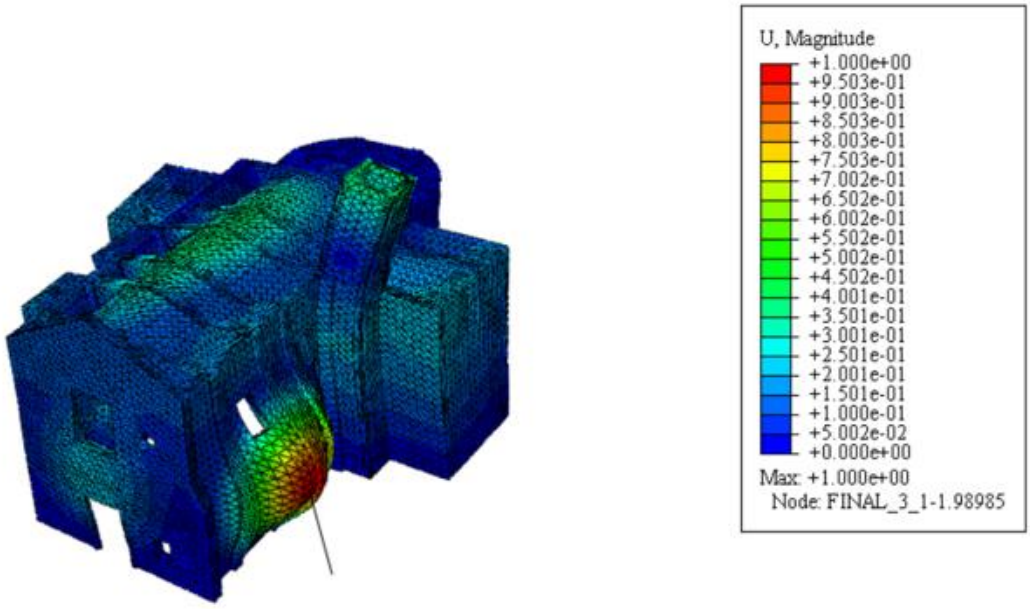

Figure 57: Mode 8, Modal Analysis

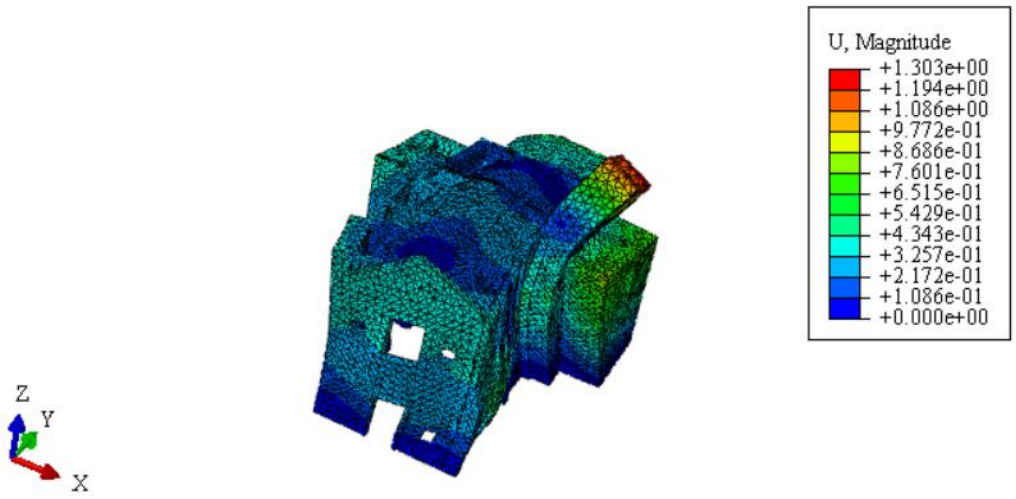

Figure 58: Mode 9, Modal Analysis

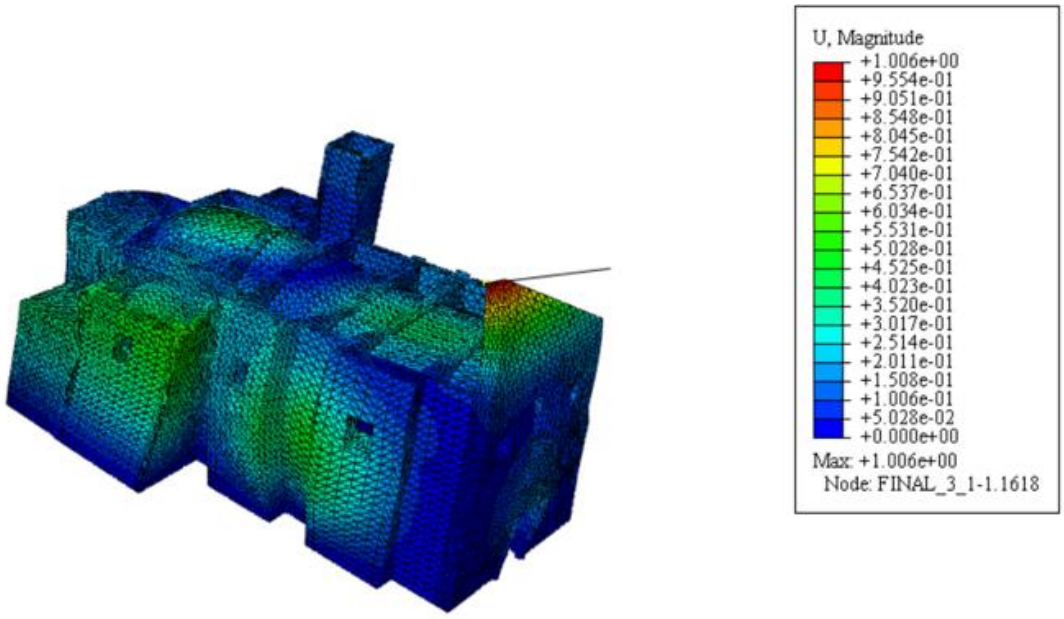

Figure 59: Mode 10, Modal Analysis

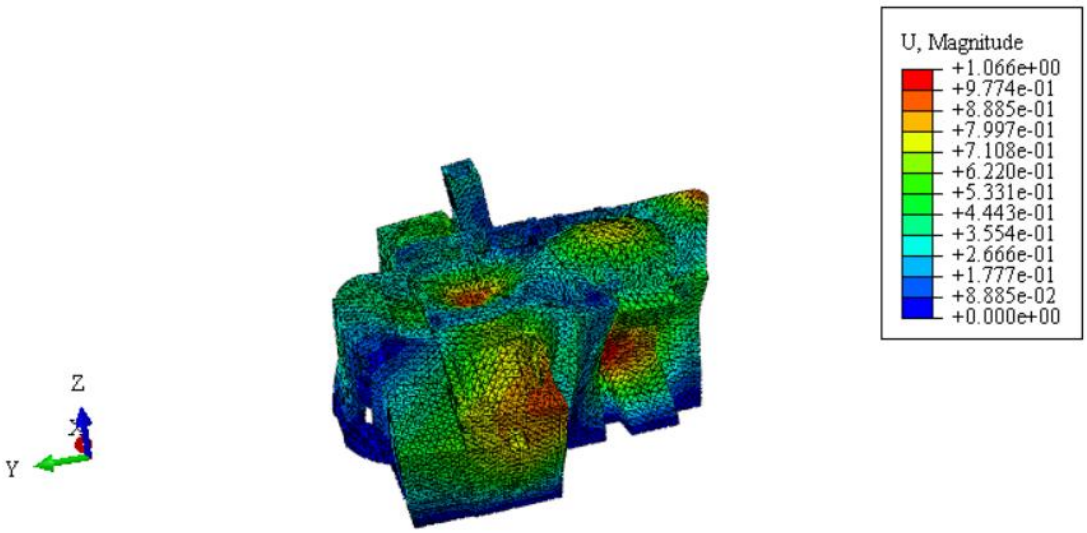

Figure 60: Mode 11, Modal Analysis

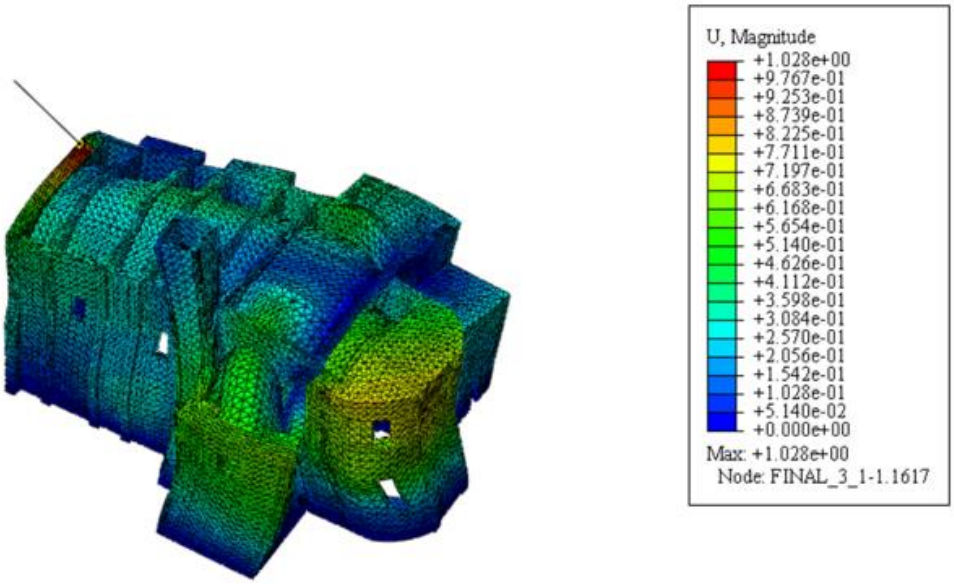

Figure 61: Mode 12, Modal Analysis

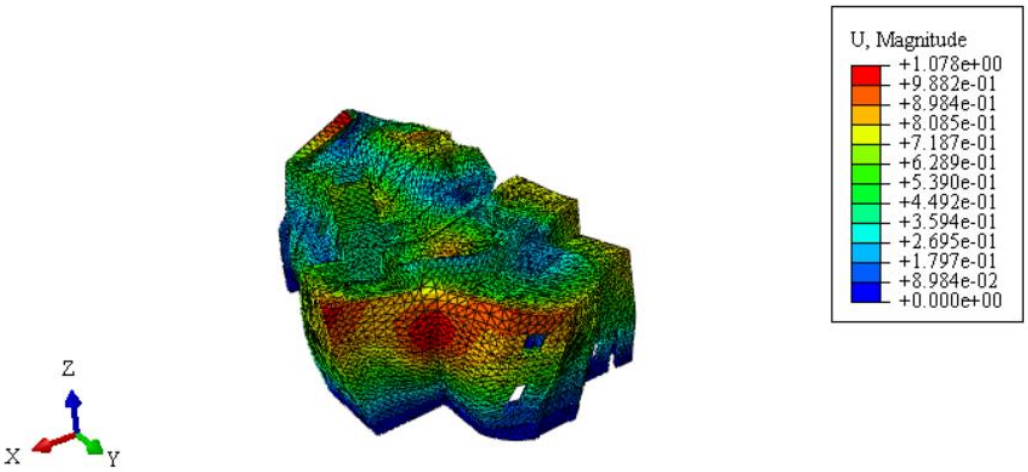

Figure 62: Mode 13, Modal Analysis

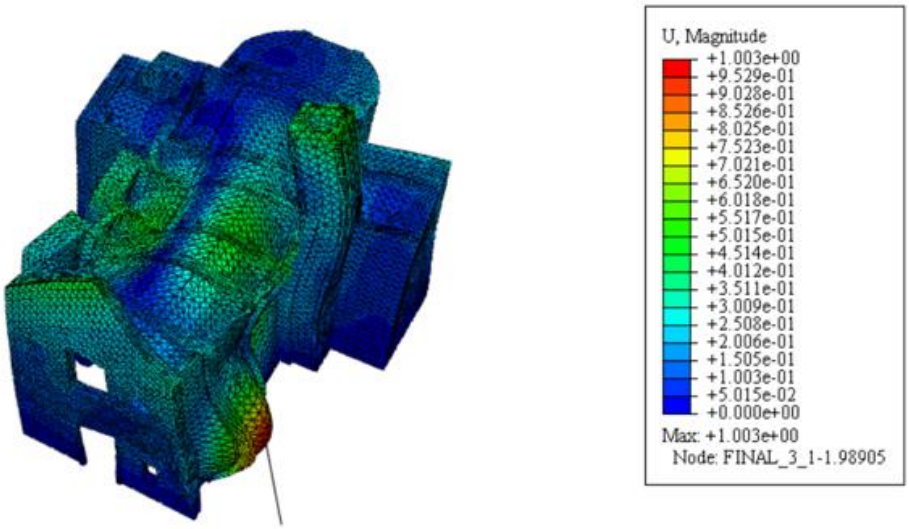

Figure 63: Mode 14, Modal Analysis

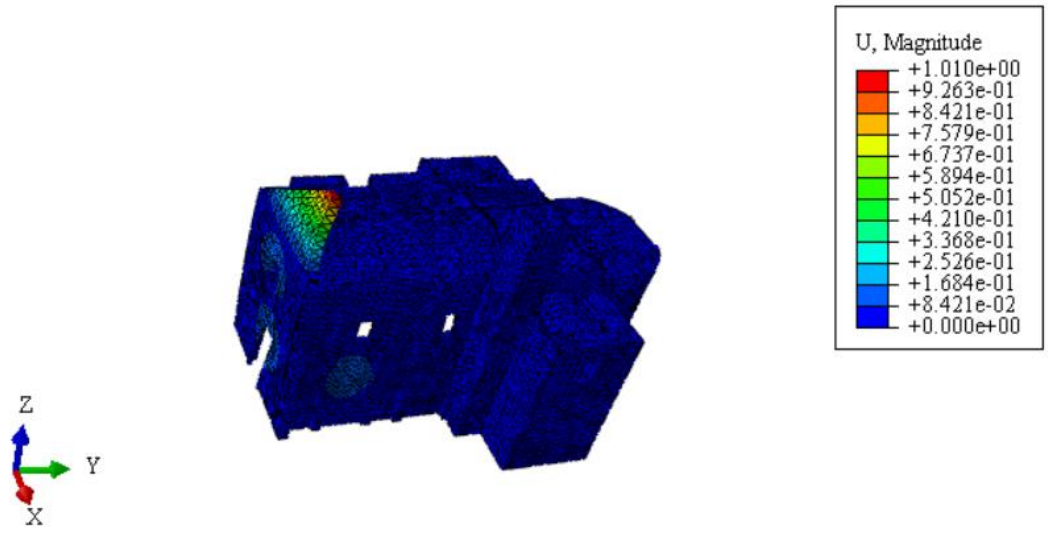

Figure 64: Mode 15, Modal Analysis

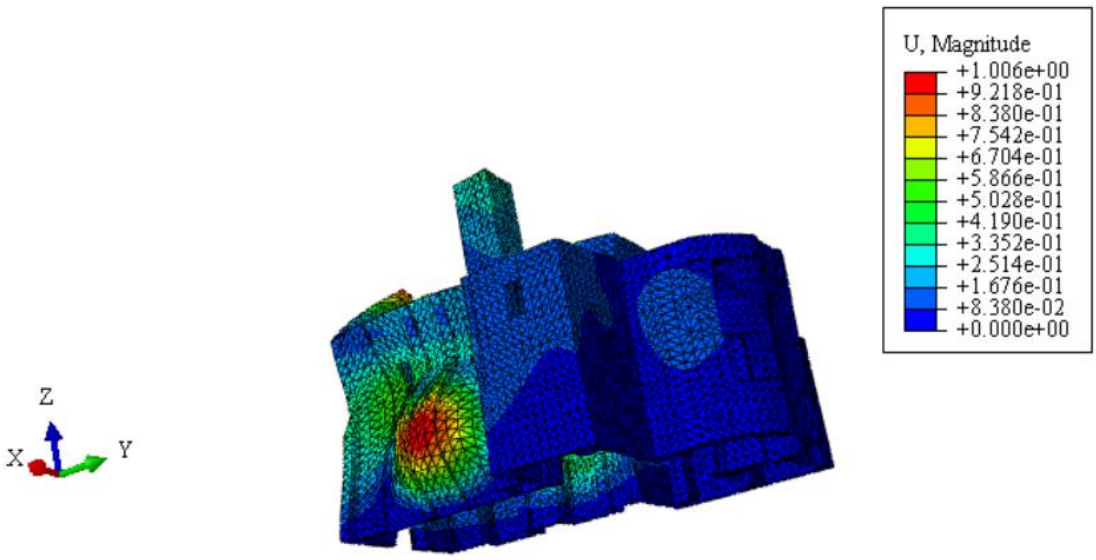

Figure 65: Mode 16, Modal Analysis

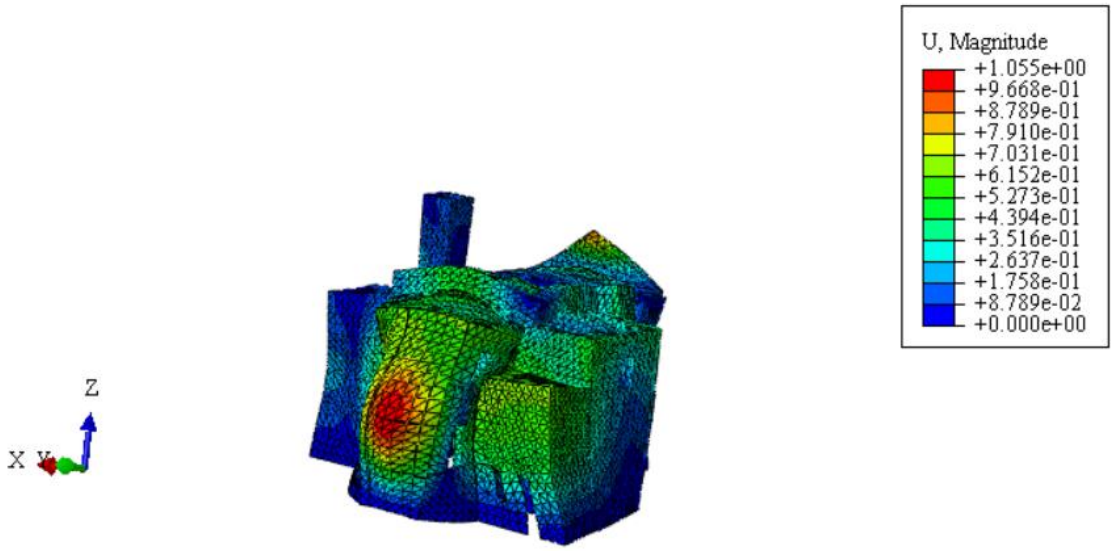

Figure 66: Mode 17, Modal Analysis

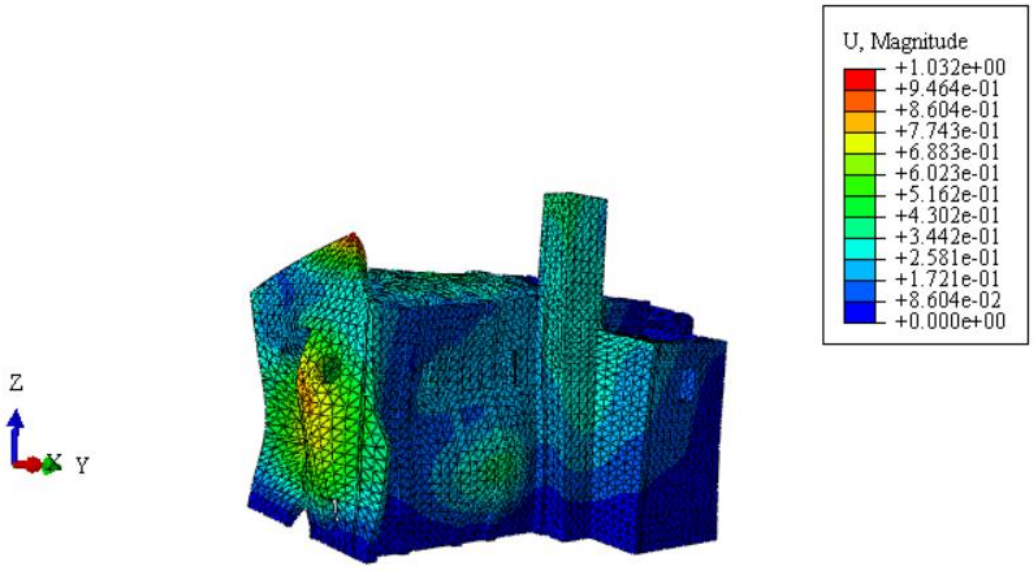

Figure 67: Mode 18, Modal Analysis

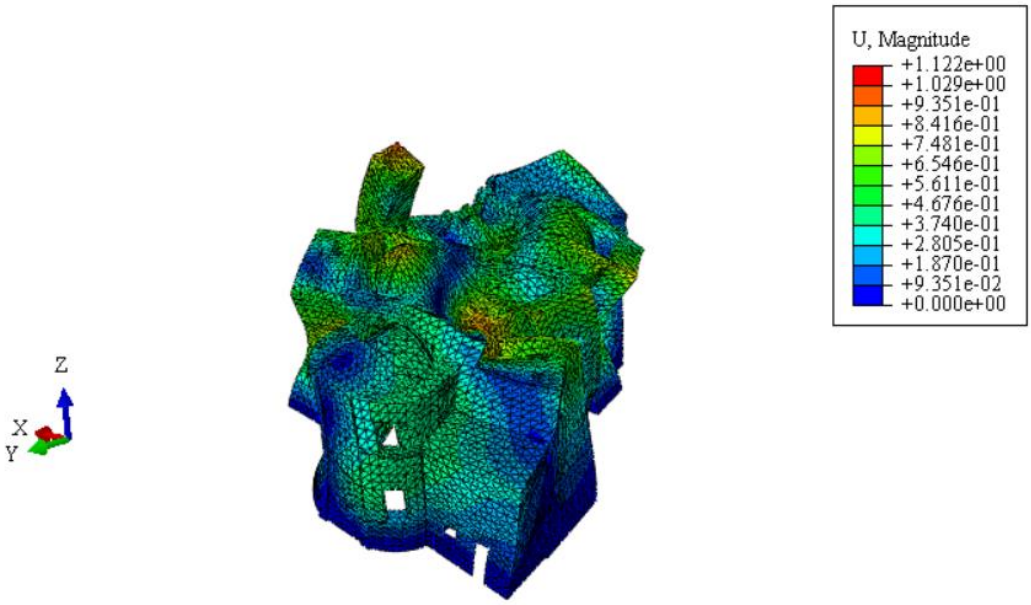

Figure 68: Mode 19, Modal Analysis

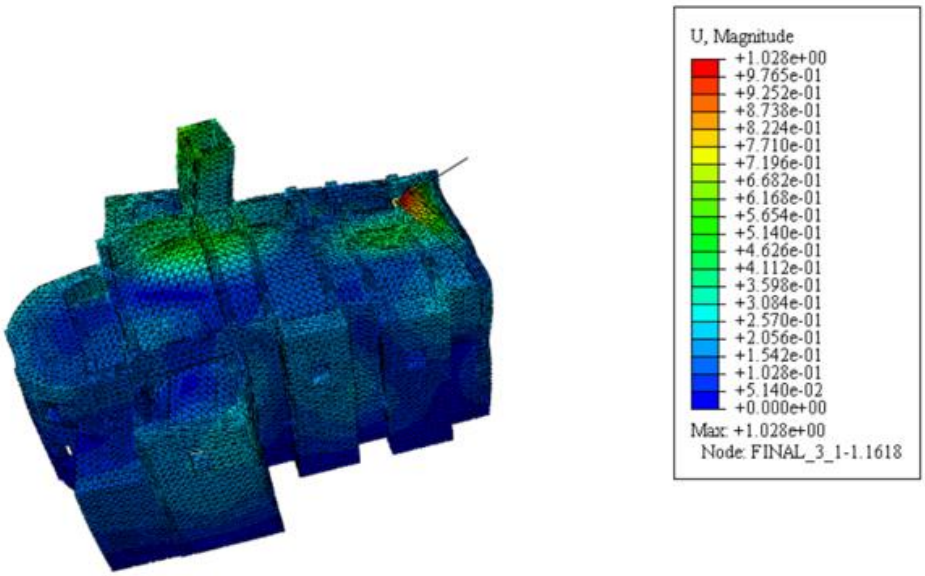

Figure 69: Mode 20, Modal Analysis

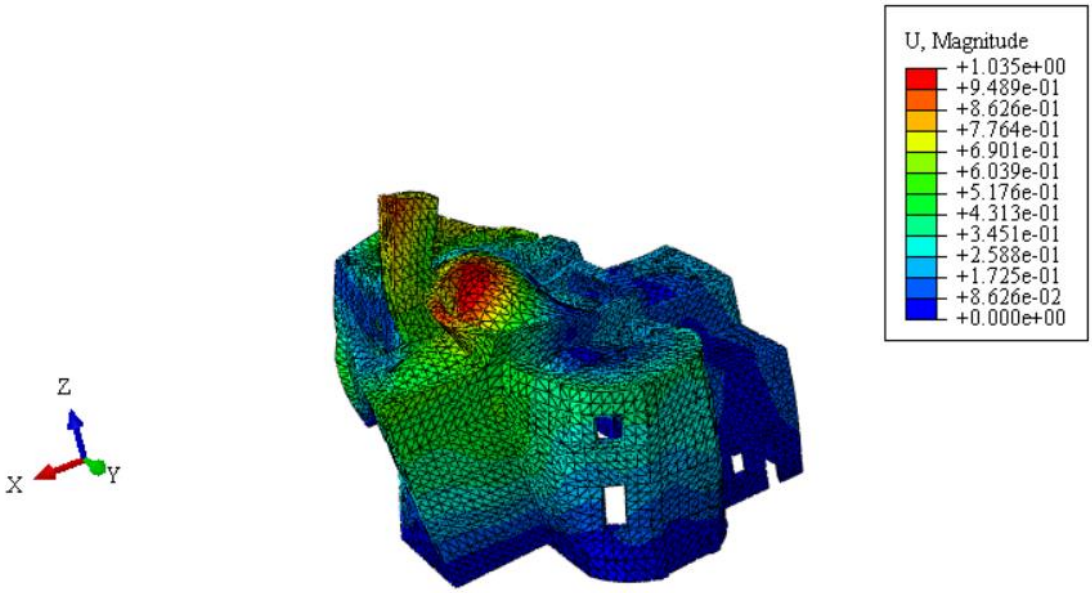

Figure 70: Mode 21, Modal Analysis

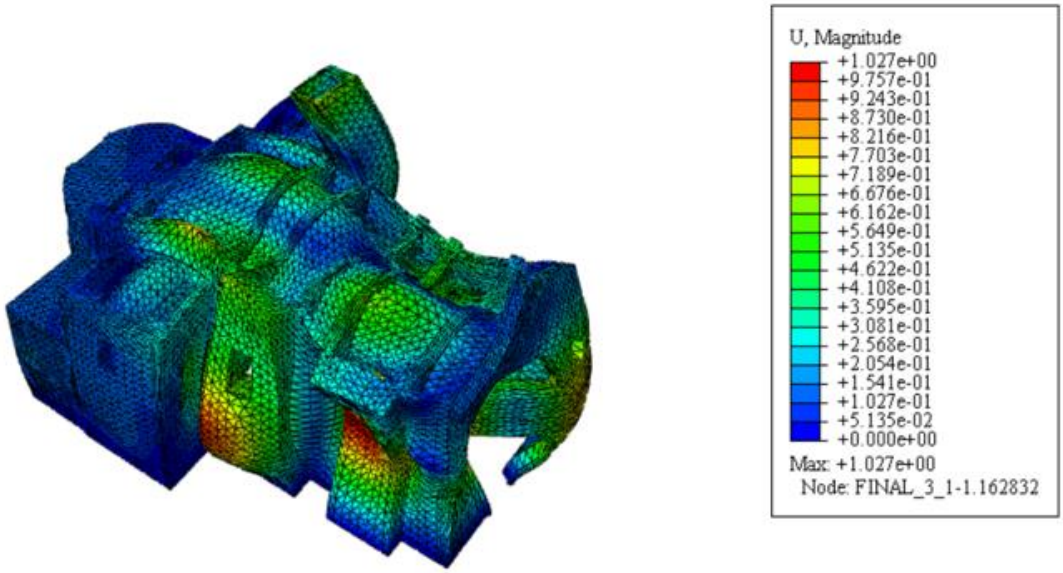

Figure 71: Mode 22, Modal Analysis

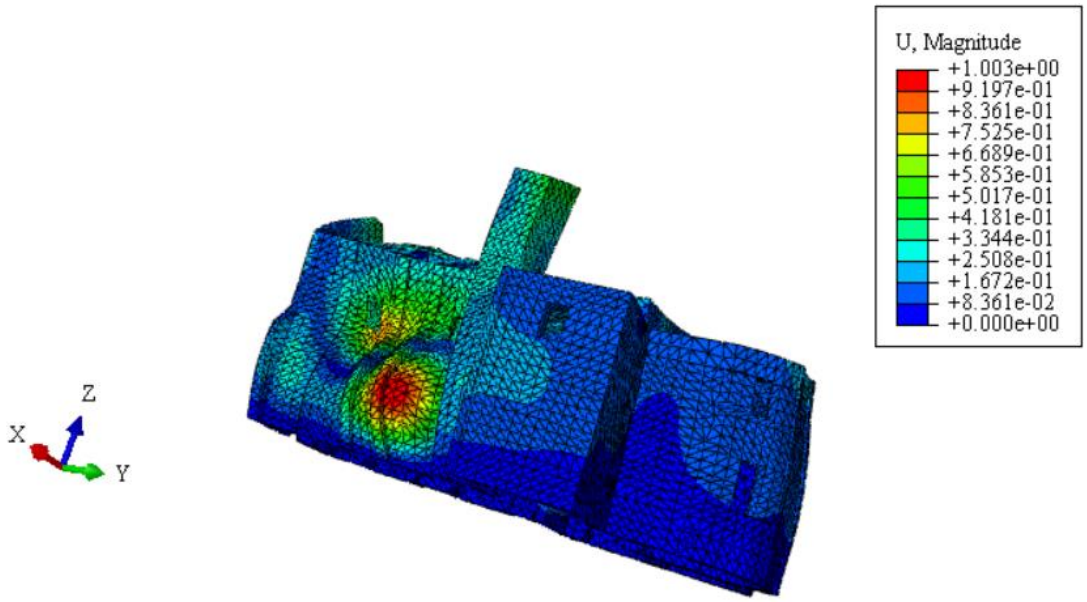

Figure 72: Mode 23, Modal Analysis

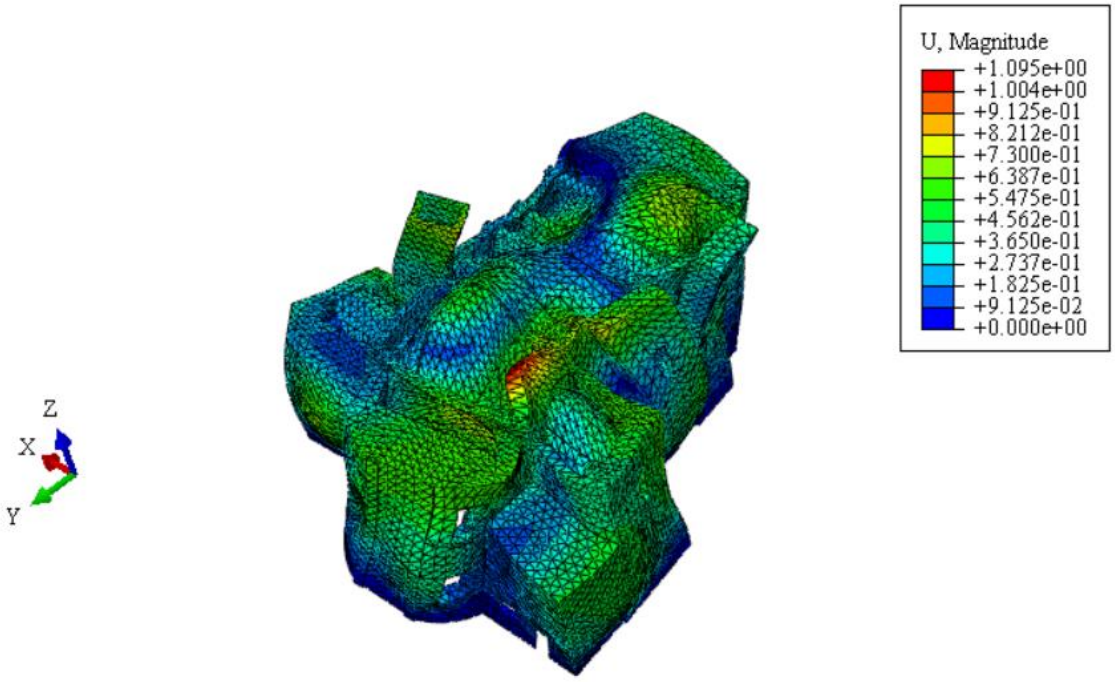

Figure 73: Mode 24, Modal Analysis

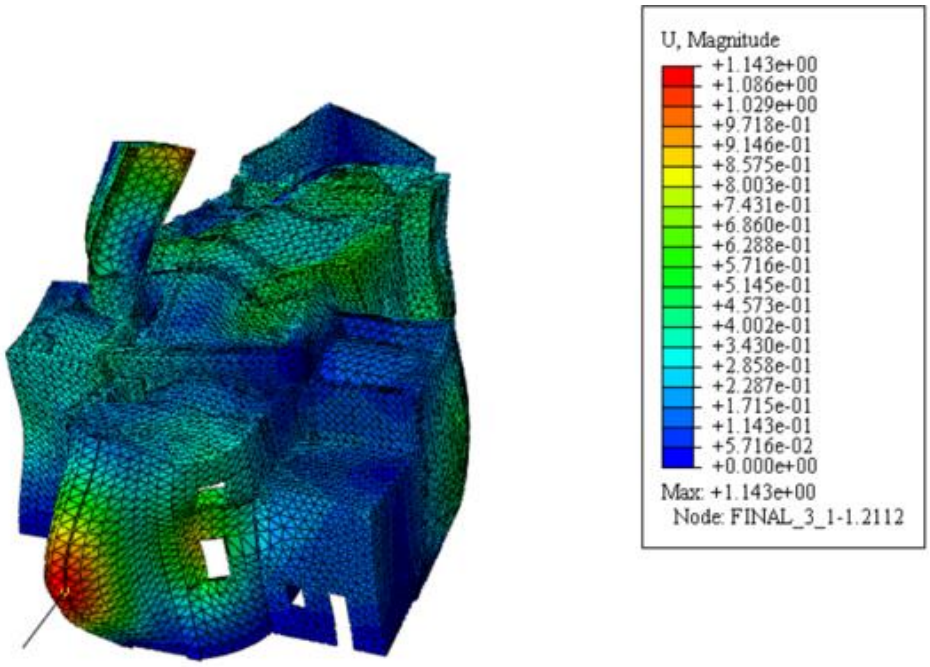

Figure 74: Mode 27, Modal Analysis

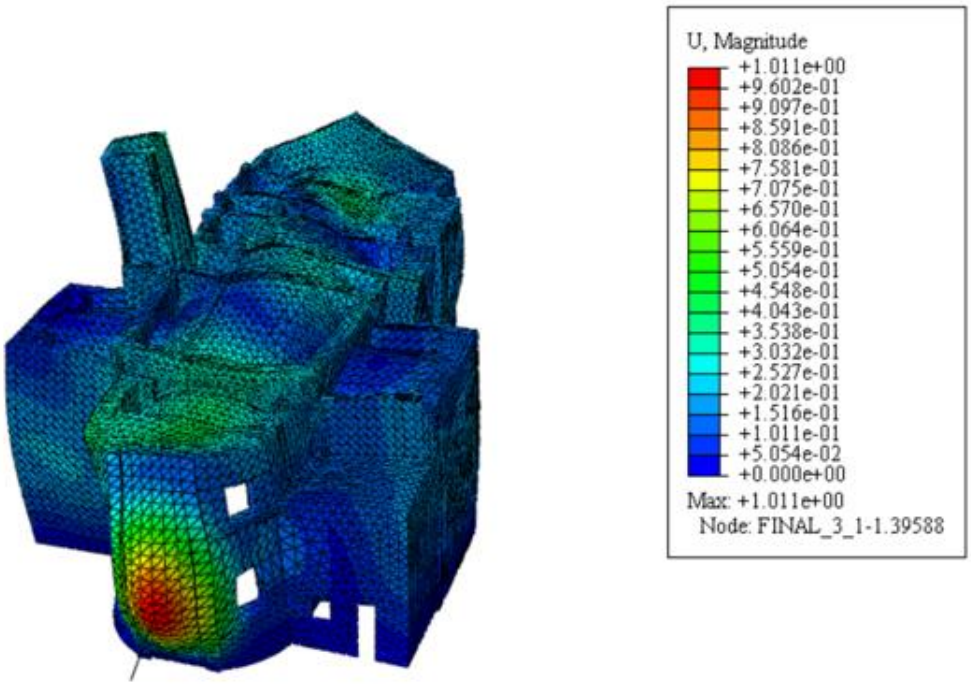

Figure 75: Mode 28, Modal Analysis

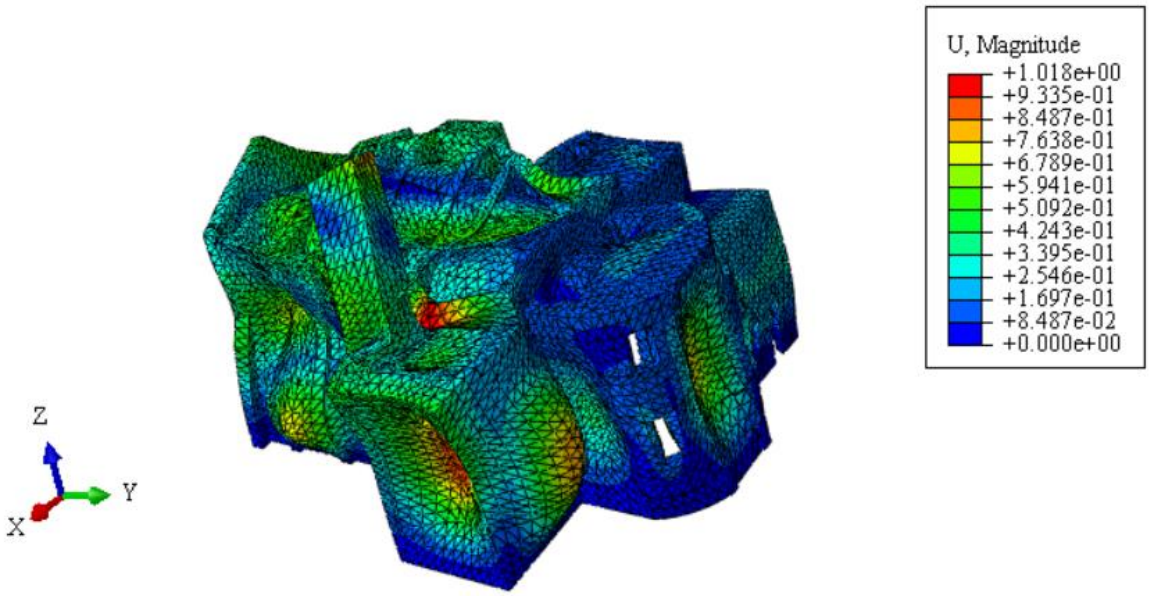

Figure 76: Mode 34, Modal Analysis

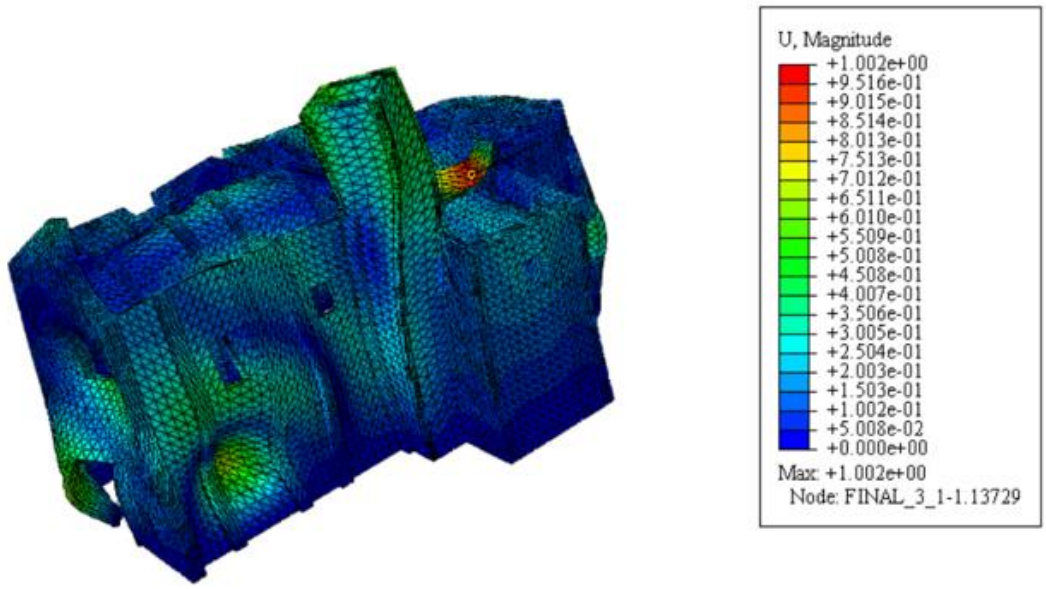

Figure 77: Mode 38, Modal Analysis

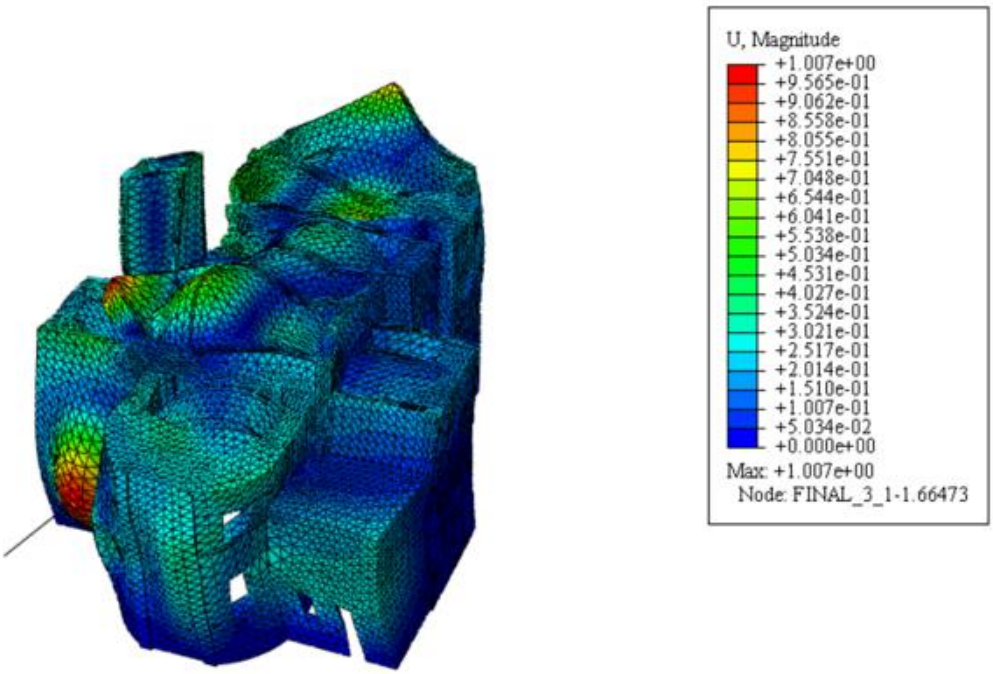

Figure 78: Mode 43, Modal Analysis

By exploiting the cumulative effective mass percent, the most important modes can be separated into X-translation and Y-translation. (See Figure 81: Cumulative Effective Mass Percent in X direction vs. Mode number, and Figure 82: Cumulative Effective Mass Percent in Y direction vs. Mode number)

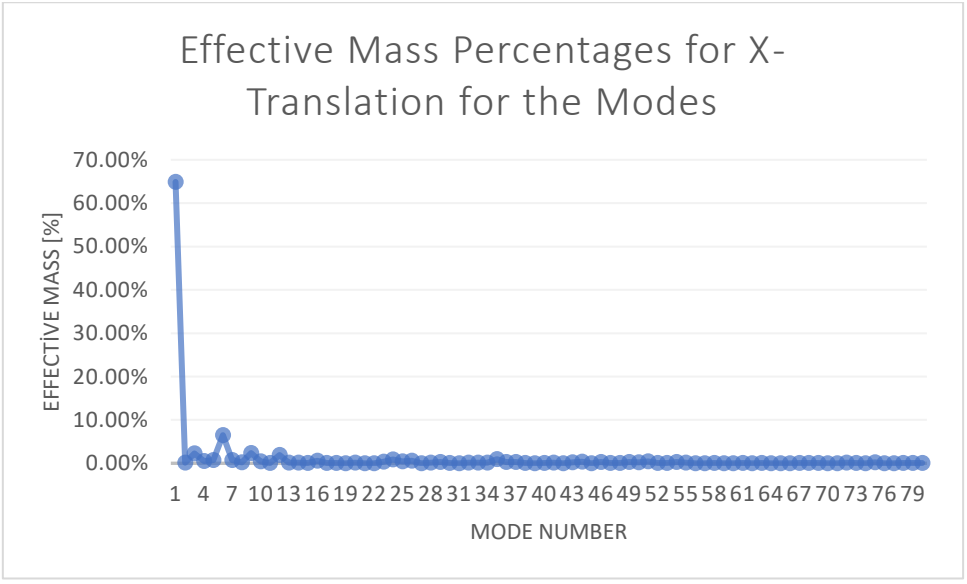

Figure 79: Effective Mass Percentages for X-Translation for the Modes

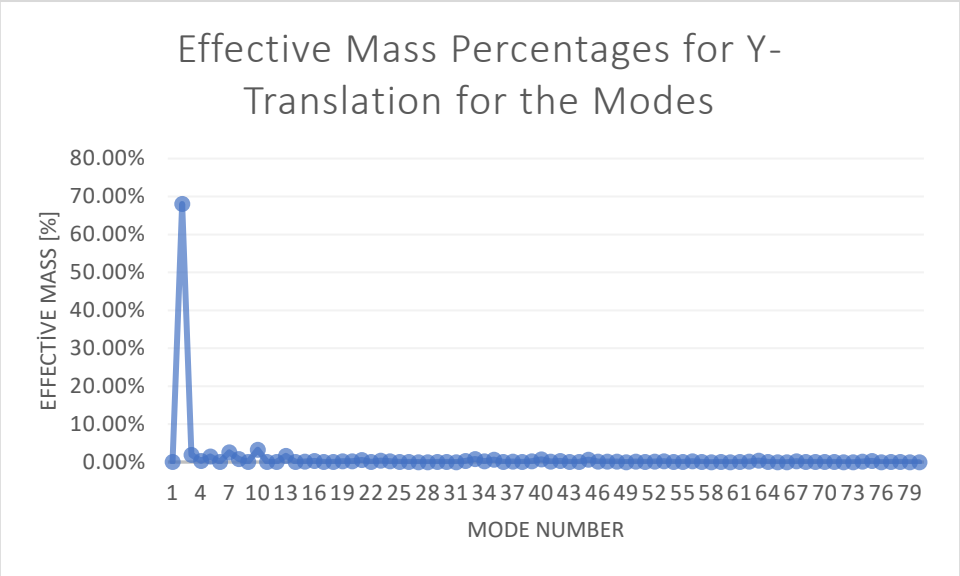

Figure 80: Effective Mass Percentages for Y-Translation for the Modes

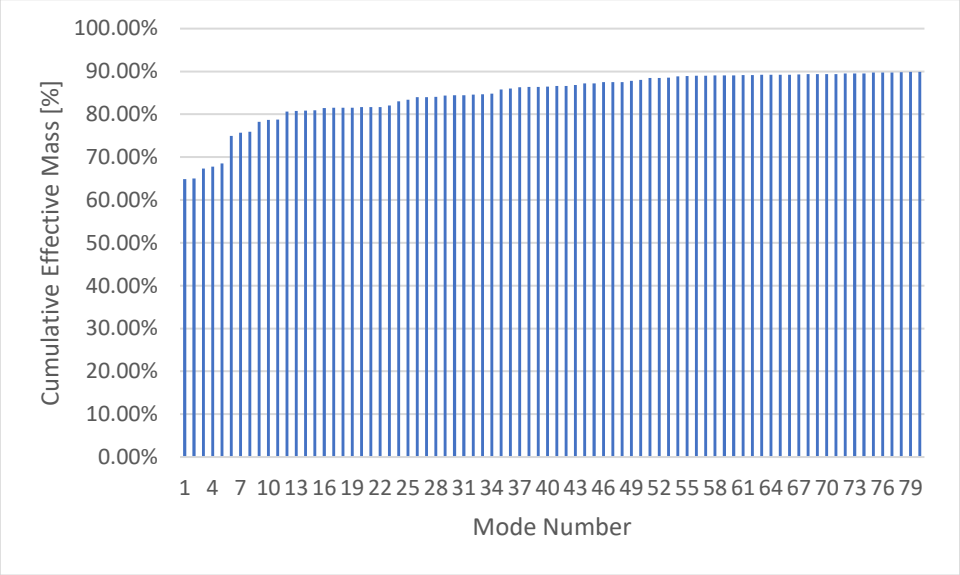

Figure 81: Cumulative Effective Mass Percent in X direction vs. Mode number

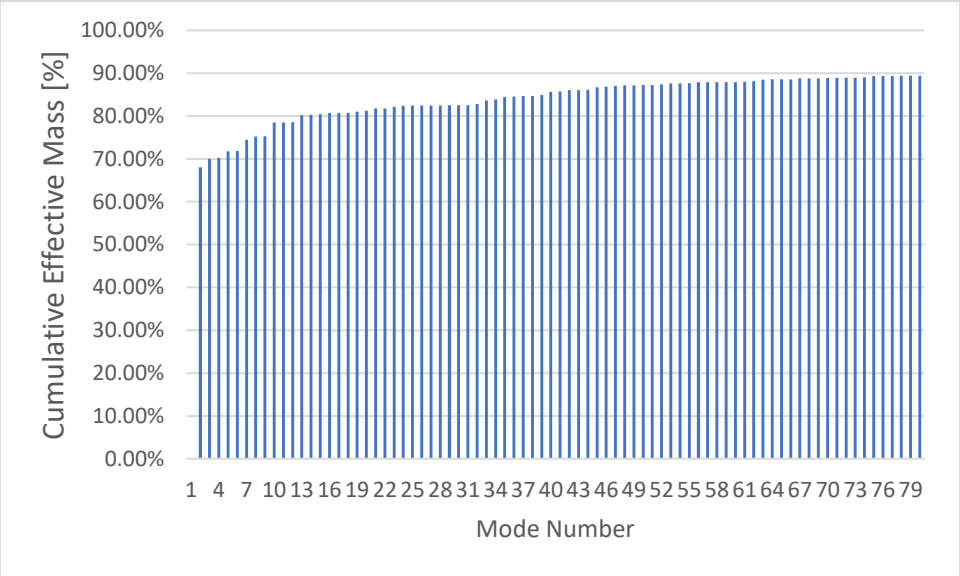

Figure 82: Cumulative Effective Mass Percent in Y direction vs. Mode number

The dominant modes in X-translation and Y-translation are shown in Table 20 and Table 21. In addition, the most important modes are indicated with the response spectrum (q=2) defined by NTC. (See Figure 83: Modal Shape Distributions in the X direction, and Response Spectrum by NTC, and Figure 84: Modal Shape Distributions in Y direction, and Response Spectrum by NTC)

Table 20: Dominant Modes in X direction

Mode Number	M_{eff}	Period [s]
1	64.90 %	0.363
3	2.31 %	0.243
6	6.47 %	0.193
9	2.32 %	0.158
12	1.90 %	0.134
Total	77.90%	

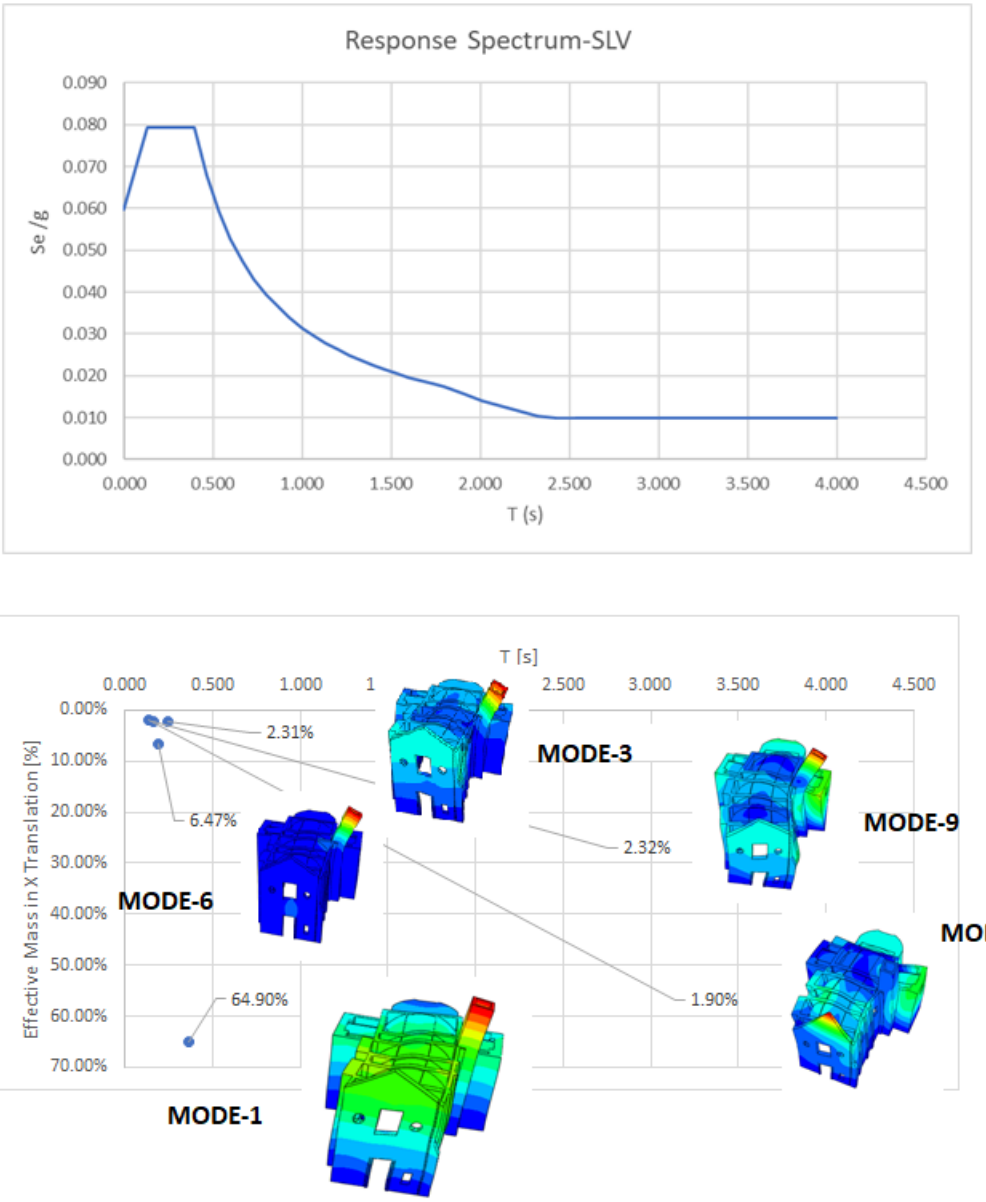

Figure 83: Modal Shape Distributions in the X direction, and Response Spectrum by NTC

In the first mode having the greatest effective mass in X-translation, the upper parts of the structure, especially, the top of the bell tower and the barrel vaults are affected at most. In addition, the upper part of the façade where the middle rectangular opening is impacted as well. The second most dominant mode is mode 6 (T=0.193 s) in which the bell tower is influenced locally. The third mode (T=0.243 s), and the ninth mode (T=0.158 s) lead to an impact on the bell tower and façade. In mode 12 (T=0.134 s), the upper part of the façade undergoes maximum displacement. Besides, the apse is considerably influenced in mode 3, mode 9, and mode 12.

Table 21: Dominant Modes in the Y direction

Mode Number	M_{eff}	Period [s]
2	68.03 %	0.276
3	1.90 %	0.243
5	1.51 %	0.206
10	3.22 %	0.144
13	1.63 %	0.129
Total	76.29 %	

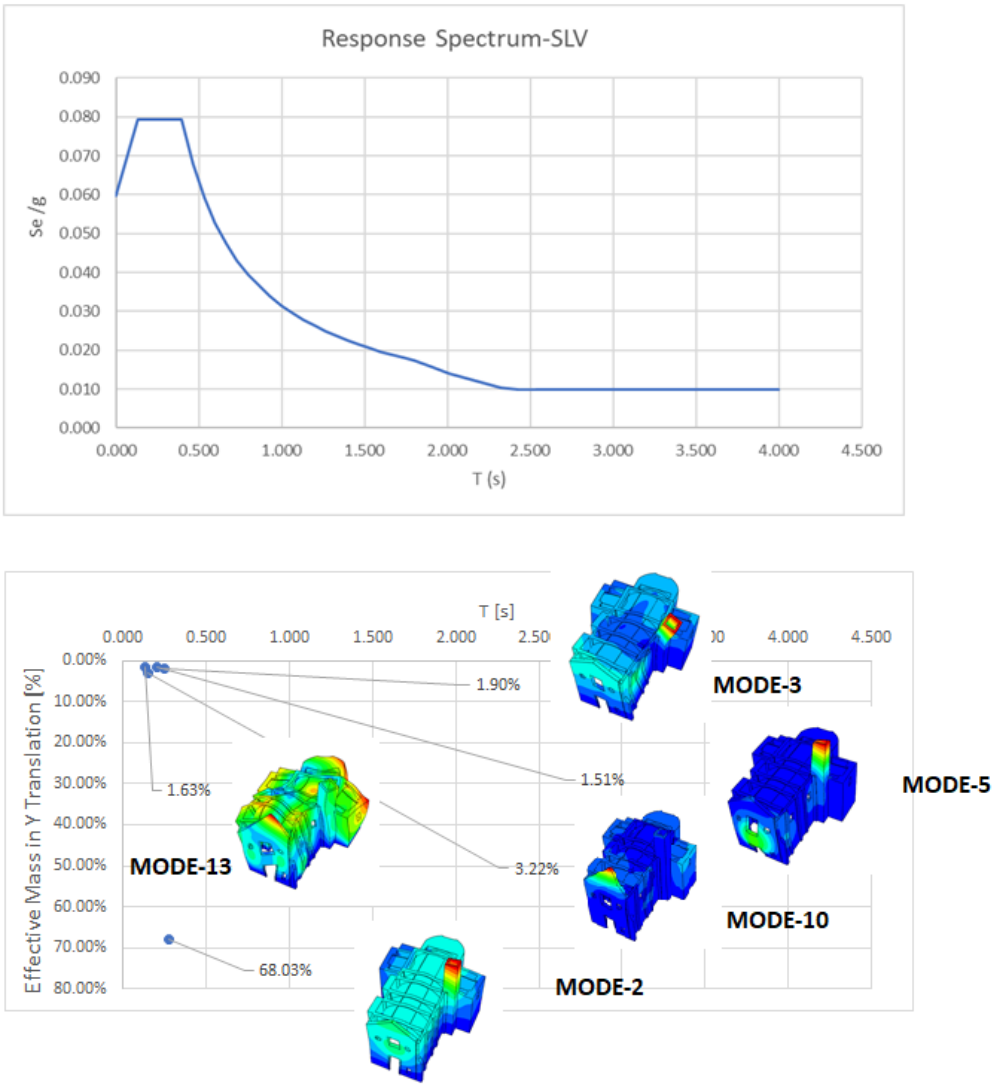

Figure 84: Modal Shape Distributions in Y direction, and Response Spectrum by NTC

Mode 2 (T=0.276 s) having a greater contribution in Y-translation gives rise to maximum displacements at the top of the bell tower and the barrel vaults beginning from the façade to

the end of the apse. Furthermore, the third mode (T=0.243 s) and fifth mode (0.206 s) are related to the bell tower as well. In mode 10 (T=0.144 s), it can be observed that the top of the façade is affected locally. In addition, mode 13 (T=0.129 s) undergoes a torsional response, and the apse and left transept are impacted in a major manner.

6.3 Response Spectrum Analysis

6.3.1 Methodology of Response Spectrum Analysis

It is known that the acceleration that is a function of time is an input of the ground motion that is deemed as an SDOF system and that is given by accelerograms. Although the seismic ground motion is endowed with an irregular form, it can be considered as a combination of several harmonic components, and each of them is identified with amplitude and frequency. It is possible to say that the variables can be changed by means of a mathematical operator named Fourier Series in a way that the motion is represented by the amplitude of each harmonic component and frequency of each harmonic component. It is also worth mentioning that some frequencies are of more interest in order to check whether resonance will take place or not.

The purpose of the Response Spectrum Analysis is to extract the maximum value of displacement from the entire response. To explain, if the maximum displacement is multiplied by the structural stiffness, then the maximum force that is generated by the earthquake on the structure can be obtained.

Equation of motion of SDOF system under earthquake actions can be interpreted as equation (26).

$$m\ddot{u}(t) + c\dot{u}(t) + ku(t) = -m\ddot{u}_g(t) \qquad (26)$$

Where:

$u(t)$: relative displacement between mass and ground

$u_g(t)$: displacement of the ground

The equation of motion can be simplified by defining the natural frequency of the system (ω_0), and damping ratio (ξ).

$$\ddot{u}(t) + 2\xi\omega_0\dot{u}(t) + {\omega_0}^2 u(t) = -\ddot{u}_g(t) \tag{27}$$

Duhamel's integral turns out the solution by defining damped natural frequency (ω_d) as follow. [35]

$$u(t) = -\int_0^t \ddot{u}_g(\tau)\frac{e^{-\xi\omega_0(1-\tau)}}{\omega_d}\sin\omega_d\,(t-\tau)d\tau \tag{28}$$

Where:

$$\omega_d = \omega_0\sqrt{1-\xi^2} \tag{29}$$

Hence, the relative displacement between mass and ground response spectrum $S_d(\xi,\omega_0)$ of the SDOF system can be computed as follow.

$$S_d(\xi,\omega_0) = |u(t)|_{max} = \frac{1}{\omega_d}\left|\int_0^t \ddot{u}_g(\tau)\,e^{-\xi\omega_0(1-\tau)}\sin\omega_d\,(t-\tau)d\tau\right|_{max} \tag{30}$$

It is also worth stating that the displacement response spectrum (S_d) is also dependent on the time history of the ground motion in terms of acceleration ($\ddot{u}_g(t)$).

In addition, the maximum relative velocity and absolute acceleration response spectra can be obtained by approximating thanks to the assumption of harmonic motion as follows.

$$S_v(\xi,\omega_0) = \omega_0 S_d(\xi,\omega_0) = S_d(\xi,\omega_0)\left(\frac{2\pi}{T}\right) \tag{31}$$

$$S_a(\xi, \omega_0) = {\omega_0}^2 S_d(\xi, \omega_0) = S_d(\xi, \omega_0)\left(\frac{2\pi}{T}\right)^2 \quad (32)$$

By considering equation (26), in the case of small damping (neglecting $2\xi\omega_0\dot{u}(t)$), pseudo acceleration response spectrum can be approximated as the maximum absolute acceleration $\left(\ddot{u}(t) + \ddot{u}_g(t)\right)$ as shown by equation (33).

$${\omega_0}^2 u(t) \cong -\left(\ddot{u}(t) + \ddot{u}_g(t)\right) \quad (33)$$

$$S_a(\xi, \omega_0) \cong max\left|\ddot{u}(t) + \ddot{u}_g(t)\right| \quad (34)$$

The maximum effect of the earthquake can be represented by Fmax.

$$F = ku(t) = -c\dot{u}(t) - m\left(\ddot{u}(t) + \ddot{u}_g(t)\right) \quad (35)$$

For getting $u(t)_{max},\ \ddot{u}(t) = 0$,

$$F_{max} = |ku(t)_{max}| = |m\ddot{x}(t)_{max}| \quad (36)$$

The maximum force acting on the structure can be considered in a way that the elastic reactions of the structure can be seen as the inertia loads generated by the earthquake on the structural mass.

Where:

$\ddot{x}(t)_{max}$: absolute maximum acceleration (pseudo acceleration)

$$F_{max} = kS_d = m{\omega_0}^2 S_d \quad (37)$$

Where:

$$\omega_0 = \sqrt{\frac{k}{m}} \tag{38}$$

$$F_{max} = mS_a \tag{39}$$

The effect of ground shaking on the structural response can be represented by a diagram called "Response Spectrum" indicating the maximum forces (F_{max}) as a function of the period (T). Furthermore, it is convenient to interpret F_{max} in non-dimensional form with reference to the weight of the structure. By doing this, the response spectrum gives the earthquake effect in terms of weight percentage acting in the horizontal direction.

$$\frac{F_{max}}{W} = \frac{mS_a}{W} = \frac{S_a}{g} \tag{40}$$

NDOF LINEAR SYSTEM SUBJECTED TO SEISMIC MOTION

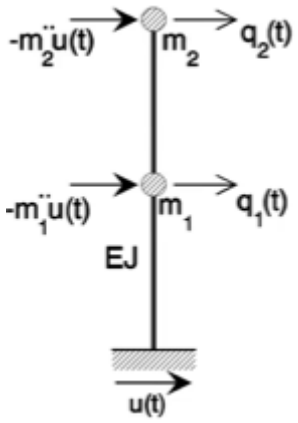

Figure 85: Free Body Diagram and Kinetic Diagram of NDOF System

The equation of motion for NDOF systems can be expressed by Equation (41).

$$m\ddot{q} + c\dot{q} + kq = -mr\ddot{u}(t) \tag{41}$$

Where:

r= 1 for the coordinates parallel to the reference motion u(t)

r=0 otherwise

The response spectrum method is based on the modal superposition approach. By means of equation (42), Lagrangian coordinates $q(t)$ can be transformed into normal coordinates $y_i(t)$

$$q(t) = \sum_{i=1}^{n} \emptyset_i y_i(t) \tag{42}$$

The left-hand side is composed of the same terms as the sdof system, right hand side contains participation factor Γ, and acceleration of the reference motion $\ddot{u}(t)$.

$$\ddot{y}_i + 2\xi\omega\dot{y}_i(t) + \omega_i^2 y_i(t) = -\frac{\varphi_i^T mr}{M_i}\ddot{u}(t) = -\Gamma_i\ddot{u}(t) \tag{43}$$

If Equation K is recalled, there is a difference between Equation (K) and Equation (Above) on the right-hand side. In this case, ground acceleration $\ddot{u}(t)$ is multiplied by participation factor Γ.

Maximum absolute value $max|y_i(t)|$ can be determined by a product of the participation factor and the response spectrum $S_d(\xi_i, T_i)$.

$$max|y_i(t)| = |\Gamma_i S_d(\xi_i, T_i)| \tag{44}$$

Where:

$$T_i = \frac{2\pi}{\omega_{0_i}} \tag{45}$$

This procedure can be applied for each normal coordinate and modal contributions to the response can be obtained by Equation (46).

$$q(t) = \sum_{i=1}^{n} \varphi_i y_i(t) = \sum_{i=1}^{n} q^{(i)}(t) \tag{46}$$

φ_i: Eigenvector of the mode i

$q^{(i)}(t)$: contribution of mode i to the total displacement vector $q(t)$

The maximum absolute value of the modal contribution can be determined by Equation (47).

$$max\left|q^i(t)\right| = max|\varphi_i y_i(t)| = |\varphi_i \Gamma_i S_d(\xi_i, T_i)| \quad (47)$$

Square Root of the Sum of the Squares (S.R.S.S.)

Since the response spectrum gives just the peak values. However, it provides information of neither when these peak values take place nor what the values of other components at that time are. Hence, to be able to estimate the summation of the individual modal contributions. It can be combined by Equation (48).

$$max|q(t)| = \sqrt{\sum_{i=1}^{n} [max|q^i(t)|]^2} \quad (48)$$

6.3.2 Response Spectrum Analysis Procedure in NTC 2008

In the Italian code (NTC 2008), the expected life of the structure is chosen. There are 4 limit states in NTC, but only two of them are related to earthquake design that is SLD (damage limit state) and SLV (ultimate limit state). For this reason, two return period values are calculated by means of equation (49). In addition, these limit states are related to probability levels as denoted in Table 22.

$$T_R = -\frac{V_R}{\ln(1 - P_{V_R})} \quad (49)$$

Table 22: Probability Levels of the Limit States

SLO	81%
SLD	63%
SLV	10%

SLC	5%

In NTC-2008, the next step is to determine the class of the soil. After that, the response spectrum turns out to be dependent on solely peak ground acceleration (PGA), Tc, and F_0 as shown in Figure 86: Flowchart of the Response Spectrum Generation in NTC-2008.

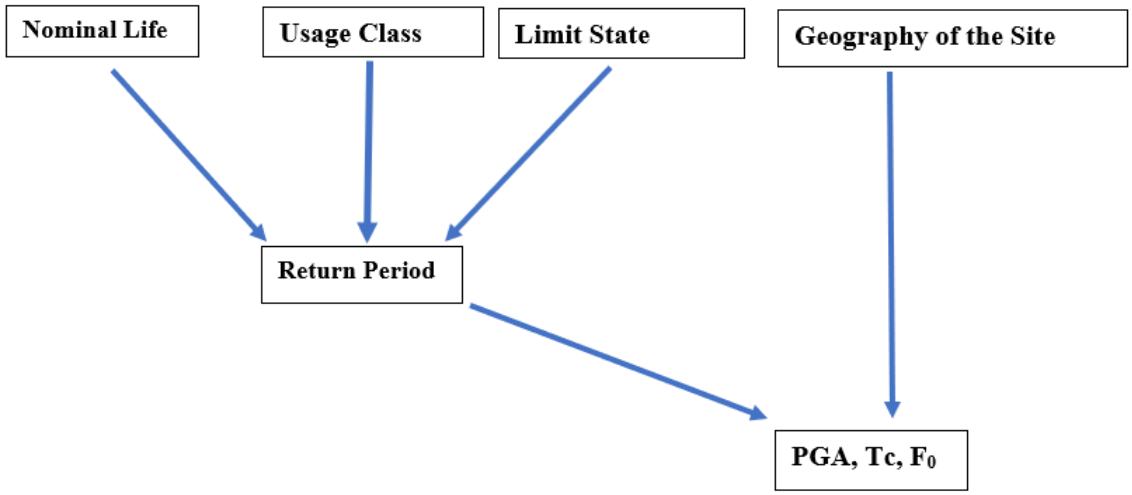

Figure 86: Flowchart of the Response Spectrum Generation in NTC-2008

Response Spectrum was obtained by a spreadsheet provided by the website of the Italian National Association of Earthquake Engineering. (see Figure 88: Entering Coordinates of San Carpoforo to Spreadsheet for Response Spectrum) By entering the coordinates and selecting the limit state, it presents the response spectrum. Coordinates and relevant information about the site are presented in Table 23. SLV Limit state was considered for the response spectrum analysis.

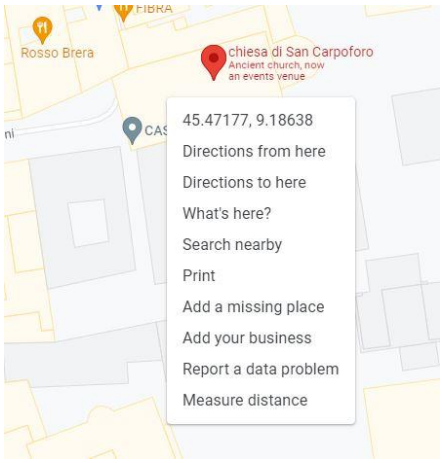

Figure 87: Local Coordinates for the site of San Carpoforo

Table 23: Geographic Information of the Location of the Structure

City, Country	Milan, Italy
Longitude	9.18637893546391
Latitude	45.47177080156896
Topographic Condition	T1
Ground Type	B

Figure 88: Entering Coordinates of San Carpoforo to Spreadsheet for Response Spectrum

Table 24: Dependent Parameters for Response Spectrum Analysis

Limit State	SLV
a_g	0.050 g
F_0	2.655
T_C^*	0.280 s
S_S	1.200
C_C	1.419
S_T	1.000
q	2.000

NTC-2008 defines the response spectrum through the equations (50), (51), (52), and (53).

$$0 \le T \le T_B \quad S_e(T) = a_g \cdot S \cdot \eta \cdot F_0 \left[\frac{T}{T_B} + \frac{1}{\eta F_0}\left(1 - \frac{T}{T_B}\right)\right] \qquad (50)$$

$$T_B \le T \le T_C \quad S_e(T) = a_g \cdot S \cdot \eta \cdot F_0 \qquad (51)$$

$$T_C \leq T \leq T_D \quad S_e(T) = a_g \cdot S \cdot \eta \cdot F_0 \cdot \left(\frac{T_C}{T}\right) \tag{52}$$

$$T_D \leq T \quad S_e(T) = a_g \cdot S \cdot \eta \cdot F_0 \cdot \left(\frac{T_C \cdot T_D}{T}\right) \tag{53}$$

Table 25: Independent Parameters for Response Spectrum Analysis

S	1.200
η	0.500
T_B	0.132 s
T_C	0.397 s
T_D	1.799 s

Where:

q: Behavior Factor

T_B: Lower limit of the period of the constant spectral acceleration branch

T_C: Upper limit of the period of the constant spectral acceleration branch

T_D: Value defining the beginning of the constant displacement response range of the spectrum

S: Soil factor

η: Damping correction factor with a reference value of η=1 for 5% viscous damping

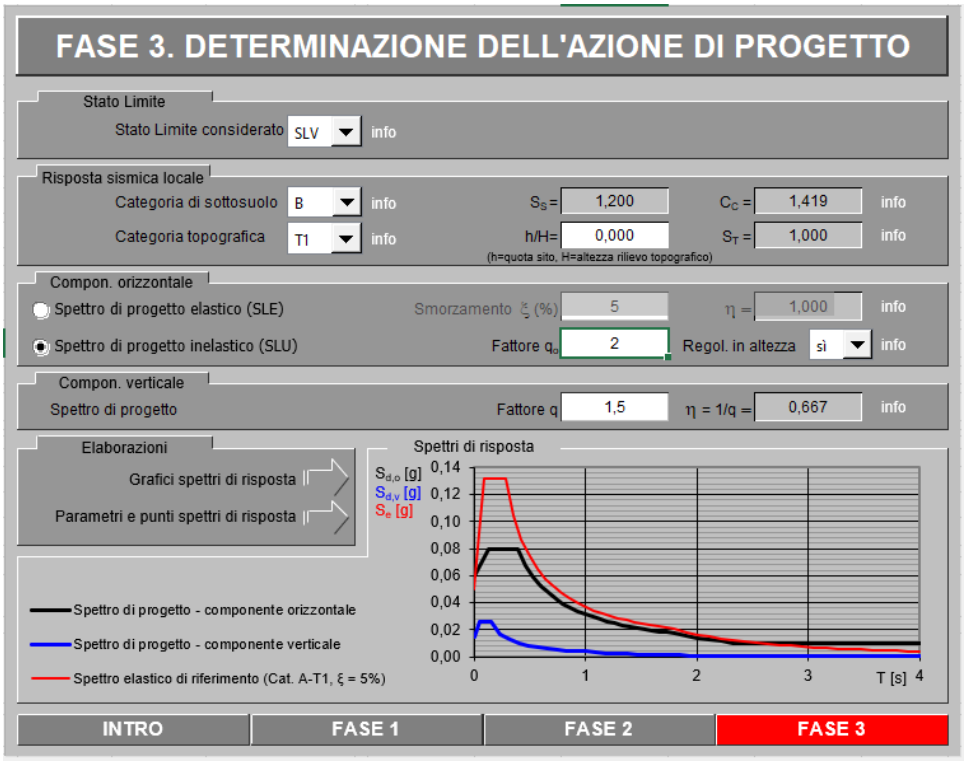

Figure 89: Spettri di Risposta vers. 1.03 Software

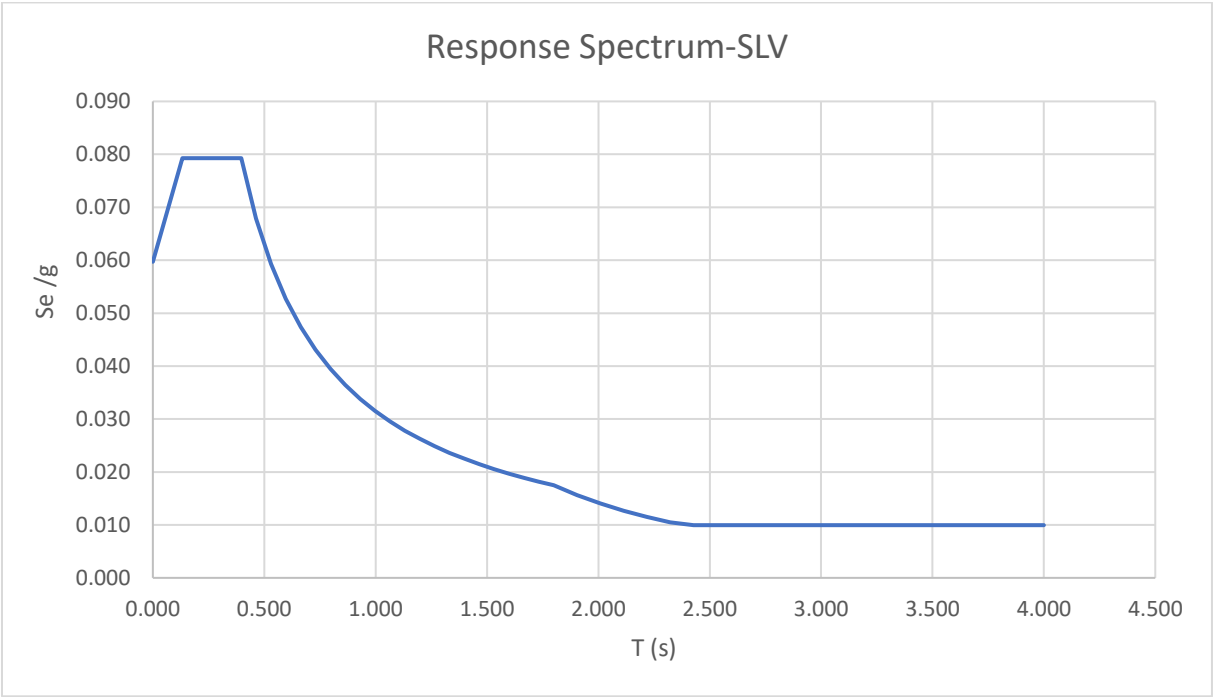

Figure 90: Response Spectrum for SLV Limit State, q=2

In ABAQUS, a new step was defined by choosing Response Spectrum. Excitations were selected as a single direction and the square root of the sum of squares (S.R.S.S.) was used as the combination method of the modes. Then, the response spectrum was defined by means of creating amplitude as shown in Figure 91.

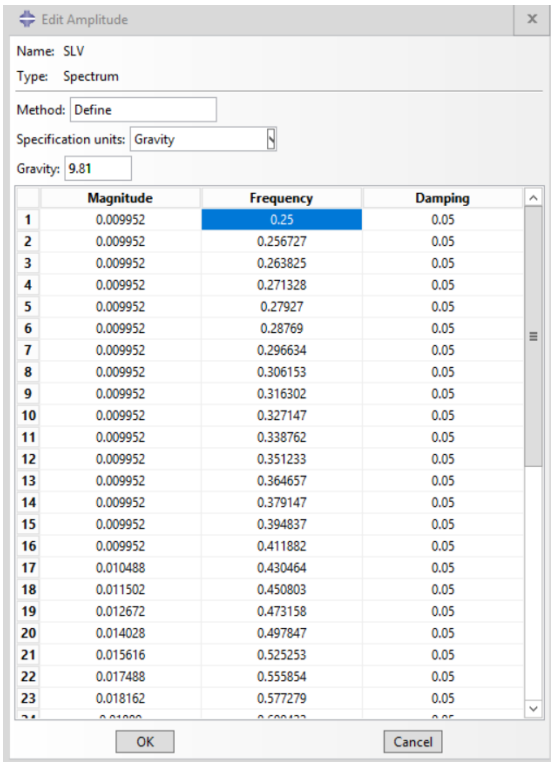

	Magnitude	Frequency	Damping
1	0.009952	0.25	0.05
2	0.009952	0.256727	0.05
3	0.009952	0.263825	0.05
4	0.009952	0.271328	0.05
5	0.009952	0.27927	0.05
6	0.009952	0.28769	0.05
7	0.009952	0.296634	0.05
8	0.009952	0.306153	0.05
9	0.009952	0.316302	0.05
10	0.009952	0.327147	0.05
11	0.009952	0.338762	0.05
12	0.009952	0.351233	0.05
13	0.009952	0.364657	0.05
14	0.009952	0.379147	0.05
15	0.009952	0.394837	0.05
16	0.009952	0.411882	0.05
17	0.010488	0.430464	0.05
18	0.011502	0.450803	0.05
19	0.012672	0.473158	0.05
20	0.014028	0.497847	0.05
21	0.015616	0.525253	0.05
22	0.017488	0.555854	0.05
23	0.018162	0.577279	0.05

Figure 91: Amplitude Definition for Response Spectrum Analysis

6.3.3 Results of Response Spectrum Analysis (q=2)

In this section, the results of the analyses are presented with tensile stress distributions, shear stress distributions, and out-of-plane displacements. Tensile Strength and shear strength of the structure were set as the maximum value in the contours as given in Table 10. Simply, the regions in which stresses exceed the strength were indicated with the gray color in the contours.

6.3.3.1 X-DIRECTION

6.3.3.1.1 Tensile Stresses

In some regions in the façade, especially the regions close to openings, it can be seen that tensile stresses are greater than the strength. (see Figure 92: Tensile Stress Distribution of Response Spectrum in X Direction, Front View, Figure 93: Tensile Stress Distribution of Response Spectrum in X Direction, at the lower part of the Façade, Figure 94: Tensile Stress

Distribution of Response Spectrum in X Direction, at the upper part of the Façade) It is in line with the expectations to have stress localizations at the openings of the structure.

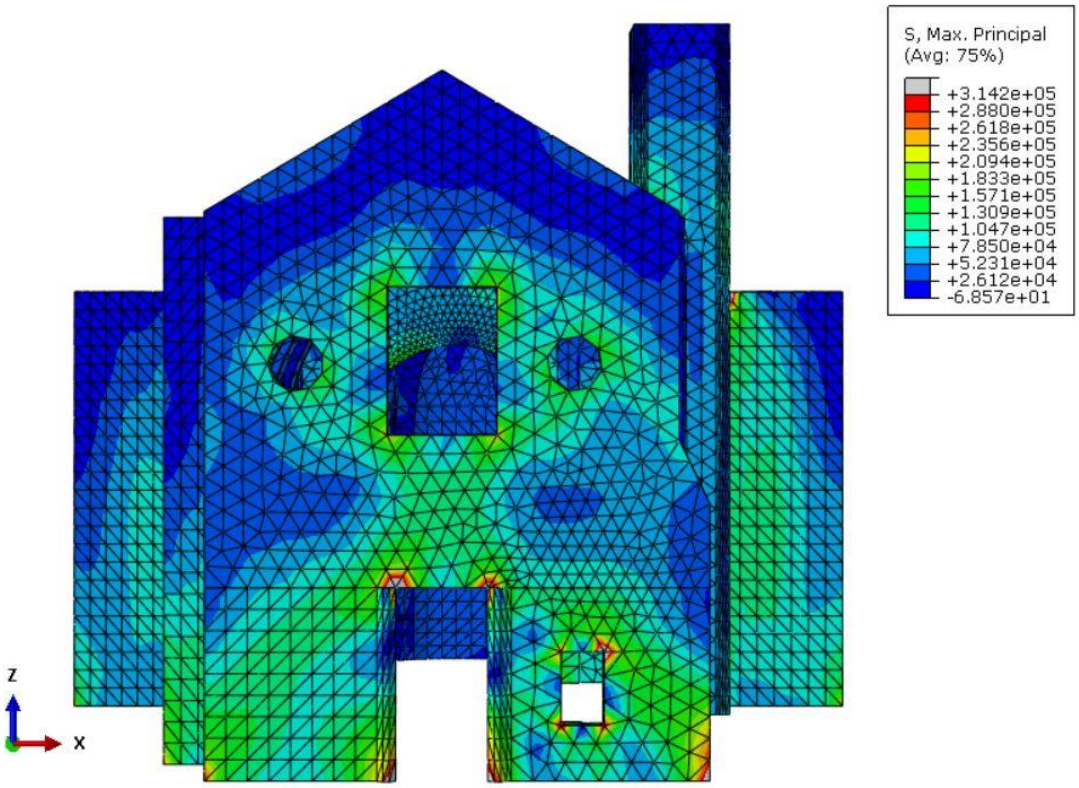

Figure 92: Tensile Stress Distribution of Response Spectrum in X Direction, Front View

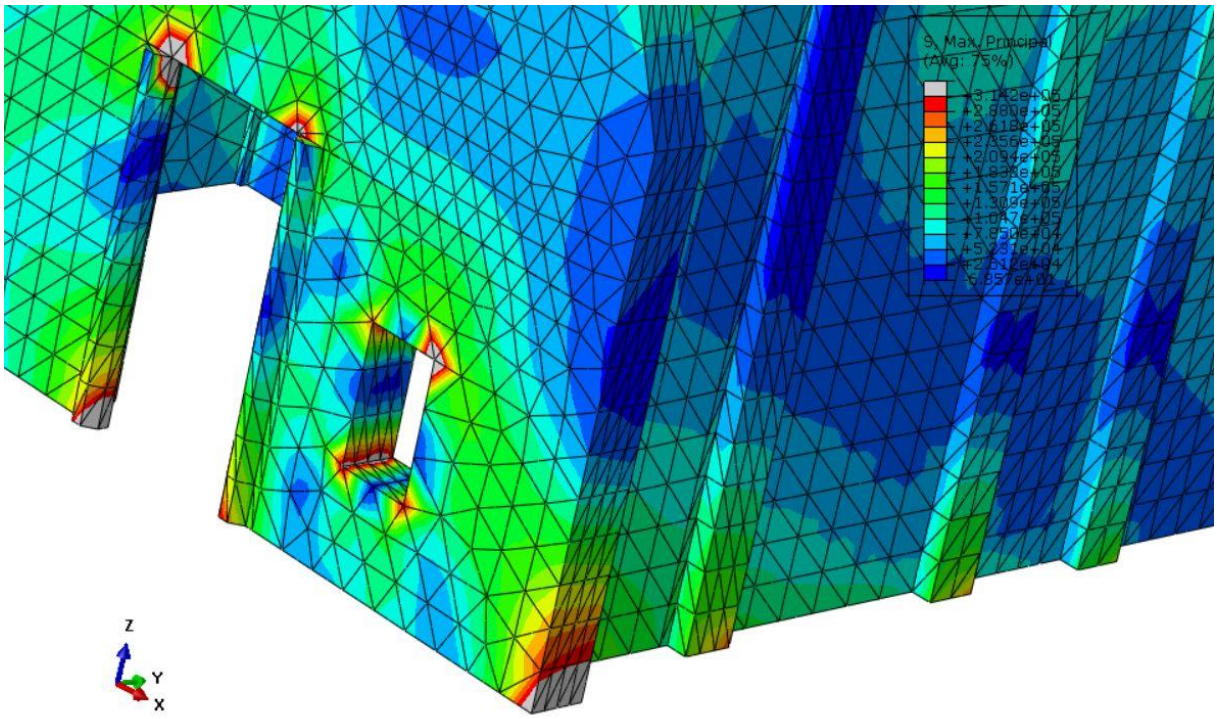

Figure 93: Tensile Stress Distribution of Response Spectrum in X Direction, at the lower part of the Façade

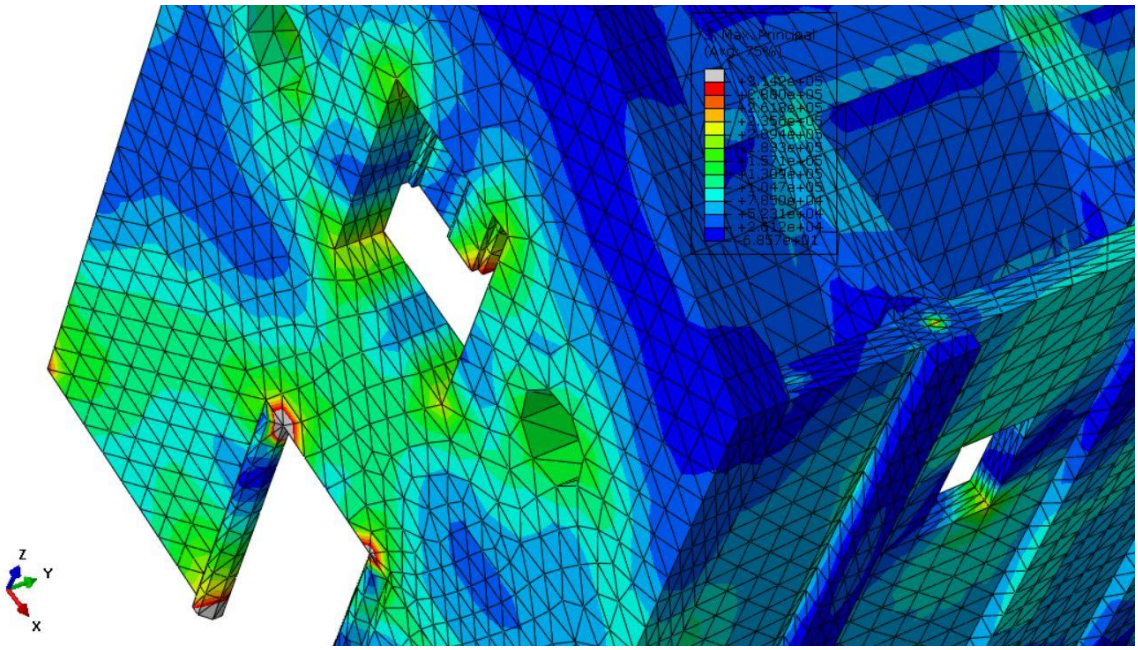

Figure 94: Tensile Stress Distribution of Response Spectrum in X Direction, at the upper part of the Façade

In addition, tensile stress distribution for left, right, isometric, and bottom views are presented in Figure 95, Figure 96, Figure 97, Figure 98, and Figure 99.

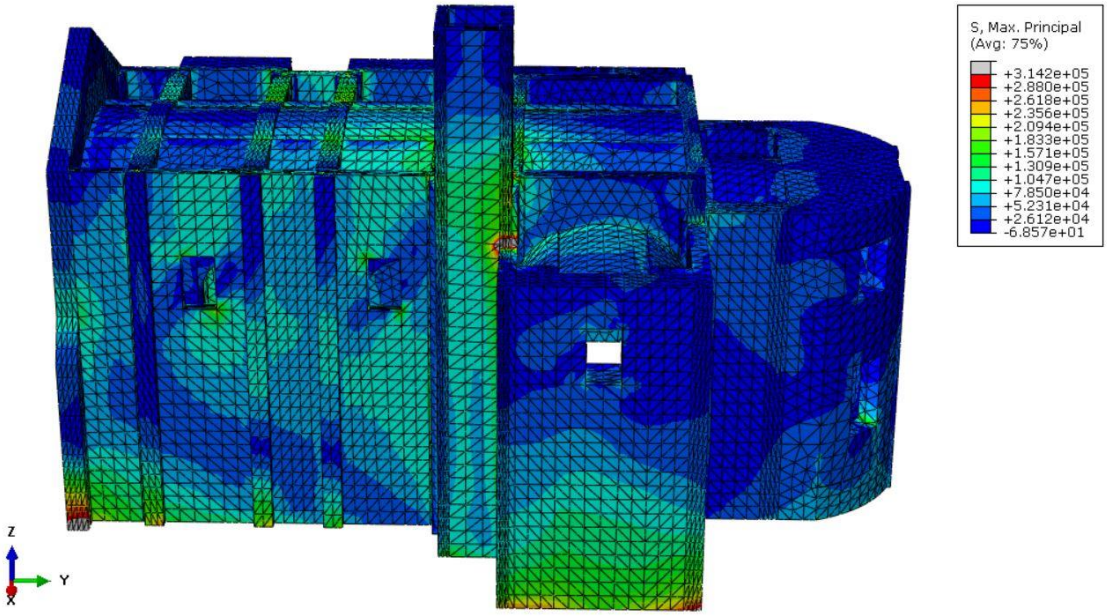

Figure 95: Tensile Stress Distribution of Response Spectrum in X Direction, Right View

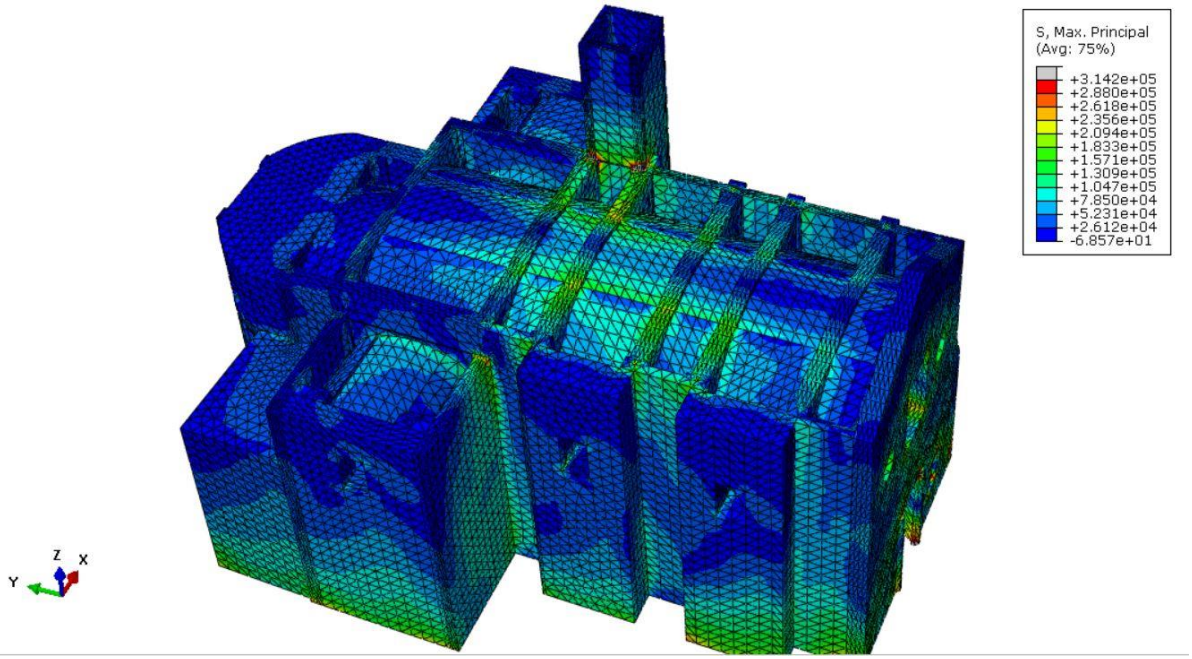

Figure 96: Tensile Stress Distribution of Response Spectrum in X Direction, Isometric View

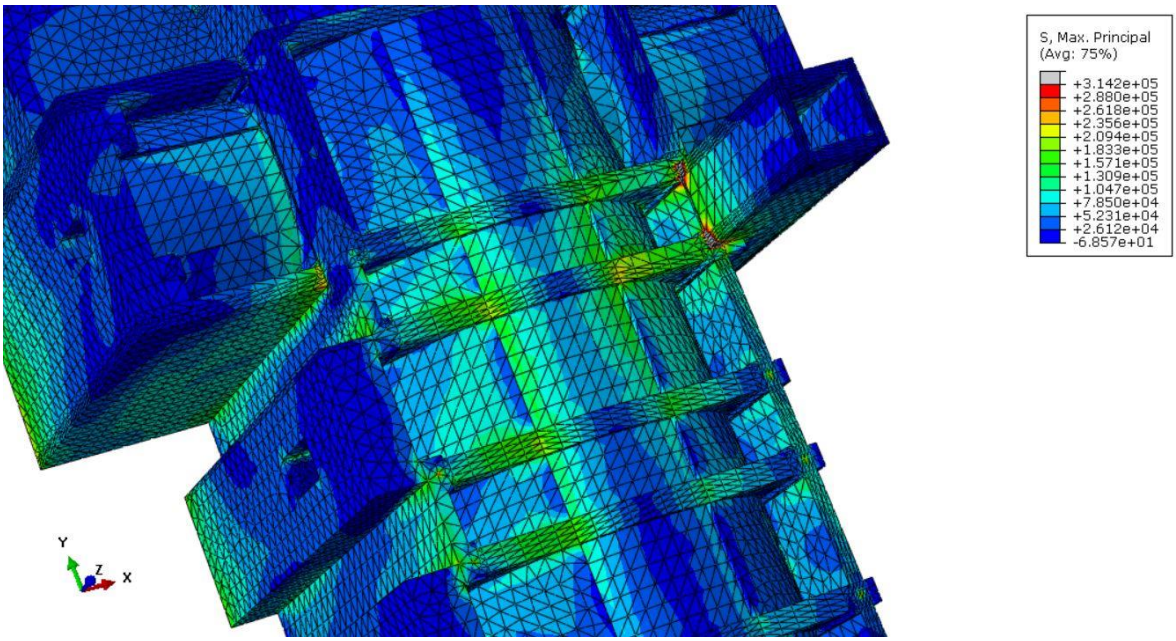

Figure 97: Tensile Stress Distribution of Response Spectrum in X Direction, Bell Tower Connection

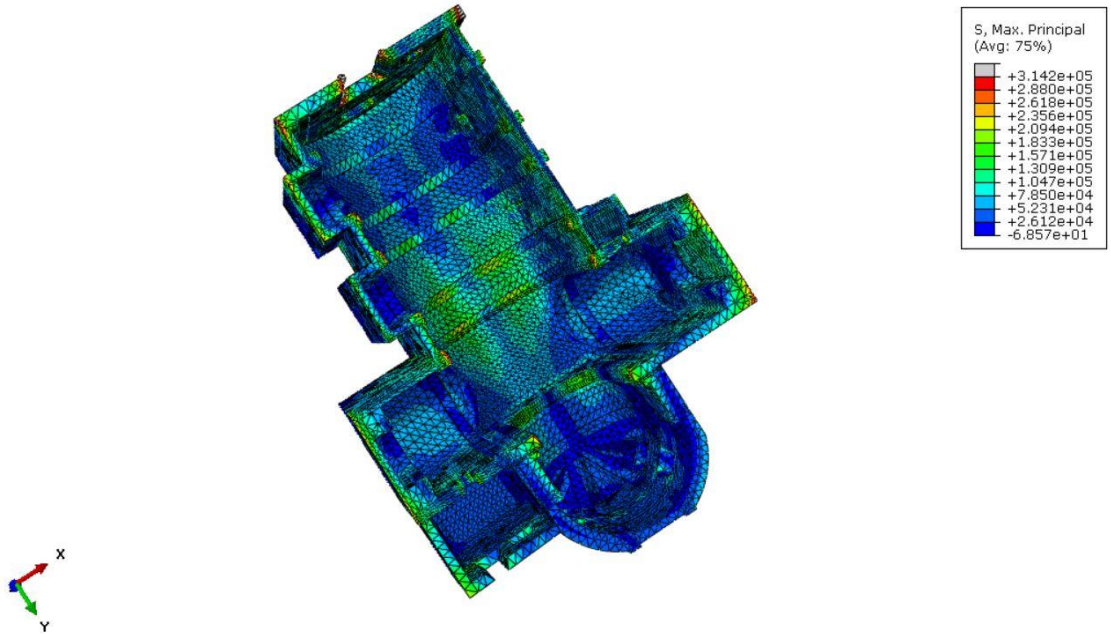

Figure 98: Tensile Stress Distribution of Response Spectrum in X Direction, Bottom View

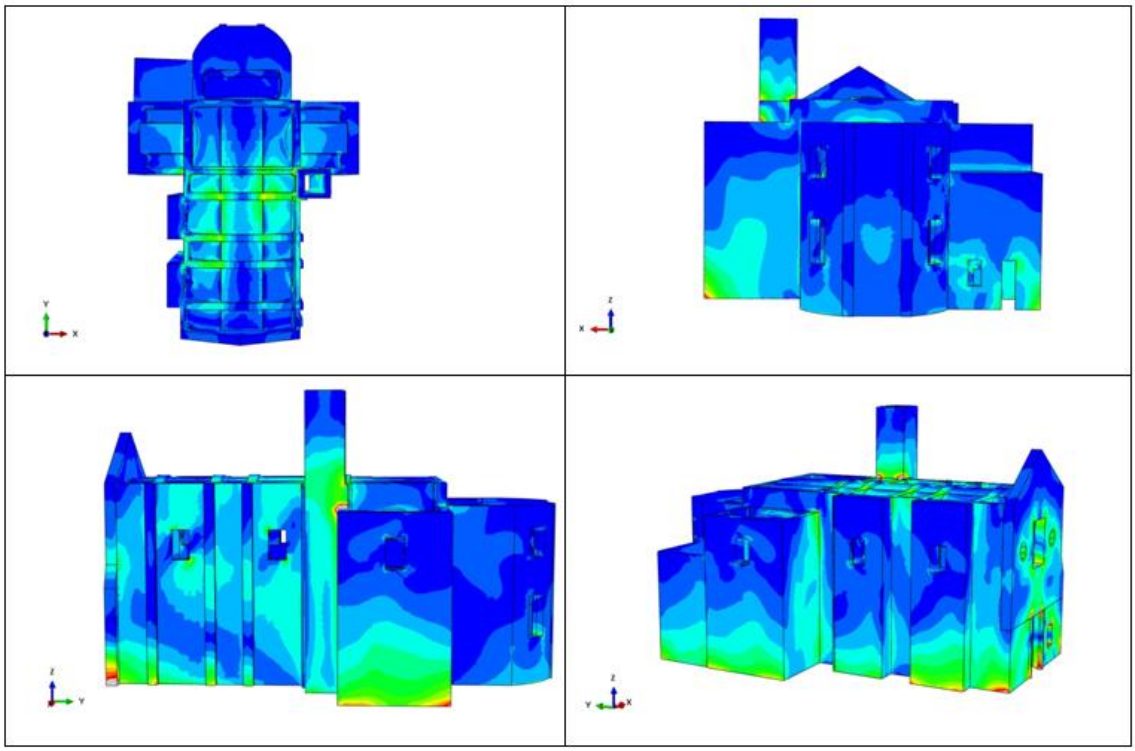

Figure 99: Tensile Stress Distribution of Response Spectrum in X Direction, Top, Back, Right, and Left View

To be able to focus on specific regions, horizontal cross sections are indicated with respect to the position of the height (z coordinate). Firstly, at z=11.0253 m corresponding to the starting point of the middle rectangular window opening, was examined. (See Figure 100: Tensile Stress Distribution of Response Spectrum in X Direction at Z=11.0253 m) At the two extremities of the opening, it is observed that tensile stress reaches the tensile strength of the material. Secondly, the connection between the bell tower and left transept where z= 16.2032 m and z=18.1645 m was observed as demonstrated in Figure 101, and Figure 102. Tensile stresses exceed the strength both in the connection between the bell tower and the left transept, and the one between the bell tower and the barrel vaults. Furthermore, at the left bottom opening in the façade, it is observed a great amount of tensile stress. (see Figure 103: Tensile Stress Distribution of Response Spectrum in X Direction at Z=1.657514 m, Figure 104: Tensile Stress Distribution of Response Spectrum in X Direction at Z=4.2375 m, Figure 105: Tensile Stress Distribution of Response Spectrum in X Direction at Z=6.0678 m)

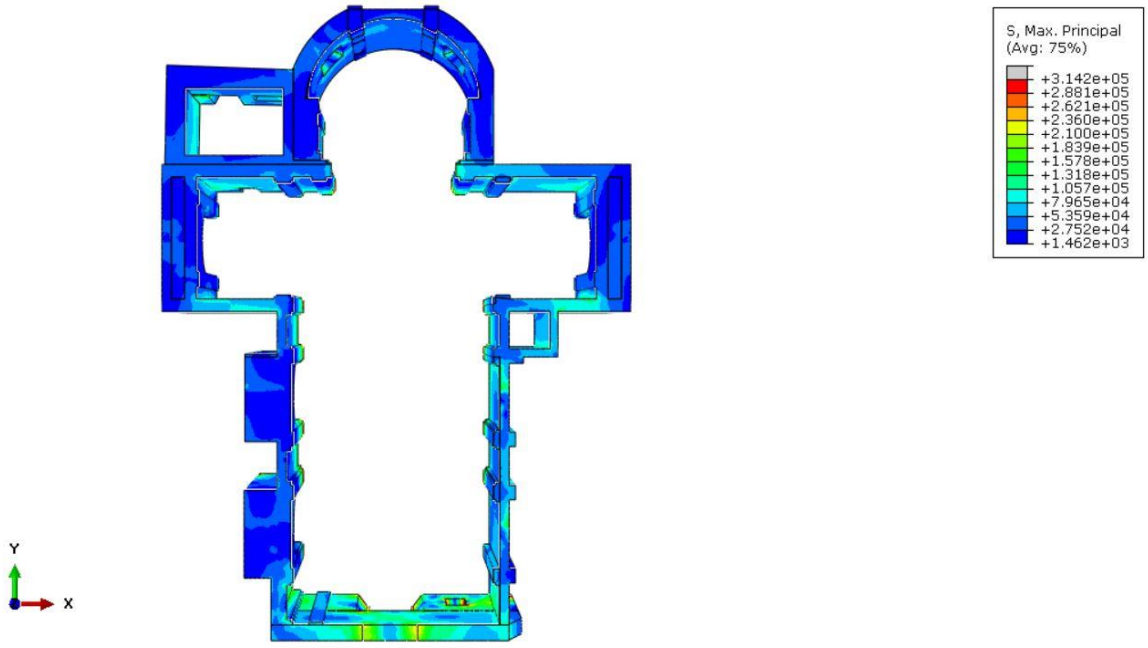

Figure 100: Tensile Stress Distribution of Response Spectrum in X Direction at Z=11.0253 m

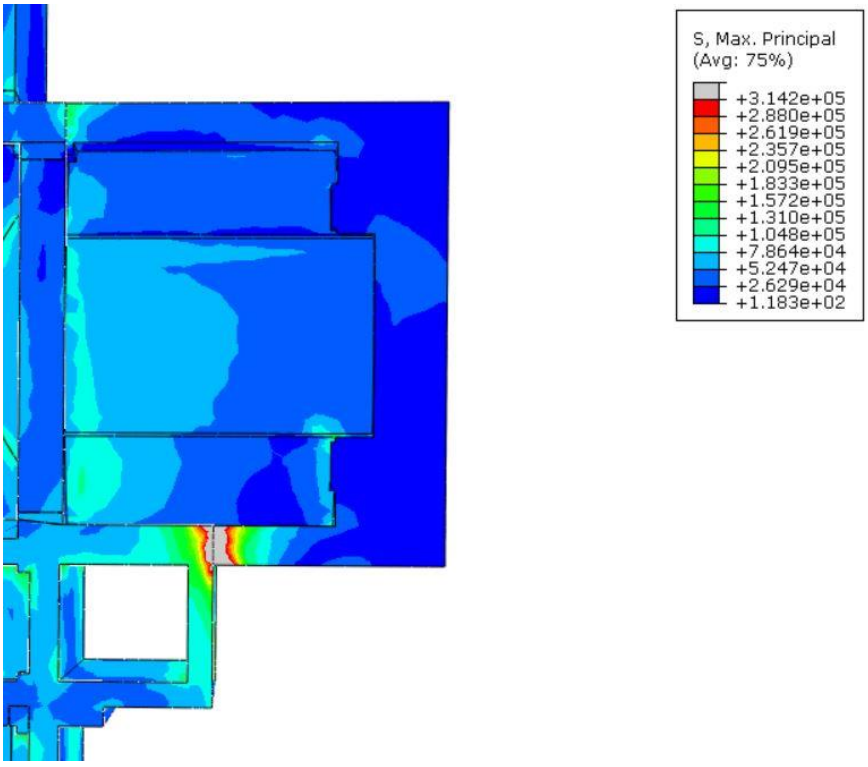

Figure 101: Tensile Stress Distribution of Response Spectrum in X Direction at Z=16.2032 m

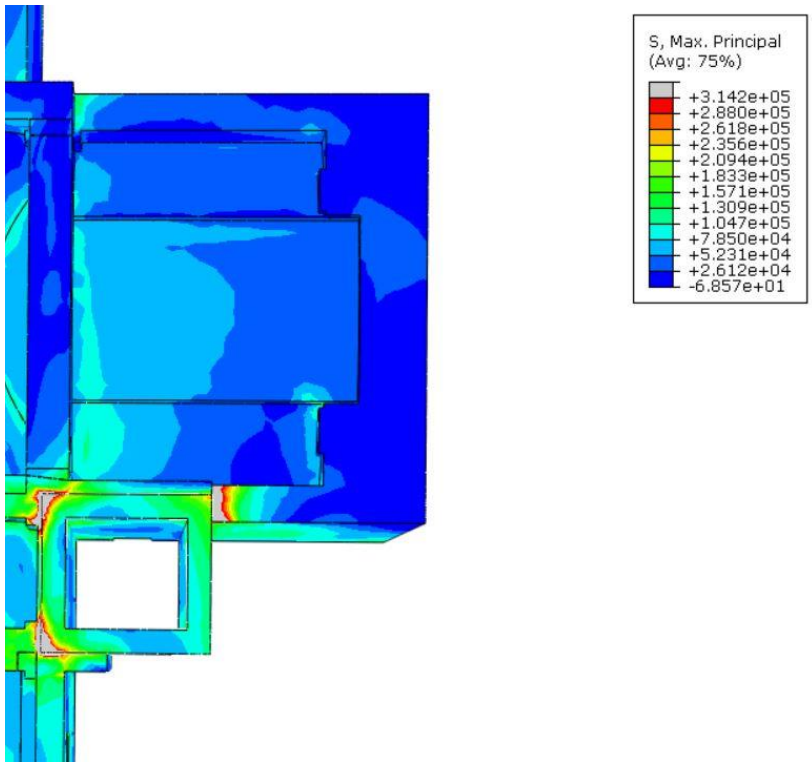

Figure 102: Tensile Stress Distribution of Response Spectrum in X Direction at Z=18.1645

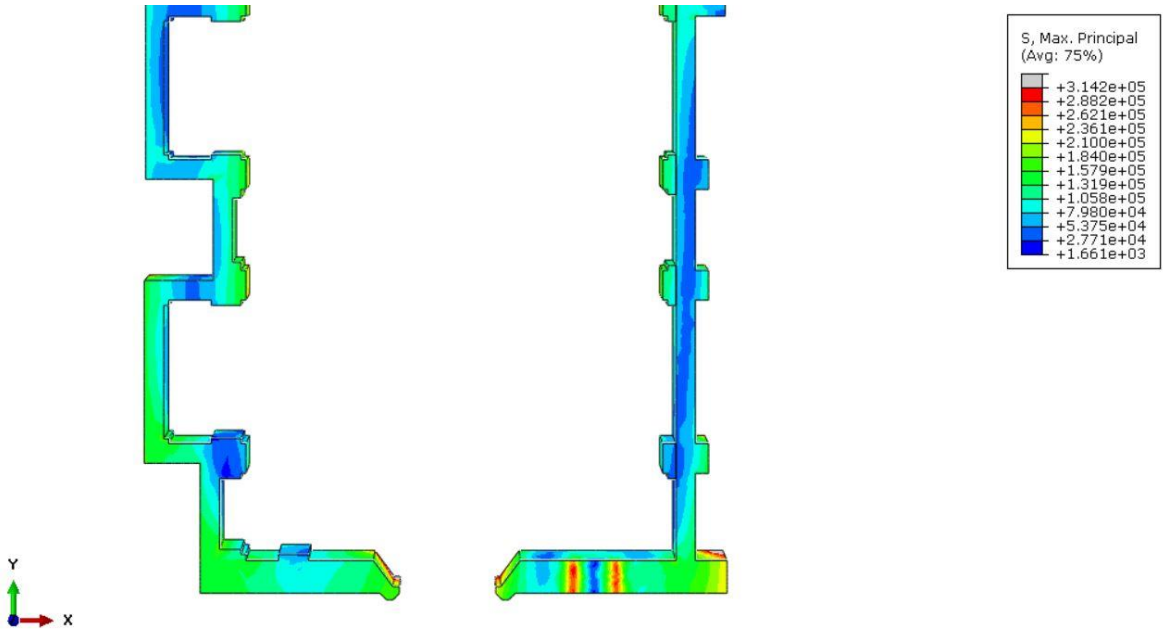

Figure 103: Tensile Stress Distribution of Response Spectrum in X Direction at Z=1.657514 m

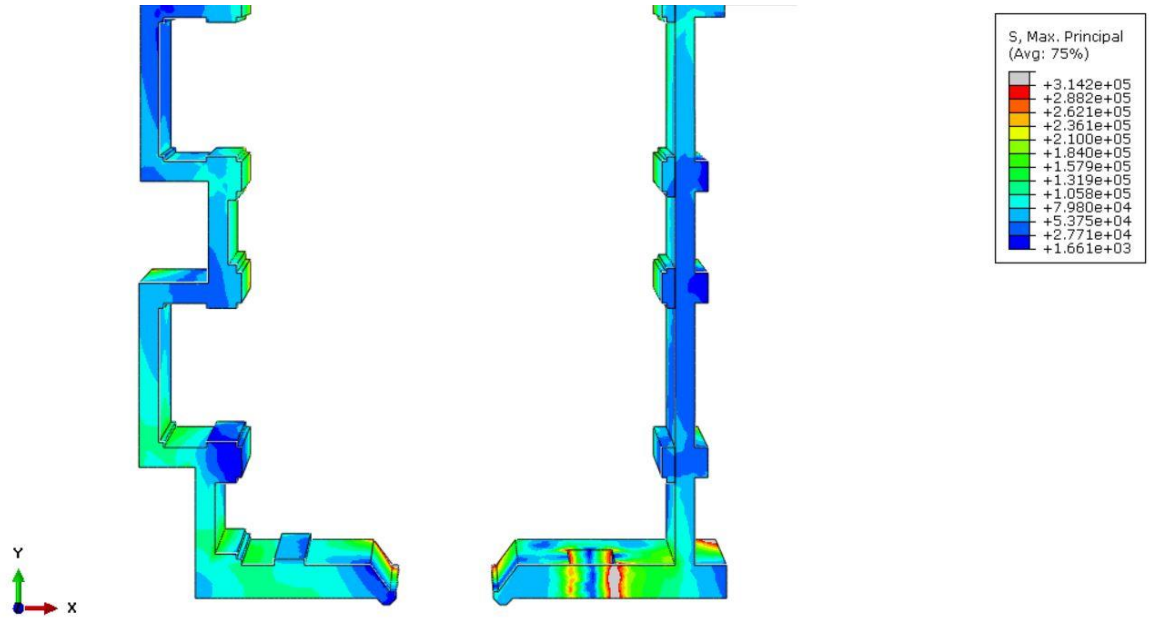

Figure 104: Tensile Stress Distribution of Response Spectrum in X Direction at Z=4.2375 m

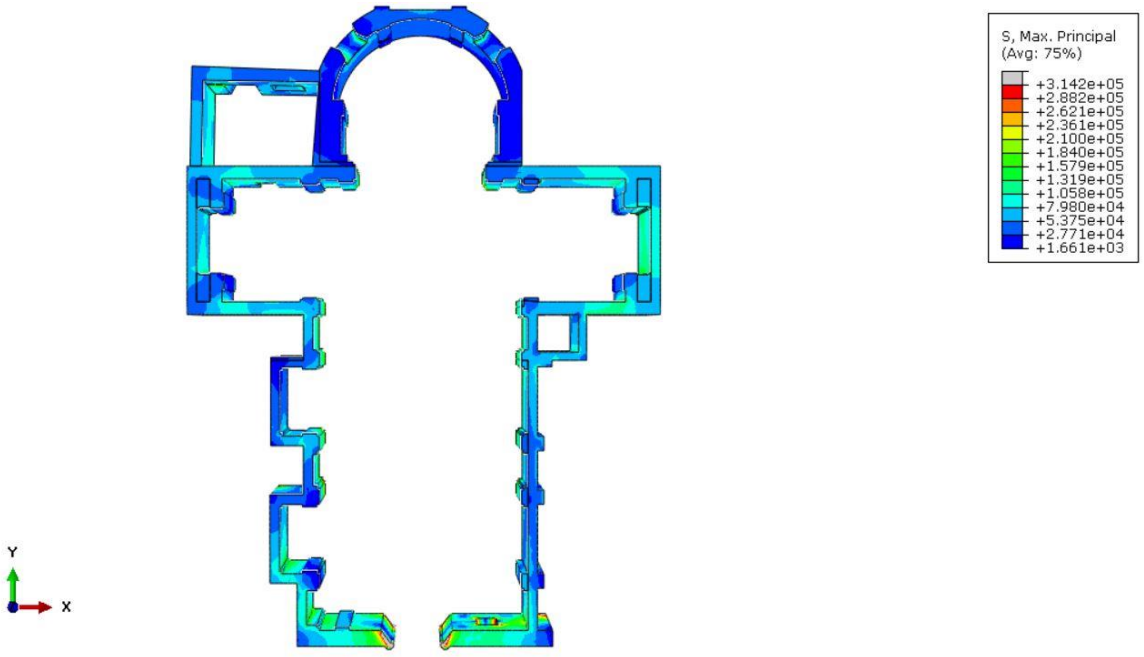

Figure 105: Tensile Stress Distribution of Response Spectrum in X Direction at Z=6.0678 m

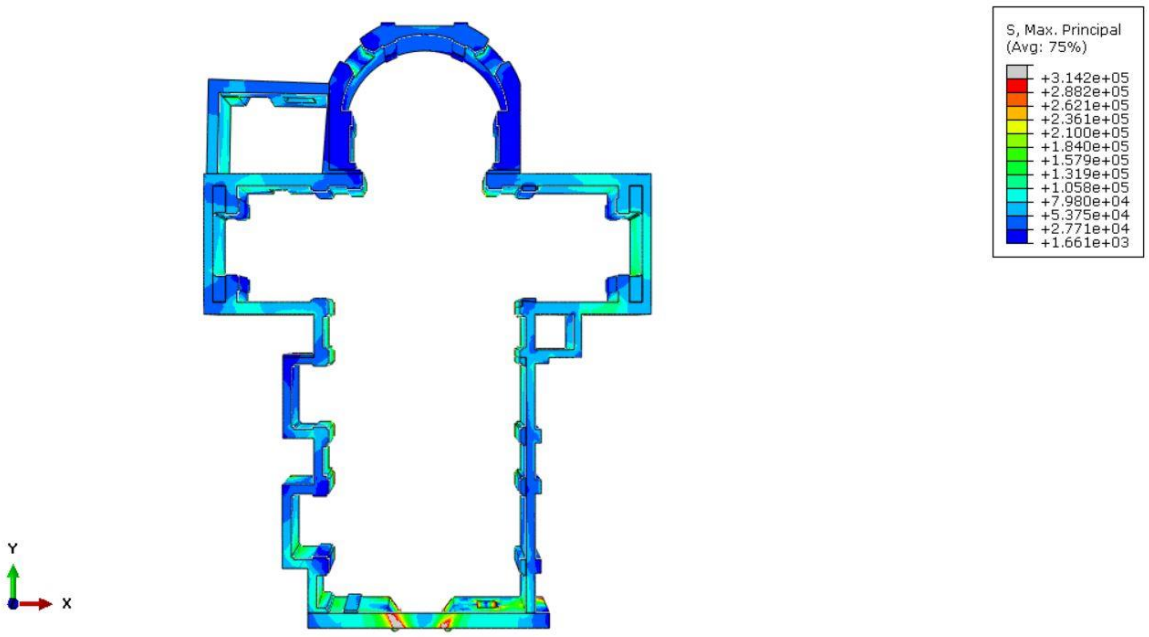

Figure 106: Tensile Stress Distribution of Response Spectrum in X Direction at Z=6.16719 m

6.3.3.1.2 Shear Stresses

Shear stress distributions are presented in Figure 107, and Figure 108. Shear stresses do not exceed the shear strength of the material, but the barrel vaults undergo around 0.055 MPa.

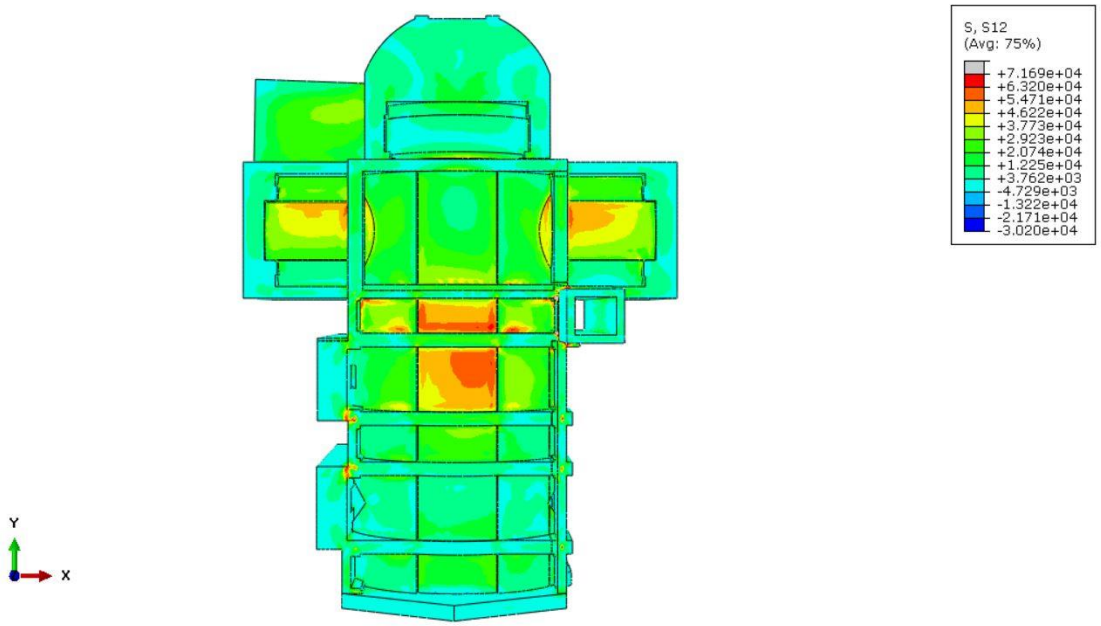

Figure 107: Shear Stress Distribution of Response Spectrum in X Direction, Top View

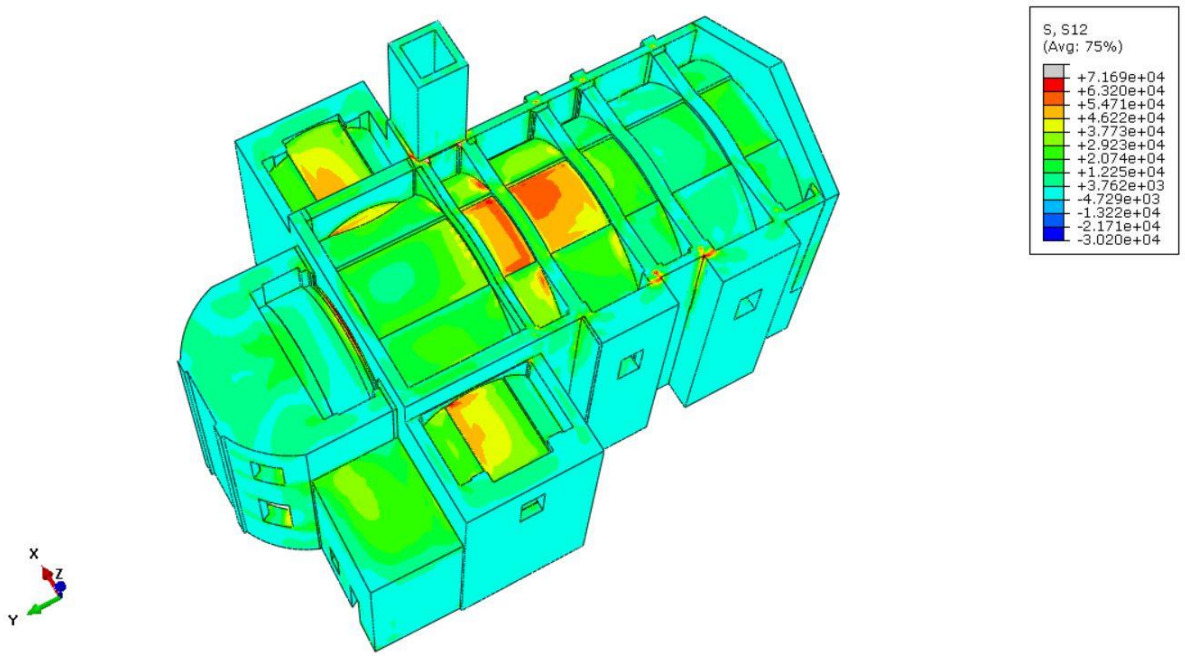

Figure 108: Shear Stress Distribution of Response Spectrum in X Direction, Isometric View

6.3.3.1.3 Out of Plane Displacement

The maximum out-of-plane displacement is observed at the top of the bell tower as 8.118 mm. As stated in the static analysis under self-weight of the structure, displacement at the middle height of the wall is important for masonry structures. The maximum displacement is computed as 3.12 mm at the left wall of the structure.

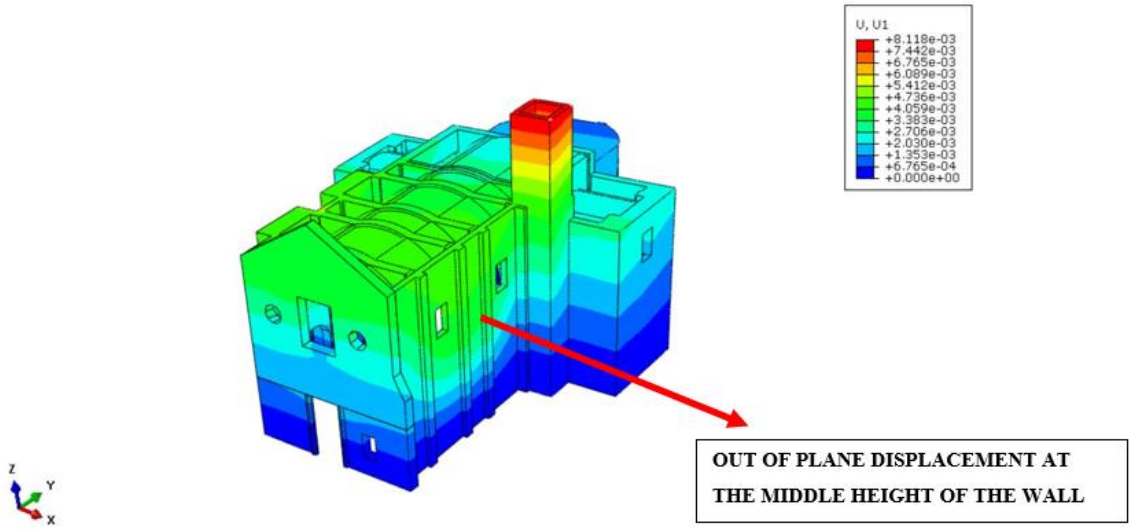

Figure 109: Out-of Plane Displacement, Response Spectrum Analysis in X Direction

6.3.3.2 Response Spectrum Analysis in Y Direction

6.3.3.2.1 Tensile Stresses

Similarly, when the amplitude defining the response spectrum acts in the Y direction, the following stress and displacement distributions are observed. In the façade, there is no region greater than the strength of the material as denoted in Figure 110. In contrast, it can be said that the left walls of the structure having a connection with the bell tower are affected at most. (see Figure 112:Tensile Stress Distribution of Response Spectrum in Y Direction, Right View, and Figure 115: Tensile Stress Distribution of Response Spectrum in Y Direction, Bell Tower-Right Wall Connection) Moreover, there are places undergoing a considerable amount of tensile stresses at the apse of the structure. (See Figure 118: Tensile Stress Distribution of Response Spectrum in Y Direction, Z=4.2623 m)

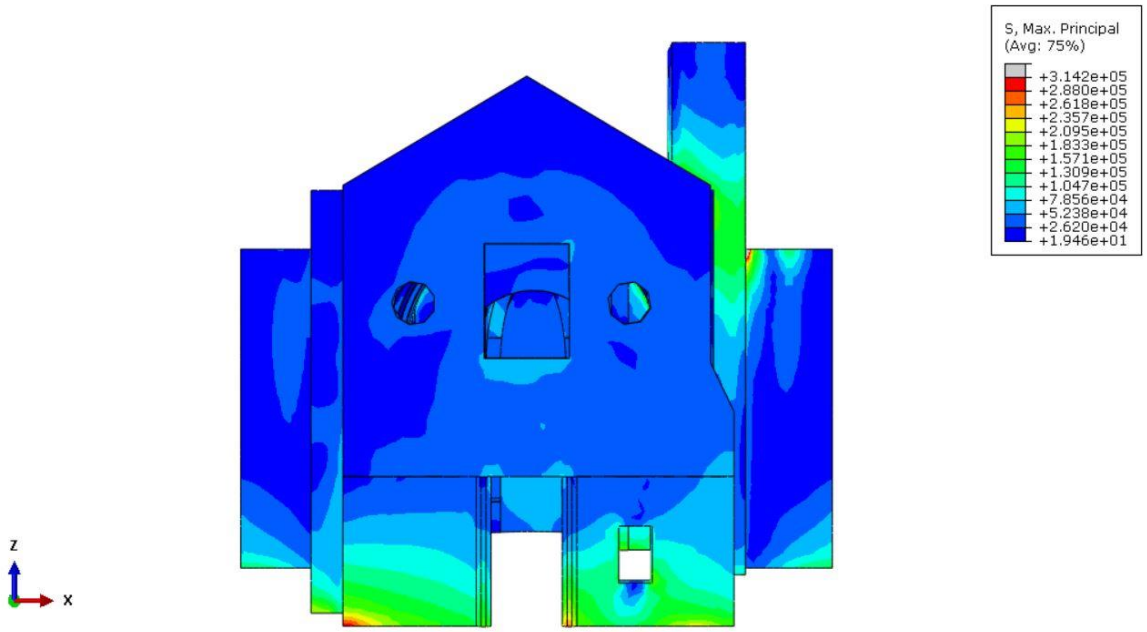

Figure 110: Tensile Stress Distribution of Response Spectrum in Y Direction, Front View

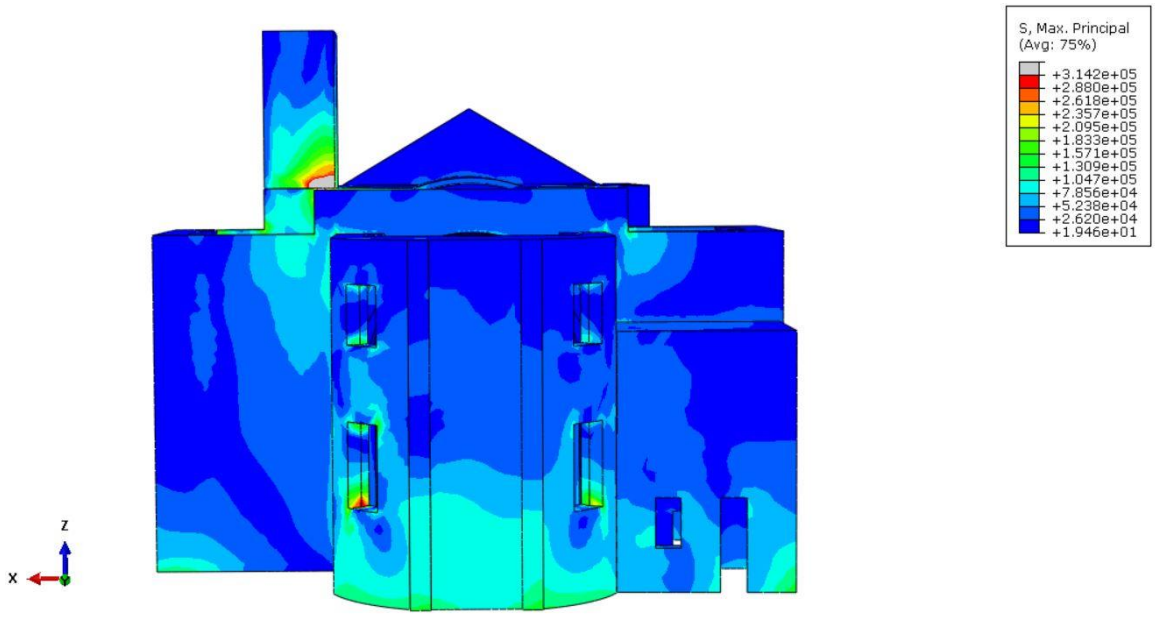

Figure 111: Tensile Stress Distribution of Response Spectrum in Y Direction, Back View

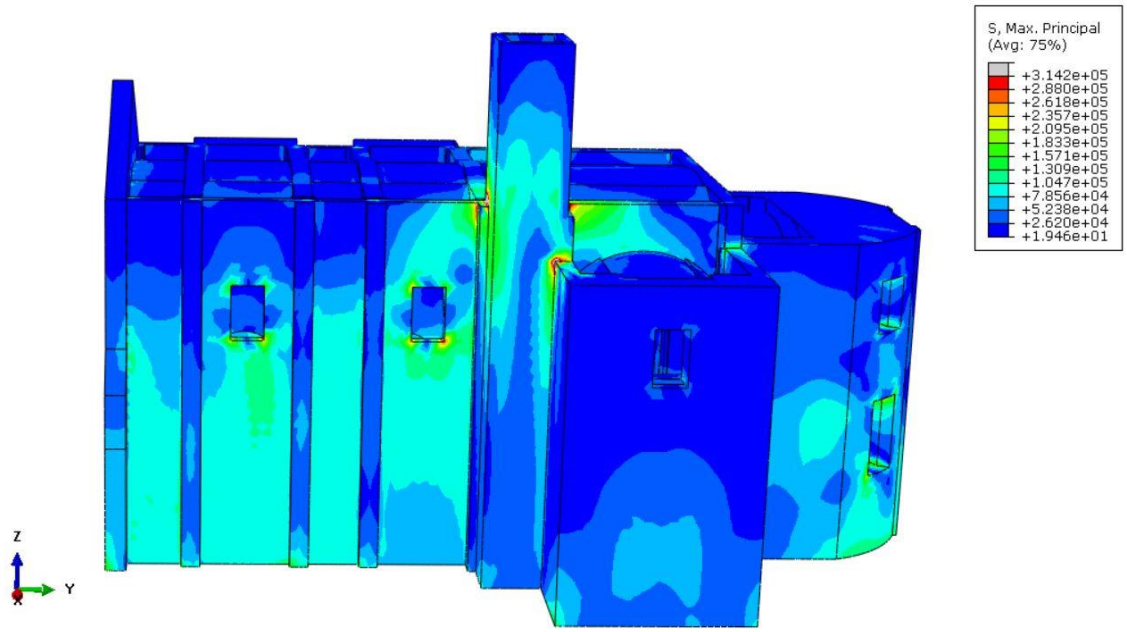

Figure 112:Tensile Stress Distribution of Response Spectrum in Y Direction, Right View

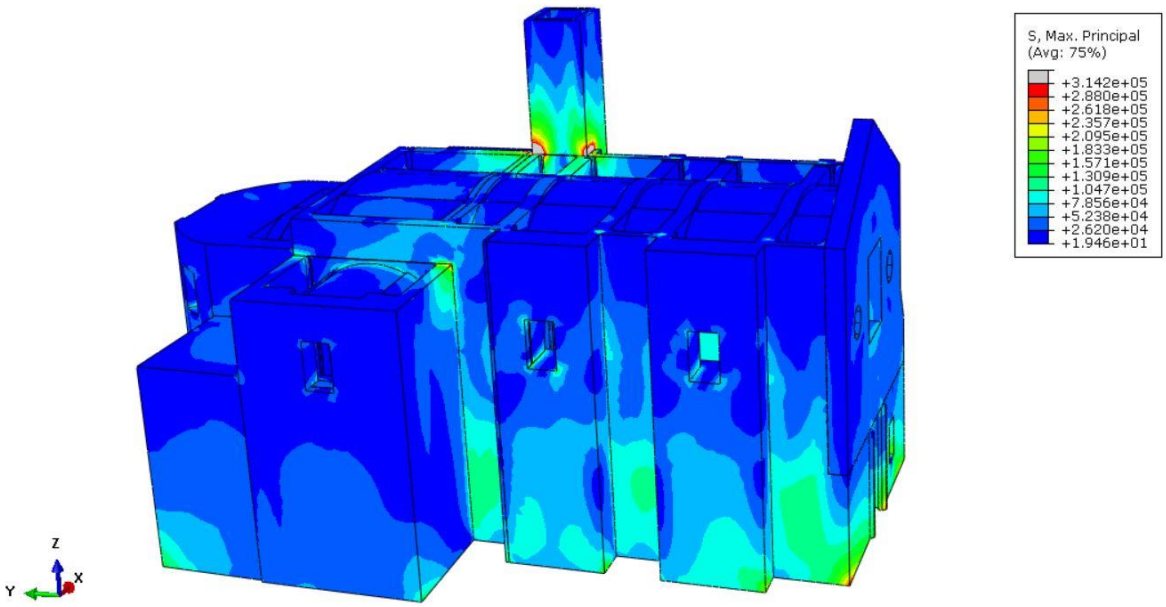

Figure 113: Tensile Stress Distribution of Response Spectrum in Y Direction, Left View

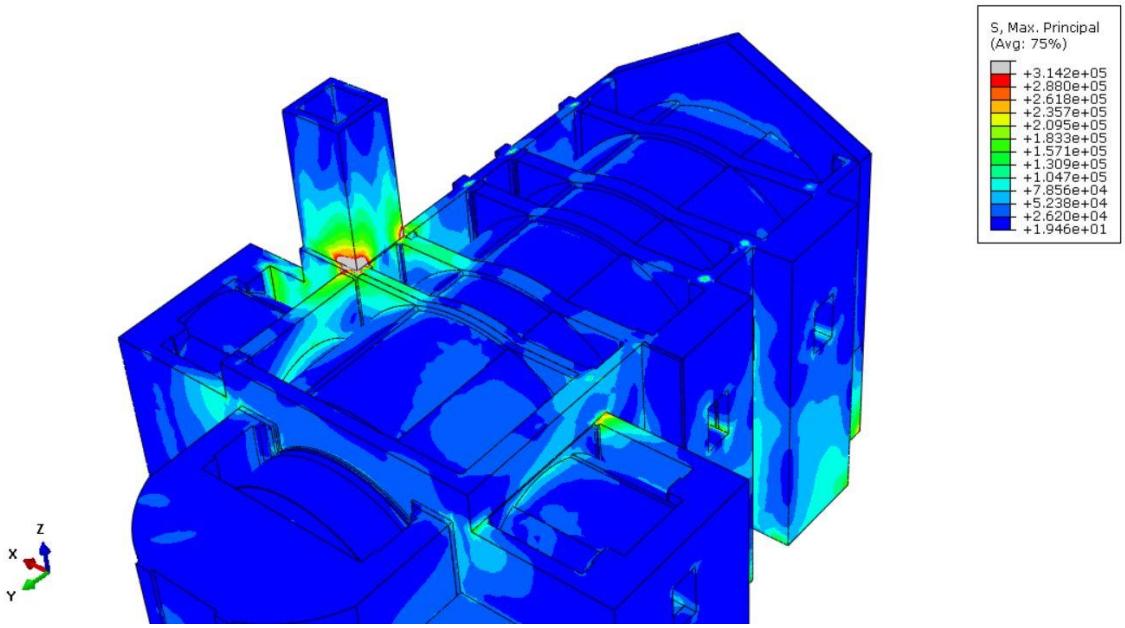

Figure 114: Tensile Stress Distribution of Response Spectrum in Y Direction, Bell Tower-Vault Connection

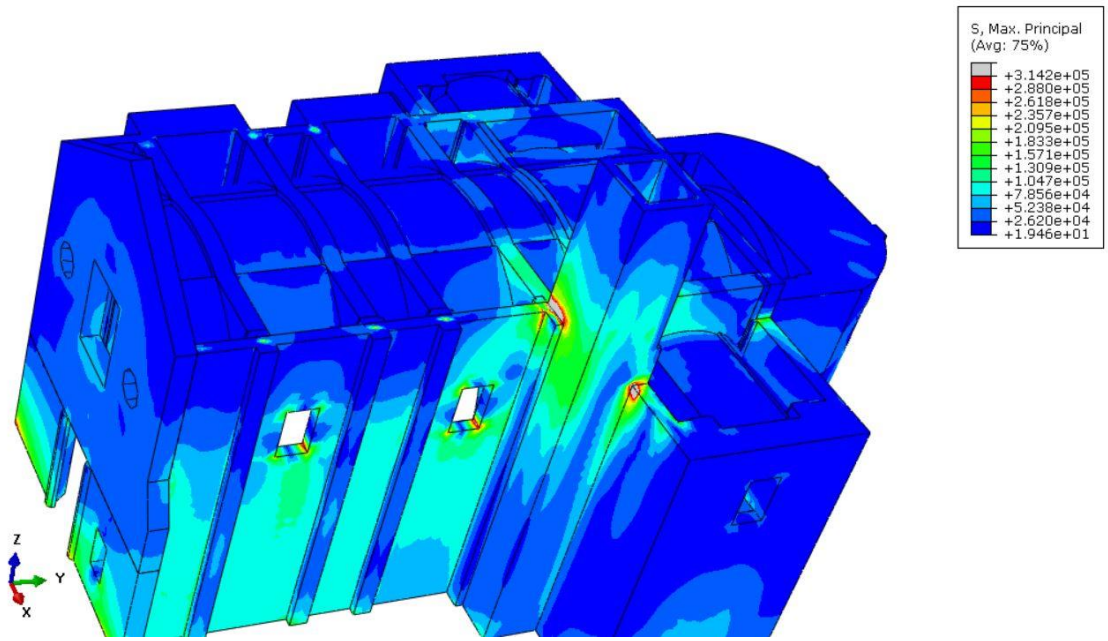

Figure 115: Tensile Stress Distribution of Response Spectrum in Y Direction, Bell Tower-Right Wall Connection

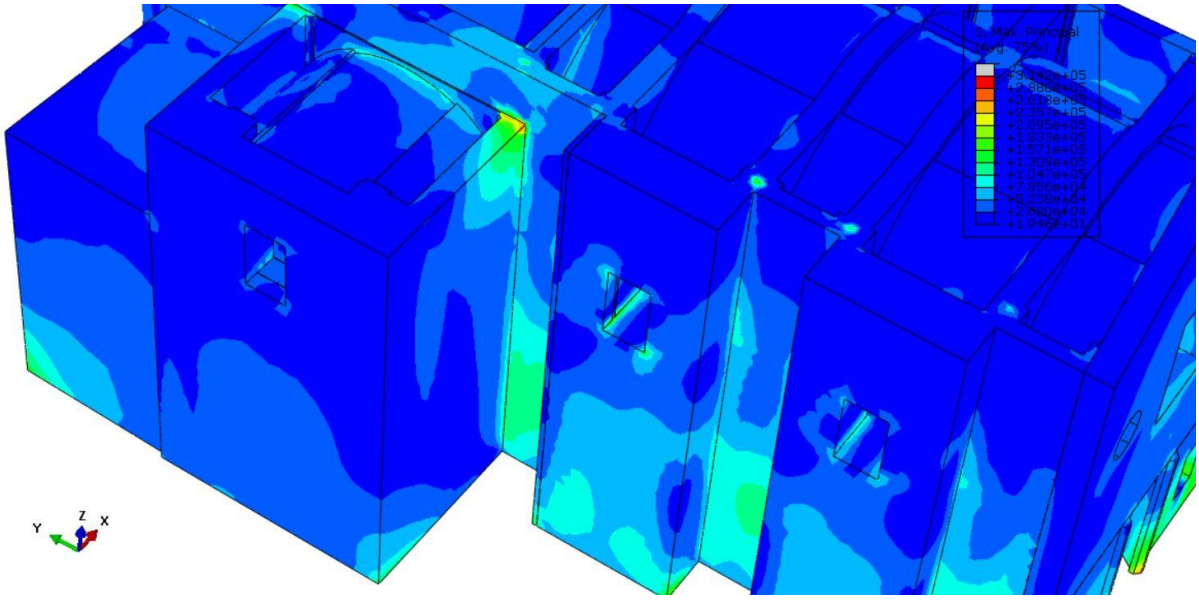

Figure 116: : Tensile Stress Distribution of Response Spectrum in Y Direction, Left Transept

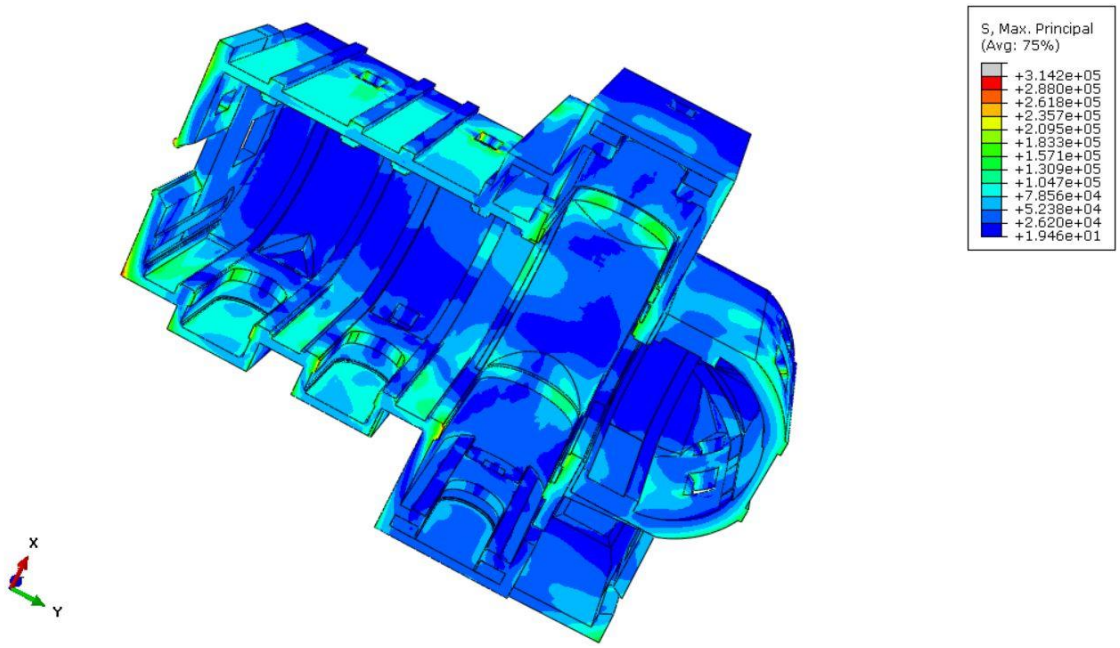

Figure 117: Tensile Stress Distribution of Response Spectrum in Y Direction, Bottom View

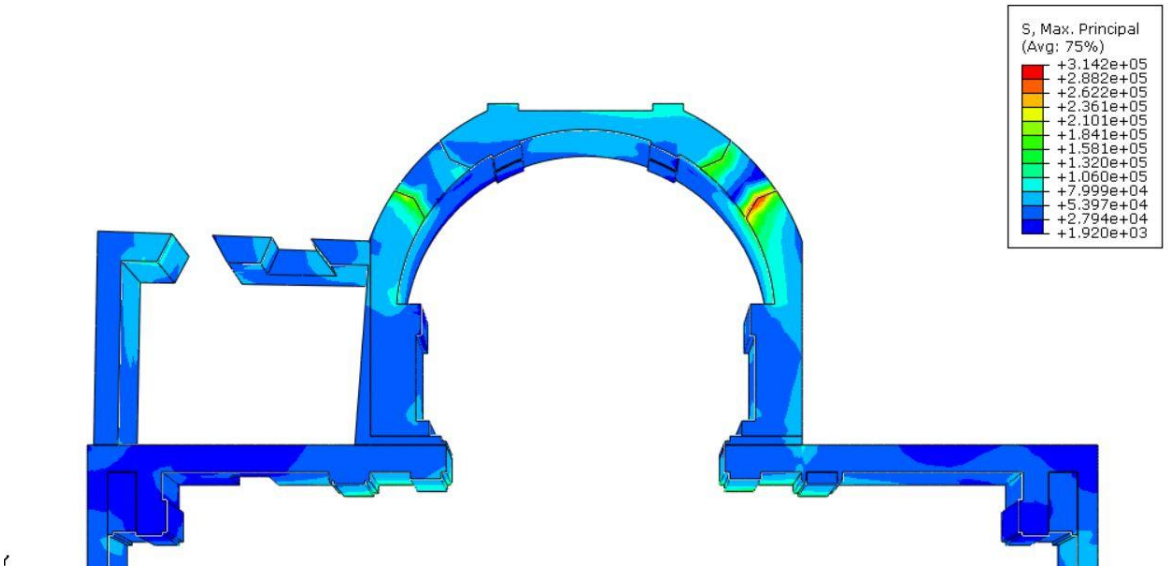

Figure 118: Tensile Stress Distribution of Response Spectrum in Y Direction, Z=4.2623 m

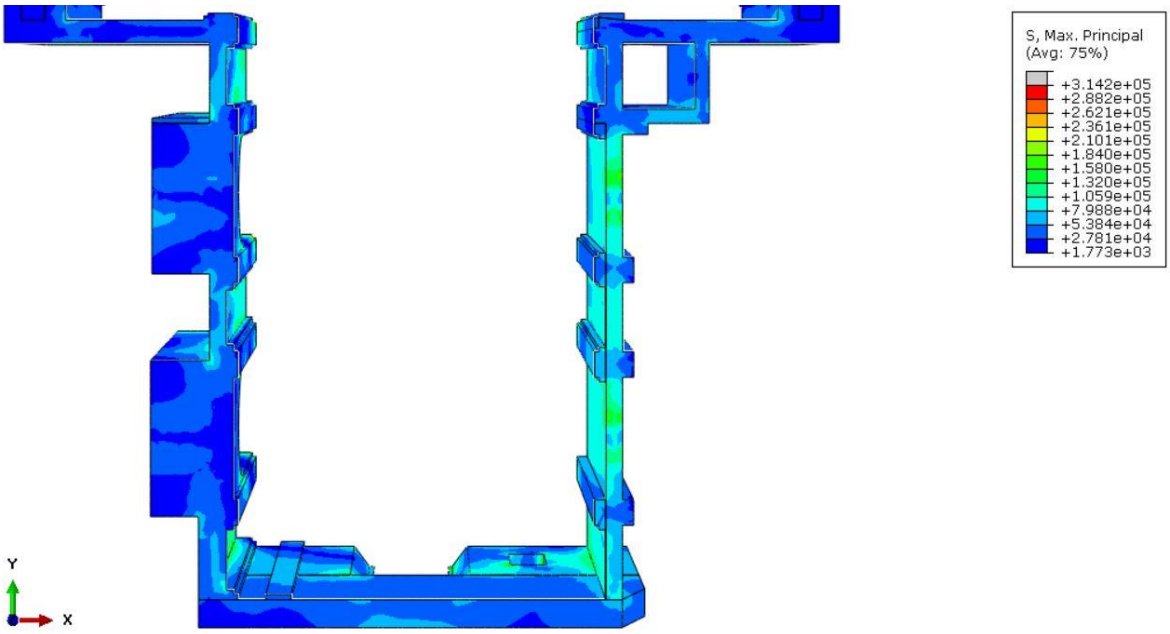

Figure 119: Tensile Stress Distribution of Response Spectrum in Y Direction, Z=10.8894 m

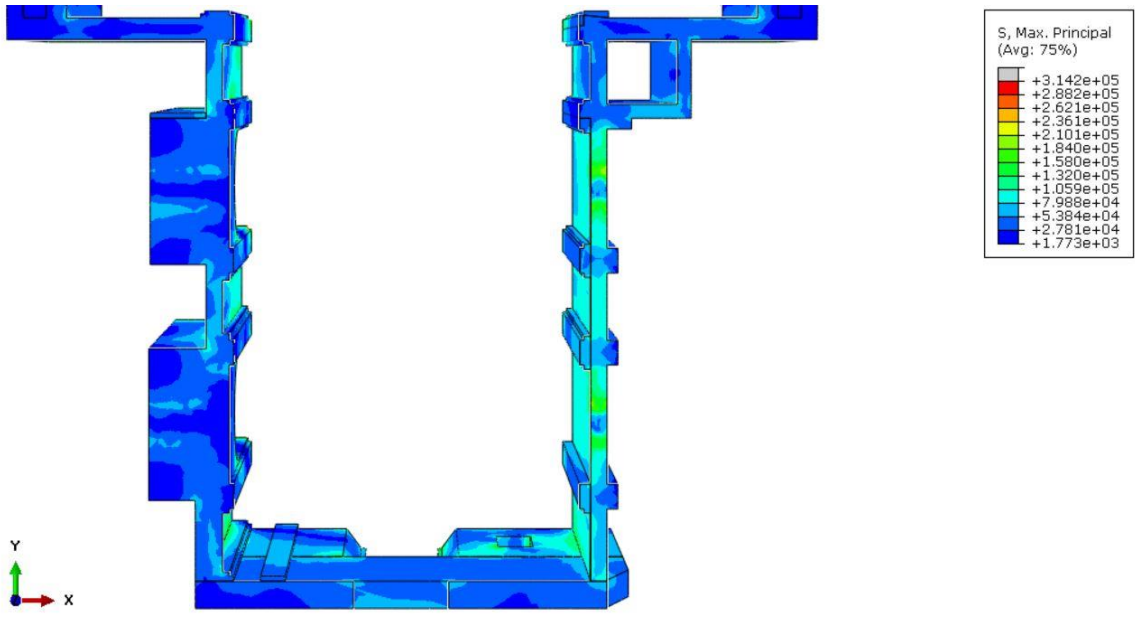

Figure 120: Tensile Stress Distribution of Response Spectrum in Y Direction, Z=11.0253 m

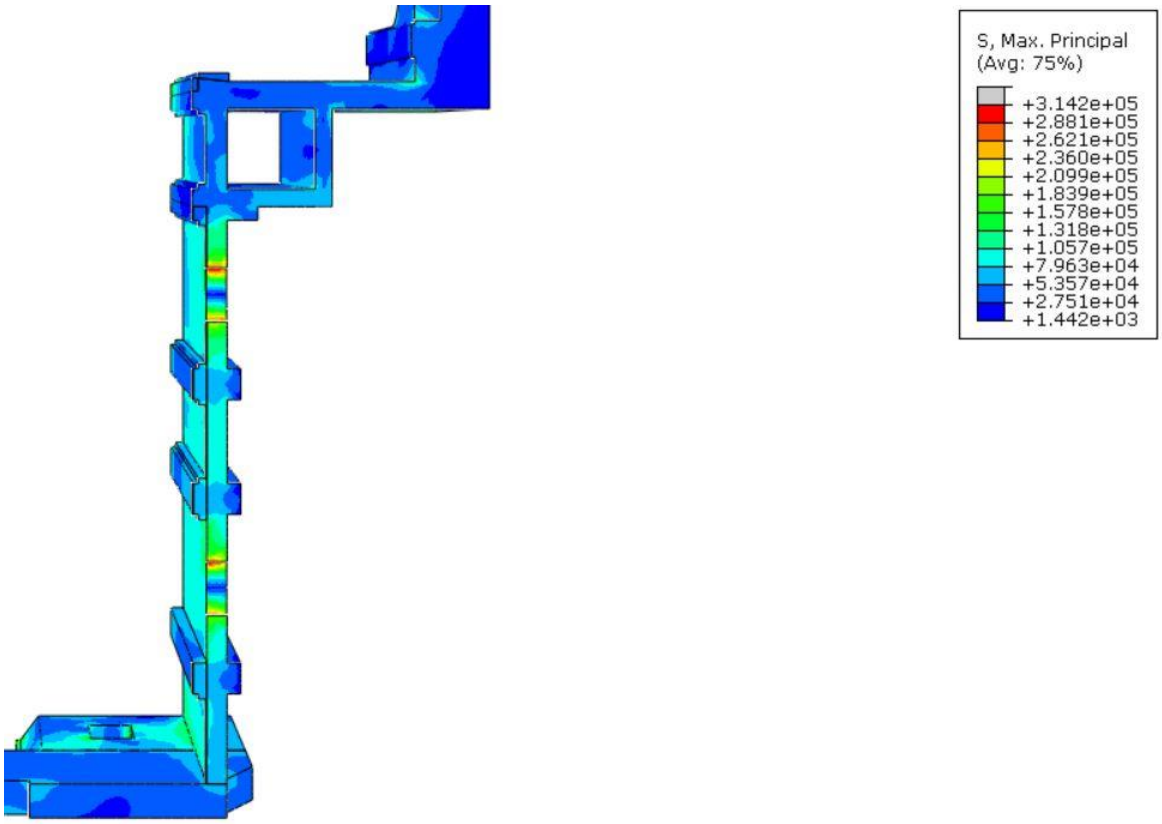

Figure 121: Tensile Stress Distribution of Response Spectrum in Y Direction, Z=11.5047 m

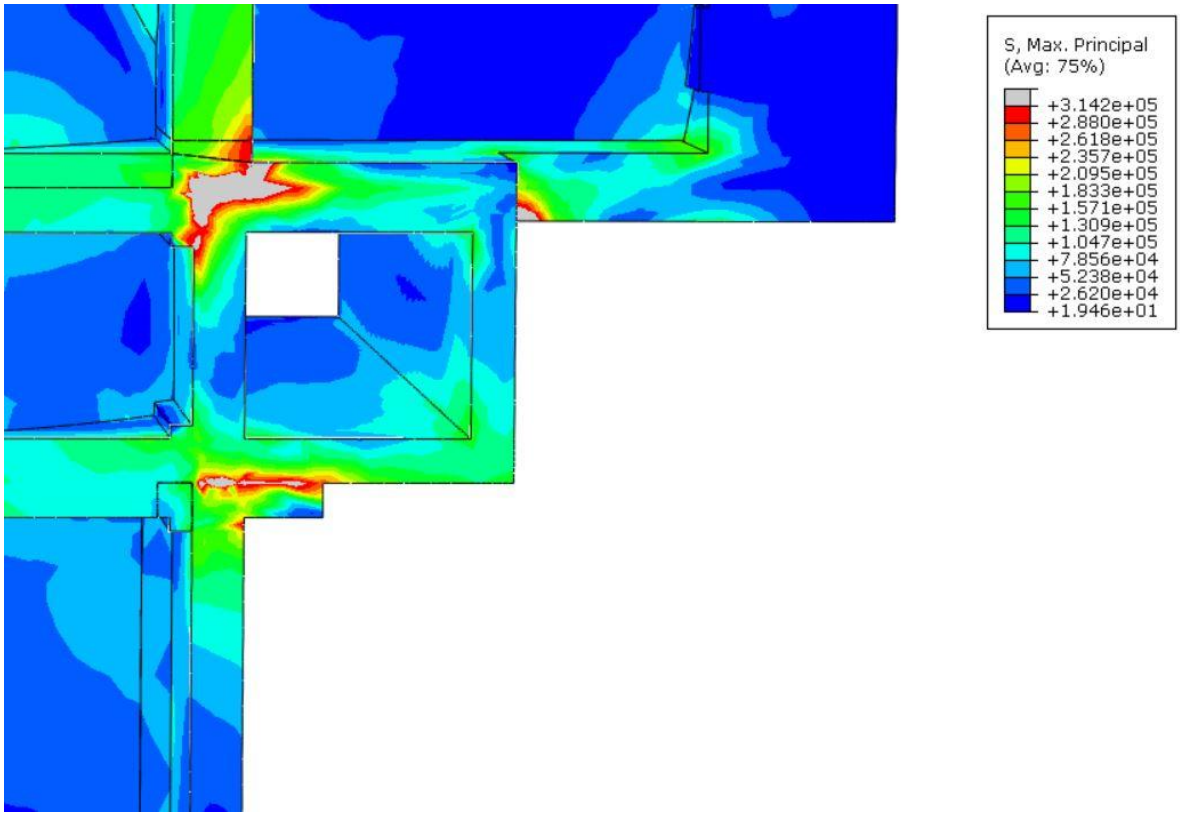

Figure 122: Tensile Stress Distribution of Response Spectrum in Y Direction, Z=18.0416 m

6.3.3.2.2 Shear Stress Distribution

Shear stress distributions under the excitation in the Y direction are given in Figure 123, and Figure 124. Similar to tensile stress distribution, the critical region corresponds to the connection between the bell tower and the left transept. Furthermore, at the openings belonging to the apse, shear stress reaches the shear strength in a local manner. (see Figure 126: Shear Stress Distribution of Response Spectrum in Y Direction, Z=4.23579 m, and Figure 129: Shear Stress Distribution of Response Spectrum in Y Direction, Z=11.5047 m)

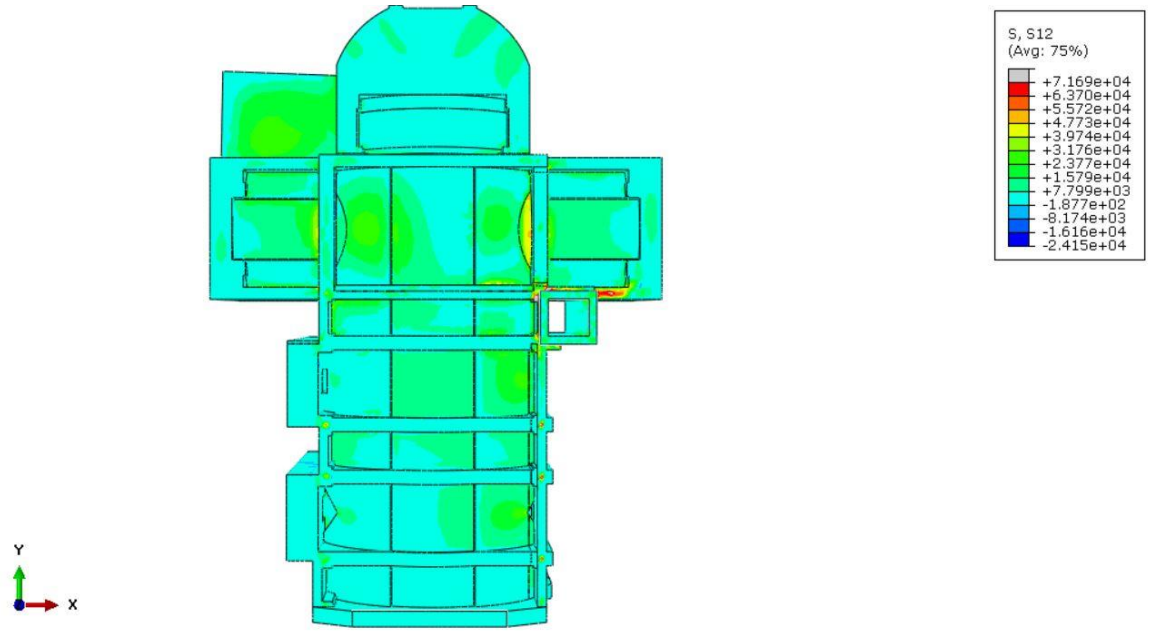

Figure 123: Shear Stress Distribution of Response Spectrum in Y Direction, Top View

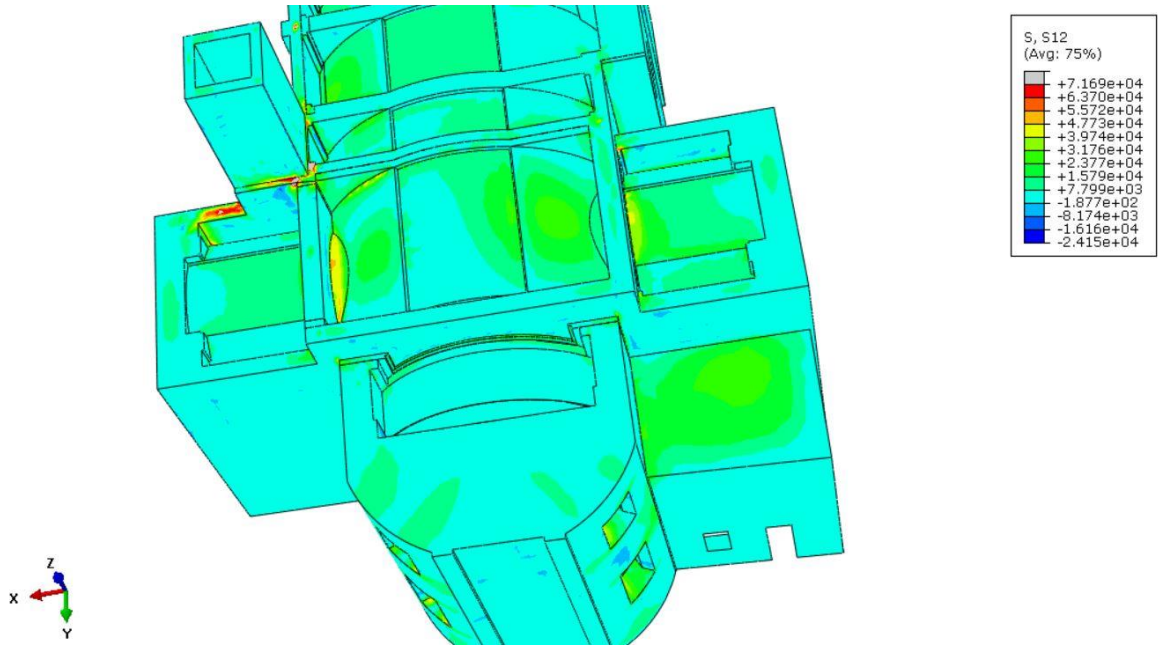

Figure 124: Shear Stress Distribution of Response Spectrum in Y Direction, Bell Tower, and Right Transept Connection

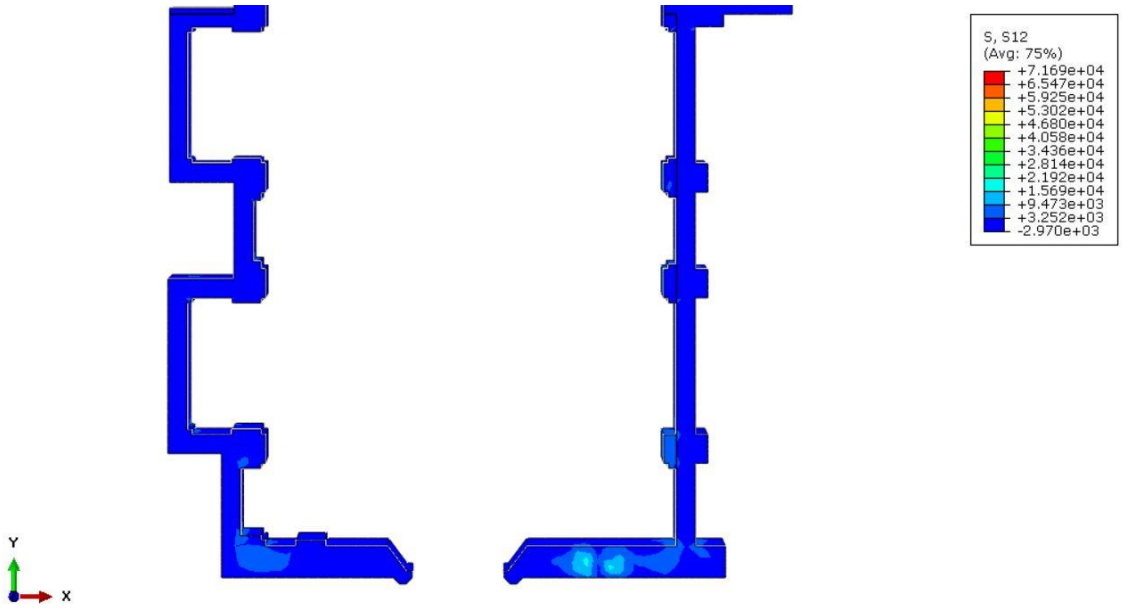

Figure 125: Shear Stress Distribution of Response Spectrum in Y Direction, Z=1.72566 m

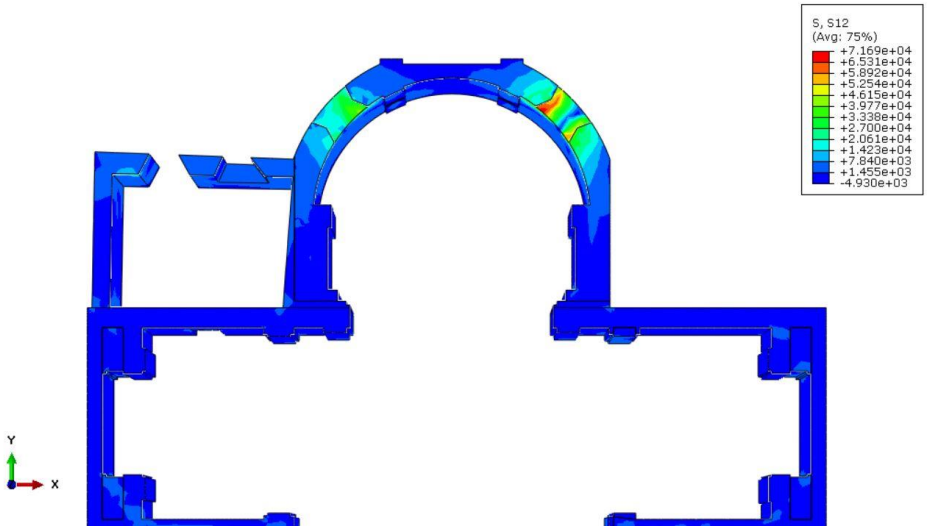

Figure 126: Shear Stress Distribution of Response Spectrum in Y Direction, Z=4.23579 m

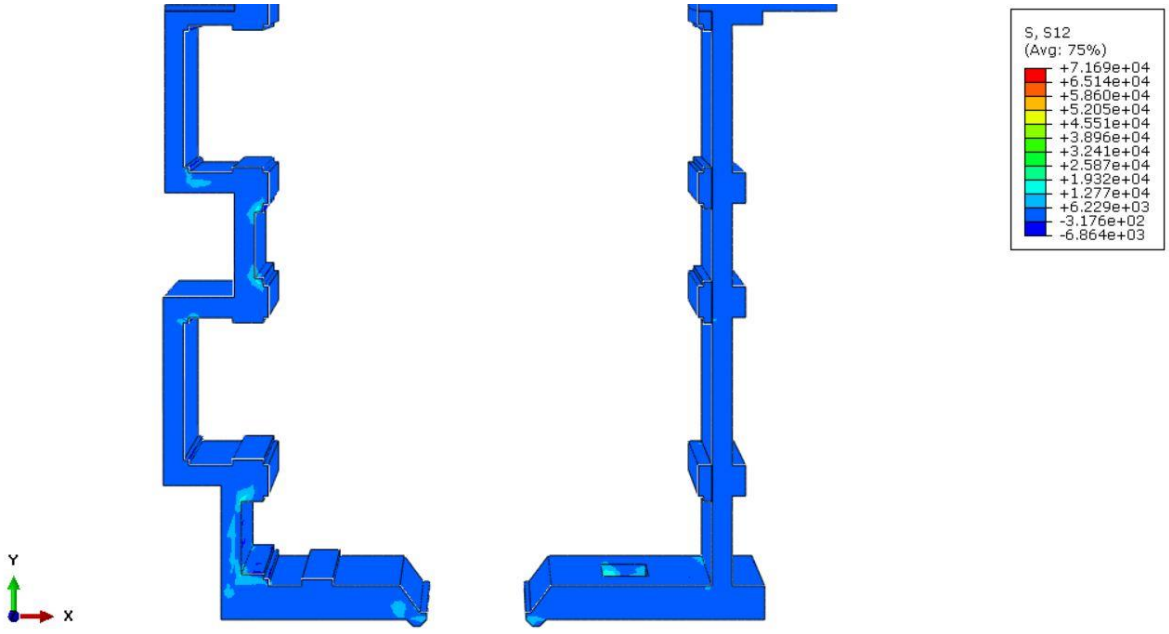

Figure 127: Shear Stress Distribution of Response Spectrum in Y Direction, Z=5.96152 m

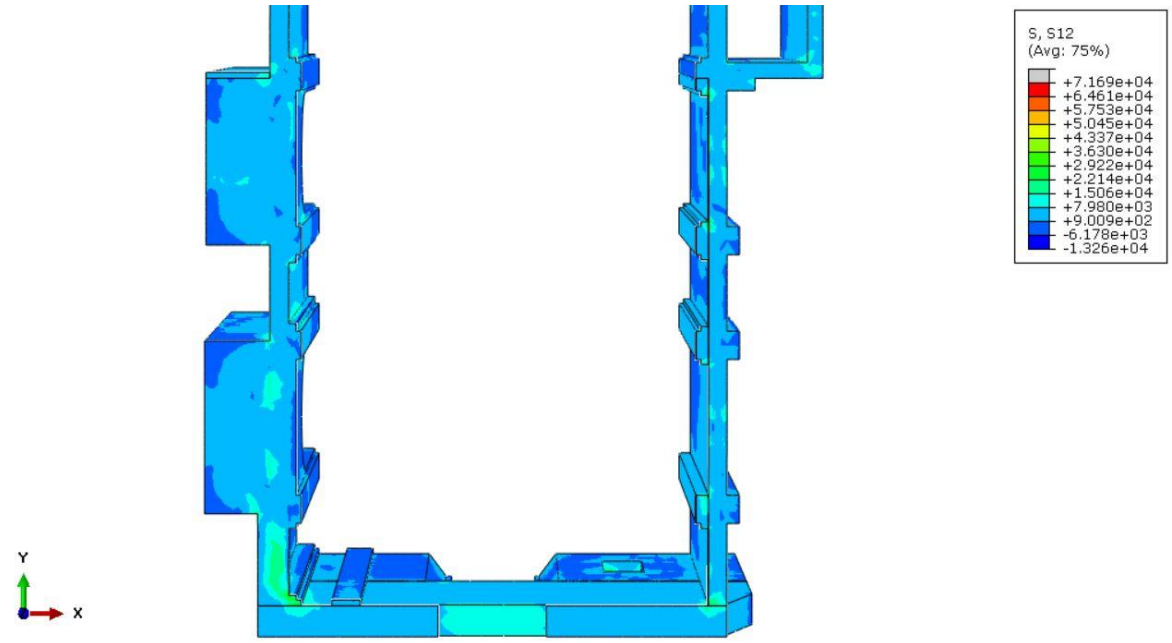

Figure 128: Shear Stress Distribution of Response Spectrum in Y Direction, Z=11.191 m

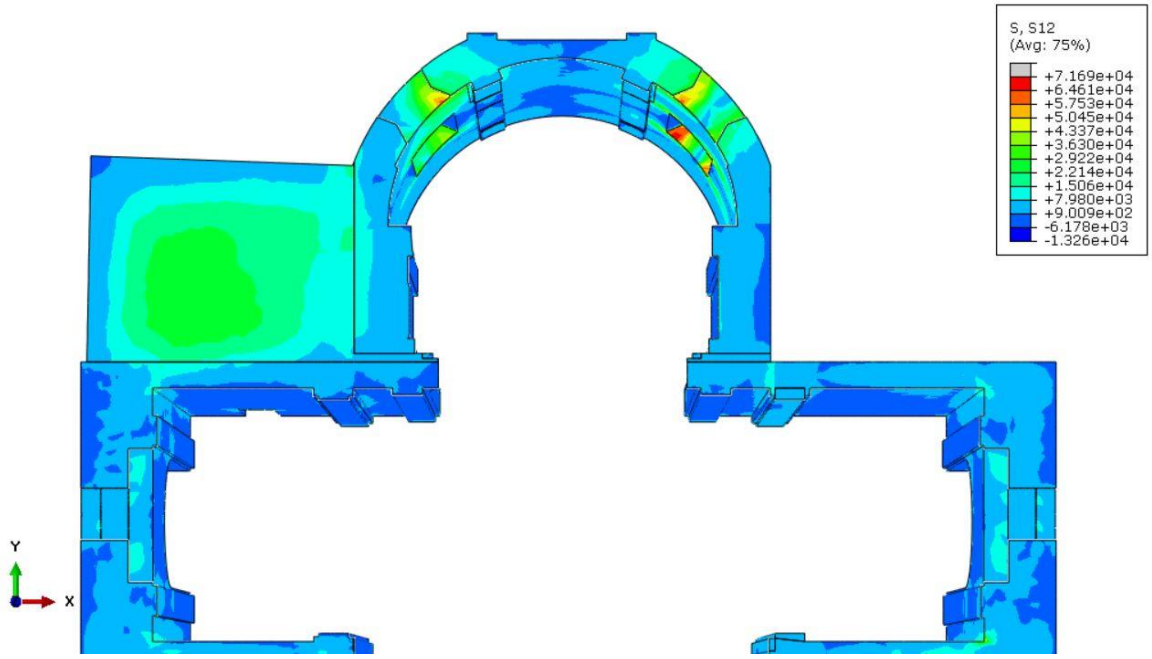

Figure 129: Shear Stress Distribution of Response Spectrum in Y Direction, Z=11.5047 m

6.3.3.2.3 Out of Plane Displacements

Maximum out-of-plane displacement was computed as 8.144 mm at the top of the bell tower. In addition, the maximum displacement at the middle height of the wall was determined as 3.313 mm.

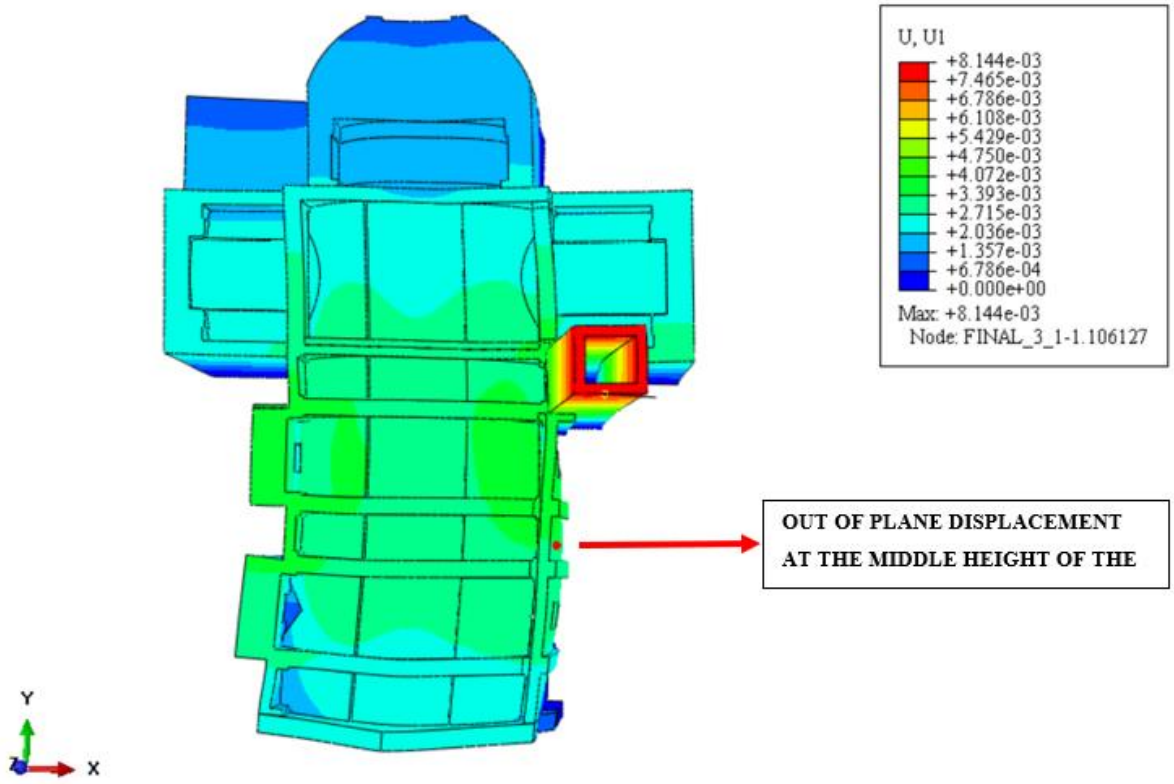
U, U1
+8.144e-03
+7.465e-03
+6.786e-03
+6.108e-03
+5.429e-03
+4.750e-03
+4.072e-03
+3.393e-03
+2.715e-03
+2.036e-03
+1.357e-03
+6.786e-04
+0.000e+00
Max: +8.144e-03
Node: FINAL_3_1-1.106127
OUT OF PLANE DISPLACEMENT
AT THE MIDDLE HEIGHT OF THE
Y
X

6.4 Pushover Analysis

There are two ways of making a non-linear analysis. One is done with the acceleration time histories that are applied to the non-linear model. Another approach is called push-over analysis which is a non-linear static method. In this approach, ground shaking is represented by an elastic spectrum that gives the displacement demand of the SDOF structure. Then, the non-linear model is exploited to compute the capacity curve that presents the capacity of the structure in terms of displacement. Once the capacity curve is obtained, it is used to set up a structure that is a non-linear SDOF oscillator. Finally, the demand and capacity of the structure are compared over the same graph.

In other words, this curve can be considered a graphical representation of the relationship between base shear (vertical axis), and horizontal displacement of the selected point (horizontal axis).

In this step, pushover analysis was carried out by applying the horizontal loads that increase monotonically, and constant gravity loads to the transversal and longitudinal directions of the structure. Both Eurocode and Italian code (NTC) presents two different load distribution for pushover analysis.

For this case study, a uniform load pattern has been considered for both X and Y directions and each one has (+) and (-) directions. In ABAQUS, two gravity loads have been defined in the static non-linear analysis step. While gravity load has kept constant, the lateral loads have been increased monotonically. It is also worth mentioning that both material and geometric nonlinearity were taken into account in this step. By activating the “Nlgeom” option in the step module in ABAQUS, nonlinear effects of large displacements and deformations are factored into the analysis. To be able to monitor the top displacement, the node at the center of the vault between the façade and apse has been chosen as a control point. (See Figure 130: Controlled Node for Pushover Analysis)

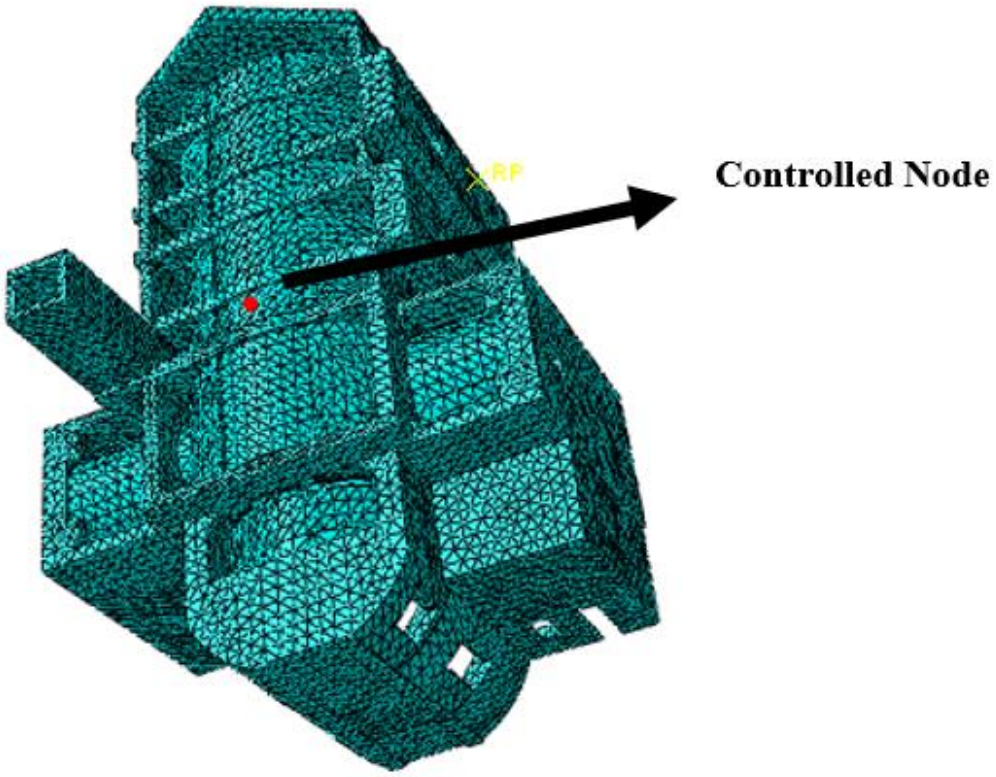

Figure 130: Controlled Node for Pushover Analysis

6.4.1 Methodology of Pushover Analysis

The history of non-linear analysis goes back to the study of the Q-model provided by Saiidi and Sozen in 1981. [35] It is a pioneering study in which they proposed a computationally low cost and effective method by considering only base moment and lateral displacement for capturing the dynamic behavior of structures. Following Q-model, Fajfar introduced a simple but effective method called the N2 method in order to assess the performance of the structures under earthquake loading in 1987 and 1989.[36] It is basically based on the comparison between the displacement capacity obtained from the pushover analysis on the NDOF system, and the response spectrum analysis on the equivalent SDOF system. In this method, firstly, the pseudo acceleration response spectrum is transformed into elastic acceleration (S_{ae}) and displacement spectrum (S_{de}) domain, namely Acceleration-Displacement Response Spectrum

(ADRS). To be able to do that, equation (54) is applied. The elastic pseudo-acceleration spectrum having 5 % damping for the structure is denoted in Figure 131.

Table 26: ADRS Spectrum Data Set

T (s)	S_e (g)	S_d [m]
0	0.05971	0
0.132291	0.158546	0.000689
0.396874	0.158546	0.006205
0.463644	0.135714	0.007249
0.530413	0.11863	0.008293
0.597183	0.105366	0.009337
0.663952	0.09477	0.010381
0.730722	0.086111	0.011425
0.797491	0.078901	0.012469
0.864261	0.072805	0.013513
0.931031	0.067584	0.014557
0.9978	0.063062	0.015601
1.06457	0.059106	0.016645
1.131339	0.055618	0.017689
1.198109	0.052518	0.018733
1.264878	0.049746	0.019777
1.331648	0.047252	0.020821
1.398417	0.044996	0.021865
1.465187	0.042945	0.022909
1.531957	0.041074	0.023953
1.598726	0.039358	0.024997
1.665496	0.03778	0.026041
1.732265	0.036324	0.027085
1.799035	0.034976	0.028129
1.903843	0.031231	0.028129
2.00865	0.028057	0.028129
2.113458	0.025343	0.028129
2.218266	0.023005	0.028129
2.323074	0.020976	0.028129
2.427882	0.019204	0.028129
2.53269	0.017648	0.028129
2.637498	0.016273	0.028129
2.742306	0.015053	0.028129
2.847113	0.013965	0.028129
2.951921	0.012991	0.028129
3.056729	0.012115	0.028129
3.161537	0.011325	0.028129
3.266345	0.01061	0.028129
3.371153	0.009961	0.028129
3.475961	0.009952	0.029878

3.580769	0.009952	0.031707
3.685576	0.009952	0.033591
3.790384	0.009952	0.035528
3.895192	0.009952	0.03752
4	0.009952	0.039567

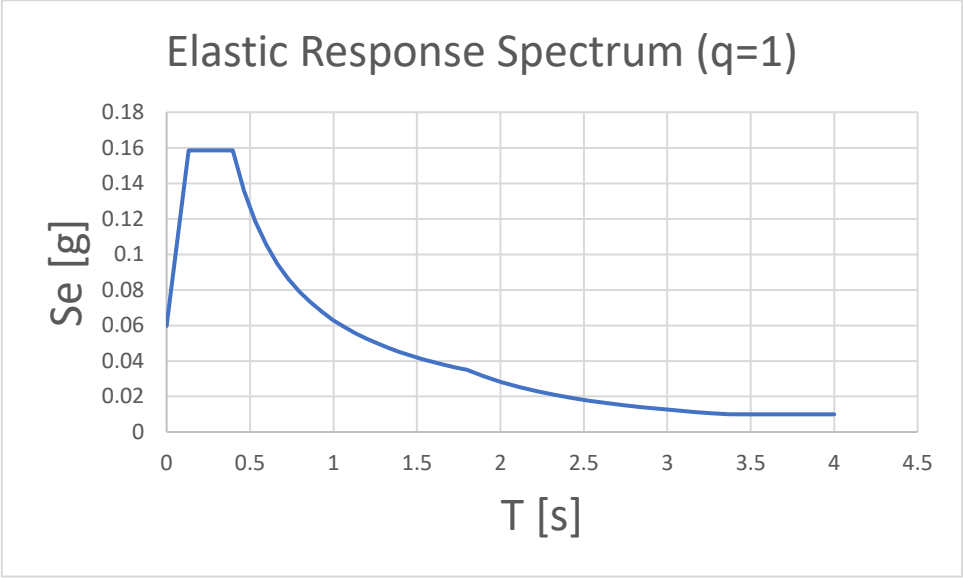

Figure 131: Elastic Pseudo-Acceleration Spectrum

Since it is much more convenient to compare the demand and the capacity of the structure on the basis of displacement, the elastic pseudo acceleration spectrum is converted into Acceleration-Displacement Response Spectrum as indicated in Figure 132.

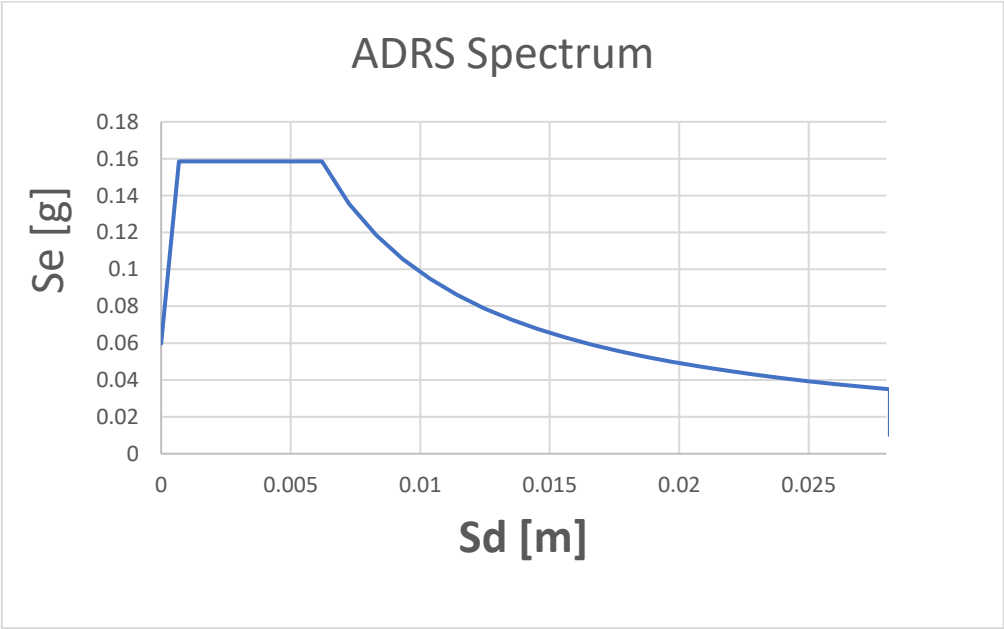

Figure 132: ADRS Spectrum

$$S_{de} = \frac{T^2}{4\pi^2} S_{ae} \tag{54}$$

In order to obtain the inelastic curves of acceleration spectrum and displacement spectrum, equation (55) and equation (56) that are a similar versions of the one proposed by Vidic et al. can be used. [36] For some constant ductility values, inelastic spectra and elastic spectrum are given in Figure 133.

$$S_a = \frac{S_{ae}}{R_\mu} \tag{55}$$

$$S_d = \frac{\mu}{R_\mu} S_{de} = \frac{\mu}{R_\mu} \frac{T^2}{4\pi^2} S_{ae} = \mu \frac{T^2}{4\pi^2} S_a \tag{56}$$

Where:

μ: ductility factor

R_μ: reduction factor

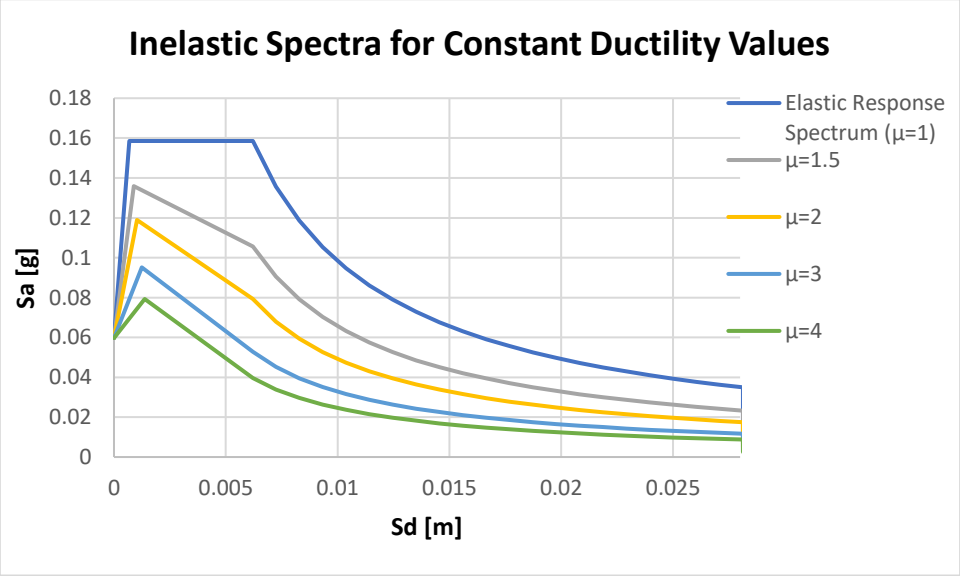

Figure 133: Inelastic spectra for constant Ductility Values

Fajfar defined the equation (57) and (58) for the reduction factor values.

$$R_\mu = (\mu - 1)\frac{T}{T_c} + 1 \qquad \text{for T<}T_c \tag{57}$$

$$R_\mu = \mu \qquad for\ T \geq T_c \tag{58}$$

At the end of pushover analysis, base shear and top displacement are collected in a graph so-called the “capacity curve.” However, this curve belongs to the NDOF (n degrees of freedom) structure. Hence, it can be turned into an SDOF (single degree of freedom) structure by means of a modal participation factor. By doing this transformation, the curve becomes bilinear in order to simplify the procedure.

$$d^* = \frac{D}{\Gamma} \tag{59}$$

$$F^* = \frac{V}{\Gamma} \tag{60}$$

Where:

Γ: Modal Participation Factor

D: Top Displacement of NDOF Structure

V: Base Shear of NDOF Structure

d^*: Top Displacement of SDOF Structure

F^*: Base Shear of SDOF Structure

In addition, the modal participation factor Γ is defined in equation (61).

$$\Gamma = \frac{\phi^T \cdot M \cdot 1}{\phi^T \cdot M \cdot \phi} = \frac{\sum m_i \phi_i}{\sum m_i {\phi_i}^2} = \frac{m^*}{\sum m_i \phi_i^2} \tag{61}$$

Where:

ϕ: Displacement Shape (Eigenvector)

m^*: Equivalent Mass of SDOF Structure

Table 27: Participation Factors for X and Y Directions

	X (+) and X (-)	Y (+) and Y (-)
Total Mass	6494143 kg	6494143 kg
Effective Mass [$\Gamma . m^*$]	4213 ton (mode 1)	4167 ton (mode 2)
Γ	1.10	1.06

In the analyses, Effective mass values for mode1 and mode-2 are taken as 4213 tons, and 4167 tons, respectively. It is also important to change the modal participation factors with respect to the value of the displacement at the control node. Having set the displacements at the control node unit, finally, modal participation factors are, in turn, 1.10 and 1.06 for X (+), X (-) and Y (+), Y (-) directions.

Besides, Fajfar proposed the elastic period of the idealized bilinear system (T^*) by equation (62).

$$T^* = 2\pi \sqrt{\frac{m^* D_y^*}{F_y^*}} \tag{62}$$

Where:

D_y^*: Yield Displacement

F_y^*: Yield Force

Then, the ordinate of the capacity curve in the acceleration displacement response spectrum domain can be found by means of equation (63).

$$S_{ay} = \frac{F_y^*}{m^*} \tag{63}$$

Lastly, the seismic demand is computed, and the procedure is divided into two ways in line with the value of the elastic period of the idealized bilinear system (T^*).

For T^*<T_c, the response is linear, and equations (64) and (65) are used in accordance with the value of $\frac{F_y^*}{m^*}$.

$$\frac{F_y^*}{m^*} \geq S_e(T^*), \qquad d_t^* = d_{et}^* \tag{64}$$

$$\frac{F_y^*}{m^*} < S_e(T^*), \qquad d_t^* = \frac{d_t^*}{q_u}\left(1 + (q_u - 1)\frac{T_c}{T^*}\right) \geq d_{et}^* \tag{65}$$

Where:

d_{et}^*: Elastic Displacement Demand

d_t^*: Inelastic Displacement Demand

In contrast, if T^*≥T_c, it is assumed as medium and long period, and the target displacement is elastic.

$$d_t^* = d_{et}^* \tag{66}$$

6.4.2 Results of the Pushover Analyses

6.4.2.1 Positive X Direction (+)

The direction of the lateral load can be seen in Figure 134.

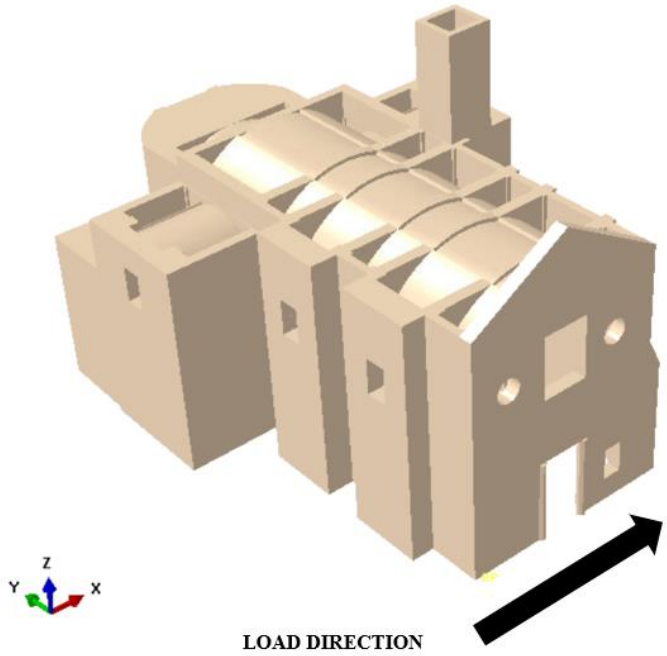

Figure 134: Positive X Load Direction

As an output of ABAQUS, the capacity curve under constant gravity load and monotonically increasing horizontal load in the X (+) direction is given in Figure 135. At the end of around 0.3 g loading, the capacity curve starts to have decreased trend.

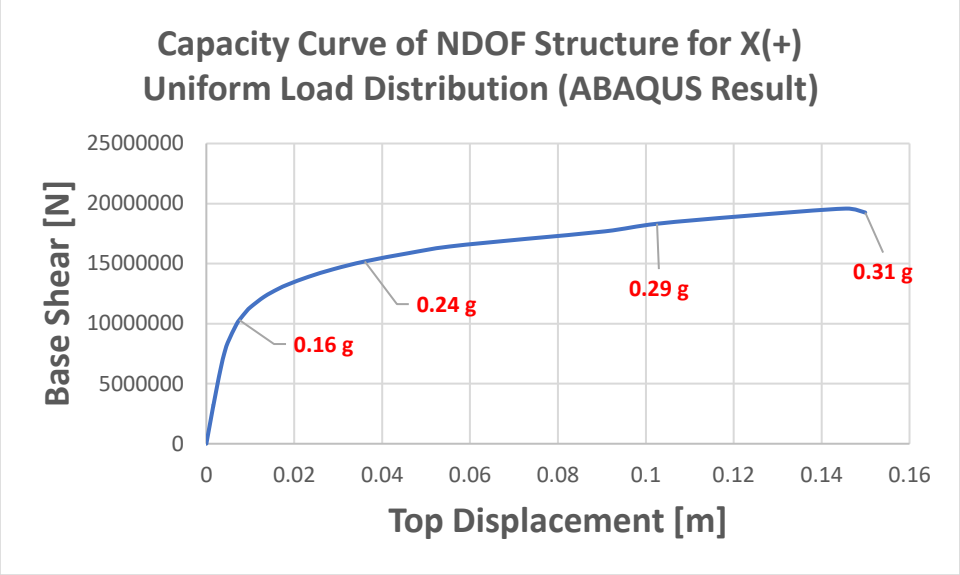

Figure 135: Capacity Curve of NDOF Structure for X (+) Direction

By equations (59) and (60), the capacity curve is scaled in order to pass the SDOF structure.

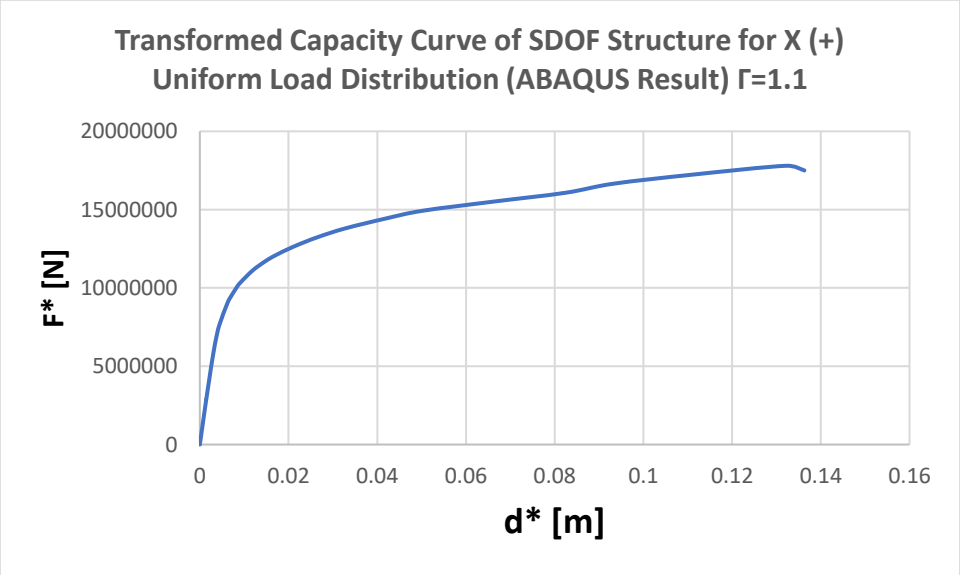

Figure 136: Capacity Curve of SDOF Structure for X (+) Direction

Then, the capacity curve was cut off until the displacement value reaches d_m^*. (See Figure 137: Chosen Capacity Curve of SDOF Structure for X (+) Direction)

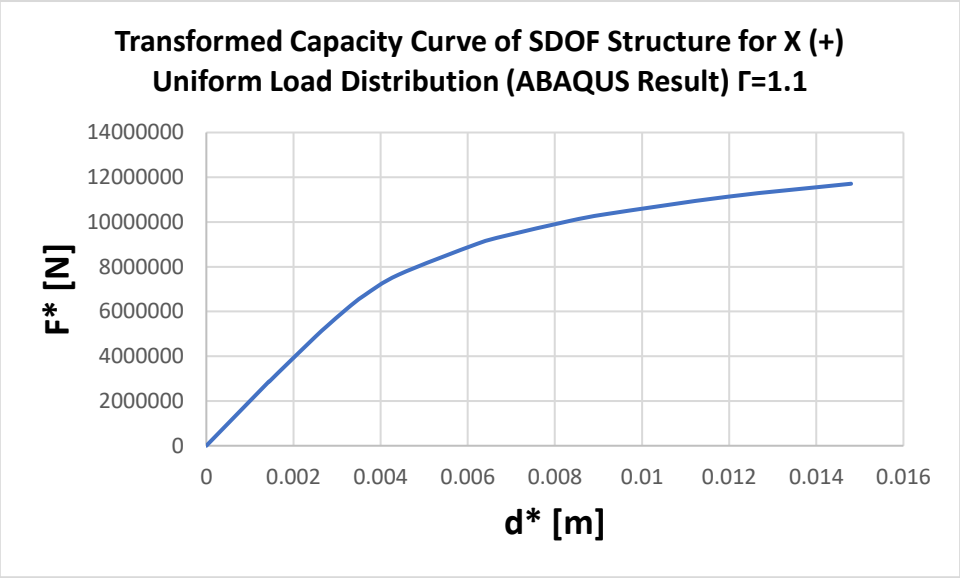

Figure 137: Chosen Capacity Curve of SDOF Structure for X (+) Direction

Firstly, the plastic mechanism is assumed to be reached at d_m^*. Then, by exploiting the same deformation energy principle for the actual curve and the bilinear one, yield displacement (d_y^*) is determined.

Having chosen target displacement (d_m^*) as 0.0148 m, the yield strength of the idealized bilinear curve became 11,711,091 N. Afterwards, the yield displacement was selected in a way that the areas under the curves become equal. Figure 138 contains the relevant quantities for the bilinearization of the actual capacity curve.

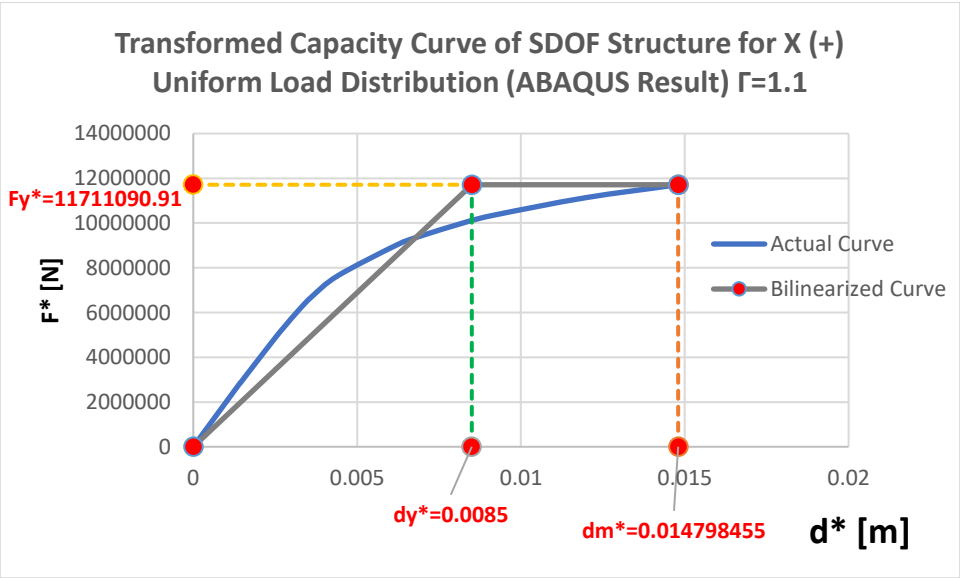

Figure 138: Transformed Capacity Curve of SDOF Structure for X (+) Uniform Load Distribution (ABAQUS Result) Γ=1.1

The final part is related to the procedure for which displacement demand is found. By means of equation (62), the elastic period of the idealized bilinear system (T^*) was computed as 0.331 s. Since T^* is lower than T_c (0.397 s) which is the ending corner period of the response spectrum, equation (64) or equation (65) should be adopted. To be able to decide which equation should be used, equation (63) must be used and the $S_e(T^*)$ that is the value of the acceleration for the value of computed T^* has to be read from the ADRS. Since $S_{ay}=F_y*/m*$ is greater than $S_e(T^*)$, equation (64) was followed. Hence, the elastic displacement demand is equal to the inelastic one. The crossing point between the demand spectrum and capacity curve gives the demand displacement for the SDOF structure (d_t^*). Lastly, this value can be converted to the one belonging to NDOF structure by multiplying (d_t^*) with the modal participation factor (Γ). As a result, it was determined that the demand displacement is lower than the capacity of the structure. The values of the relevant quantities are listed in Table 28.

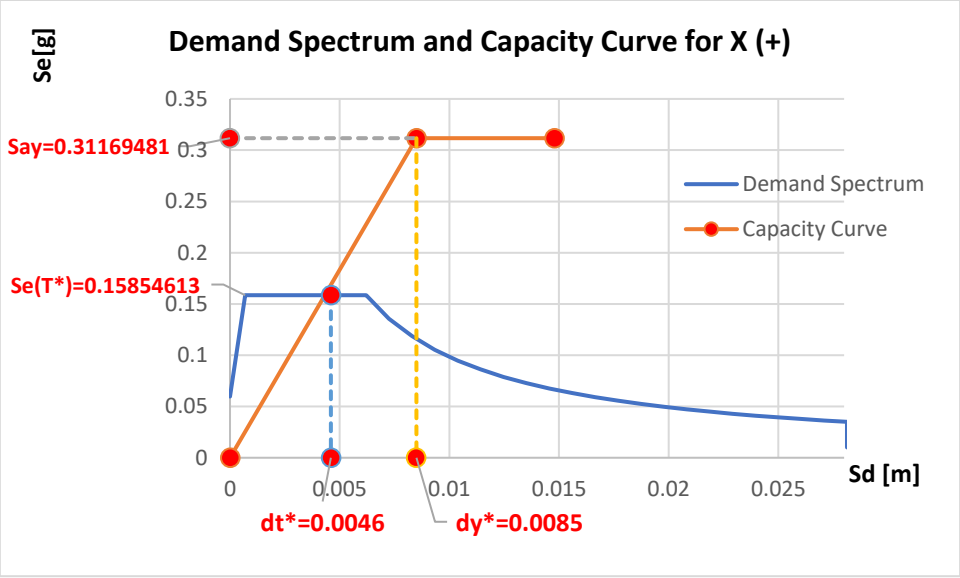

Figure 139: Demand Spectrum and Capacity Curve for X (+) Direction

Table 28: Comparison of Demand and Capacity for Pushover Analysis in X (+)

Participation Factor [Γ]	1.10
Equivalent Mass [m*]	3830 ton
Effective Mass [$\Gamma . m^*$]	4213 ton
d_m*	0.0243 m
d_y*	0.008 m

F_y^*	11,711,091N
$T^* = 2\pi\sqrt{\frac{m^* D_y^*}{F_y^*}}$	0.331 s
Tc	0.397
S_{ay}=Fy*/m*	0.4083 g
S_e(T*)	0.1586 g
d_t^*.=d_{et}^*.	0.0046 m
Demand Displacement for NDOF structure [d_t^*. Γ]	0.00506 m
Capacity Displacement for NDOF structure [Dt]	0.0148 m
d_t^*. · Γ=0.00506 m < 0.0148 m=Dt	

6.4.2.2 Pushover Analysis for X (-) Direction

The direction of the lateral load can be seen in Figure 140.

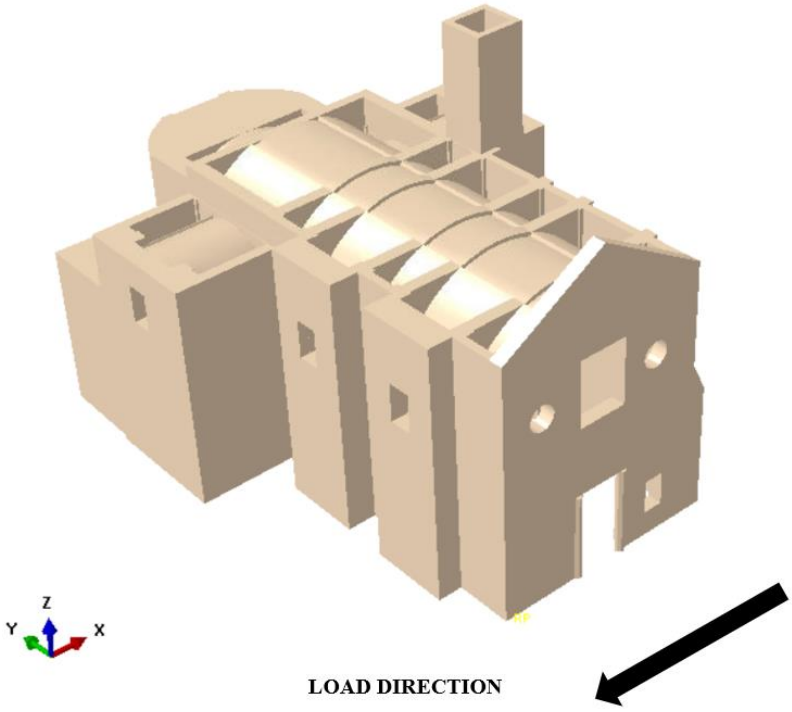

Figure 140: Load Direction of X (-)

By following the same procedure, the capacity curve of the NDOF structure was transformed into the one for the SDOF structure as given in Figure 141.

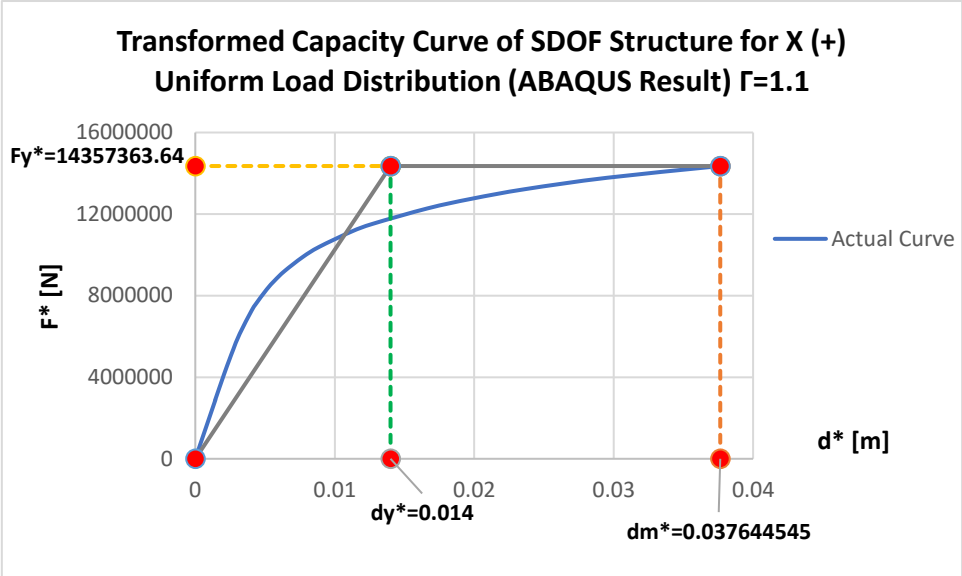

Figure 141: Transformed Capacity Curve of SDOF Structure for X (-) Uniform Load Distribution (ABAQUS Result) Γ=1.1

Then, the bilinear capacity curve is placed on the acceleration-displacement response spectrum domain as demonstrated in Figure 142.

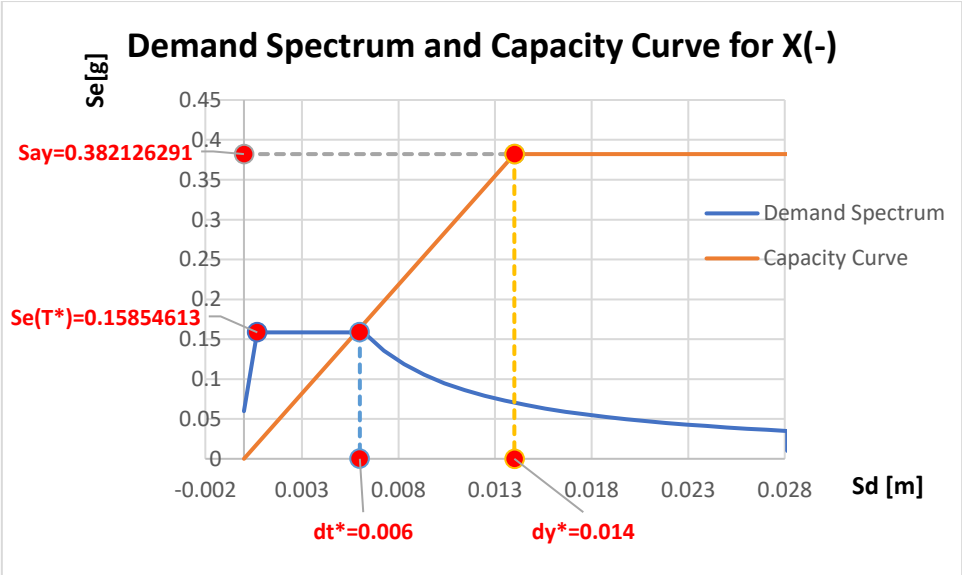

Figure 142: Demand Spectrum and Capacity Curve for X (-) Direction

Computed quantities and the result is listed in Table 29.

Table 29: Comparison of Demand and Capacity for Pushover Analysis in X (-)

Participation Factor [Γ]	1.10
Equivalent Mass [m*]	3830 ton
Effective Mass [$\Gamma . m^*$]	4213 ton
d_m*	0.037644545 m
d_y*	0.014 m
F_y^*	14,357,364 N
$T^* = 2\pi \sqrt{\frac{m^* D_y^*}{F_y^*}}$	0.383 s
Tc	0.397
S_{ay}=Fy*/m*	0.382 g
S_e(T*)	0.1586 g
d_t^*.=d_{et}^*.	0.006 m
Demand Displacement for NDOF structure [d_t^*. Γ]	0.0066 m
Capacity Displacement for NDOF structure [Dt]	0.041 m
d_t^*. · Γ=0.00606 m < 0.041 m=Dt	

6.4.2.3 Pushover Analysis for Y (+) Direction

The direction of the lateral load can be seen in Figure 143.

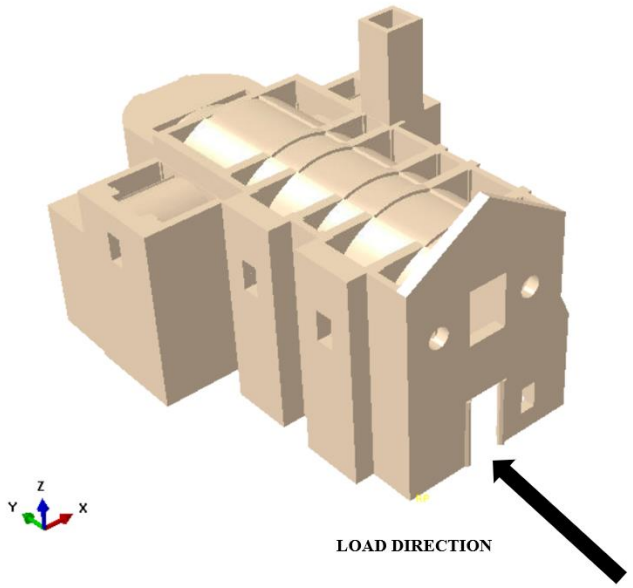

Figure 143: Load Direction of Y (+)

As an output of ABAQUS, the capacity curve under constant gravity load and monotonically increasing horizontal load in the Y (+) direction is given in Figure 144. At the end of around 0.43 g loading, the capacity curve starts to have decreased trend.

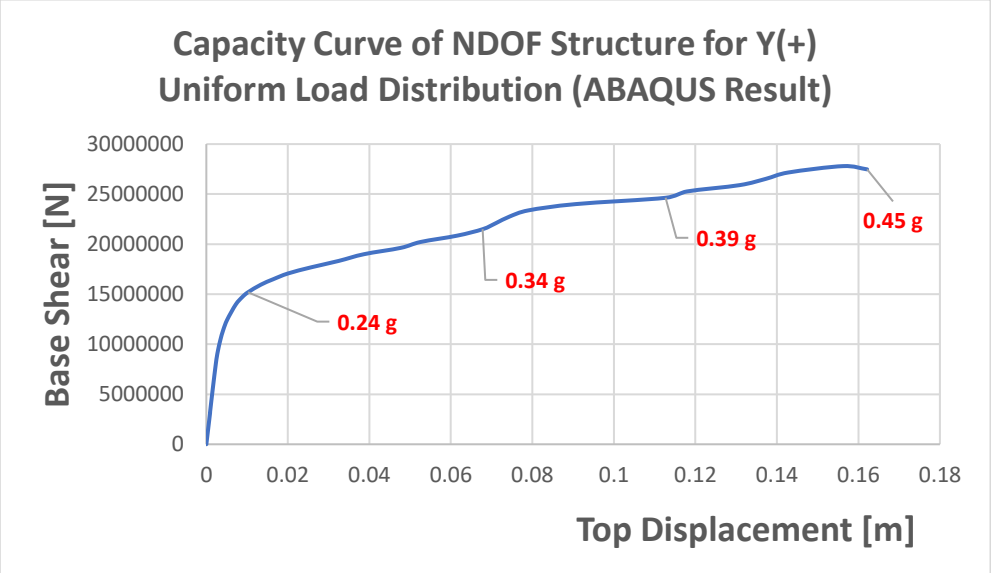

Figure 144: Capacity Curve of NDOF Structure for Y (+) Direction

By means of equations (59) and (60), the capacity curve is scaled in order to pass the SDOF structure.

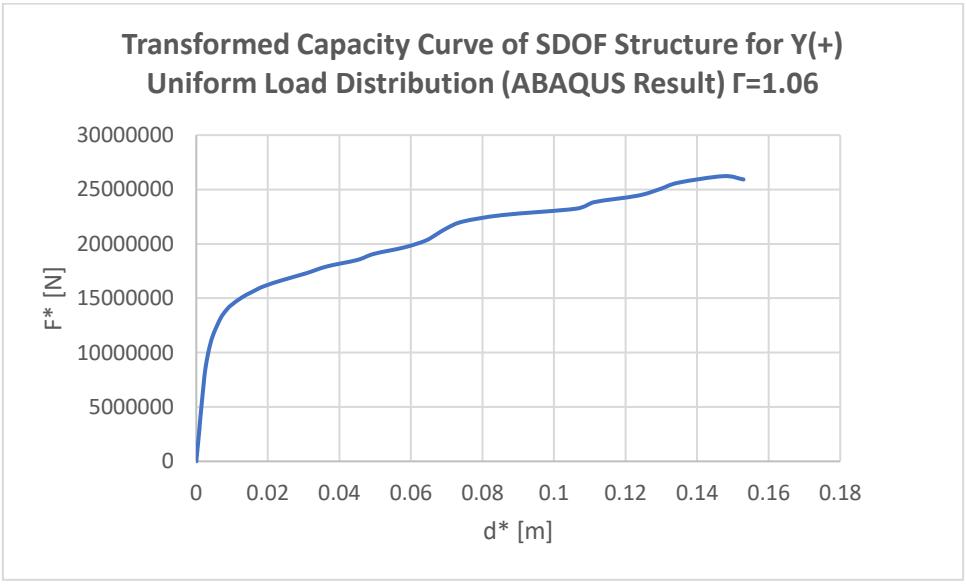

Figure 145: Capacity Curve of SDOF Structure for Y (+) Direction

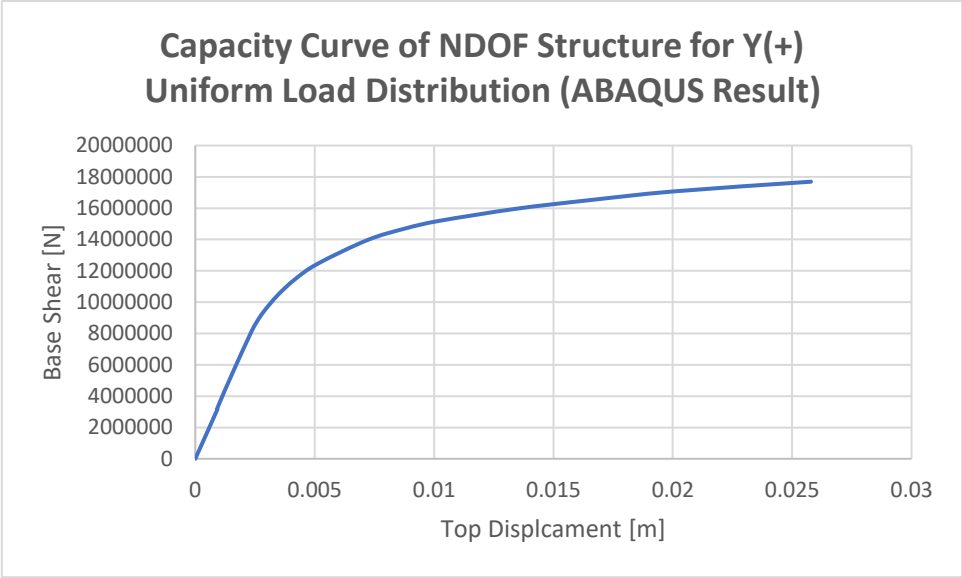

Figure 146: Chosen Capacity Curve of SDOF Structure for Y (+) Direction

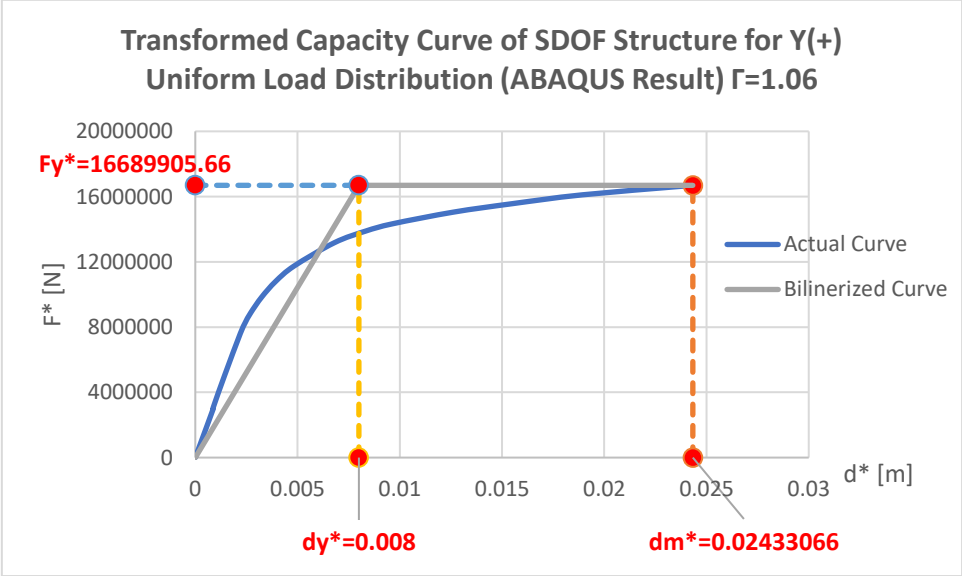

Figure 147: Transformed Capacity Curve of SDOF Structure for Y (+) Uniform Load Distribution (ABAQUS Result) Γ=1.06

By means of equation (62), the elastic period of the idealized bilinear system (T^*) was computed as 0.279 s. Since T^* is lower than T_c (0.397 s) which is the ending corner period of the response spectrum and $S_{ay}=F_y*/m*$ is greater than $S_e(T^*)$, equation (64) was exploited. The intersection point between the demand spectrum and capacity curve gives the demand displacement for the SDOF structure (d_t^*). To summarize, the demand displacement does not exceed the capacity of the structure. The values of the relevant quantities are listed in Table 30.

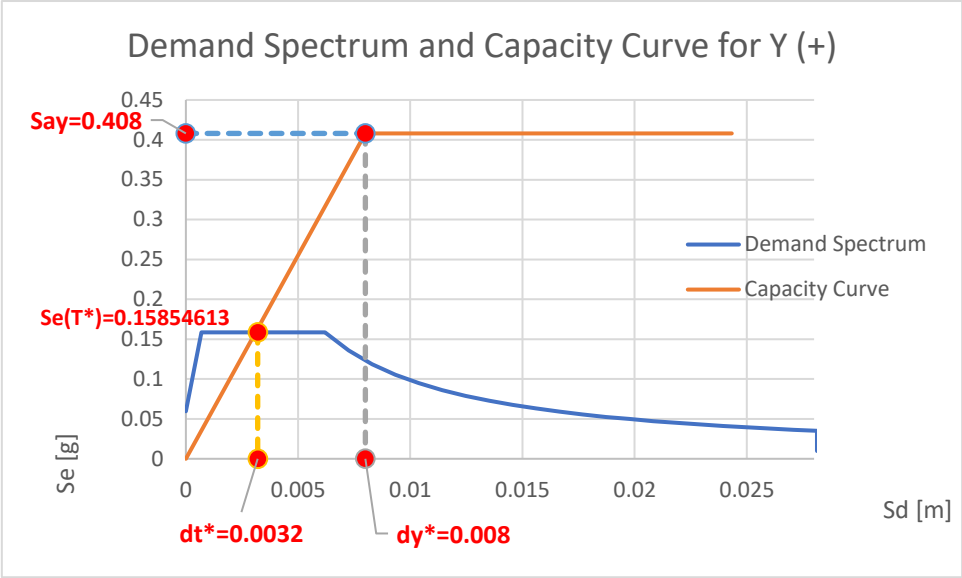

Figure 148: Demand Spectrum and Capacity Curve for Y (+) Direction

Table 30: Comparison of Demand and Capacity for Pushover Analysis in Y (+)

Participation Factor [Γ]	1.06
Equivalent Mass [m*]	4167 ton
Effective Mass [$\Gamma . m^*$]	4417 ton
dm*	0.0243 m
dy*	0.008 m
Fy*	16,689,906 N
$T^* = 2\pi\sqrt{\frac{m^* D_y^*}{F_y^*}}$	0.279 s
Tc	0.397
Say=Fy*/m*	0.4083 g
Se(T*)	0.1586 g
$d_{t.}^*=d_{et.}^*$	0.0032 m
Demand Displacement for NDOF structure [$d_{t.}^*$. Γ]	0.0034 m
Capacity Displacement for NDOF structure [Dt]	0.026 m
$d_{t.}^*$ · Γ=0.0034 m < 0.026 m=Dt	

6.4.2.4 Pushover Analysis for Y (-) Direction

The direction of the lateral load can be seen in Figure 149.

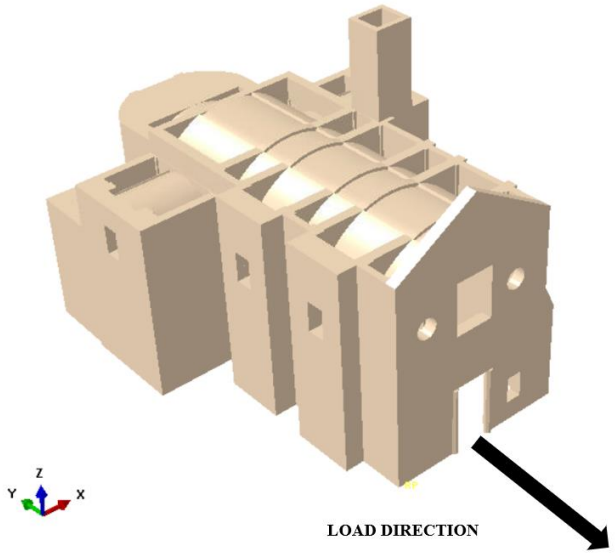

Figure 149: Load Direction of Y (-)

As an output of ABAQUS, the capacity curve under constant gravity load and monotonically increasing horizontal load in Y (-) direction is given in Figure 150. At the end of around 0.40 g loading, the capacity curve starts to have decreased trend. The same procedure was followed and reported in Table 31.

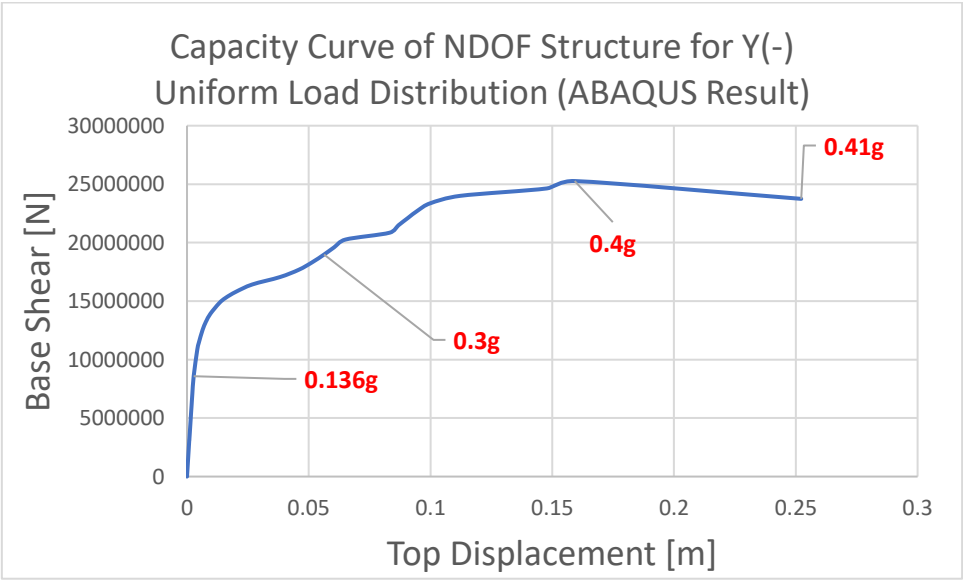

Figure 150: Capacity Curve of NDOF Structure for Y (-) Direction

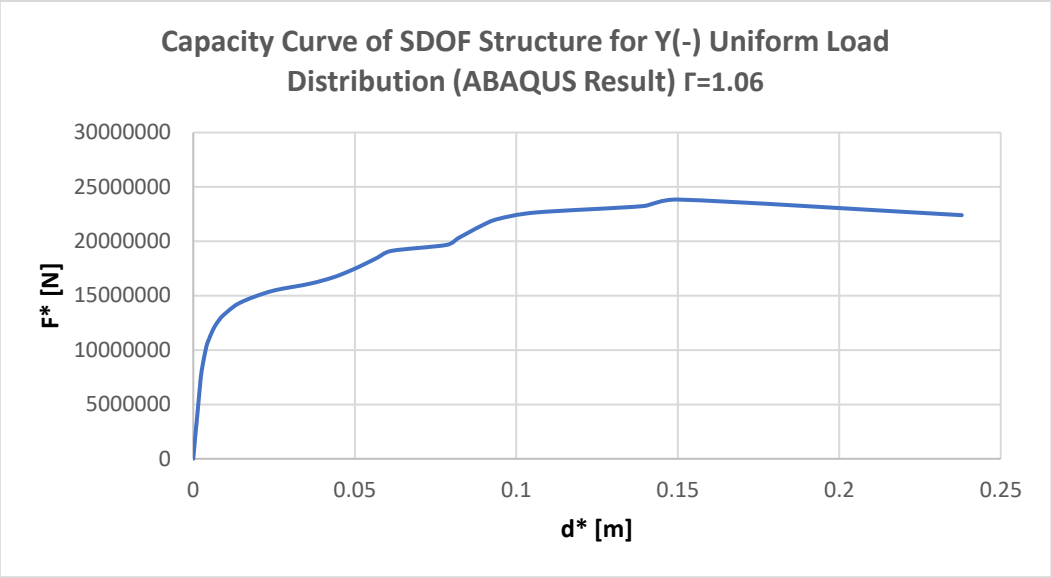

Figure 151: Capacity Curve of SDOF Structure for Y (-) Direction

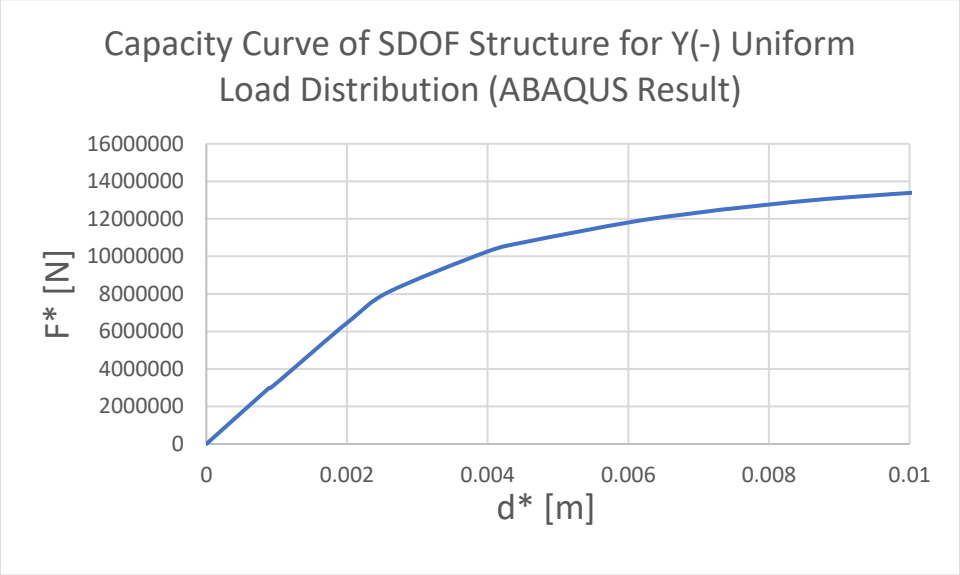

Figure 152: Chosen Capacity Curve of SDOF Structure for Y (-) Direction

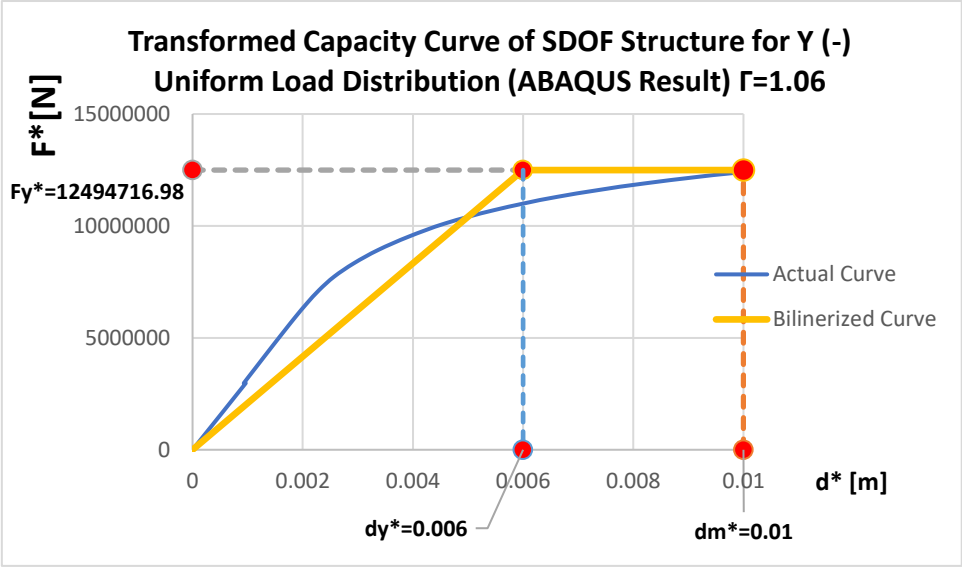

Figure 153: Transformed Capacity Curve of SDOF Structure for Y (-) Uniform Load Distribution (ABAQUS Result) Γ=1.06

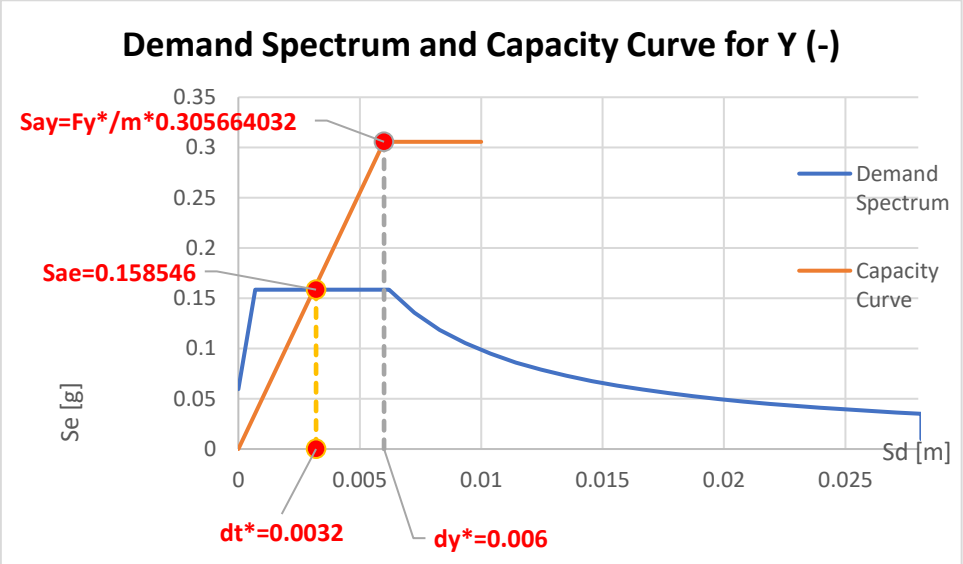

Figure 154: Demand Spectrum and Capacity Curve for Y (-) Direction

Table 31: Comparison of Demand and Capacity for Pushover Analysis in Y (-)

Participation Factor [Γ]	1.06
Equivalent Mass [m*]	4167 ton
Effective Mass [$\Gamma . m^*$]	4417 ton
dm*	0.0243 m
dy*	0.008 m
Fy*	12,494,717 N

$T^* = 2\pi\sqrt{\frac{m^* D_y^*}{F_y^*}}$	0.80 s
Tc	0.397
Say=F_y^*/m^*	0.4083 g
Se(T*)	0.1586 g
d_t^*.=d_{et}^*.	0.0032 m
Demand Displacement for NDOF structure [d_t^*. Γ]	0.0034 m
Capacity Displacement for NDOF structure [Dt]	0.0106 m
d_t^*. · Γ=0.0034 m < 0.0106 m=Dt	

6.4.2.5 Tensile Damage Distributions

In this part, the possible tensile damage patterns in the collapse situation are presented at the end of the applied monotonically increased horizontal loads in four directions and constant gravity. ABAQUS allows users to tensile damages and compressive damages for the non-linear analyses by defining the concrete damage plasticity model (CDP).

6.4.2.5.1 X (+) Direction

Tensile Damage distributions are shown in Figure 155, Figure 156, and Figure 157. It is seen that, for the façade, the damage is localized around the middle opening and the right rectangular opening.

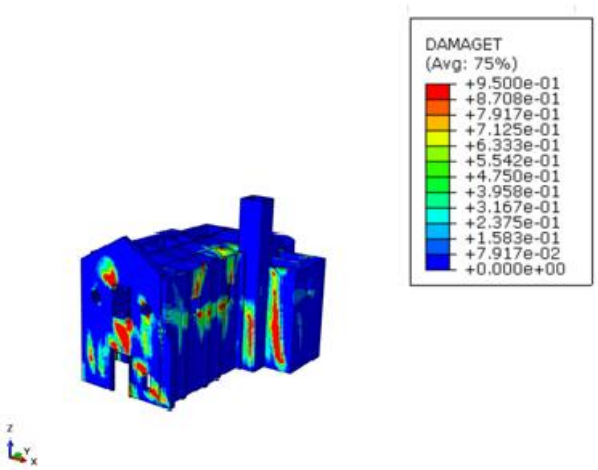

Figure 155: Tensile Damage Distribution under Pushover Loading in X (+), Right View

Moreover, the connection between the right transept and the nave undergoes considerably tensile damage. (See Figure 156: Tensile Damage Distribution under Pushover Loading in X (+), Left View)

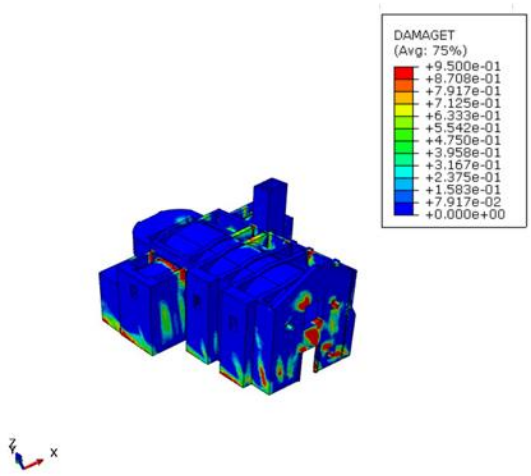

Figure 156: Tensile Damage Distribution under Pushover Loading in X (+), Left View

In addition, it is also noticed that the back of the left transept and the apse are exposed to tensile damage as seen in Figure 157.

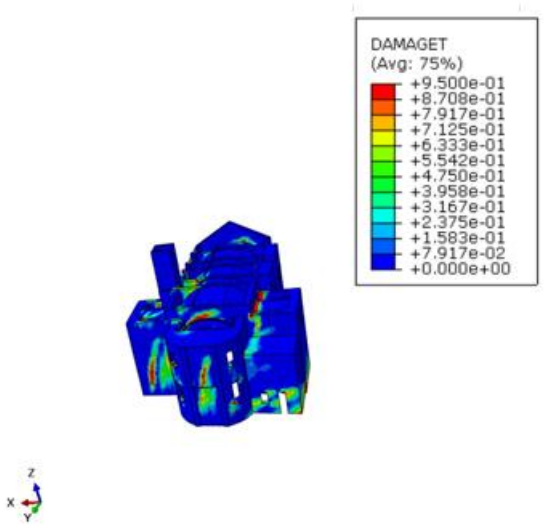

Figure 157: Tensile Damage Distribution under Pushover Loading in X (+), Back View

6.4.2.5.2 X (-) Direction

Similarly, for the loading in X (-), the façade undergoes tensile damage around the middle rectangular opening. (See Figure 158: Tensile Damage Distribution under Pushover Loading in X (-), Left View)

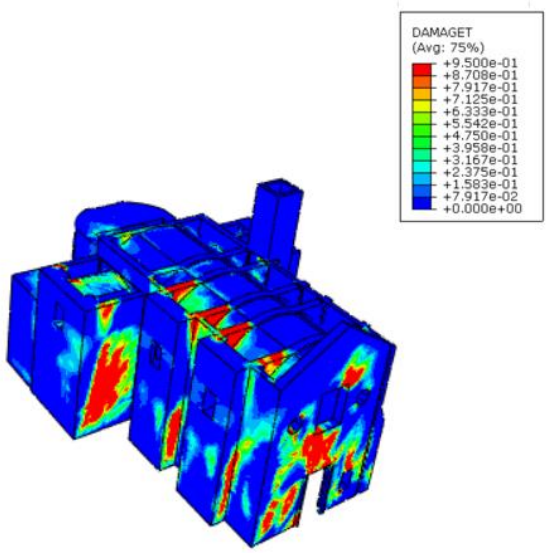

Figure 158: Tensile Damage Distribution under Pushover Loading in X (-), Left View

In Figure 159, tensile damages are accumulated at the right part of the barrel vaults, and the connection between the room-right transept has considerably tensile damages.

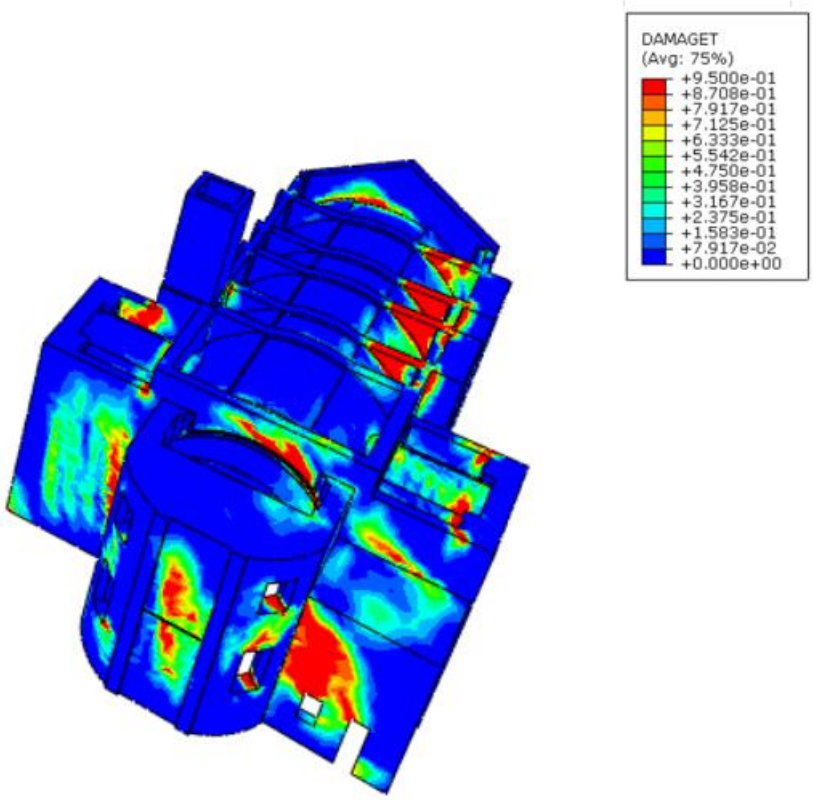

Figure 159: Tensile Damage Distribution under Pushover Loading in X (-), Back View

6.4.2.5.3 Y (+) Direction

Under this loading right walls, bell tower, and right transept are affected due to tensile damages.

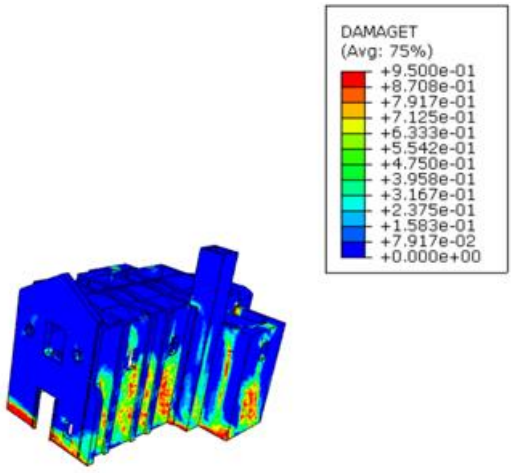

Figure 160: Tensile Damage Distribution under Pushover Loading in Y (+), Isometric View

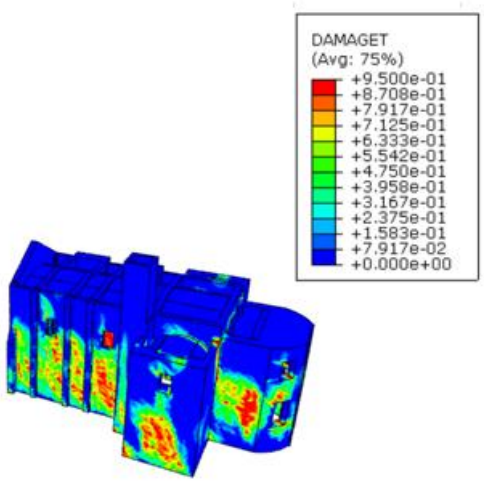

Figure 161: Tensile Damage Distribution under Pushover Loading in Y (+), Right View

6.4.2.5.4 Y (-) Direction

It can be observed that the back of the apse is extremely exposed to tensile damage. (See Figure 162: Tensile Damage Distribution under Pushover Loading in Y (-), Back View)

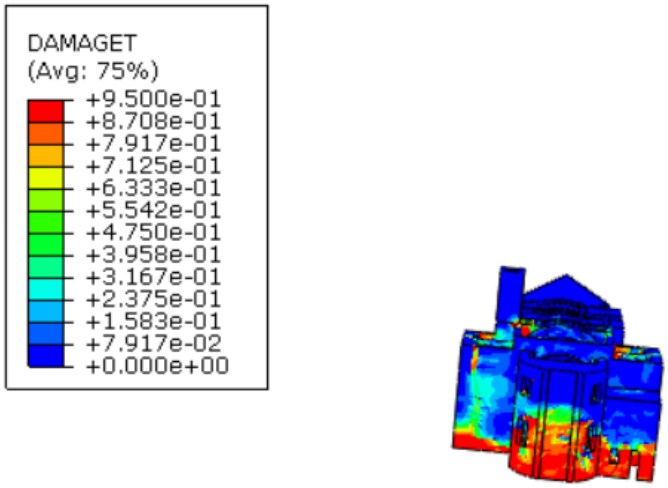

Figure 162: Tensile Damage Distribution under Pushover Loading in Y (-), Back View

Furthermore, both the lower levels of the openings at the right and left walls and the connection between the bell tower and right transept are damaged.

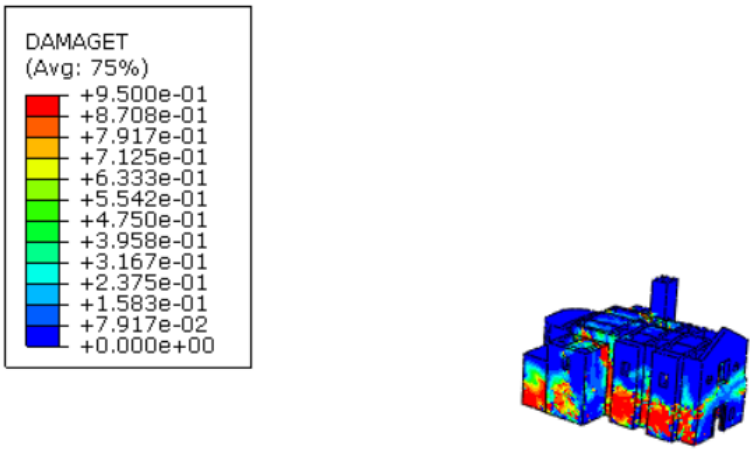

Figure 163: Tensile Damage Distribution under Pushover Loading in Y (-), Left View

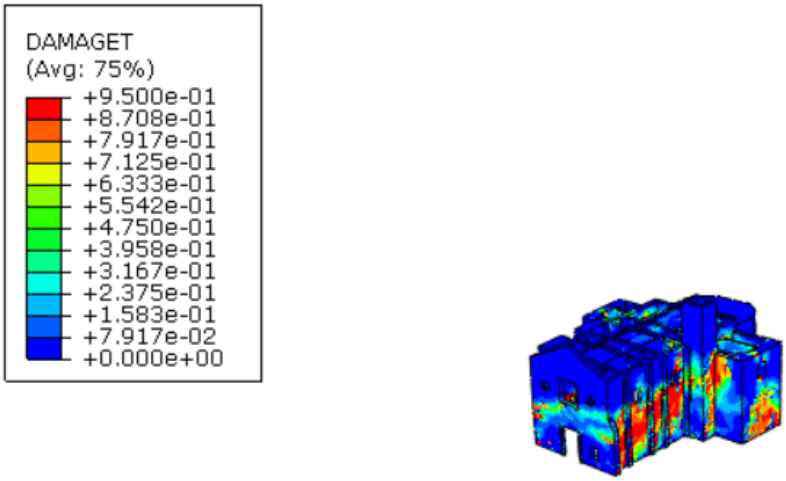

Figure 164: Tensile Damage Distribution under Pushover Loading in Y (-), Right View

7 Conclusion

In this study, the behavior of an ancient masonry church has been examined for seismic actions. Although advanced geometric models and numerical models are possible nowadays, it is still challenging work to model the peculiar geometries of churches. The usage of the 3-D solid elements is essential for the non-linear analyses of this kind of structure. Additionally, it should also be underlined that mimicking the bending behavior of walls needs careful numerical models. However, the complex geometries of the masonry churches and need for the solid elements make the numerical model extremely heavy. That's why still balancing the computation cost and the capability of capturing the behavior of structures plays a significant role in the 3-D Non-linear Finite Element Analyses. Once the dominant modes had been evaluated at the end of modal analysis, more affected regions of the structure were observed. Mode-1 has 64.9 percent effective mass for translation in the X direction, and 68.03 percent of mass for translation in the Y direction is excited in mode 2. Linear analyses carried out by self-weight loads and response spectrum method point out that the structure has limited acted stress levels. Hence, for the undamaged condition of the structure, it can be deemed to be at a safe level. The results of the static non-linear analyses also showed that the structure has high resistance levels for seismic actions. For future study, the dynamic non-linear analysis could be carried out and its results can be compared with the one performed in this study. In addition, it is also worth reminding that laboratory tests would be the most accurate method in order to obtain the material properties of the masonry.

8 Bibliography

[1] M. Zizi, J. Rouhi, C. Chisari, D. Cacace, and G. De Matteis, “Seismic vulnerability assessment for masonry churches: An overview on existing methodologies,” *Buildings*, vol. 11, no. 12, 2021, doi: 10.3390/buildings11120588.

[2] S. Huerta, “The Analysis of Masonry Architecture: A Historical Approach,” *Archit. Sci. Rev.*, vol. 51.4, pp. 297–328, 2008.

[3] G. Brandonisio, G. Lucibello, E. Mele, and A. De Luca, “Damage and performance evaluation of masonry churches in the 2009 L’Aquila earthquake,” *Eng. Fail. Anal.*, vol. 34, pp. 693–714, 2013, doi: 10.1016/j.engfailanal.2013.01.021.

[4] F. Clementi, E. Quagliarini, F. Monni, E. Giordano, and S. Lenci, “Cultural Heritage and Earthquake: The Case Study of ‘Santa Maria Della Carità’ in Ascoli Piceno,” *Open Civ. Eng. J.*, vol. 11, no. 1, pp. 1079–1105, 2018, doi: 10.2174/1874149501711011079.

[5] J. C. Scrivener, *Reinforced masonry*, vol. 5, no. 4. 1972.

[6] M. Como, *Statics of Historic Masonry Constructions: An Essay*. 2015.

[7] A. Bayraktar, A. Şahin, D. M. Özcan, and F. Yildirim, “Numerical damage assessment of Haghia Sophia bell tower by nonlinear FE modeling,” *Appl. Math. Model.*, vol. 34, no. 1, pp. 92–121, 2010, doi: 10.1016/j.apm.2009.03.033.

[8] P. B. Lourenço, J. G. Rots, and J. Blaauwendraad, “Continuum Model for Masonry: Parameter Estimation and Validation,” *J. Struct. Eng.*, vol. 124, no. 6, pp. 642–652, 1998, doi: 10.1061/(asce)0733-9445(1998)124:6(642).

[9] A. Jain, M. Acito, and C. Chesi, “Seismic sequence of 2016–17: Linear and non-linear interpretation models for evolution of damage in San Francesco church, Amatrice,” *Eng. Struct.*, vol. 211, no. March, p. 110418, 2020, doi: 10.1016/j.engstruct.2020.110418.

[10] A. Formisano and A. Marzo, “Simplified and refined methods for seismic vulnerability assessment and retrofitting of an Italian cultural heritage masonry building,” *Comput. Struct.*, vol. 180, pp. 13–26, 2017, doi: 10.1016/j.compstruc.2016.07.005.

[11] A. Ferrante, E. Giordano, F. Clementi, G. Milani, and A. Formisano, “Fe vs. De modeling for the nonlinear dynamics of a historic church in central italy,” *Geosci.*, vol. 11, no. 5, pp. 1–20, 2021, doi: 10.3390/geosciences11050189.

[12] E. Giordano, F. Clementi, A. Nespeca, and S. Lenci, “Damage assessment by numerical modeling of sant’agostino’s sanctuary in offida during the central italy 2016–2017 seismic sequence,” *Front. Built Environ.*, vol. 4, no. January, pp. 1–17, 2019, doi: 10.3389/fbuil.2018.00087.

[13] F. Clementi, “Failure analysis of apennine masonry churches severely damaged during the 2016 central italy seismic sequence,” *Buildings*, vol. 11, no. 2, pp. 1–17, 2021, doi: 10.3390/buildings11020058.

[14] R. Illampas, I. Ioannou, and P. B. Lourenço, “Seismic appraisal of heritage ruins: The case study of the St. Mary of Carmel church in Cyprus,” *Eng. Struct.*, vol. 224, no. April, p. 111209, 2020, doi: 10.1016/j.engstruct.2020.111209.

[15] M. Betti and A. Vignoli, “Assessment of seismic resistance of a basilica-type church under earthquake loading: Modelling and analysis,” *Adv. Eng. Softw.*, vol. 39, no. 4, pp. 258–283, 2008, doi: 10.1016/j.advengsoft.2007.01.004.

[16] M. Resta, A. Fiore, and P. Monaco, “Non-linear finite element analysis of masonry towers by adopting the damage plasticity constitutive model,” *Adv. Struct. Eng.*, vol. 16, no. 5, pp. 791–803, 2013, doi: 10.1260/1369-4332.16.5.791.

[17] E. Hökelekli, A. Demir, E. Ercan, H. Nohutçu, and A. Karabulut, “Seismic assessment in a historical masonry minaret by linear and non-linear seismic analyses,” *Period. Polytech. Civ. Eng.*, vol. 64, no. 2, pp. 438–448, 2020, doi: 10.3311/PPci.15126.

[18] A. C. Altunişik, A. Bayraktar, and A. F. Genç, “A study on seismic behaviour of masonry mosques after restoration,” *Earthq. Struct.*, vol. 10, no. 6, pp. 1331–1346, 2016, doi: 10.12989/eas.2016.10.6.1331.

[19] F. Cakir, B. S. Seker, A. Durmus, A. Dogangun, and H. Uysal, “Seismic assessment of a historical masonry mosque by experimental tests and finite element analyses,” *KSCE J. Civ. Eng.*, vol. 19, no. 1, pp. 158–164, 2015, doi: 10.1007/s12205-014-0468-4.

[20] “St. Carpoforo in Milan | LostFaith.” http://lostfaith.altervista.org/san-carpoforo/?doing_wp_cron=1641285127.8248999118804931640625 (accessed Mar. 16, 2022).

[21] “File:Chiesa sconsacrata di San Carpoforo.jpg - Wikimedia Commons.” https://commons.wikimedia.org/wiki/File:Chiesa_sconsacrata_di_San_Carpoforo.jpg

(accessed Mar. 16, 2022).

[22] T. . Tassios and M. P. Chronopoulos, “A seismic dimensioning of interventions (repairs/strengthening) on low-strength masonry building,” 1986.

[23] N. Mendes and P. B. Lourenço, “Seismic assessment of historic masonry structures: out-of-plane effects,” *Numer. Model. Mason. Hist. Struct. From Theory to Appl.*, pp. 141–162, Jan. 2019, doi: 10.1016/B978-0-08-102439-3.00004-X.

[24] Y. Kucukkagnici and S. Zakaria, “Seismic Assessment of the Ancient San Carpoforo Church in Milan, MSc. Thesis,” 2019.

[25] A. Borri and A. De Maria, “Scheda di valutazione dell’IQM (indice di qualità muraria,” *ReLUIS 3rd year report, Annex 3b.1-UR06-01*.

[26] A. Borri and A. De Maria, “Esempi compilati di scheda di valutazione dell’IQM,” *ReLUIS 3rd year report, Annex 3b.1-UR06-3.*

[27] A. Borri and A. De Maria, “Allegato 1 - LINEE GUIDA PER LA COMPILAZIONE DELLA SCHEDA IQM,” pp. 1–49, 2015.

[28] L. Rovero, V. Alecci, J. Mechelli, U. Tonietti, and M. De Stefano, “Masonry walls with irregular texture of L’Aquila (Italy) seismic area: validation of a method for the evaluation of masonry quality,” *Mater. Struct. Constr.*, vol. 49, no. 6, pp. 2297–2314, 2016, doi: 10.1617/s11527-015-0650-2.

[29] A. Borri, M. Corradi, G. Castori, and A. De Maria, “A method for the analysis and classification of historic masonry,” *Bull. Earthq. Eng.*, vol. 13, no. 9, pp. 2647–2665, 2015, doi: 10.1007/s10518-015-9731-4.

[30] A. Borri, M. Corradi, and A. De Maria, *The Failure of Masonry Walls by Disaggregation and the Masonry Quality Index*, vol. 3, no. 4. 2020.

[31] M. Acito, M. Bocciarelli, C. Chesi, and G. Milani, “Collapse of the clock tower in Finale Emilia after the May 2012 Emilia Romagna earthquake sequence: Numerical insight,” *Eng. Struct.*, vol. 72, no. May 2012, pp. 70–91, 2014, doi: 10.1016/j.engstruct.2014.04.026.

[32] A. B. Habieb, G. Milani, T. Tavio, and F. Milani, “Low Cost Frictional Seismic Base-Isolation of Residential New Masonry Buildings in Developing Countries: A Small

Masonry House Case Study," *Open Civ. Eng. J.*, vol. 11, no. 1, pp. 1026–1035, 2018, doi: 10.2174/1874149501711011026.

[33] S. Tiberti, M. Acito, and G. Milani, "Comprehensive FE numerical insight into Finale Emilia Castle behavior under 2012 Emilia Romagna seismic sequence: Damage causes and seismic vulnerability mitigation hypothesis," *Eng. Struct.*, vol. 117, pp. 397–421, 2016, doi: 10.1016/j.engstruct.2016.02.048.

[34] *Abaqus Theory Manuel*. .

[35] M. Saiidi and M. A. Sozen, "Simple Nonlinear Seismic Analysis of R/C Structures," *ASCE J Struct Div*, vol. 107, no. 5, pp. 937–952, 1981, doi: 10.1061/jsdeag.0005714.

[36] P. Fajfar and M.EERI, "A Nonlinear Analysis Method for Performance-Based Seismic Design," *Earthq. Spectra*, vol. 16, no. 3, pp. 573–592, 2000, doi: https://doi.org/10.1193/1.1586128.